Multiscale nonlinear and viscous numerical modelling of wave impact loads

Gatin, Inno

Doctoral thesis / Disertacija

2018

University of Zagreb
Faculty of Mechanical Engineering and Naval Architecture

Inno Gatin

Multiscale nonlinear and viscous numerical modelling of wave impact loads

DOCTORAL THESIS

Zagreb, 2018

University of Zagreb
Faculty of Mechanical Engineering and Naval Architecture

Inno Gatin

Multiscale nonlinear and viscous numerical modelling of wave impact loads

DOCTORAL THESIS

Supervisor: prof. Hrvoje Jasak, PhD

Zagreb, 2018

Sveučilište u Zagrebu
Fakultet strojarstva i brodogradnje

Inno Gatin

Multiskalno nelinearno i viskozno numeričko modeliranje udarnih valnih opterećenja

DOKTORSKI RAD

Mentor: prof. dr. sc. Hrvoje Jasak

Zagreb, 2018

Acknowledgements

I would like to express my sincere gratitude to my mentor and supervisor, Prof. Hrvoje Jasak, for exhaustive knowledge and guidance that shaped my scientific work. His relentless drive to do better and more pushed me towards achieving this thesis, giving me at the same time plenty of freedom to pursue my research interests and goals. He always strived to support me in my work with all available means, and for this I am greatly indebted.

Achieving the knowledge and skill to bring this study to a successful end would not be possible without my dear colleague and friend Dr. Vuko Vukčević. He is responsible for endless hours of discussion and instruction that had made an invaluable contribution to my work. Together with him, I want to thank my colleagues Tessa, Gregor, Vanja and Robert for making the days run by smoothly in good humour and plenty of fun.

The financial and scientific support received from Bureau Veritas, Paris, France, is greatly acknowledged. I want to thank Dr. Šime Malenica from Bureau Veritas for supporting me in my research, and for providing advices and insights that helped in making the outcome of this work more industrially relevant.

Finally, I owe a great deal to my wife Lucija for supporting me and dealing with me on my bad days, to whom together with my daughter Jana I dedicate my work.

Abstract

Numerical framework for simulation of wave impact loads on ships and offshore structures in ocean environment is developed in this study, where fully nonlinear, viscous, turbulent and compressible two–phase flow is considered. Number of numerical methods and models are developed, tested and applied to provide a clear, comprehensive, reliable, robust and efficient numerical procedure for assessing wave impact loads on marine structures, with emphasis on green sea loads.

The computational efficiency of the framework is improved by developing enhanced hydro–mechanical coupling strategies which reduce the number of nonlinear iterations required for the fluid flow–rigid body motion coupling to converge. A detailed verification and validation of the present numerical model is performed in order to ascertain the accuracy and precision in calculating green sea pressure loads, where a novel geometrical Volume–of–Fluid method is used and evaluated. Furthermore, a two–phase flow model is developed where water is assumed to be incompressible, while air is modelled as ideal adiabatic gas. The abrupt change in fluid properties across the interface, mainly density and compressibility, is handled with the Ghost Fluid Method, while Volume–of–Fluid method is used for interface capturing. The Ghost Fluid Method allows a one–cell–sharp representation of the interface with respect to the density field as well as compressibility effects, thus accurate and conservative trapped air cushioning effects can be captured, which is the main goal of the present numerical model. A pressure based formulation and the assumption of isentropic compression/expansion results in a highly efficient method, where no notable overheads exist with respect to the incompressible version of the model. The model is thoroughly verified and validated for flows without significant compressibility effects, as well as events where trapped air compression effects are important, such as breaking wave impact and free fall impact.

Finally, a complete procedure for assessing wave impact loads is conducted with the developed model for an Ultra Large Container Ship, where green water loads on a deck structure at the bow are sought. The procedure relies on linear frequency domain method to provide a long term distribution of ship response, which is in turn used to define a deterministic design wave. Two different approaches for defining the design wave are used and compared.

The development conducted in this work is performed within the Naval Hydro Pack software library, which is based on collocated Finite Volume method–based Computational Fluid Dynamics software `foam-extend`, community driven fork of the open–source software `OpenFOAM`.

Keywords:
Wave impact loads, Green sea loads, Two–phase compressible flow, Ghost Fluid Method, Polyhedral Finite Volume method, Naval Hydro Pack, foam–extend

Prošireni Sažetak

Brodovi i pučinski objekti izloženi su djelovanju vjetra i valova, pri čemu udarna valna opterećenja predstavljaju posebnu opasnost za sigurnost posade, opreme i broda. Relativno niska vjerojatnost pojave ekstremnih valnih udara čini ih teškim za opisati i predvidjeti, dok predstavljaju vrlo značajan faktor prilikom projektiranja konstrukcija pomorskih objekata. Ekstremna valna opterećenja zbog toga predstavljaju važan izazov ne samo zbog sigurnosti konstrukcija već i zbog potencijalnih ušteda koje se mogu postići smanjenjem dimenzija konstruktivnih elemenata novogradnje uslijed boljeg poznavanja pojave valnog udara. Postoje razne pojave koje su vezane uz udarna valna opterećenja poput udaranja pramca (eng. "*slamming*") i opterećenja uslijed vode na palubi (eng. "*green sea*"). Karakteristike takvih pojava su komplicirana i brzo mijenjajuća geometrija slobodne površine, te visoki gradijenti tlaka tokom udara uz moguće utjecaje stlačivosti zarobljenih mjehura zraka. Trendovi u pomorskoj industriji usmjereni su projektima koji u sve većoj mjeri izlažu objekte nepovoljnim valnim udarima, poput sve dužih brodova za prijevoz kontejnera kod kojih velika vertikalna gibanja na pramcu uzrokuju udaranje pramca te opterećenje uslijed vode na palubi, ili Floating Production, Storage and Offloading objekata koji se sidre na način da im je ograničeno zaošijanje zbog čega se nisu u mogućnosti okrenuti pramcem u smjer vala i vjetra, te su iz tog razloga izloženi velikim amplitudama ljuljanja prilikom čega dolazi do prolijevanja vode na palubu [1].

Prilikom predviđanja takvih opterećenja, linearne spektralne metode koje se zasnivaju na potencijalnom modelu strujanja su vrlo korisne [2]. Koristeći spektralan pristup odzivu pomorskih objekata moguće je odrediti dugoročan odziv konstrukcije, koji pruža važne informacije vezane za cijeli životni vijek objekta koje su od velike važnosti prilikom projektiranja. Pomoću spektralne analize može se odrediti vjerojatnost premašivanja određenog ekstremnog događaja što je vrlo korisno za detekciju i opis takvog događaja. Iako se vjerojatnost premašivanja može odrediti za ekstreman događaj, predviđanje lokalnog odziva konstrukcije

uslijed istog nadilazi mogućnosti pojednostavljene linearne spektralne metode. Iz tog se razloga pribjegava metodama koje točnije opisuju fiziku poput eksperimentalnih ispitivanja ili Računalne Dinamike Fluida (RDF). Eksperimentalne metode imaju dugu tradiciju i visoku točnost, te se desetljećima uspješno koriste za određivanje ekstremnih valnih opterećenja. Numeričke metode kao što je RDF su pod intenzivnim razvojem u industriji i akademskom svijetu, te je potreban daljnji razvoj na području robusnosti i isplativosti za svakodnevno korištenje u industriji.

Iako su eksperimentalne metode pouzdane, često su kompleksne, skupe i dugotrajne, zbog čega se u industrijskom projektiranju uglavnom koriste za konačnu potvrdu projekta, ili unutar velikih industrijskih istraživanja. S obzirom na navedeno, postoji potreba za bržim metodama koje se mogu koristiti ranije u projektnom procesu. Numeričke metode su jeftinije, brže i mogu se vršiti u prirodnoj veličini izbjegavajući problem skaliranja, zbog čega predstavljaju alternativu eksperimentalnom ispitivanju. Razna istraživanja se bave poboljšanjem točnosti, robusnosti i pouzdanosti RDF metoda kako bi se mogle koristiti u industrijske svrhe. Postoje dvije osnovne grupe RDF metoda: metoda Lagrangeovih čestica (eng. "*Smoothed Particle Hydrodynamics*") i metode kontrolnih volumena (eng. "*Finite Volume*"). Obje grupe metoda imaju određene prednosti i nedostatke, međutim u posljednje vrijeme metode bazirane na kontrolnim volumenima dobivaju više pozornosti zbog šireg raspona aplikacije te računalne učinkovitosti.

Prilikom valnog udara mjehur zraka može ostati zarobljen unutar vode ili između slobodne površine i površine trupe pomorskog objekta. Zarobljen zrak može značajno promijeniti trajanje i intenzitet tlačnih opterećenja prilikom udara [3, 4, 5, 6]. Stlačivost zraka ima značajan utjecaj tokom udara zbog prijenosa mehaničke energije između vala i zračnog mjehura zbog čega volumen, tlak i gustoća zraka osciliraju. Stlačivost zraka prilikom udara produžuje djelovanje tlačnog opterećenja na konstrukciju, što može uzrokovati veći prijenos energije na konstrukciju te veći strukturni odziv. Nadalje, ako je zračni mjehur u doticaju s objektom, površina na koju djeluje udarni tlak se povećava [6]. Dakle, pouzdano modeliranje kompresibilnosti zraka je vrlo važno kako bi metoda mogla generalno odrediti pojavu udarnih valnih opterećenja.

Tema ovog rada je numeričko modeliranje udarnih valnih opterećenja pomoću metode kontrolnih volumena s naglaskom na praktičnu primjenu u industriji. Glavni cilj rada je doći do sveobuhvatnog, pouzdanog, robusnog i računalno učinkovitog numeričkog okruženja za predviđanje udarnih valnih opterećenja na pomorske objekte, s naglaskom na opterećenja uslijed vode na palubi. Razne metode su razvijene, testirane i primijenjene u ovom radu. Kako bi se poboljšala računalna učinkovitost, unaprijeđena je sprega gibanja krutog tijela i jednadžbe tlaka što omogućuje smanjenje broja nelinearnih iteracija vodeći do manjeg ukupnog proračunskog vremena. Provedena je detaljna verifikacija i validacija numeričkog okruženja za proračune opterećenja uslijed vode na palubi, kako bi se odredila točnost i preciznost pristupa. Testiranje, validacija i sprega nelinearne metode viših redova (eng. "*Higher Order Spectral method*", HOS) za efikasne proračune propagacije morskih valova je provedena. HOS pruža rubne uvjete RDF metodi za modeliranje kompleksnih valnih polja, kako bi se smanjilo trajanje i domena RDF proračuna. Najveći doprinos ovog rada je razvoj dvofaznog modela strujanja sa stlačivim modelom zraka, čija je točnost, robusnost i računalna učinkovitost pokazana u detaljnoj verifikaciji i validaciji provedenoj u ovom radu. Metoda je u mogućnosti modelirati zračne mjehure tijekom valnog udara, što je demonstrirano na primjeru udara slamajućeg vala. Kao konačni ishod rada, razvijene numeričke metode su sintetizirane kako bi se proveo proračun opterećenja palubne konstrukcije broda za prijevoz kontejnera. Proračun koristi rezultate linearne spektralne metode koja je korištena kako bi se definiralo projektno stanje mora relevantno za ekstremno opterećenje uslijed vode na palubi.

I Cilj i hipoteza

Cilj ovog rada je uspostava sveobuhvatnog, pouzdanog, robusnog i računalno učinkovitog numeričkog okruženja za proračune udarnih valnih opterećenje na pomorske objekte s naglaskom na opterećenja uslijed vode na palubi. U ovom višeskalnom pristupu je potrebno lokalna udarna valna opterećenja povezati s dugoročnim odzivom pomorskog objekta kako bi se u obzir uzela cjeloživotna eksploatacija. Na ovaj način je statistički opis odziva objekta povezan s determinističkim opterećenjem koje se može koristiti prilikom projektiranja.

Hipoteza rada je da razvoj dvofaznog modela strujanja baziranog na metodi kontrolnih volumena pri čemu se u obzir uzima stlačivost zraka bez značajnog povećanja potrebnih računalnih resursa omogućuje generalne proračune udarnih valnih opterećenja. Uz napredan algoritam za spregu gibanja krutog tijela i linearnu spektralnu metodu za proračun odziva pomorskog objekta takva metoda bi omogućila proračune realističnih i relevantnih strukturnih opterećenja uz razumne računalne resurse.

II Znanstveni doprinos

Ovaj rad doprinosi znanstvenom polju brodogradnje pružajući računalno učinkovito, sveobuhvatno i robusno numeričko okruženje za proračun udarnih valnih opterećenja. Metode koje su razvijene, validirane i primijenjene u ovom radu su kombinirane kako bi se dobio generalan hidrodinamički model koji može modelirati udare morskih valova u punoj veličini. Relativno niske potrebe za računalnim resursima omogućuju da se proračuni provedu unutar jednog dana na osobnom računalu, omogućujući da se metoda koristi u procesu projektiranja.

Dvofazni model strujanja koji u obzir uzima stlačivost zraka proširuje valjanost pristupa na širok spektar tipova valnih udara u usporedbi s konvencionalnim nestlačivim modelom strujanja. Fenomen zračnog jastuka može imati velik utjecaj na prostornu i vremensku distribuciju tlačnih opterećenja, pri čemu često dolazi do povećanja prijenosa energije s vala na konstrukciju. Razvijeni model strujanja koristi jedinstveni pristup modeliranju slobodne površine u smislu diskontinuiteta karakteristika fluida na slobodnoj površini koji se zasniva na metodi kontrolnih volumena i Ghost Fluid Method. Nadalje, razvijeni algoritmi za spregu gibanja krutog tijela i jednadžbe tlaka unaprjeđuju računalnu učinkovitost metode pri simulacijama gibajućih objekata na valovima. Dodatan doprinos je ostvaren primjenom nove metode za praćenje slobodne površine koja se zove `"isoAdvector"`, koja je detaljno testirana i validirana za primjenu na opterećenja uslijed vode na palubi.

Osim razvoja novih numeričkih modela, rad doprinosi usporedbom dva različita pristupa definicije tzv. projektnog vala baziranog na dugoročnom odzivu objekta. Metode su uspoređene na temelju opterećenja, računalne učinkovitosti i praktičnosti, što pruža objektivnu procjenu dva pristupa.

Contents

List of Figures

1. Introduction

Marine objects encounter different types of loadings that are characteristic to the ocean environment. Extreme wave loads are one of the more dangerous ones when it comes to structural integrity and survivability of the vessel. Relatively small probability of occurrence of these events makes them difficult to predict and describe, while they often influence the structural scantlings to a large extent. Thus, prediction of extreme wave loads presents an important challenge not only for safety reasons but also financial savings of the new–build. There are several distinct types of wave impact phenomena which are of interest, such as slamming and green sea loads. The characteristics of these phenomena are violent free surface flows with rapidly changing geometry, accompanied by high pressure gradients during the impact and possible air compressibility effects. The trends in the naval and offshore industry drive towards designs that are more exposed to wave impact loads, such as longer container ships resulting in more extreme vertical motion of the bow exposing the bow to both larger slamming loads due to large bow flare, and green sea loads. Another example are the Floating Production, Storage and Offloading (FPSO) vessels that are being anchored with confined yaw rotation, rendering them unable to weather–vane [1] and exposing them to large roll motions resulting in significant water shipping.

A large portion of the response caused by extreme wave loadings can be predicted with linear frequency domain methods [2], which can be effectively used in order to establish long term predictions. These predictions are invaluable in the design process as they provide information regarding the entire life–time of the vessel, including probability levels of extreme response that are of interest and identification of the same. However, they suffer from the fact that only linear response can be captured excluding highly nonlinear phenomena which are usually associated with extreme wave impact loading and may cause structural failure. This is where high–fidelity methods come into play in order to predict deterministic loads, which can be divided into two basic groups: experimental and numerical. Experimental approach enjoys a long tradition and high level of confidence, and it has been successfully used for decades to obtain more detailed information regarding wave impact loads. High fidelity numerical methods such as Computational Fluid Dynamics (CFD) are undergoing intensive development, where a lot of room remains to improve the reliability and feasibility of these methods to be used daily within the industrial design process.

Whereas experimental methods are well established and reliable, they are often cumbersome, time–consuming and expensive. Additionally, for phenomena related with wave impact the scaling of results presents a significant source of error and uncertainty, even more so if compressibility effects are present. Thus, within industrial design processes, they are mostly used to confirm a final project, or within large industrial research projects. Thus, the need for faster methods is present in order to be able to iterate early in the design process. Numerical methods generally require smaller amount of time and are less expensive, thus presenting a viable alternative. For this reason, significant effort is being exerted in academia and industry to enhance the accuracy, robustness and reliability of CFD methods. There are two distinct groups of CFD methods that are the most prominent for simulating violent wave impacts: Finite Volume (FV) based methods and Smoothed Particle Hydrodynamics (SPH) methods. Both groups have respective advantages and disadvantages; however it seems that FV based methods provide a more computationally efficient framework, as well as a more flexible range of applications.

During wave impact a significant air volume can remain trapped inside the body of water or between the free surface and the hull surface. The trapped air can significantly change the pressure loads during the impact, both in intensity and duration [3, 4, 5, 6]. Compressible air properties play an important role during the impact due to the energy transfer between the wave and the air bubble, causing the air bubble to oscillate in volume, pressure and density. The compression of air prolongs the force peak acting upon the structure, which in general enables a larger amount of energy to be transferred to the structure causing more severe structural response. Furthermore, if the air pocket is in contact with the structure, it can increase the surface area where the high pressure is acting [6]. Thus, in order to have a general numerical framework for assessing wave impact loads air compressibility needs to be taken into account. Furthermore, the method should be able to accurately describe the evolution of the free surface during violent impacts from far field to the point of impact.

This study focuses on the FV numerical modelling of wave impact loads with emphasis on everyday practical industrial applications. The goal is to establish a clear, comprehensive, reliable, robust and efficient numerical framework for assessing wave impact loads on marine structures, with emphasis on green sea loads. For that purpose, a number of numerical models are developed, tested and applied to the problem. For the sake of computational efficiency, enhanced hydro–mechanical coupling algorithms are developed enabling smaller number of nonlinear iteration loops, resulting in smaller overall computational time. Detailed verification and validation is performed in order to assess the accuracy and precision of the framework in calculating green sea loads. A nonlinear potential flow based method for propagation of irregular wave fields called the Higher Order Spectral (HOS) method is tested, validated and coupled to CFD framework to provide a highly resolved wave field without additional cost of large–scale, long–time CFD simulations. The largest contribution of this study is a robust, accurate and efficient compressible two–phase flow model that is developed, verified and validated, handling violent breaking wave impacts with trapped air pockets. Finally, the numerical models are synthesised into a complete green sea load analysis of a deck structure on an Ultra Large Container Ship (ULCS), starting from the linear spectral–domain ship response analysis all the way to pressure loads acting on the structure.

1.1. Previous and Related Studies

In order to simulate green water loads in a physically realistic manner, a proper flow model needs to be applied without posing limitations with respect to the characteristics of wave impact, and the interaction between the flow and the floating object needs to be accounted for in a numerically stable and efficient way. Another key aspect in two–phase FV models is interface capturing for modelling the two immiscible fluids.

1.1.1. Interface Capturing

In this study the free surface is modelled using interface capturing techniques. Several interface capturing methods are commonly used in CFD: volume fraction based Volume–of–Fluid (VOF) method [10, 11]; Level Set (LS) method [12], which is often based on the signed distance function; and the Phase Field (PF) method [13], where a hyperbolic tangent function is used as the indicator field.

VOF is broadly used in FV algorithms due to its intrinsic conservative nature, which preserves the individual mass of each phase to machine tolerance. Two main approaches are present regarding the VOF method: algebraic and geometric approach. The downside of algebraic VOF is the smearing of the interface, which encouraged many authors to develop special compressive schemes [14, 11, 15] or include additional compressive terms in the transport equation [16, 17]. To describe the interface more precisely, geometric reconstruction methods have emerged, such as the Piecewise Linear Reconstruction Calculation (PLIC) method developed by Gueyffier et al. [18], as well as the approach described by Popinet [19], used in the Gerris flow solver. In this study, both algebraic and geometric VOF methods will be used, where a new geometric method recently developed by Roenby et al. [20] called `isoAdvector` will be thoroughly tested. It provides a sharp interface with no mass conservation issues, while it generalises to arbitrary polyhedra and parallelises without overhead.

In the LS method, signed distance function is often used to capture the interface [21, 22]. The sharp interface is defined as zero value iso–surface (or level set) of the distance function. In LS, special attention is needed to preserve the signed distance profile of the LS field during advection, which is often achieved by additional redistancing equation [23], or by calculating the distance directly after solving the LS transport equation in a narrow band near the interface. LS method based on signed distance function does not conserve mass, thus conservative LS methods [24, 25] have emerged, which convect a Heaviside function bounded between 0 and 1, where the 0.5 contour presents the interface.

In the PF method, a tangent hyperbolic function is used to capture the location of the interface [13], which remains preserved during advection as opposed to the signed distance function in LS method. The fundamental advantage of the method is that there exists a transport equation which converts the hyperbolic tangent function without deformation and whose source terms can be made into fully implicit transport terms [26]. To harness the advantages of both PF and LS method, Sun and Beckermann [27, 28] used the LS method to derive a modified LS transport equation, which has additional terms that implicitly redistance the signed distance function. Such procedure avoids the need for additional redistancing equations or explicit calculation [26].

In addition to interface capturing, interface modelling requires additional treatment regarding kinematic and dynamic free surface boundary conditions. Kinematic boundary condition ensures the continuity of velocity field across the interface, while the dynamic boundary condition yields discontinuities of pressure gradient and tangential velocity gradient, caused by discontinuity of density and viscosity. The discontinuities can be modelled using conditional averaging [29], yielding the two–phase momentum equation which includes the density gradient, as used by many authors [30, 31, 32, 33, 34, 35, 36]. The density field is calculated by blending the densities of the two phases at the interface, resulting in a smeared density variation at the interface approximating the sharp discontinuity. The non–zero density gradient at the interface should be balanced by the discontinuity of the pressure gradient at the free surface. In the conditionally averaged approach, this balance is resolved in the momentum equation, often causing spurious acceleration of the lighter phase [37].

To model the discontinuities at the interface more accurately, the free surface jump conditions arising from free surface boundary conditions should also be taken into account. Free surface jump conditions are often taken into account using the Embedded Free Surface method [38, 39, 40] or the GFM [41, 42, 43, 44, 45, 46, 47, 48, 49, 50], which differ in the numerical treatment of the interface jump conditions. The GFM along with LS method for interface capturing was first presented by Fedkiw et al. [48, 49]. Kange et al. [47] adopted the method for multi–phase laminar flow, while Desjardins et al. [42] used the GFM with the conservative LS formulation to simulate incompressible two–phase turbulent atomization of liquid diesel jet. The GFM has also been used with VOF interface capturing method for compressible multiphase flows by Bo and Grove [41]. Huang et al. [50] presented Finite Difference (FD) based GFM with LS for curvilinear structured grids, with simplified tangential stress balance jump condition. The above mentioned publications regarding Embedded Free Surface method and GFM rely on structured grids. Queutey and Visonneau [35] present an approach similar to GFM for arbitrary polyhedral grids, with the assumption that the interface is aligned with the internal grid faces. Recently, Vukčević [37] implemented second order–accurate GFM on arbitrary polyhedral grids, where the kinematic free surface boundary condition and the normal stress balance are taken into account exactly, with a simplified model for tangential stress balance. Such a simplification is justified for large–scale problems where surface tension and viscosity play a minor role [50].

1.1.2. Hydro–Mechanical Coupling

The occurrence of green sea critically depends on the motion of the vessel with respect to the free surface. It is for that reason that special attention should be dedicated towards the coupling between the equations that govern the fluid flow and rigid body motion.

The coupling of body motion and fluid flow is commonly performed on the level of the nonlinear pressure–velocity loop (SIMPLE or PIMPLE), i.e. after the flow solution rigid body motion equations are solved and the computational grid is moved accordingly. The procedure is then repeated within each time–step until convergence. This is the conventional strongly coupled, partitioned approach. The PIMPLE algorithm is comprised of multiple PISO pressure–velocity loops, where pressure is updated multiple times per one momentum equation–update [51]. This approach has been verified in numerous publications. Orihara and Miyata [52] use a predictor–corrector algorithm for the in–house code WISDAM–X, where they recalculate the entire flow field after every body motion correction. Castiglione et al. [53] imply that the in–house code CFDShip-Iowa uses a similar approach, where the complete fluid flow solution is obtained in each body motion–fluid flow iteration. Wu et al. [54] describe the execution sequence of the CFD code used in their study where a similar procedure is employed. To achieve convergence of the coupling, multiple body motion–fluid flow iterations are needed. Simonsen et al. [55] and Vukčević and Jasak [56] reported that a minimum of five nonlinear iterations were needed per time–step to ensure convergence. For the fluid flow itself to converge, smaller number of nonlinear iterations is sufficient, typically two for wave related problems. Thus, the body motion–fluid flow coupling presents a considerable overhead in terms of computational time.

Efforts have been made by some authors to enhance the hydro–mechanical coupling, however mostly in cases where the moving body is also deforming, and the volume of the body is discretised. In these cases, it is possible to monolithically couple the matrices that arise from discretising the fluid flow and the structure. This approach is mostly applied using the Finite Element method [57, 58, 59, 60, 61, 62, 63, 64], however in some publications FV is used as well [65, 66, 67]. Some authors state that the monolithic FSI model with a discretised structure can calculate rigid body dynamics as a special case. Hachem et al. [59] state that the rigid body can be modelled by imposing special conditions to the Navier–Stokes equations for the stencils inside the structure. Legay et al.[63] and Mosher et al. [68] show that rigid body can be simulated within the presented model by substituting the structural system of equations with the rigid body motion equations. For marine hydrodynamic applications, discretising the structure presents a cumbersome and unnecessary task. Thus, the existing monolithic approaches are not appropriate for marine hydrodynamics.

1.1.3. Calculating Green Sea Loads With CFD

Temarel et al. [69] give an extensive overview of experimental and numerical studies related to wave impact loads, assessing the current level of readiness for tackling present industrial challenges. For green sea loads, which are of primary interest in this study, the authors concluded that limited success is achieved both with experimental and numerical approach in quantifying realistic operational loads. Thus, this field presents an active area of research, which is confirmed by the large number of recently published papers on the subject. Greco et al. [70] used the numerical solver developed by Greco and Lugni [71] to calculate wave loads on a patrol ship, including green sea loads with comparison to the experiments. Lu et al. [72] developed a time domain numerical method based on Finite Volume (FV) method used for green sea load simulations. Xu [73] used SPH to simulate breaking wave plunging onto a deck. Zhao et al. [74] studied the influence of structure motion on pressure loads due to green sea effects using a FV based method. Kim et al. [75] used a linear method for assessing the ship motion, and a nonlinear viscous method to calculate green sea loads on a container vessel. Ruggeri et al. [76] used WAMIT software based on the potential flow model and a viscous FV code StarCCM+ to devise guidelines for green sea load calculations. Zhu et al. [77] conducted numerical simulations of green sea events for a FPSO vessel. Kudupudi and Datta [78] calculated green sea loads on a moving vessel where the motion is calculated with a panel method software where comparable results are obtained with respect to experimental measurements. Silva et al. [1] conducted an experimental campaign with green sea events in oblique waves upon a FPSO. The tested wave field settings are selected based on the frequency domain linear method, while experimental measurements are used to detect the absolute maximum RWA, which is reproduced using CFD in the subsequent publication [79]. The simulation includes rigid body motion and it successfully reproduces the experimental measurements. Pakozdi et al. [80] used CFD in order to predict green water loads on a Tension Leg Platform (TLP) in a 10 000 year extreme event. They used an approach that is equivalent to the Regular Equivalent Design Wave [81], however the selection of regular wave characteristics are based on crest height and free surface elevation rise velocity based on irregular wave measurements in a wave tank, instead on a long term statistical distribution. The authors state that this approach reduces the required computational time since it does not require irregular wave propagation in CFD. However, the drawback of this approach is that it requires experimental measurements to detect the irregular extreme events in order to measure the steepness and rise time.

In order to reduce the overall computational time for assessing green water loads, Pakozdi et al. [82] developed a framework where a potential theory based method is coupled with CFD in order to minimise the CFD domain and the duration of the simulated time. A reasonable comparison with experimental measurements were achieved. Joga et al. [83] compared two commercial CFD codes in assessing water ingress into open cargo holds of a container ship during green sea events in irregular beam seas. Both codes predicted motion with reasonable accuracy, whereas authors concluded that assessing volume of shipped water poses a greater challenge.

Majority of FV based methods mentioned above use the incompressible two–phase free surface flow model, which is adequate for most naval hydrodynamic applications. However, in extreme wave impacts compressibility effects can play an important role [6]. Thus, flow models where air is considered compressible have been developed by numerous authors as shown in the subsequent section.

1.1.4. Compressible Two–Phase Flow

SPH based methods have been applied to compressible two–phase flows by numerous authors. Guilcher et al. [84] investigated scale effects on a wave impact against a wall with trapped air pocket, successfully applying the developed compressible SPH method. In another publication, Guilcher et al. [9] showed a validation of the approach on benchmark cases, namely the liquid piston case and free–falling water column, which will be used in this study as well. Luo et al. [85, 86] used a Consistent Particle Method to simulate wave breaking with trapped air pocket and sloshing in two connected tanks, showing good agreement with the experiment. Rostami and Ketabdari [87] validated their weakly compressible SPH method on a 2D dam break with horizontal column impact, however no trapped air pockets were investigated. Lind et al. [88] showed a novel SPH method with a sharp interface treatment, validated on a dam break case with trapped air pocket.

The shortcomings of SPH methods prevent them from being used for industrial problems on a daily basis despite the fact that they can effectively be used to simulate aerated wave impacts and related phenomena. The computational cost is often too great, and simulating complex geometries such as ships with superstructure becomes a problem, as well as accurate integration of 6–degrees–of–freedom motion of a floating object due to difficult treatment of impermeable boundary conditions. It is for this reason that FV based methods receive more attention and popularity, for they allow a more efficient numerical handling, while the treatment of body boundary conditions is straightforward, where automatic meshing strategies are available for generating body–fitted grids [89]. FV methods have certain disadvantages with respect to SPH based methods that need to be recognised, such as treatment of the sharp interface dividing the two phases. Nonetheless, there is an increasing number of publications dealing with development and application of FV methods for compressible two–phase flow in naval hydrodynamics.

Braeunig et al. [7] used a FV based numerical method to explore the possibility of exact scaling between model–scale and full–scale LNG sloshing and derived the gas that should be used in model scale to ensure good quality scaling. Dumbser [90] developed a higher order WENO FV method for compressible two–phase flow. The method is validated on a number of dam–break cases comparing the results to experiments and shallow water flow theory. Plumerault et al. [91] developed a two–phase compressible method that allows aerated water flow, which can be very important in highly violent wave impacts. The method is validated against experimental results for a wave impact against a wall with entrained air. Costes at al. [92] used a nonlinear potential flow based numerical method in conjunction with a compressible two–phase FV method to simulate wave impact with trapped air pocket. The potential flow solver is used to propagate the wave field, while the more expensive FV compressible method is used only in the vicinity of the structure. Miller et al. [93] developed a compressible two–phase method specialised for simulating underwater explosions, where both air and water compressibility are accounted for. A three–dimensional shallow water explosion simulation is shown, where mass is not fully conserved. Ma et al. [8] developed a higher–order FV method for handling aerated two–phase wave impacts, where the dispersion of air in water is handled with the VOF approach. The method proved accurate for fundamental cases as well as for a 2D wave impact case with trapped air pocket. The approach was also used to study rigid plate entry [94] where the influence of aeration was investigated experimentally and numerically, showing good correspondence between the two sets of results. Furthermore, sloshing with trapped air effects is investigated in de-pressurised tank with experimental comparison [95], showing once more the accuracy of the presented numerical approach. However, the drawback of higher–order numerical schemes is that they generally suffer from instabilities and are computationally more expensive. Calderón–Aánchez et al. [96] investigated a free fall of a horizontal water column with rectangular cross–section using OpenFOAM software, where the compressibility is explicitly accounted for. The ability of the code to capture compressible impact effects on this simple canonical case is demonstrated for various density ratios between the two phases. Zou et al. [97] used a commercial software FLUENT to investigate the effects of viscosity and air compressibility on violent sloshing events, concluding that lower pressures are obtained when a compressible air model is used as opposed to the incompressible model. Lyu et al. [98] investigated different interface capturing methods in a FV framework for simulating sloshing impacts, where both compressible and incompressible methods are used. They concluded that VOF based interface capturing is the most suitable to predict the motion of the liquid and pressure loads.

1.2. Objective and Hypothesis of Research

The objective of this research is to establish a clear, comprehensive, reliable, robust and efficient numerical framework for assessing wave impact loads on marine structures, with emphasis on green sea loads. The local wave impact loads are to be related with the long term response covering the entire life–time of the vessel in a multiscale approach. In this manner, the statistical description of the vessel's response is related to deterministic loads which can be used in the structural design process.

The hypothesis is that developing a two–phase flow model based on FV framework where the air compressibility effects are taken into account without increasing the computational demands would provide a general method for assessing wave impact loads. Thus, a single simulation could be performed where air cushioning effects can be taken into account, if they occur, with only a minor computational overhead. Together with advanced hydro–mechanical coupling strategies and the linear frequency domain methods, realistic and relevant structural loads can be assessed that can be used in the design process.

1.3. Scientific Contribution

The present study contributes by providing an efficient, comprehensive and robust numerical framework for assessing wave impact loads. The methods that are developed, applied and validated in this study are combined to create a unique, versatile and high–fidelity flow model which can tackle general large–scale ocean wave impacts. Relatively low computational demands enable the calculations to be performed within reasonable amount of time on a desktop computer, facilitating the design process.

The two–phase flow model which models volumetric compressibility of air widens the range of wave impact types that can be considered with respect to the commonly used incompressible approach. Air cushioning effects can play an important role in distributing the impact loads over large surfaces and longer time intervals, intensifying the energy transfer to the structure. The model features unique numerical treatment of the sharp change in compressibility properties between water and air based on the Ghost Fluid Method. Next, the developed hydro–mechanical coupling strategies reduce the overall computational time required for simulations with floating objects. Additional contribution is related to application of a novel geometric interface capturing method called isoAdvector, which was thoroughly tested and validated for green water loads in this study.

In addition to the development of new numerical models, thesis contributes by giving a comparison of two different methods for defining the design wave condition based on the long term ship response distribution. The methods are compared in terms of loads, computational efficiency, and ease of use, giving an objective judgement of the two approaches.

2. Discussion of Method and Results

The conducted research will be briefly outlined and discussed in this chapter point by point. The relevance and outcomes of each developed method and conducted study will be discussed in terms of the goal of the research. The chapter is comprised of the following topics, that correspond to attached papers:

1. Higher Order Spectral method; nonlinear spectral wave propagation method based on potential flow theory (PAPER 1),

2. Enhanced hydro–mechanical coupling; advanced strategies for coupling rigid body motion equations and the pressure equation (PAPER 3 and PAPER 4),

3. Verification and validation of the numerical model for assessing green sea loads (PAPER 5),

4. Development of a two–phase flow model where air is modelled as a compressible ideal gas (PAPER 6),

5. Operational green sea loads calculation for an Ultra Large Container Ship (PAPER 7).

2.1. Higher Order Spectrum Method

Higher Order Spectral method is a nonlinear potential flow based method for propagating irregular wave fields with high computational efficiency. In this study the method was validated, coupled with CFD and tested for the present application. The validation and CFD coupling is published in PAPER 1. The original idea was to use HOS in irregular wave green sea simulations in order to resolve nonlinear wave–to–wave interaction and wave modulation outside of the CFD domain (temporally and spatially), reducing the CFD domain to a minimum. This sort of application is depicted in PAPER 1, where a long–time evolution of a short–crested irregular wave field is performed with HOS, the extreme wave is detected and simulated with CFD, and a response of a container ship is calculated.

Although the coupling of HOS and CFD showed to be efficient and produced the desired outcome, it is difficult to relate results form HOS with operational profile of a ship. Since HOS is nonlinear, it cannot be used in conjunction with frequency domain methods for calculating ship response. Thus, in order to obtain statistically meaningful data, long–time CFD simulations including ship motion needs to be conducted. This sort of simulation was performed in the course of this study, as shown in PAPER 8. It takes more than a week for this sort of simulation to calculate on a coarse grid using substantial computer resources (48–core cluster), which is not feasible in industrial setting. It is for this reason that it was concluded that HOS will not be used for this purpose. Instead, linear motion response is used to define wave conditions that can be used in a CFD simulation to calculate realistic green sea loads, as discussed in Sec. 2.5.

Except for random irregular wave fields, HOS can be used to simulate focused irregular wave groups, where phase shifts of wave components are not random. This can be used to check the level of nonlinearity developing during focusing, which can be high if the obtained wave system is steep. HOS was applied for this purpose in PAPER 2, where it showed that the difference with respect to the linear solution is small, thus rendering the linear solution adequate for simulations that will reproduce experimental measurements (Fig. 2.1). Since focused wave groups represent a type of design waves, this is a relevant application for this study.

Another application of HOS related to CFD which is not applicable to this study is wave spectrum calibration. When performing irregular wave simulations where a longer CFD domain is required which permits developments of significant amounts of wave–to–wave nonlinearities and wave modulations, the wave power spectrum obtained in the simulation does not correspond to the target spectrum. This is also present in experimental measurements. In order to resolve this, wave calibration is performed where the input spectrum is modified in order to pro-

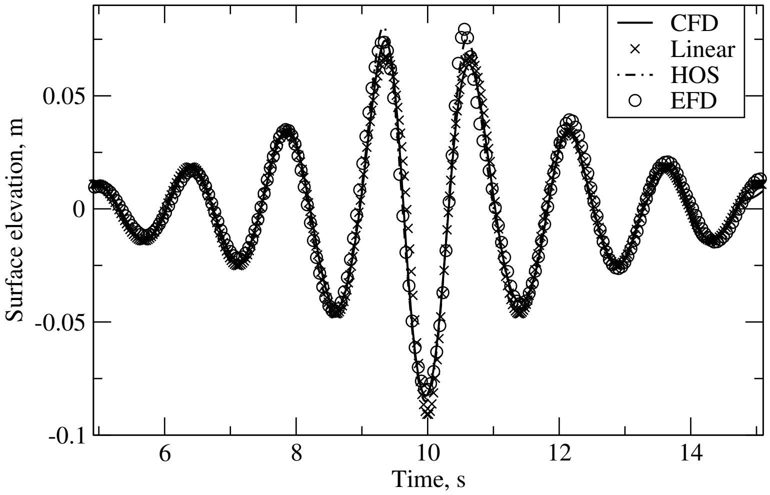

Figure 2.1: Surface elevation of a focused wave obtained with HOS and CFD (PAPER 2).

duce the target spectrum once the nonlinearities have changed it. Using HOS the calibration can be performed at a fraction of the computational cost compared to CFD. An attempt of calibrating the sea spectrum with HOS is shown in PAPER 8.

Tu summarise, during this research project it was found that HOS has limited applicability to the considered problem, but it is useful for other applications.

2.2. Enhanced Hydro–Mechanical Coupling

The efficiency of the coupling between fluid flow and rigid body motion can have a large influence on the overall efficiency of the simulation. If the coupling requires more nonlinear iterations per time–step with respect to a simulation where no rigid body motion is simulated, it increases the computational time. In this study, two enhanced approaches are developed in order to minimise the computational overhead of simulating rigid body motion coupled with CFD.

In PAPER 3, an enhanced strategy for coupling the pressure equation and rigid body motion equations is developed, verified and validated. The two sets of equations are more tightly coupled by performing rigid body motion integration once per pressure equation step updating the boundary velocity of the object, at which the position of the computational grid is not updated, saving computational time. The method is tested on a seakeeping case, where it shown to be up to four times more efficient while obtaining equivalently accurate results. Fig. 2.2 shows the comparison of first order heave amplitude and phase with respect to the number of nonlinear iterations per time–step. The enhanced approach produced the reference solution with 3 iterations, while it took 8 with the conventional approach.

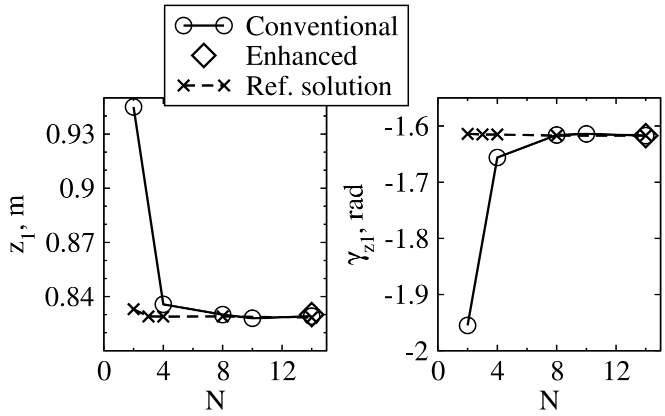

Figure 2.2: Convergence of heave motion items with the conventional and enhanced hydro–mechanical coupling algorithms (PAPER 3). z_1 stands for the first order amplitude, γ_{z1} stands for the phase shift of heave while N stands for the number of nonlinear iteration loops per time–step.

In PAPER 4, a monolithic strategy where the pressure equation and rigid body motion are coupled at the level of linear equation system solver is devised. At each iteration of the linear solution process for the pressure equation, rigid body motion equations are solved with the latest available pressure field. The motion increment resulting from the updated pressure change is introduced directly into the linear system, achieving two–way coupling. The method is verified and validated, while a seakeeping performance test showed that acceleration of 2.4 times in computational time is achieved.

The two coupling methods that are developed showed significant advantages over the existing coupling strategy in terms of computational efficiency. For problems including rigid body motion in this study, the enhanced approach proved to be sufficient, whereas the monolithic approach unnecessary over–resolves the coupling. Since the enhanced approach is slightly more efficient than the monolithic method, it is used in this study in order to achieve savings in computational time. The monolithic approach proved to be useful for cases with added mass instabilities.

2.3. Green Sea Loads Verification & Validation

In order to ascertain the accuracy of the numerical framework in predicting pressure loads caused by green sea or water on deck, a detailed verification and validation study is performed and published in PAPER 5. Experimental results published by Lee et al. [99] are used for the comparison, where pressure on deck of a fixed FPSO model is measured in nine different incident regular waves. The fixed object case is selected in order to minimise the possible source of error in the final results. For this study the incompressible two–phase flow model is used [100] which utilises the GFM and `isoAdvector` interface capturing method.

The results showed high level of accuracy in comparison to experimental results, with numerical uncertainties being comparable to the experimental uncertainties. Fig. 2.3 shows comparison of peak pressures at different pressure gauges for one of the wave cases, where the two sets of results show similar behaviour.

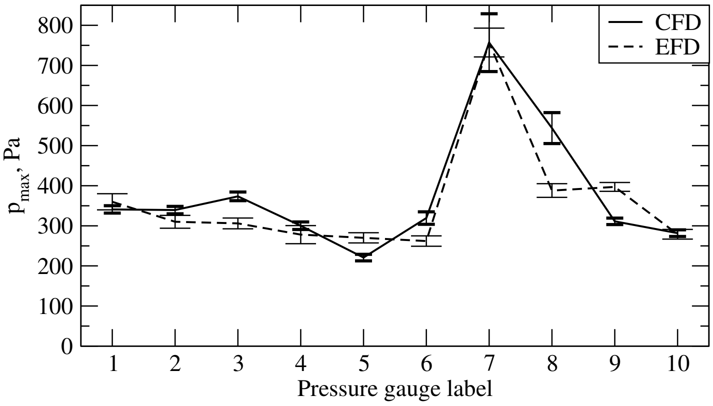

Figure 2.3: Pressure peak results comparison for wave case ID 5 (PAPER 5).

In PAPER 5, a novel geometric interface capturing method based on VOF approach called `isoAdvector` [20] is applied to the present numerical framework and compared to the existing algebraic version. The method proved to give a significant improvement to the resolution of the free surface in violent wave impact cases, as shown in Fig. 2.4. The `isoAdvector` provides a sub–grid resolution of the interface, enabling intricate geometry of the free surface to be captured with relatively coarse grids. Fig. 2.4 shows that droplets and air bubbles are resolved with the `isoAdvector`, while the algebraic VOF method results in significant smearing of the interface.

Notwithstanding the less accurate representation of the interface, the algebraic VOF approach produces only slightly less accurate result for the pressure loads. Fig. 2.5 shows the comparison of pressure integrals between the experimental results, `isoAdvector` and algebraic VOF, where the algebraic VOF exhibits slightly larger under–prediction comparing to the `isoAdvector`. Since `isoAdvector` is fully explicit in time, it requires the CFL number to be below one. The algebraic VOF method is implicit, enabling larger time–steps which reduces the overall computational time. Thus, the algebraic VOF presents a more reasonable choice for industrial–grade simulations which need to be computed efficiently and where pressure loads are of primary interest as opposed to the geometry of the interface.

The numerical framework on which the study is based proved to be accurate in terms of green sea loads. The verification and validation study shows that it can be used in order to conduct green sea loads studies for industrial cases with high level of confidence (see PAPER 5 for more details).

2.4. Compressible Two–Phase Flow

In violent wave impacts occurring in irregular waves, trapped air effects can influence the energy transferred from the wave to the structure. The cushioning effect of trapped air bubble distributes the impact pressure over larger area and longer duration of time, which increases the force impulse exerted on the structure [6]. Although such effects are more frequent in slamming events, they can also occur in violent, plunging type green sea events. In order for this study to result in

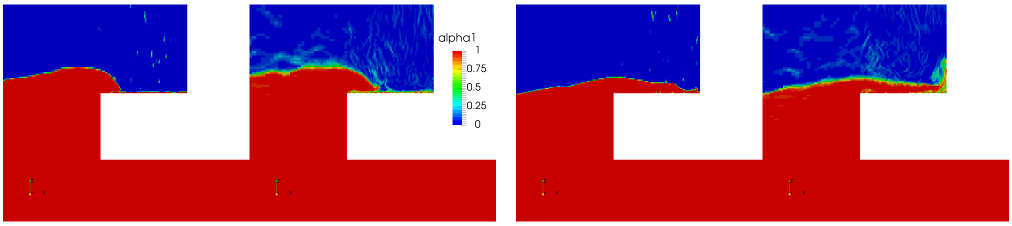

(a) t = 0.06 T, (b) t = 0.19 T,

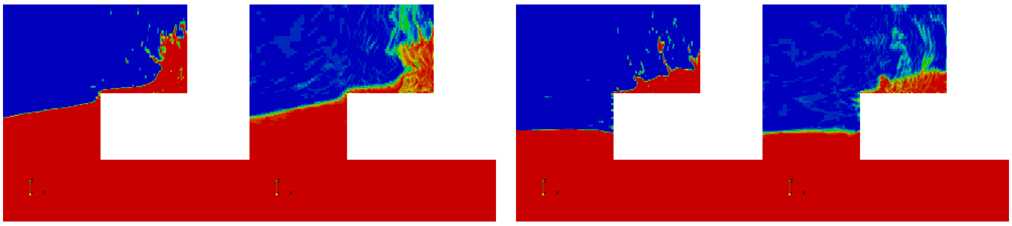

(c) t = 0.32 T, (d) t = 0.45 T,

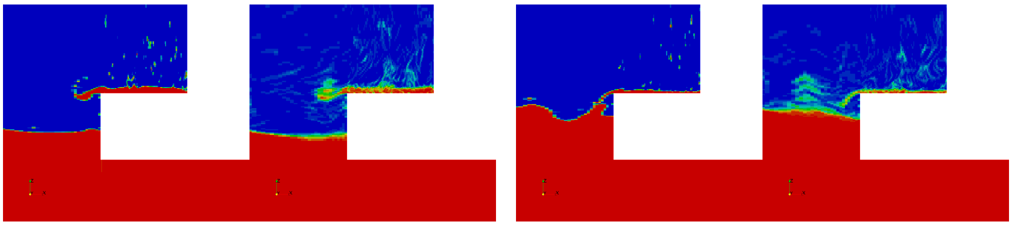

(e) t = 0.58 T, (f) t = 0.71 T,

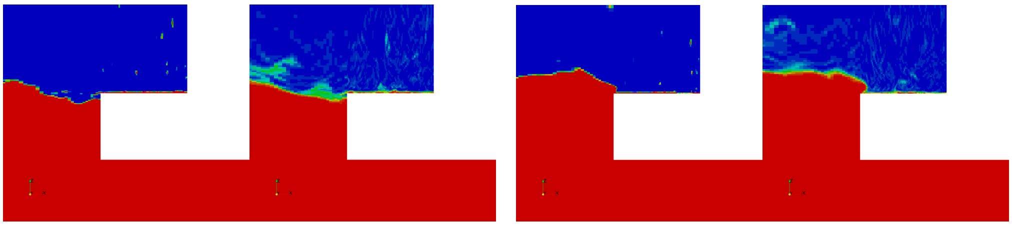

(g) t = 0.84 T, (h) t = 0.97 T.

Figure 2.4: Visual comparison of the volume fraction field α (denoted "alpha") in simulation where the `isoAdvector` (left) and the algebraic VOF method (right) are used (PAPER 5).

a general numerical tool for assessing extreme wave impact loads, the compressibility of the air phase must be taken into account. PAPER 6 presents detailed mathematical and numerical background of a numerical model developed in this study, including an extensive verification and validation of the model.

The developed two–phase numerical method models water as an incompressible liquid, while air is assumed to be a compressible ideal adiabatic gas. The simplification of the air phase model results in a numerically stable and efficient

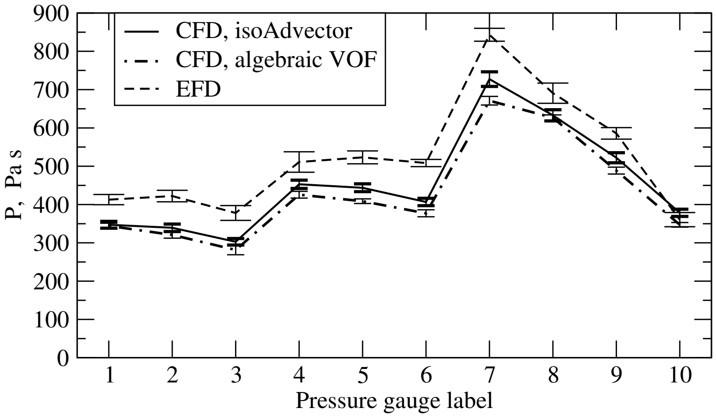

Figure 2.5: Pressure integral comparison between the `isoAdvector` and the algebraic VOF method for wave 9 (PAPER 5).

method, while accounting for compressible effects that are important in naval hydrodynamics. The aim of this development is to be able to capture effects where air is volumetrically compressed, i.e. compression effects caused by applying external forces on a closed air domain. The compressibility effects due to high air velocities, as well as pressure shock modelling, are of no interest. Thus, a numerical method was devised under these premises in order to minimise the overhead in terms of computational resources while maintaining the same level of accuracy and robustness.

Verification and validation performed in PAPER 6 shows that high level of accuracy and precision can be achieved with the developed model, while no overhead in terms of computational resources are exhibited with respect to the counterpart incompressible numerical method. As an example, Fig. 2.6 shows the comparison of impact pressure of a square water column against a flat surface, as shown in Fig. 2.7. The present model reproduces the results reported by other authors, accurately describing the oscillation of the air bubble. In order to compare the accuracy of the developed compressible approach to its counterpart incompressible version, and to validate that it can be used for green sea simulations accurately, one of the cases from Sec. 2.3. is repeated. Fig. 2.8 shows the comparison of peak pressure obtained in the experiment, with the incompressible flow model and the present compressible model. The two numerical models show very similar results, validating the current approach for green water loads, with good overall agreement with the experiment. Another aspect that is important from the industrial application point of view is the computational efficiency of the method. Ideally, the compressible method would be equally fast as the incompressible one if no compressibility effects are present. This is tested on a regular head wave seakeeping case, where both accuracy and computational time are shown to be comparable between the incompressible and compressible formulation. It took 4.7 hours to simulate one wave period with the incompressible method on a Intel Core i5-3570K processor, while it took 3.6 hours with the compressible formulation on a slightly faster Intel Core i7-4820K processor.

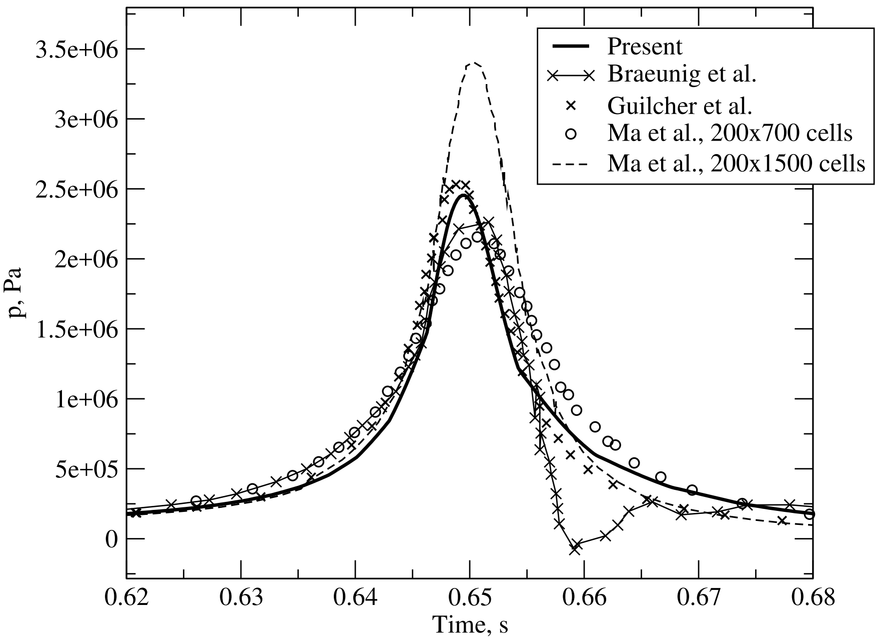

Figure 2.6: Pressure signal comparison during the impact of the falling water column. Pressure measured at the center of the bottom boundary is compared to Braeunig et al. [7], Ma et al. [8] and Guilcher et al. [9] (PAPER 6).

The main objective of the developed compressible two–phase model is to be able to predict violent wave impacts with air cushioning effects. To that end, large–scale experimental wave impacts with trapped air conducted by Bullock et al. [6] are used as a benchmark case. Fig. 2.9 shows the evolution of the breaking

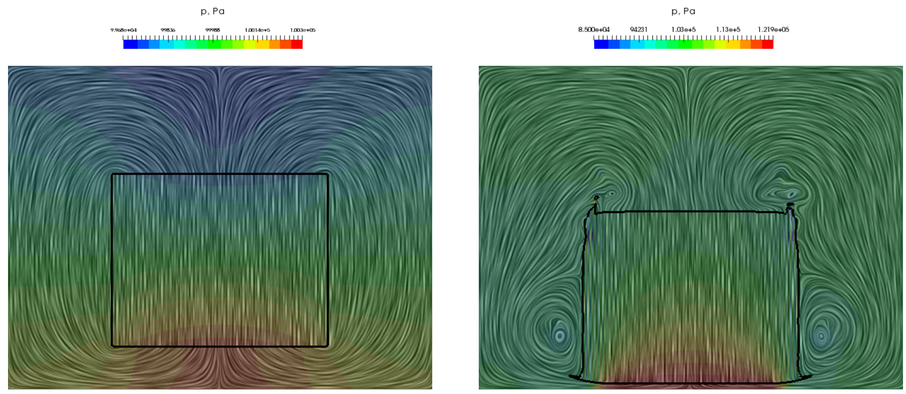

(a) $t = 0.05$ s, (b) $t = 0.60$ s,

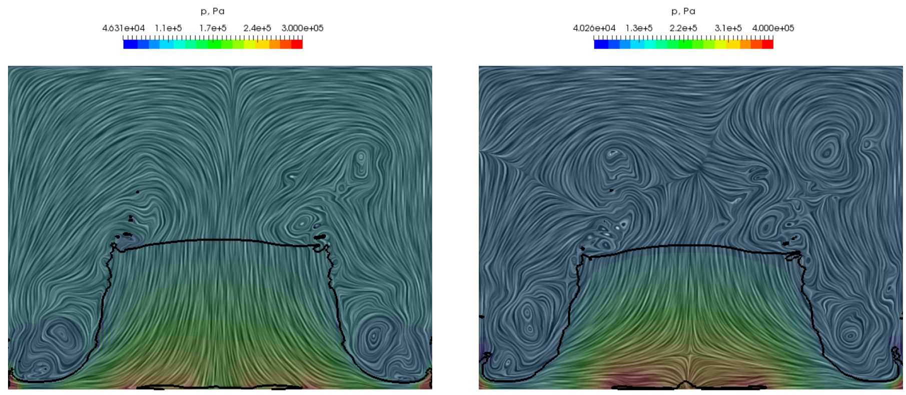

(c) $t = 0.85$ s, (d) $t = 0.90$ s,

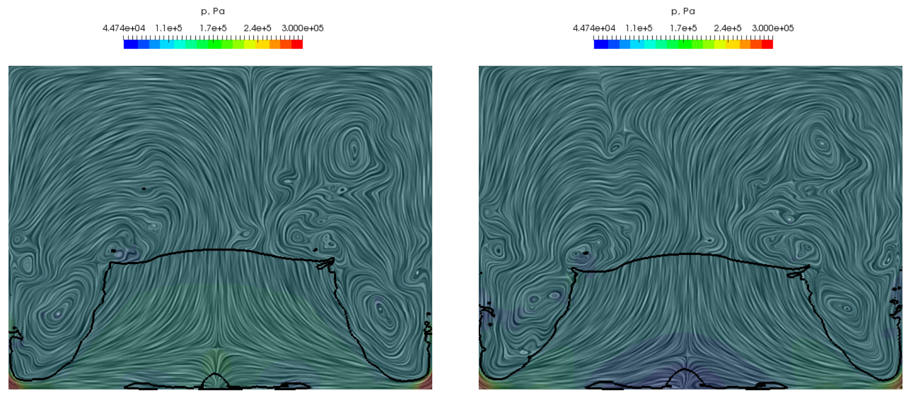

(e) $t = 0.95$ s, (f) $t = 1.00$ s,

Figure 2.7: Evolution of the interface, velocity and pressure field in the free fall of the water column (PAPER 6).

wave impacting a vertical wall, where a trapped air bubble can be seen. Comparison of the pressure force measured at the wall during the impact is shown in Fig.

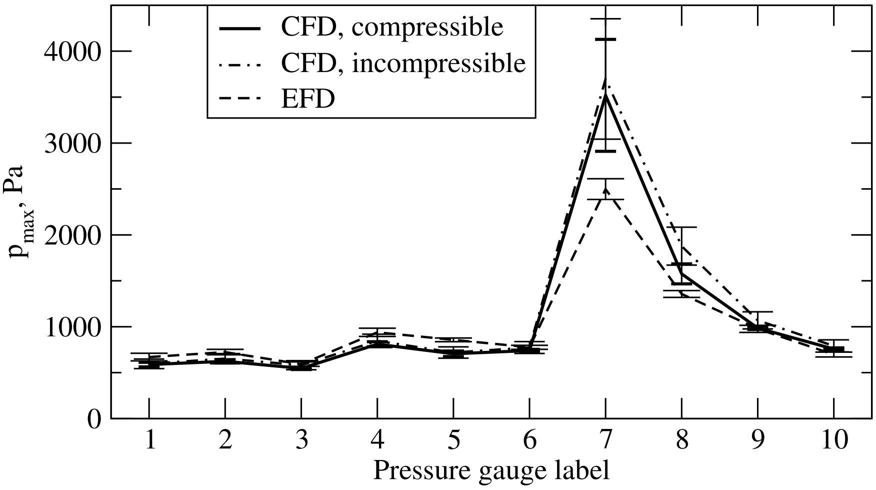

Figure 2.8: Comparison of average pressure peaks for the green sea loading case (PAPER 6).

2.10. The pressure force rise and the force peak are well predicted, as well as the first sub–atmospheric peak. As discussed in PAPER 6, the pressure oscillations caused by air bubble expansion and contraction are damped more rapidly in the experiment compared to the CFD simulation. There are two probable reasons: i) the structural response of the vertical wall and the surrounding wave flume structure was significant, where according to Bullock et al. [6] the vibrations could be felt which is also evident from the video recording of a camera mounted on the wave flume side; ii) in the experiment the vertical wall had holes going all the way through the structure, enabling the trapped air to escape during the impact, evacuating part of the impact energy with it. Fig. 2.11 shows a photograph of the vertical wall, where the 10 cm diameter holes are visible. In future studies, the holes will be taken into account in a 3D simulation.

Overall, the novel two–phase compressible method proved to be accurate, robust and efficient, rendering it applicable to industrial wave impact problems. Specifically, the seakeeping and green sea tests showed that it can be used in realistic green sea event predictions where motion response of a ship is calculated along with water on deck causing pressure loads on deck structures, which is the topic of the next section.

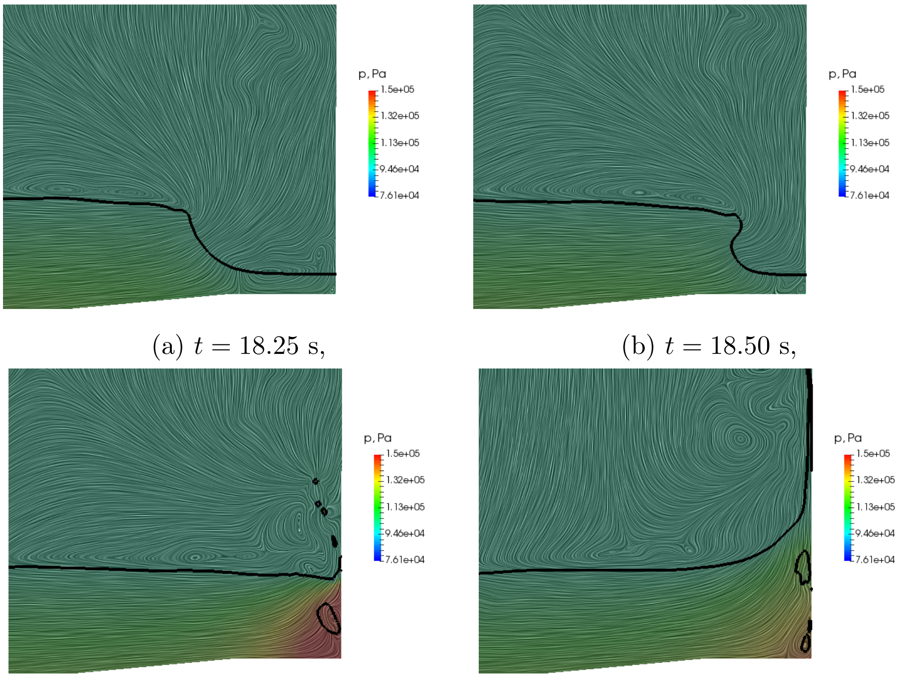

(a) $t = 18.25$ s, (b) $t = 18.50$ s,

(c) $t = 18.75$ s, (d) $t = 19.00$ s,

Figure 2.9: Evolution of the interface, velocity and pressure field in breaking wave impact event with trapped air (PAPER 6).

2.5. Irregular Waves Green Sea Loads

The ultimate outcome of this study is a numerical framework for predicting green sea loads on ships or offshore objects. To demonstrate and test the numerical framework developed in this study a complete, industrial–grade green sea load calculation procedure is performed for an Ultra Large Container Ship, shown in PAPER 7. The procedure starts by calculating long term distribution of the Relative Wave Amplitude (RWA) which denotes the vertical position of the free surface with respect to an arbitrary point on the deck of the ship. The long term distribution is obtained by employing the linear frequency domain method for predicting ship response in irregular waves. Based on the long term prediction, different types of Equivalent Design Wave (EDW) are defined, which are deterministic wave fields allowing time–domain realisation. Two different types of EDW are tested and compared in PAPER 7:

- Regular Equivalent Design Wave: a monochromatic incident wave;

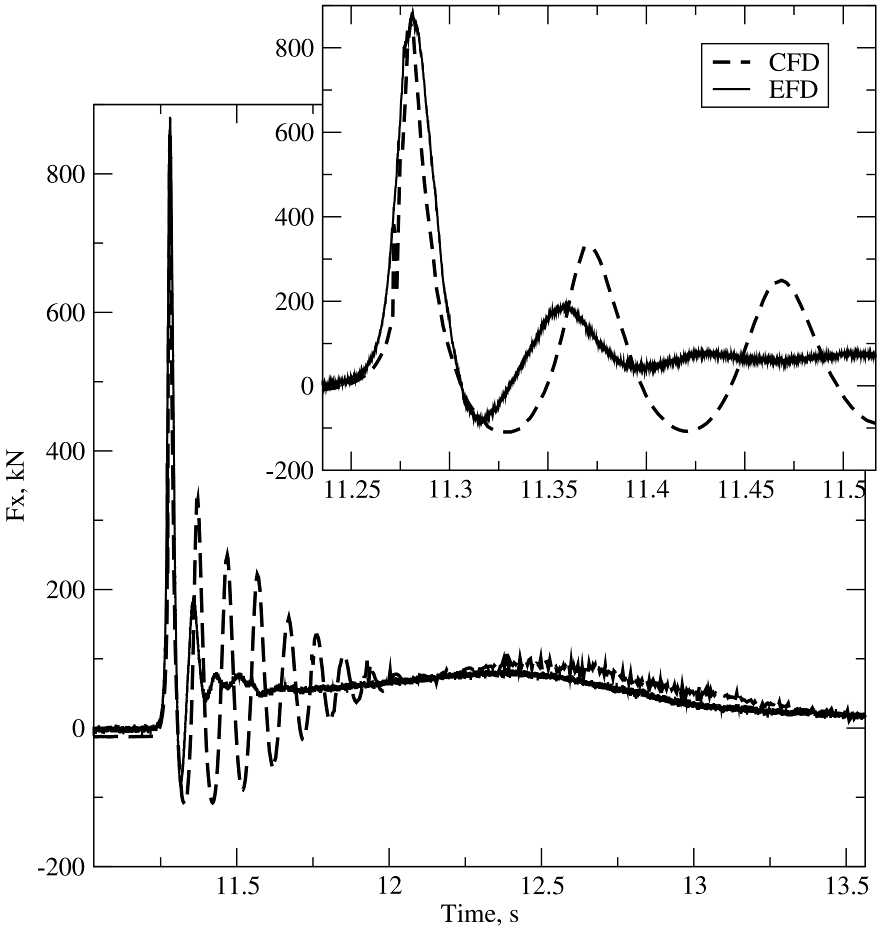

Figure 2.10: Force signal comparison for the breaking wave case (PAPER 6).

- Response Conditioned Wave: irregular wave with non–random phase shifts, where the wave components depend on wave and response spectra.

For each of the design wave approaches, a CFD simulation is performed with the compressible two–phase method. They are compared with respect to green water loading occurring on the breakwater positioned at the deck of the ULCS, required computational resources and modelling complexity. For the Response Conditioned Wave, time–realised linear solution of heave and pitch motion is used in order to initialise the simulation a small amount of time prior to the extreme event. In this way the time that needs to be simulated with CFD is minimised, reducing the overall computational time. The Response Conditioned Wave produced a green sea event even though the linear realisation predicted a RWA maximum close to the freeboard height. Fig. 2.12 shows the RWA and

Figure 2.11: Photograph of the vertical wall from the breaking wave impact experiment [6] (PAPER 6), with holes going through the wall that are not included in the present CFD study.

the linear realisation of the surface elevation at the fore perpendicular in the Response Conditioned Wave case, while Fig. 2.13 shows the green sea event.

In terms of pressure loads the Regular Equivalent Design Wave produced the most severe green sea event resulting in highest pressure loads exerted on the breakwater. The Response Conditioned Wave approach resulted in loads that were 1.9 time smaller. In terms of computational resources, the three methods are comparable where it takes between 14 and 17 hours of computational time to obtain the result on a desktop PC, depending on the processor speed. From the point of view of the complexity of setting up the CFD simulation, the Regular Equivalent Design Wave is more simple and requires a smaller amount of man–hours. The Response Conditioned Wave approach require a linear realisation in order to provide initial conditions, which adds a layer of complexity in the pre–processing step.

In PAPER 7 the developed numerical framework proved to be robust and computationally efficient, allowing industrial–grade simulations to be conducted where impact wave loads can be calculated and used in the design process. The computational resources and time required to perform the simulation allow the framework to be used in every–day design process, since moderate computational time is needed on modest desktop PC-s. With the availability of larger computer resources the computational time would reduce to within one working day, enabling the iterative design process.

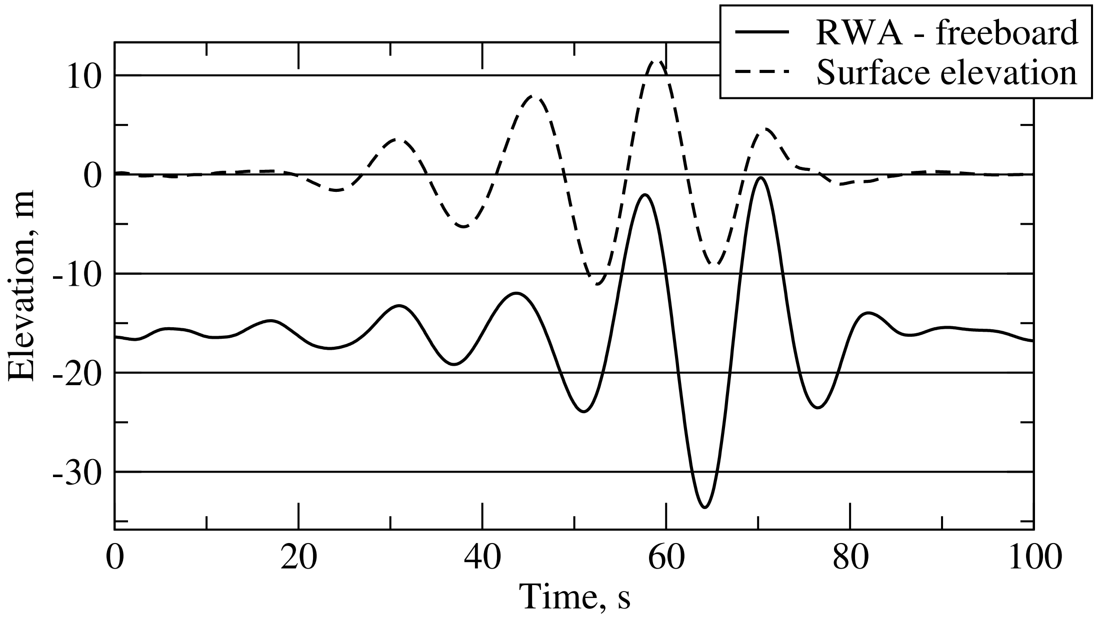

Figure 2.12: Linear realisation of the free surface elevation and RWA at F_P in the Response Conditioned Wave approach (PAPER 7).

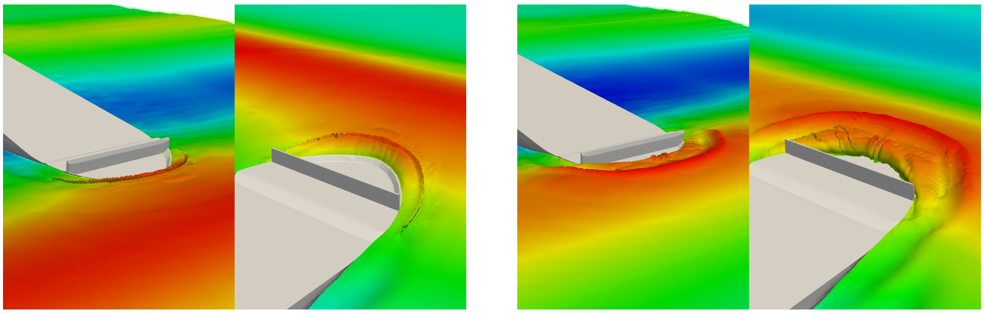

(a) $t = 56.4$ s,

(b) $t = 58.0$ s,

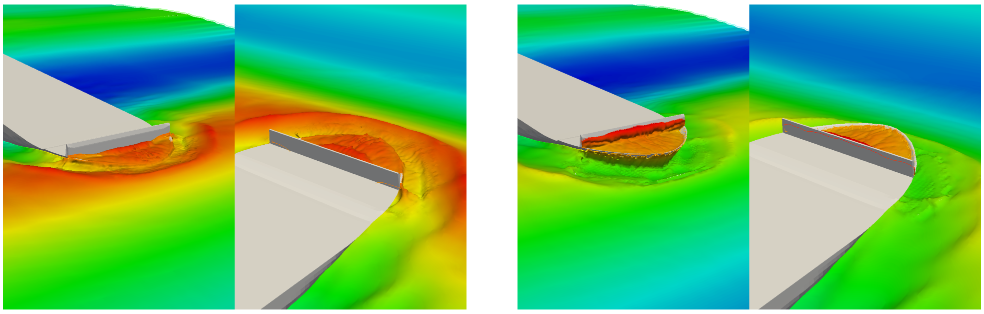

(c) $t = 58.8$ s,

(d) $t = 59.6$ s,

Figure 2.13: The green sea event from the Response Conditioned Wave simulation (PAPER 7).

3. Conclusions and Future Work

Assessing wave impact loads on marine objects exposed to ocean environment presents a challenging and important problem in the design process. The violent and complex nature of wave impacts makes them difficult to predict and reproduce. Experimental and numerical approaches are being developed and used in order to provide a more accurate description of these phenomena, however they are often too expensive and time–consuming for a typical every–day design process. Thus, a need exists for methods that allow quick and accurate assessment of complex wave impact loads on realistic intricate geometries.

A comprehensive, robust, efficient and accurate numerical framework based on the FV method is developed for performing industrial–grade wave impact loads calculations which can be used in a realistic design process. The key feature of the approach is the two–phase flow model where air is modelled as an ideal compressible gas, allowing physical wave impacts to be simulated where air cushioning effects influence the phenomenon. Together with the enhanced hydro–mechanical coupling strategy, the framework permits complex, realistic industrial–grade simulations to be performed on a desktop PC in a reasonable amount of time, rendering it a useful design tool.

The two–phase flow model treats water as an incompressible liquid, while air is modelled as an adiabatic ideal gas. The interface between the two phases is modelled using the VOF interface capturing method, where both algebraic and geometric approaches are tested and used in this study. The discontinuity of density and compressibility across the interface is handled by employing the Ghost Fluid Method method, where specialised numerical schemes are devised to provide a one–cell–sharp change in fluid properties. The model is verified and validated in detail, exhibiting adequate level of accuracy and good agreement with other methods in the literature, including experimental results. Additionally, the developed model proved to be capable of capturing compressible wave impact pressure oscillations due to a trapped air bubble, where the results are compared to large–scale experimental data.

In order to assess the accuracy of the numerical framework an extensive verification and validation study is performed for a simple 3–D geometry of a FPSO, where green sea pressure loads are compared to experimental results. The study showed that acceptable accuracy can be achieved and that the framework can assess wave impact pressures with good accuracy. Here, the geometric and algebraic VOF methods are compared, and it is concluded that while the geometric approach offers a more resolved interface, the algebraic approach presents a more computationally efficient method while attaining acceptable level of accuracy with respect to pressure impact loads, which are of primary interest.

Finally, the numerical framework is tested on industrial–grade, multi–scale calculation of green sea pressure loads on a deck structure of an Ultra Large Container Ship. The long term response of the ship is calculated using linear frequency–domain method, which is used to define the deterministic Equivalent Design Wave, which in turn is used to perform the CFD simulations, where ship motion is calculated as well. The robustness and efficiency of the framework is demonstrated, where a desktop PC is used to preform the simulations, while the computational grid is generated using an automatic meshing software, resulting in an unstructured topology.

In future study, the developed framework will be tested for other wave impact related phenomena, namely slamming and sloshing. Sloshing of liquid cargo in ship holds presents an important problem from the structural integrity point of view, since sloshing induced wave impacts can cause high pressure loads on the cargo hold bulkheads. Compressibility of the gas phase plays an important role for sloshing, since the wave impact of the most adverse cases often include trapped gas pockets. In the present framework the sloshing excitation can be naturally calculated by performing a complete simulation of the ship in waves together with cargo holds.

Another goal for future work is to expand the framework to be capable of calculating the structural response to the wave impact. Pressure loads calculated in CFD can be transferred to a structural model, where the response in terms of deformation and stress could be calculated, giving valuable information for the structural design.

Bibliography

[1] D. F. Silva, P. T. Esperança, A. L. Coutinho, Green water loads on FPSOs exposed to beam and quartering seas, Part II: CFD simulations, Ocean Engineering 140 (2017) 434–452. doi:10.1016/j.oceaneng.2016.11.008.

[2] J. M. J. Journeé, W. Massie, Offshore Hydromechanics, Delft University of Technology, Cambridge University Press, 2001.

[3] C. Lugni, M. Brocchini, O. M. Faltinsen, Evolution of the air cavity during a depressurized wave impact. II. The dynamic field, Physics of Fluids 22 (5) (2010) 1–13. doi:10.1063/1.3409491.

[4] D. H. Peregrine, Water-Wave Impact On Walls, Annual Review of Fluid Mechanics 35 (1) (2003) 23–43. doi:10.1146/annurev.fluid.35.101101.161153.
URL http://www.annualreviews.org/doi/abs/10.1146/annurev.fluid.35.101101.161153

[5] E. S. Chan, W. K. Melville, Erratum: Deep-Water Plunging Wave Pressures on a Vertical Plane Wall, Proceedings of the Royal Society A: Mathematical, Physical and Engineering Sciences 419 (1857) (1988) 380–380. doi:10.1098/rspa.1988.0114.

[6] G. N. Bullock, C. Obhrai, D. H. Peregrine, H. Bredmose, Violent breaking wave impacts . Part 1 : Results from large-scale regular wave tests on vertical and sloping walls, Coastal Engineering 54 (2007) 602–617. doi:10.1016/j.coastaleng.2006.12.002.

[7] J.-P. Braeunig, L. Brosset, F. Dias, J.-M. Ghidaglia, Phenomenological Study of Liquid Impacts through 2D Compressible Two-fluid Numerical Simulations, in: 19th International Offshore and Polar Engineering Conference, Vol. 1, 2009, pp. 21–29.

[8] Z. H. Ma, D. M. Causon, L. Qian, C. G. Mingham, H. B. Gu, P. M. Ferrer, A compressible multiphase flow model for violent aerated wave impact problems, Proceedings of the Royal Society A: Mathematical, Physical and Engineering Sciences 470 (2172) (2014) 20140542–20140542. `doi:10.1098/rspa.2014.0542`.

URL `http://rspa.royalsocietypublishing.org/cgi/doi/10.1098/rspa.2014.0542`

[9] P. M. Guilcher, G. Oger, E. Jacquin, L. Brosset, N. Grenier, D. L. Touzé, Simulation of liquid impacts with a Two-Phase Parallel SPH model, International Journal of Offshore and Polar Engineering 24 (1) (2014) 11–20.

[10] C. Hirt, B. Nicholls, Volume of fluid method for dynamics of free boundaries, J. Comput. Phys. 39 (1981) 201–221.

[11] O. Ubbink, R. I. Issa, A method for capturing sharp fluid interfaces on arbitrary meshes, J. Comput. Phys. 153 (1999) 26–50.

[12] M. Sussman, P. Smereka, S. Osher, A level set approach for computing solutions to incompressible two-phase flow, J. Comput. Phys. 114 (1994) 146–159.

[13] R. Folch, J. Casademunt, A. Hernández-Machado, Phase–field model for Hele–Shaw flows with arbitrary viscosity contrast. I. Theoretical approach, Phys. Rev. E 60 (1999) 1724.

[14] O. Ubbink, Numerical prediction of two fluid systems with sharp interfaces, Ph.D. thesis, Imperial College of Science, Technology & Medicine, London (1997).

[15] S. Muzaferija, M. Perić, P. Sames, T. Schelin, A two–fluid Navier–Stokes solver to simulate water entry, in: Proceedings of the 22nd Symposium on Naval Hydrodynamics, 1998, pp. 638–651.

[16] H. Rusche, Computational fluid dynamics of dispersed two - phase flows at high phase fractions, Ph.D. thesis, Imperial College of Science, Technology & Medicine, London (2002).

[17] H. Jasak, V. Vukčević, D. Christ, Rapid Free Surface Simulation for Steady-State Hull Resistance with FVM using OpenFOAM, in: 30th Symposium on Naval Hydrodynamics, 2014, pp. 548–554.

[18] D. Gueyffier, J. Li, A. Nadim, R. Scardovelli, S. Zaleski, Volume-of-fluid interface tracking with smoothed surface stress methods for three-dimensional flows, J. Comput. Phys. 152 (2) (1999) 423–456.

[19] S. Popinet, An accurate adaptive solver for surface-tension-driven interfacial flows, J. Comput. Phys. 228 (16) (2009) 5838 – 5866.

[20] J. Roenby, H. Bredmose, H. Jasak, A computational method for sharp interface advection, Open Science 3 (11). `doi:10.1098/rsos.160405`.

[21] J. A. Sethian, Level Set Methods: Evolving Interfaces in Geometry, Fluid Mechanics, Computer Vision and Materials Science, Cambridge University Press, 1996.

[22] S. Osher, R. Fedkiw, Level Set Methods and Dynamic Implicit Surfaces, Springer, 2003.

[23] M. Sussman, E. Fatemi, An efficient, interface-preserving level set redistancing algorithm and its application to interfacial incompressible fluid flow, SIAM J. Sci. Comput. 20 (4) (1999) 1165–1191.

[24] E. Olsson, G. Kreiss, A conservative level set method for two phase flow, J. Comput. Phys. 210 (1) (2005) 225 – 246.

[25] T. Waclawczyk, A consistent solution of the re-initialization equation in the conservative level-set method, J. Comput. Phys. 299 (2015) 487 – 525.

[26] V. Vukčević, H. Jasak, S. Malenica, Decomposition model for naval hydrodynamic applications, Part I: Computational method, Ocean Eng. 121 (2016) 37–46. `doi:10.1016/j.oceaneng.2016.05.022`.

[27] Y. Sun, C. Beckermann, Sharp interface tracking using the phase–field equation, J. Comput. Phys. 220 (2007) 626–653.

[28] Y. Sun, C. Beckermann, A two–phase diffusive–interface model for Hele–Shaw flows with large property contrasts, Physica D 237 (2008) 3089–3098.

[29] C. Dopazo, On conditional averages for intermittent turbulent flows, J. Fluid Mech. 81 (1977) 433–438.

[30] N. G. Jacobsen, D. R. Fuhrman, J. Fredsøe, A wave generation toolbox for the open-source CFD library: OpenFoam®, Int. J. Numer. Meth. Fluids 70 (9) (2012) 1073–1088. doi:10.1002/fld.2726.

[31] P. Higuera, J. Lara, I. J. Losada, Realistic wave generation and active wave absorption for Navier-Stokes models: Application to OpenFoam®, Coast. Eng. 71 (2013) 102–118. doi:10.1016/j.coastaleng.2012.07.002.

[32] P. Higuera, J. Lara, I. J. Losada, Simulating coastal engineering processes with OpenFoam ®, Coast. Eng. 71 (2013) 119–134. doi:10.1016/j.coastaleng.2012.06.002.

[33] B. T. Paulsen, H. Bredmose, H. B. Bingham, An efficient domain decomposition strategy for wave loads on surface piercing circular cylinders, Coast. Eng. 86 (2014) 57–76. doi:10.1016/j.coastaleng.2014.01.006.

[34] B. T. Paulsen, H. Bredmose, H. B. Bingham, N. G. Jacobsen, Forcing of a bottom-mounted circular cylinder by steep regular water waves at finite depth, J. Fluid Mech. 755 (2014) 1–3. doi:10.1017/jfm.2014.386.

[35] P. Queutey, M. Visonneau, An interface capturing method for free–surface hydrodynamic flows, Comput. Fluids 36 (2007) 1481–1510. doi:10.1002/j.compfluid.2006.11.007.

[36] R. Luppes, B. Düz, H. van der Heiden, P. van der Plas, A. Veldman, Numerical simulations of two–phase flow with COMFLOW: past and recent developments, in: Proceedings of the ECCOMAS 2012 Conference, 2012, pp. 1–16.

[37] V. Vukčević, Numerical modelling of coupled potential and viscous flow for marine applications, Ph.D. thesis, Faculty of Mechanical Engineering and Naval Architecture, University of Zagreb, PhD Thesis (2016).

[38] H. Johansen, P. Colella, A Cartesian Grid Embedding Boundary Method for Poisson's Equation on Irregular Domains, J. Comput. Phys. 147 (1998) 60–85. doi:10.1006/jcph.1998.5965.

[39] R. K. Crockett, P. Colella, D. T. Graves, A Cartesian Grid Embedded Boundary Method for Solving the Poisson and Heat Equations with Discontinuous Coefficients in Three Dimensions, J. Comput. Phys. 230 (2010) 613–628. doi:10.1016/j.jcp.2010.12.017.

[40] S. Wang, J. Glimm, R. Samulyak, X. Jiao, C. Diao, An Embedded Boundary Method for Two Phase Incompressible Flow, ArXiv e-prints.arXiv:1304.5514.

[41] W. Bo, J. W. Grove, A volume of fluid method based ghost fluid method for compressible multi-fluid flows, Comput. Fluids 90 (2014) 113–122.

[42] O. Desjardins, V. Moureau, H. Pitsch, An accurate conservative level set/ghost fluid method for simulating turbulent atomization, J. Comput. Phys. 227 (18) (2008) 8395–8416.

[43] M. Kaneda, T. Haruna, K. Suga, Ghost-fluid-based boundary treatment in lattice boltzmann method and its extension to advancing boundary, Applied Thermal Engineering 72 (1) (2014) 126–134.

[44] B. Lalanne, L. R. Villegas, S. Tanguy, F. Risso, On the computation of viscous terms for incompressible two-phase flows with level set/ghost fluid method, J. Comput. Phys. 301 (2015) 289–307.

[45] H. Terashima, G. Tryggvason, A front-tracking/ghost-fluid method for fluid interfaces in compressible flows, J. Comput. Phys. 228 (11) (2009) 4012–4037.

[46] R. P. Fedkiw, T. Aslam, S. Xu, The ghost fluid method for deflagration and detonation discontinuities, J. Comput. Phys. 154 (2) (1999) 393–427.

[47] M. Kang, R. P. Fedkiw, X.-D. Liu, A boundary condition capturing method for multiphase incompressible flow, J. Sci. Comput. 15 (3) (2000) 323–360.

[48] R. P. Fedkiw, T. Aslam, B. Merriman, S. Osher, A non-oscillatory eulerian approach to interfaces in multimaterial flows (the ghost fluid method), J. Comput. Phys. 152 (2) (1999) 457 – 492.

[49] R. P. Fedkiw, T. Aslam, S. Xu, The ghost fluid method for deflagration and detonation discontinuities, J. Comput. Phys. 154 (2) (1999) 393 – 427.

[50] J. Huang, P. M. Carrica, F. Stern, Coupled ghost fluid/two–phase level set method for curvilinear body–fitted grids, Int. J. Numer. Meth. Fluids 44 (2007) 867–897. doi:10.1002/fld.1499.

[51] R. I. Issa, Solution of the implicitly discretised fluid flow equations by operator-splitting, J. Comput. Phys. 62 (1986) 40–65.

[52] H. Orihara, H. Miyata, Evaluation of added resistance in regular incident waves by computational fluid dynamics motion simulation using an overlapping grid system, Journal of Marine Science and Technology 8 (2003) 47–60. doi:10.1007/s00773-003-0163-5.

[53] T. Castiglione, F. Stern, S. Bova, M. Kandasamy, Numerical investigation of the seakeeping behavior of a catamaran advancing in regular head waves, Ocean Engineering 38 (2011) 1806–1822. doi:10.1016/j.oceaneng.2011.09.003.

[54] C.-S. Wu, D.-C. Zhou, L. Gao, Q.-M. Miao, CFD computation of ship motions and added resistance for a high speed trimaran in regular head waves, International Journal of Naval Architecture and Ocean Engineering 3 (2011) 105–110. doi:10.3744/jnaoe.2011.3.1.105.

[55] C. D. Simonsen, J. F. Otzen, S. Joncquez, F. Stern, EFD and CFD for KCS heaving and pitching in regular head waves, Journal of Marine Science and Technology 18 (2013) 435–459. doi:10.1007/s00773-013-0219-0.

[56] V. Vukčević, H. Jasak, Seakeeping validation and verification using decomposition model based on embedded free surface method, in: Tokyo 2015: A workshop on CFD in Ship Hydrodynamics, 2015.

[57] S. Bna, S. Manservisi, E. Aulisa, A MultiLevel Domain Decomposition Solver for Monolithic Fluid-Structure Interaction Problems, Vol. 1558 of Rhodes, Greece, AIP Conference Proceedings, 2013, pp. 871–874. doi:10.1063/1.4825635.

[58] P. Farah, A. T. Vuong, W. A. Wall, A. Popp, Volumetric coupling approaches for multiphysics simulations on non-matching meshes, International Journal for Numerical Methods in Engineering 108 (12) (2016) 1550–1576. doi:10.1002/nme.5285.

[59] E. Hachem, S. Feghali, R. Codina, T. Coupez, Immersed stress method for fluidstructure interaction using anisotropic mesh adaptation, International Journal for Numerical Methods in Engineering 94 (9) (2013) 805–825. doi:10.1002/nme.4481.

[60] M. Heil, A. L. Hazel, J. Boyle, Solvers for large-displacement fluid-structure interaction problems: segregated versus monolithic approaches, Computational Mechanics 43 (1) (2008) 91–101. doi:10.1007/s00466-008-0270-6.

[61] C. S. Jog, R. K. Pal, A monolithic strategy for fluid-structure interaction problems, International Journal for Numerical Methods in Engineering 85 (4) (2011) 429–460. doi:10.1002/nme.2976.

[62] U. Langer, H. D. Yang, Robust and efficient monolithic fluid-structure-interaction solvers, International Journal for Numerical Methods in Engineering 108 (4) (2016) 303–325. doi:10.1002/nme.5214.

[63] A. Legay, A. Zilian, C. Janssen, A rheological interface model and its space-time finite element formulation for fluid-structure interaction, International Journal for Numerical Methods in Engineering 86 (6) (2011) 667–687. doi:10.1002/nme.3060.

[64] P. Yang, J. Xiang, F. Fang, D. Pavlidis, J. P. Latham, C. C. Pain, Modelling of fluid-structure interaction with multiphase viscous flows using an immersed-body method, Journal of Computational Physics 321 (2016) 571–592. doi:10.1016/j.jcp.2016.05.035.

[65] A. Eken, M. Sahin, A parallel monolithic algorithm for the numerical simulation of large-scale fluid structure interaction problems, International Journal for Numerical Methods in Fluids 80 (12) (2016) 687–714. `doi:10.1002/fld.4169`.

[66] Z. Hu, W. Y. Tang, H. X. Xue, X. Y. Zhang, A simple-based monolithic implicit method for strong-coupled fluid-structure interaction problems with free surfaces, Computer Methods in Applied Mechanics and Engineering 299 (2016) 90–115. `doi:10.1016/j.cma.2015.09.011`.

[67] G. C. J., W. H. G., A unified formulation for continuum mechanics applied to fluid–structure interaction in flexible tubes, International Journal for Numerical Methods in Engineering 64 (12) (2005) 1575–1593. `arXiv:https://onlinelibrary.wiley.com/doi/pdf/10.1002/nme.1409`, `doi:10.1002/nme.1409`.
URL `https://onlinelibrary.wiley.com/doi/abs/10.1002/nme.1409`

[68] A. Robinson-Mosher, C. Schroeder, R. Fedkiw, A symmetric positive definite formulation for monolithic fluid structure interaction, Journal of Computational Physics 230 (4) (2011) 1547–1566. `doi:10.1016/j.jcp.2010.11.021`.

[69] P. Temarel, W. Bai, A. Bruns, Q. Derbanne, D. Dessi, S. Dhavalikar, N. Fonseca, T. Fukasawa, X. Gu, A. Nestegård, A. Papanikolaou, J. Parunov, K. H. Song, S. Wang, Prediction of wave-induced loads on ships: Progress and challenges, Ocean Engineering 119 (2016) 274–308. `doi:10.1016/j.oceaneng.2016.03.030`.

[70] M. Greco, B. Bouscasse, C. Lugni, 3-D seakeeping analysis with water on deck and slamming. Part 2: Experiments and physical investigation, Journal of Fluids and Structures 33 (2012) 127–147. `doi:10.1016/j.jfluidstructs.2012.04.005`.
URL `{%}3CGoto`

[71] M. Greco, C. Lugni, 3-D seakeeping analysis with water on deck and slamming. Part 1: Numerical solver, Journal of Fluids and Structures 33 (2012) 127–147.

[72] H. Lu, C. Yang, R. Loehner, Numerical Studies of Green Water Impact on Fixed and Moving Bodies, International Society of Offshore and Polar Engineers 22, 2012.

[73] H. Xu, Numerical Simulation of Breaking Wave Impact on the Structure, Ph.D. thesis, National University of Singapore, Singapore (2013).

[74] X. Zhao, Z. Ye, Y. Fu, Green water loading on a floating structure with degree of freedom effects, Journal of Marine Science and Technoly 19 (2014) 302–313. `doi:10.1007/s00773-013-0249-7`.

[75] S. Kim, C. Y. Kim, D. Cronin, Green water impact loads on breakwaters of large container carriers, in: Proceedings of the 12th International Symposium on Practical Design of Ships and Other Floating Structures PRADS, Changwon, Korea, 2013.

[76] F. Ruggeri, R. A. Wata, H. Brisson, P. A. Mello, C. M. P. e Silva, D. P. Vieira, Numerical prediction of green water events in beam seas, in: Proceedings of the 12th International Symposium on Practical Design of Ships and Other Floating Structures PRADS, Changwon, Korea, 2013.

[77] R. C. Zhu, G. P. Miao, Z. W. Lin, Numerical Research on FPSOs With Green Water Occurrence, Journal of Ship Research 53 (1) (2009) 7–18.

[78] R. Kudupudi, R. Datta, Numerical investigation of the effect due to vessel motion on green water impact on deck, Proceedings of the International Conference on Offshore Mechanics and Arctic Engineering - OMAE 7A-2017 (2009) (2017) 1–10. `doi:10.1115/OMAE2017-61054`.

[79] D. F. Silva, P. T. Esperança, A. L. Coutinho, Green water loads on FPSOs exposed to beam and quartering seas, part II: CFD simulations, Ocean Engineering 140 (May) (2017) 419–433. `doi:10.1016/j.oceaneng.2017.05.005`. URL `http://dx.doi.org/10.1016/j.oceaneng.2016.11.008`

[80] C. Pakozdi, A. Östman, G. Ji, C. T. Stansberg, O. Reum, S. Ovrebo, T. Vestbøstad, C. Sorvaag, J. Ersland, Estimation of Wave Loads due to Green Wa-

ter Events in 10000-Year Conditions on a TLP Deck Structure (49927) (2016) V001T01A050.

[81] G. D. Hauteclocque, Q. Derbanne, A. El-gharbaoui, Comparison of Different Equivalent Design Waves with Spectral Analysis, 31st International Conference on Ocean, Offshore and Arctic Engineering (2012) 1–9doi:10.1115/OMAE2012-83405.

[82] C. Pakozdi, A. Östman, C. T. Stansberg, D. F. Carvalho, Green water on FPSO analyzed by a coupled Potential-Flow-NS- VOF method, in: Proceedings of the 33rd International Conference on Ocean, Offshore and Arctic Engineering OMAE, San Francisco, USA, 2014.

[83] R. Joga, J. Saripilli, S. Dhavalikar, A. Kar, Numerical simulations to compute rate of water ingress into open holds due to green waters, in: Proceedings of the 24th International Offshore and Polar Engineering Conference ISOPE, Busan, Korea, 2014.

[84] P. M. Guilcher, N. Couty, L. Brosset, D. Le Touzé, Simulations of breaking wave impacts on a rigid wall at two different scales with a two-phase fluid compressible SPH model, International Journal of Offshore and Polar Engineering 23 (4) (2013) 241–253.

[85] M. Luo, C. G. Koh, W. Bai, M. Gao, A particle method for two-phase flows with compressible air pocket, International Journal for Numerical Methods in Engineering 108 (7) (2016) 695–721. arXiv:1010.1724, doi:10.1002/nme.5230.

[86] M. Luo, C. G. Koh, Shared-Memory parallelization of consistent particle method for violent wave impact problems, Applied Ocean Research 69 (2017) 87–99. doi:10.1016/j.apor.2017.09.013.

[87] M. Rostami V., M. J. Ketabdari, Application of the Modified Weakly Compressible SPH Method to the 3D Turbulent Wave Breaking Impact, Transactions of FAMENA 40 (1) (2016) 69–86.

[88] S. J. Lind, P. K. Stansby, B. D. Rogers, Incompressible-compressible flows with a transient discontinuous interface using smoothed particle hydrodynamics (SPH), Journal of Computational Physics 309 (2016) 129–147. doi:10.1016/j.jcp.2015.12.005.

[89] H. Jasak, OpenFOAM: Open source CFD in research and industry, International Journal of Naval Architecture and Ocean Engineering 1 (2) (2009) 89–94.

[90] M. Dumbser, A simple two-phase method for the simulation of complex free surface flows, Computer Methods in Applied Mechanics and Engineering 200 (9-12) (2011) 1204–1219. doi:10.1016/j.cma.2010.10.011.

[91] L. R. Plumerault, D. Astruc, P. Maron, The influence of air on the impact of a plunging breaking wave on a vertical wall using a multifluid model, Coastal Engineering 62 (2012) 62–74. doi:10.1016/j.coastaleng.2011.12.002.

[92] J. Costes, F. Dias, J. M. Ghidaglia, A. Mrabet, Simulation of Breaking Wave Impacts on a Flat Rigid Wall by a 2D Parallel Finite Volume Solver with Two Compressible Fluids and an Advanced Free Surface Reconstruction, Proceedings of 23rd International Offshore and Polar Engineering Conference (ISOPE) 9 (2013) 880653.

[93] S. T. Miller, H. Jasak, D. A. Boger, E. G. Paterson, A. Nedungadi, A pressure-based, compressible, two-phase flow finite volume method for underwater explosions, Computers and Fluids 87 (2013) 132–143. doi:10.1016/j.compfluid.2013.04.002.
URL http://dx.doi.org/10.1016/j.compfluid.2013.04.002

[94] Z. H. Ma, D. M. Causon, L. Qian, C. G. Mingham, T. Mai, D. Greaves, A. Raby, Pure and aerated water entry of a flat plate, Physics of Fluids 28 (1). doi:10.1063/1.4940043.

[95] Z. H. Ma, D. M. Causon, L. Qian, C. G. Mingham, P. Martínez Ferrer, Numerical investigation of air enclosed wave impacts in a depressurised tank, Ocean Engineering 123 (2016) 15–27. doi:10.1016/j.oceaneng.2016.06.044.

[96] J. Calderón-Sánchez, D. Duque, J. Gómez-Go˜ni, Modeling the impact pressure of a free falling liquid block with OpenFOAM, Ocean Engineering 103. doi:10.1016/j.oceaneng.2015.04.060.

[97] C. F. Zou, D. Y. Wang, Z. H. Cai, Effects of boundary layer and liquid viscosity and compressible air on sloshing characteristics, International Journal of Naval Architecture and Ocean Engineering 7 (4) (2015) 670–690. doi:10.1515/ijnaoe-2015-0047.

[98] W. Lyu, O. el Moctar, R. Potthoff, J. Neugebauer, Experimental and numerical investigation of sloshing using different free surface capturing methods, Applied Ocean Research 68 (2017) 307–324. doi:10.1016/j.apor.2017.09.008.

[99] H.-H. H. Lee, H.-J. J. Lim, S. H. Rhee, Experimental investigation of green water on deck for a CFD validation database, Ocean Engineering 42 (2012) 47–60. doi:10.1016/j.oceaneng.2011.12.026.

[100] V. Vukčević, H. Jasak, I. Gatin, Implementation of the Ghost Fluid Method for free surface flows in polyhedral Finite Volume framework , Computers & Fluids 153 (2017) 1 – 19.

Abbreviations

3–D three–dimensional. 31

CFD Computational Fluid Dynamics. 2, 4, 14–16, 32

CFL Courant–Friedrichs-Lewy. 19

EDW Equivalent Design Wave. 25

FD Finite Difference. 6

FE Finite Element. 7

FPSO Floating Production, Storage and Offloading. 1, 18, 31

FSI Fluid–Structure Interaction. 7

FV Finite Volume. 2–4, 7–10, 12, 30

GFM Ghost Fluid Method. 5, 6, 12, 18, 30

HOS Higher Order Spectral. 3, 14–16

LS Level Set. 4, 5

PF Phase Field. 4, 5

PIMPLE Combination of SIMPLE and PISO Algorithms. 6

PISO Pressure Implicit with Splitting of Operator. 6

PLIC Piecewise Linear Reconstruction Calculation. 4

RWA Relative Wave Amplitude. 25

SIMPLE Semi–Implicit Method for Pressure Linked Equations. 6

SPH Smoothed Particle Hydrodynamics. 2, 8–10

TLP Tension Leg Platform. 8

ULCS Ultra Large Container Ship. 3, 14, 25, 26, 31

VOF Volume–of–Fluid. 4, 11, 18, 19, 30, 31

Curriculum Vitae

Inno Gatin, born in Zabok, Croatia on 24 April 1991 has finished the XV. high school in Zagreb, 2010. On the same year he started the undergraduate program in the field of Naval Architecture and Ocean Engineering at the Faculty of Mechanical Engineering and Naval Architecture at University of Zagreb. He finished the undergraduate program and started with the graduate study program in 2014., finally graduating in 2015. During the studies he received several awards, such as the Rector's award in 2015. Always drawn to the hydrodynamical aspect of Naval Architecture, he wrote the Bachelor's Thesis on the topic of numerical wave loading calculation using OpenFOAM, continuing towards the Master's Thesis during which he implemented a spectral nonlinear method for wave propagation coupled to OpenFOAM. Upon his graduation he started his PhD study, and stared working as a Research Assistant a year later in 2016. on a project called "Numerical CFD Study of Irregular Wave Loads in OpenFOAM".

Declaration

Parts of the work presented in this Thesis have been published in some articles presented below.

List of Publications

[1] H. Jasak, I. Gatin, V. Vukčević, Monolithic coupling of the pressure and rigid body motion equations in computational marine hydrodynamics, Journal of Marine Science and Application 16 (4) (2017) 375–381.

[2] I. Gatin, V. Vukčević, H. Jasak, H. Rusche, Enhanced coupling of solid body motion and fluid flow in finite volume framework, Ocean Engineering 143 (2017) 295–304.

[3] I. Gatin, V. Vukčević, H. Jasak, A framework for efficient irregular wave simulations using Higher Order Spectral method coupled with viscous two phase model, Journal of Ocean Engineering and Science 2 (4) (2017) 253–267.

[4] V. Vukčević, H. Jasak, I. Gatin, Implementation of the Ghost Fluid Method for free surface flows in polyhedral Finite Volume framework , Computers & Fluids 153 (2017) 1 – 19.

[5] I. Gatin, V. Vukčević, H. Jasak, J. Seo, S. H. Rhee, CFD verification and validation of green sea loads, Ocean Engineering 148 (2018) 500–515.

[6] I. Gatin, G. Cvijetić, V. Vukčević, H. Jasak, Š. Malenica, Harmonic Balance method for nonlinear and viscous free surface flows, Ocean Engineering 157 (2018) 164–179.

[7] H. Jasak, V. Vukčević, I. Gatin, Numerical Simulation of Wave Loads on Static Offshore Structures, in: CFD for Wind and Tidal Offshore Turbines, Springer Tracts in Mechanical Engineering, 2015, pp. 95–105.

[8] I. Gatin, V. Vukčević, H. Jasak, Validation and Verification of Steady Resistance KCS Simulations with Dynamic Sinkage and Trim of KCS using Embedded Free Surface Method, in: Tokyo 2015: A workshop on CFD in Ship Hydrodynamics, 2015.

[9] G. Cvijetić, I. Gatin, H. Jasak, Applications of Harmonic Balance Method in Periodic Flows, in: The 4th Annual OpenFOAM User Conference, 2016.

[10] I. Gatin, V. Vukčević, H. Jasak, Implementation of Higher Order Spectral method for nonlinear wave propagation in OpenFOAM, in: OpenFOAM Workshop (18; 2015), 2015.

[11] I. Gatin, V. Vukčević, H. Jasak, CFD Validation of a Container Ship in Calm Water and Head Seas, in: Proceedings of the 18th Numerical Towing Tank Symposium, TuTech, 2015, pp. 53–58.

[12] I. Gatin, V. Vukčević, H. Jasak, Primjena Naval Hydro Paketa za Proračun Valnih Opterećenja, Zbornik radova Šestoga Susreta Hrvatskoga društva za mehaniku (2014) 73–78.

[13] I. Gatin, V. Vukčević, H. Jasak, Validation of Seakeeping CFD Simulations in Head and Oblique Waves Using the Naval Hydro Pack, in: 11th OpenFOAM Workshop, 2016.

[14] I. Gatin, V. Vukčević, H. Jasak, Monolithic coupling of rigid body motion and the pressure field in foam-extend, in: VII International Conference on Computational Methods in Marine Engineering, MARINE, International Center for Numerical Methods in Engineering (CIMNE), 2017, pp. 663–668.

[15] I. Gatin, V. Vukčević, H. Jasak, Simulation of Wave Impact Loads in OpenFOAM, in: Proceedings of the 21st symposium on Theory and Practice of Shipbuilding, In Memoriam prof. Leopold Sorta, 2014.

[16] I. Gatin, V. Vukčević, H. Jasak, Coupling of higher order spectral method and computational fluid dynamics, in: Proceedings of the 22nd symposium on Theory and Practice of Shipbuilding, In Memoriam prof. Leopold Sorta, 2016.

[17] V. Vukčević, B. Šojat, I. Gatin, H. Jasak, Validation and Verification of Seakeeping in OpenFOAM, in: Proceedings of the 22nd symposium on

Theory and Practice of Shipbuilding, In Memoriam prof. Leopold Sorta, 2016, pp. 135–142.

[18] I. Gatin, G. Cvijetić, V. Vukčević, H. Jasak, Wave Diffraction CFD Nonlinear Time–Spectral Simulations in foam–extend, in: 19th Numerical Towing Tank Symposium, 2016.

[19] V. Vukčević, G. Cvijetić, I. Gatin, H. Jasak, The Harmonic balance method for temporally periodic free surface flows in marine hydrodynamics, in: 11th OpenFOAM Workshop, 2016.

[20] I. Gatin, V. Vukčević, H. Jasak, Rapid seakeeping simulations in OpenFOAM, in: Sedmi susret Hrvatskog društva za mehaniku, 2016.

[21] I. Gatin, V. Vukčević, H. Jasak, Simulacija udarnih valnih opterećenja u OpenFOAM-u, in: Conference proceedings of the 21st symposium Theory and practice shipbuilding, in memoriam prof. Leopold Sorta, 2014, pp. 377–384.

[22] V. Vukčević, H. Jasak, I. Gatin, T. Uroić, Ship scale self propulsion CFD simulation results compared to sea trial measurements, in: VII International Conference on Computational Methods in Marine Engineering, MARINE 2017, 2017.

[23] I. Gatin, V. Vukčević, H. Jasak, Brze simulacije pomorstvenosti broda u OpenFOAM-u, Zbornik radova sedmog susreta Hrvatskog društva za mehaniku (2016) 73–78.

[24] G. Cvijetić, I. Gatin, V. Vukčević, H. Jasak, Harmonic Balance Developments in OpenFOAM, in: 12th OpenFOAM® Workshop, 2017.

[25] H. Jasak, I. Gatin, V. Vukčević, Accurate green water loads calculation using Naval Hydro Pack, in: IOP Conference Series: Materials Science and Engineering, Vol. 276, IOP Publishing, 2017, p. 012011.

[26] V. Vukcevic, H. Jasak, I. Gatin, S. Malenica, Seakeeping sensitivity studies using the decomposition CFD model based on the Ghost Fluid Method, in:

Proceedings of the 31st Symposium on Naval Hydrodynamics, Monterey, 2016.

[27] I. Gatin, N. Vladimir, Šime Malenica, H. Jasak, Green sea loads in irregular waves with finite volume method, Ocean Engineering 171 (2019) 554 – 564. `doi:https://doi.org/10.1016/j.oceaneng.2018.10.061`.
URL `http://www.sciencedirect.com/science/article/pii/S0029801818313672`

Summary of Papers

PAPER 1

Gatin I., Vukčević V., Jasak H. *A framework for efficient irregular wave simulations using Higher Order Spectral method coupled with viscous two phase model.* Journal of Ocean Engineering and Science, 2017;2:253-267.

In this paper a framework for efficient irregular wave simulations using Higher Order Spectral method coupled with fully nonlinear viscous, two-phase Computational Fluid Dynamics (CFD) model is presented. CFD model is based on solution decomposition via Spectral Wave Explicit Navier–Stokes Equation method, allowing efficient coupling with arbitrary potential flow solutions. Higher Order Spectrum is a pseudo-spectral, potential flow method for solving nonlinear free surface boundary conditions up to an arbitrary order of nonlinearity. It is capable of efficient long time nonlinear propagation of arbitrary input wave spectra, which can be used to obtain realistic extreme waves. To facilitate the coupling strategy, Higher Order Spectrum method is implemented in foam-extend alongside the CFD model. Validation of the Higher Order Spectrum method is performed on three test cases including monochromatic and irregular wave fields. Additionally, the coupling between Higher Order Spectrum and CFD is validated on three hour irregular wave propagation. Finally, a simulation of a 3D extreme wave encountering a full scale container ship is shown.

The implementation, validation and testing of the Higher Order Spectrum method were performed by Gatin. The paper was written by Gatin and reviewed by Jasak and Vukčević.

PAPER 2

Gatin I., Jasak H., Vukčević V., Downie S. *Focused Wave Loading on a Fixed FPSO using Naval Hydro Pack.* The Twenty-Eighth (2018) International Ocean and Polar Engineering Conference, Sapporo, Hokkaido, Japan, June 10−15, 2018.

Validation of the Naval Hydro CFD software pack for focused wave loading on a fixed FPSO is presented in this paper. Naval Hydro Pack is based on Finite Volume CFD software called foam–extend, and it is specialised for large–scale, two-phase surface flows encountered in naval hydrodynamics. Simulations are performed using SWENSE method (Spectral Wave Explicit Navier–Stokes Equations) for solution decomposition, while implicit relaxation zones are employed for wave initialisation and damping. Numerical results are submitted to a blind comparison with experimental results within the CCP–WSI Blind Test Workshop. Six cases are considered altogether where different incident waves and incident angles are considered. Prssure loads and free surface elevation are considered in this work.

The implementation of the New Wave model and simulations were performed by Gatin. Downie contributed by evaluating the results. The paper was written by Gatin and reviewed by Jasak, Downie and Vukčević.

PAPER 3

Gatin I., Vukčević V., Jasak H., Rusche H. *Enhanced coupling of solid body motion and fluid flow in finite volume framework.* Ocean Engineering, 2017;143:295-304.

An enhanced coupling strategy for the resolution of 6–degrees–of–freedom rigid body motion and unsteady incompressible fluid flow in Finite Volume collocated arrangement using PIMPLE algorithm and rigid mesh motion is presented in this paper. The improved coupling is achieved by calculating the 6–degrees–of–freedom motion equations after each pressure correction step in the pressure–velocity PISO (Pressure Implicit With Splitting of Operators) algorithm. Solving the

6–degrees–of–freedom equations after each solution of the pressure equation of the PISO loop accelerates the convergence, leading to smaller number of nonlinear pressure–velocity iterations needed per time–step. The novel approach is verified and validated on a heaving decay case, while the achieved acceleration in terms of the number of nonlinear iterations is demonstrated on seakeeping simulations of a container ship.

In this paper the implementation, verification and validation of the method were performed by Gatin. Vukčević and Rusche devised the coupling strategy. The paper was written by Gatin and reviewed by Jasak and Vukčević.

PAPER 4

Jasak H., Gatin I., Vukčević V. *Monolithic coupling of the pressure and rigid body motion equations in computational marine hydrodynamics.* Journal of Marine Science and Application, 2017;16:375-381.

In Fluid Structure Interaction (FSI) problems encountered in marine hydrodynamics, the pressure field and the velocity of the rigid body are tightly coupled. This coupling is traditionally resolved in a partitioned manner by solving the rigid body motion equations once per nonlinear iteration, updating the position of the body and solving the fluid flow equations in the new configuration. The partitioned approach requires a large number of nonlinear iterations per time–step. In order to enhance the coupling, a monolithic approach is proposed in Finite Volume (FV) framework, where the pressure equation and the rigid body motion equations are solved in a single linear system. The coupling is resolved by solving the rigid body motion equations once per linear solver iteration of the pressure equation, where updated pressure field is used to calculate new forces acting on the body, and by introducing the updated rigid body boundary velocity into the pressure equation. In this paper the monolithic coupling is validated on a simple 2D heave decay case. Additionally, the method is compared to the traditional partitioned approach (i.e. “strongly coupled” approach) in terms of computational efficiency and accuracy. The comparison is performed on a seakeeping case in regular head waves, and it shows that the monolithic approach achieves similar accuracy with fewer nonlinear correctors per time–step. Thus, significant savings in computational time can be achieved while retaining the same level of accuracy.

In this paper the implementation, verification and validation of the method were performed by Gatin. Jasak and Vukčević devised the monolithic strategy. The paper was written by Gatin and reviewed by Jasak and Vukčević.

PAPER 5

Gatin I., Vukčević V., Jasak H., Seo J., Rhee S H. *CFD verification and validation of green sea loads.* Ocean Engineering, 2017;148:500-515.

An extensive verification and validation for green sea load simulations is presented. The calculations are performed using the Naval Hydro Pack, a library based on foam–extend, which is an open source Computational Fluid Dynamics software. The geometric Volume of Fluid method is used for interface advection, while the Ghost Fluid Method is employed to discretise the free surface boundary conditions at the interface. Pressure measured at the deck of a fixed structure is compared to experimental data for nine regular waves. Verification is performed using four refinement levels in order to reliably assess numerical uncertainties. A detailed uncertainty analysis comprises both numerical and experimental data. Comparable uncertainties are obtained in simulations and experiments, with good agreement of results.

In this paper the verification and validation were performed by Gatin. Seo and Rhee post–processed and supplied the experimental data. The paper was written by Gatin and reviewed by Jasak and Vukčević.

PAPER 6

Gatin I., Liu S., Vukčević V., Jasak H. *Finite Volume Method for General Compressible Naval Hydrodynamics*, Submitted to Ocean Engineering, 2018.

An efficient, pressure based two–phase method with compressible gas phase and incompressible liquid phase model within collocated Finite Volume approach is shown in this paper. Incompressible treatment of the heavier phase enables efficient long evolutions of wave fields without the need for a separate solver for handling wave field evolution. Air is treated as isentropic ideal gas, removing the need for an additional energy equation, as well as related numerical difficulties. The discontinuity in properties between the two phases is treated using the Ghost Fluid Method, correctly accounting for the abrupt change in density and compressibility. Detailed verification and validation is conduced on three simple test cases comprising a liquid piston showing proper treatment of the compressible phase, free fall impact of a horizontal water column and a regular wave propagation case to test the stability and accuracy for cases without compressibility effects. The present approach is compared to the incompressible formulation for industrial–grade simulations, showing that same level of accuracy can be achieved without significant overhead in terms of computational time. Finally, a compressible wave breaking impact from a large–scale experimental campaign is reproduced, showing that the method is capable of capturing trapped air cushioning effects.

In this paper the formulation, implementation, verification and validation of the numerical model were performed by Gatin. Liu performed the breaking wave impact simulation. The paper was written by Gatin and reviewed by Jasak and Vukčević.

PAPER 7

Gatin I., Vladimir N., Malenica Š., Jasak H. *Green Sea Loads in Irregular Waves with Finite Volume Method*, Ocean Engineering, 2018;171:554-564.

Green sea loads upon a vertical deck structure of an Ultra Large Container Ship are calculated in this paper using Finite Volume based CFD, where two different approaches for the definition of the Equivalent Design Wave are used. Linear frequency–domain method is used to calculate the long term response in terms of Relative Wave Amplitude, which in turn is used to define the Equivalent Design Wave, which is then used in the CFD simulation. Regular Equivalent Design Wave and Response Conditioned Wave approaches are used and compared in terms of loads exerted on the deck structure and required computational resources. Large differences in loads are found between the methods, whilst similar computational resources are required. The Regular Equivalent Design Wave gives the highest loads, making it the safest choice. However, Response Conditioned Wave takes into account the response of the ship, resulting in smaller, more realistic loads.

In this paper the numerical CFD modelling and CFD simulations were performed by Gatin. Vladimir performed linear frequency–domain calculations, while Malenica provided guidance on the topic. The paper was written by Gatin and reviewed by Vladimir, Malenica, Jasak and Vukčević.

PAPER 8

Gatin I., Vukčević V., Jasak H. *Towards multiscale green sea loads simulations in irregular waves with Naval Hydro pack.* 12th OpenFOAM Workshop, Exeter, 24th–27th July, 2017.

An overview of the current state of the ongoing effort to devise a comprehensive multiscale procedure for determination of green sea loads on ships and offshore structures is given in this paper. The aim of the research is to asses deterministic green water loads on arbitrary deck structures and equipment that corresponds to the stochastic nature of the sea states which the naval object encounters.

The simulations in this work were performed by Gatin. Development of the linearised free surface model was performed by Vukčević. The paper was written by Gatin and reviewed by Jasak and Vukčević.

PAPER 1

Available online at www.sciencedirect.com
ScienceDirect
Journal of Ocean Engineering and Science 2 (2017) 253–267
www.elsevier.com/locate/joes

A framework for efficient irregular wave simulations using Higher Order Spectral method coupled with viscous two phase model

Inno Gatin[a,*], Vuko Vukčević[a], Hrvoje Jasak[a,b]

[a] *Faculty of Mechanical Engineering and Naval Architecture, University of Zagreb, Ivana Lučića 5, Zagreb, Croatia*
[b] *Wikki Ltd., 459 Southbank House, SE1 7SJ London, United Kingdom*

Received 10 May 2017; received in revised form 24 July 2017; accepted 6 September 2017
Available online 14 September 2017

Abstract

In this paper a framework for efficient irregular wave simulations using Higher Order Spectral method coupled with fully nonlinear viscous, two-phase Computational Fluid Dynamics (CFD) model is presented. CFD model is based on solution decomposition via Spectral Wave Explicit Navier–Stokes Equation method, allowing efficient coupling with arbitrary potential flow solutions. Higher Order Spectrum is a pseudo-spectral, potential flow method for solving nonlinear free surface boundary conditions up to an arbitrary order of nonlinearity. It is capable of efficient long time nonlinear propagation of arbitrary input wave spectra, which can be used to obtain realistic extreme waves. To facilitate the coupling strategy, Higher Order Spectrum method is implemented in foam-extend alongside the CFD model. Validation of the Higher Order Spectrum method is performed on three test cases including monochromatic and irregular wave fields. Additionally, the coupling between Higher Order Spectrum and CFD is validated on three hour irregular wave propagation. Finally, a simulation of a 3D extreme wave encountering a full scale container ship is shown.

Keywords: Higher Order Spectral method; Irregular waves; Extreme waves; CFD; Foam-extend.

1. Introduction

With increased availability of CPU resources during past few decades, Computational Fluid Dynamics (CFD) is becoming a standard practice for simulation of transient free-surface waves. CFD methods that model fully-nonlinear, two-phase, viscous flow exhibit high computational costs, which prohibit long time wave evolution in a large domain. This disadvantage is partially overcome using domain decomposition strategies, where the flow in a small, relevant part of the domain is resolved using CFD, while the farfield flow is resolved using potential flow, a computationally cheaper model. Given the potential flow solution, the CFD simulation naturally develops nonlinear, viscous flow with vorticity effects. First decomposition method was developed by Van Dalsem and Steger [1], called Fortified Navier–Stokes (FNS) method. Van Dalsem and Steger used the decomposition to ‘fortify’ the solution of subset equations in the boundary layer, while solving ordinary Navier–Stokes in the rest of the domain. Jacobsen et al. [2] introduced a domain decomposition method for wave modelling using relaxation zones. Paulsen et al. [3] used one-way coupling between fully nonlinear potential flow solver (developed by Ensig-Karup et al. [4]) and fully nonlinear viscous CFD solver to investigate wave loads on a circular surface piercing cylinder. The same method was used to calculate steep regular wave loads on a bottom mounted cylinder [5]. Pistidda and Ottens [6] used the Euler Overlay Method for domain decomposition to calculate the Response Amplitude Operator (RAO) for a moonpool of a deep water construction vessel.

Vukčević and Jasak [7] developed a modified Spectral Wave Explicit Navier–Stokes Equation (SWENSE) [8–10] solution decomposition method which is used alongside domain decomposition. The solution is decomposed into incident and

---

[*] Corresponding author.

E-mail addresses: inno.gatin@fsb.hr, innogatin@gmail.com (I. Gatin), vuko.vukcevic@fsb.hr (V. Vukčević), h.jasak@wikki.co.uk, hrvoje.jasak@fsb.hr (H. Jasak).

http://dx.doi.org/10.1016/j.joes.2017.09.003

diffracted fields, where the incident field is obtained from the potential flow model, while the diffracted field is solved via two-phase, viscous CFD model. All of the above mentioned CFD methods are computationally expensive because they are modelling highly resolved spatial flow features with nonlinear and coupled equations in time domain. Hence, they cannot be used to perform a large number of long time irregular wave field propagations needed to obtain a naturally emerging extreme wave.

Extreme wave loads are gaining more attention due to increasing number of offshore objects being installed worldwide. Extreme waves emerge due to focusing of wave spectrum components, which is influenced by nonlinear wave modulation and wave-to-wave interaction. It is considered that the influence of wind and atmospheric pressure, bathymetry and current [11] also plays a role in extreme wave generation. Apart from the focusing of unidirectional spectrum, geometric focusing of directional spectrum can also cause extreme wave events.

Assessment of extreme wave loads demands accurate wave modelling. Since extreme waves occur randomly in an irregular sea state, in order to obtain a statistically and physically accurate extreme wave, irregular sea state needs to be evolved for a long time on a large domain. Moreover, the evolution of the irregular sea state has to take into account nonlinear effects of wave interaction and modulation. CFD takes into account all nonlinearities of the flow, and inherently the nonlinearities of wave-to-wave interaction and wave modulation. However, even with domain decomposition methods, it is challenging to propagate arbitrary wave field for a sufficient amount of time to observe a natural emergence of extreme waves. Apart from that, long time CFD simulation might accumulate discretization errors which will inevitably influence the wave field. To obtain a realistic extreme wave in an irregular sea state, as much as a thousand peak periods need to be simulated. Paulsen et al. [3] reported that one irregular wave peak period took 8 hours to compute on 10 CPU's, extrapolating to almost a year for 1000 peak periods, which might be necessary to obtain a realistic extreme wave.

Nonlinear wave field can be efficiently propagated using spectral potential flow approach. In this work, potential flow pseudo-spectral Higher Order Spectral (HOS) method is used. Nonlinearities of wave-to-wave interaction and wave modulation are taken into account, while viscous effects, vorticity, wave breaking, diffraction and radiation are neglected. Since the latter effects have minor influence on extreme wave emergence, HOS method can be used to perform a long time evolution of an irregular wave field on a large-scale domain to obtain a statistically and physically consistent extreme wave. HOS can then be coupled with CFD in a small spatial domain containing the extreme wave, and for a short period of time to capture viscous effects, wave breaking and fluid–structure interaction. In this work one-way coupling between HOS and CFD is achieved using the decomposition model [7].

HOS method was first developed by Dommermuth and Yue [12] and West et al. [13] independently. West et al. used order consistent Taylor and perturbation series expansion, which is adopted by most HOS algorithms today [14,15]. Since the publication of the original method in 1987, numerous authors continued its development. Ducrozet et al. [15] enhanced numerical efficiency and aliasing treatment, while Tanaka [14] combined HOS with complex amplitude function. Dommermuth [16] developed a time relaxation scheme which enables HOS calculation to be initialized with a linear solution. This is of crucial importance since wave energy spectra are defined for linear wave components.

In this paper a mathematical overview of the HOS method is given, followed by a detailed description of numerical procedure. The CFD model and coupling with potential flow by Vukčević and Jasak [7] is used. Three test cases are considered for HOS validation purposes. The first case considers monochromatic wave train propagation, where modal amplitudes are compared with analytical Stokes solution. Second test case considers propagation of four uniformly steep spectra, where the HOS solution is compared to viscous, two-phase CFD solution. Third test case shows naturally occurring Benjamin–Feir instabilities [17]. In addition to the validation of the implemented HOS model, the coupling between HOS and CFD using SWENSE is also validated on a three hour irregular wave propagation case. Finally, an example simulation of a 3D extreme wave encountering a full scale container ship is shown. According to ITTC guidelines, the present method applied on this case presents a fully-nonlinear seakeeping calculation.

2. Mathematical model

In this section mathematical model for the HOS method is outlined; the reader is referred to [12–15] for more details.

Pseudo-spectral HOS method is used to reformulate nonlinear partial differential equation set via perturbation, Taylor and Fourier series into a set of ordinary differential equations.

2.1. Governing equations

In this model, free-surface flow is assumed irrotational, inviscid and incompressible. Surface gravity wave propagation is described with the following governing equations:

- Laplace equation for incompressible, irrotational, inviscid flow:

  $$\nabla^2\phi(x, y, z, t) = 0, \tag{1}$$

  where ϕ is the velocity potential, while x, y, z are spatial coordinates and t is time.
- Dynamic free surface boundary condition:

  $$\frac{\partial\phi}{\partial t} + gz + \frac{1}{2}(\nabla\phi)^2 = 0, \tag{2}$$

  where g is the gravitational acceleration in the direction of negative z axis.
- Kinematic free surface boundary condition:

  $$\frac{\partial\eta}{\partial t} + \left(\frac{\partial\phi}{\partial x}, \frac{\partial\phi}{\partial y}\right) \cdot \left(\frac{\partial\eta}{\partial x}, \frac{\partial\eta}{\partial y}\right) = \frac{\partial\phi}{\partial z}, \tag{3}$$

where $\eta = \eta(x, y, t)$ is a single valued function of the free surface displacement.

Depth is considered uniform and the bottom impermeable, while the domain is assumed periodic in the horizontal directions [15].

Eqs. (2) and (3) can be rewritten in terms of surface potential $\psi(x, y, t) = \phi(x, y, \eta(x, y, t), t)$, as they are valid for $z = \eta(x, y, t)$:

$$\frac{\partial \psi}{\partial t} + g\eta + \frac{1}{2}\left(\frac{\partial \psi}{\partial x}, \frac{\partial \psi}{\partial y}\right)^2 - \frac{1}{2}\left(\left.\frac{\partial \phi}{\partial z}\right|_{z=\eta}\right)^2 \left(1 + \left(\frac{\partial \eta}{\partial x}, \frac{\partial \eta}{\partial y}\right)^2\right) = 0, \tag{4}$$

$$\frac{\partial \eta}{\partial t} + \left(\frac{\partial \psi}{\partial x}, \frac{\partial \psi}{\partial y}\right) \cdot \left(\frac{\partial \eta}{\partial x}, \frac{\partial \eta}{\partial y}\right) - \left.\frac{\partial \phi}{\partial z}\right|_{z=\eta} \left(1 + \left(\frac{\partial \eta}{\partial x}, \frac{\partial \eta}{\partial y}\right)^2\right) = 0. \tag{5}$$

2.2. Higher Order Spectral method

A pseudo-spectral, HOS method has been used to obtain a nonlinear solution of free surface boundary conditions, Eqs. (4) and (5). All spatial derivatives are evaluated in wave number space, while time derivatives are evolved in physical space instead of the frequency domain. The shape function for velocity potential used in the wave number space is:

$$\phi(x, y, z, t) = \sum_k \sum_l c_{k,l}(t) \frac{\cosh\left(K_{k,l}(z + d)\right)}{\cosh(K_{k,l} d)} e^{iK_k x} e^{iK_l y}, \tag{6}$$

where $c_{k,l}(t)$ are the time-dependent Fourier coefficients, while $K_{k,l}$, K_k and K_l are wave numbers defined as:

$$K_k = \frac{2\pi k}{L_x}, \tag{7}$$

$$K_l = \frac{2\pi l}{L_y}, \tag{8}$$

$$K_{k,l} = \sqrt{K_k^2 + K_l^2}. \tag{9}$$

Fourier series decomposition given by Eq. (6) allows us to calculate horizontal derivatives analytically, whereas vertical derivative needs special treatment as it represents vertical velocity of the free surface W, at the unknown wave elevation η. Hence, it is necessary to use the full form of the shape function given by Eq. (6), calculate its derivative it in z direction, and evaluate it at the exact free surface location. This presents a Dirichlet problem for the velocity potential ϕ on a boundary of complicated shape $\eta(x, y, t)$. In order to circumvent this difficulty, the surface potential is expanded in a Taylor series around $z = 0$ in terms of η:

$$\phi(x, y, \eta, t) = \psi(x, y, t) = \sum_{i=0}^{\infty} \frac{\eta^i}{i!} \frac{\partial^i}{\partial z^i} \phi(x, y, 0, t). \tag{10}$$

The vertical derivative of surface potential is:

$$W(x, y, t) = \left.\frac{\partial \phi}{\partial z}\right|_{z=\eta} = \sum_{i=0}^{\infty} \frac{\eta^i}{i!} \frac{\partial^{i+1}}{\partial z^{i+1}} \phi(x, y, 0, t). \tag{11}$$

To keep the solution up to an arbitrary order of nonlinearity, the potential is expanded in perturbation series in terms of wave slope $\epsilon = Ka$, where K is the wave number and a is the wave amplitude:

$$\phi(x, y, z, t) = \phi_1 + \epsilon \phi_2 + \epsilon^2 \phi_3 + \cdots = \sum_{m=1}^{M} \phi^{(m)}, \tag{12}$$

where M is the perturbation series order of nonlinearity. With every order of ϕ expanded in a Taylor series using Eq. (10), surface potential can be written as:

$$\psi(x, y, t) = \sum_{m=1}^{M} \sum_{i=0}^{M-m} \frac{\eta^i}{i!} \frac{\partial^i}{\partial z^i} \phi^{(m)}(x, y, 0, t). \tag{13}$$

The orders of nonlinearities are determined with respect to the product of η^i and $\partial^i \phi^{(m)}/\partial z^i$, and the second sum in Eq. (13) is truncated at $M - m$ to account for order consistency. The unknowns in Eq. (13) are the individual orders of velocity potential $\phi^{(m)}$, which are calculated sequentially by equating the terms of the same order:

$$\phi^{(1)} = \psi(x, y, t),$$

$$\phi^{(2)} = -\eta \frac{\partial}{\partial z} \phi^{(1)},$$

$$\vdots$$

$$\phi^{(m)} = -\sum_{i=1}^{m-1} \frac{\eta^i}{i!} \frac{\partial^i}{\partial z^i} \phi^{(m-i)}; \quad m = 2, 3 \ldots, M. \tag{14}$$

Once the individual orders of ϕ are obtained, vertical velocity W can be evaluated. Vertical velocity of the free surface is also expanded in a perturbation series, while the individual orders are calculated using orders of ϕ as follows:

$$W^{(m)} = \sum_{i=0}^{m-1} \frac{\eta^i}{i!} \frac{\partial^{(i+1)}}{\partial z^{(i+1)}} \phi^{(m-i)}; \quad m = 1, 2, \ldots, M. \tag{15}$$

Total vertical velocity is then obtained by summing all individual orders:

$$W(x, y, t) = \sum_{m=1}^{M} W^{(m)}. \tag{16}$$

In theory, the order of nonlinearity M at which the expansion is truncated is arbitrary. The main advantage of this approach is that no iterations are needed per time step to resolve the coupling of the boundary conditions. Furthermore, Fourier transform facilitates the calculation of spatial derivatives, accelerating the numerical procedure.

3. Numerical model

The Fast Fourier Transform (FFT) algorithm is used for efficient calculation of the Fourier transform, while the fifth-order Cash–Karp embedded Runge–Kutta scheme with error control and adjustable time-step size [18] is used to solve ordinary differential equations. In this section, emphasis is given on numerical procedure and initialisation of HOS calculation. Dealiasing, time integration and coupling with CFD are also briefly explained.

3.1. Numerical procedure

The numerical procedure starts with a discrete surface potential ψ and surface elevation η which are obtained from the previous time step or initial conditions. The discrete values are located on a uniform discrete mesh with nodes equidistantly spaced along the domain's length L_x and width L_y. Hence, the mesh is fully defined with a number of nodes N_x in x and N_y in y direction, yielding mesh resolution $\Delta x = L_x/N_X$ and $\Delta y = L_y/N_y$. Using Eq. (6), the vertical derivative of velocity potential can generally be written as:

$$\frac{\partial^j \phi}{\partial z^j} = \frac{\partial^j}{\partial z^j}\left(\sum_k \sum_l c_{k,l}(t)\,\frac{\cosh\left(K_{k,l}(z+d)\right)}{\cosh(K_{k,l}d)}\, e^{iK_k x}\, e^{iK_l y}\right)$$
$$= \sum_k \sum_l c_{k,l}(t)\, K_{k,l}^j\, \frac{\sinh\left(K_{k,l}(z+d)\right)}{\cosh(K_{k,l}d)}\, e^{iK_k x}\, e^{iK_l y}. \quad (17)$$

While calculating individual terms of a given order in Eq. (14), the spatial derivatives are calculated in wave number space. After evaluating each order $\phi^{(m)}$ in physical space, it is transformed via FFT into wave number space. This is required in order to efficiently calculate vertical derivative of $\phi^{(m)}$, used in calculation of $\phi^{(m+1)}$. Once the individual derivatives are calculated, they are inversely transformed back into physical space before multiplying with a corresponding power of η. In the following equations, Fourier transform of a discrete field f is denoted with $\mathscr{F}(f)$, and the inverse transform is denoted with $\mathscr{F}^{-1}(f)$. Eq. (14) can be written as:

$$\phi^{(1)} = \psi(x_n, t),$$
$$\phi^{(m)} = -\sum_{j=1}^{m-1} \frac{\eta^j}{j!}\, \mathscr{F}^{-1}\left\{\sum_k \sum_l c_{k,l}^{(m-j)}(t)\, K_{k,l}^j\, e^{iK_k x}\, e^{iK_l y}\right\};$$
$$m = 2, 3, \ldots, M, \quad (18)$$

where $c_{k,l}^{(m-j)}(t)$ is the Fourier coefficient of order $m-j$ of the $k,\, l$th Fourier mode. It is calculated by performing FFT on preceding orders of ϕ on a discrete spatial mesh:

$$c_{k,l}^{(m-j)}(t) = \mathscr{F}\left\{\phi^{(m-j)}(x, y, t)\right\}. \quad (19)$$

Once all the orders of ϕ are evaluated, orders of vertical velocity W are calculated using Eq. (15):

$$W^{(1)} = \mathscr{F}^{-1}\left\{\sum_k \sum_l c_{k,l}^{(1)}(t)\, K_{k,l}\, e^{iK_k x}\, e^{iK_l y}\right\},$$
$$W^{(m)} = \sum_{j=0}^{m-1} \frac{\eta^j}{j!}\, \mathscr{F}^{-1}\left\{\sum_k \sum_l c_{k,l}^{(m-j)}(t)\, K_{k,l}^{(j+1)}\, e^{iK_k x}\, e^{iK_l y}\right\};$$
$$m = 1, 2, \ldots, M. \quad (20)$$

The inverse Fourier transforms occurring in Eq. (20) are already calculated in Eq. (18), except for the last order of vertical velocity $W^{(M)}$, for which the inverse Fourier transform has to be calculated separately. The inverse Fourier transforms calculated in Eq. (18) are hence stored for efficiency.

Once ϕ, η and W are known, we proceed by evaluating the coupling terms in Eqs. (4) and (5). Spatial horizontal derivatives are calculated in the wave number space, hence the surface elevation displacement η (available on discrete spatial mesh) has to be transformed via FFT. When all the derivatives are calculated, they are transformed back to the physical space and multiplied. Time marching boundary condition equations, Eqs. (4) and (5) can finally be written as:

$$\frac{\partial \psi(x, y, t)}{\partial t} = -g\,\eta(x, y, t)$$
$$-\frac{1}{2}\left(\mathscr{F}^{-1}\left\{\sum_k \sum_l c_{k,l}^{\psi}(t)\, iK_{k,l}\, e^{iK_k x}\, e^{iK_l y}\right\}\right)^2$$
$$+\frac{1}{2}W^2\left(1 + \left(\mathscr{F}^{-1}\left\{\sum_k \sum_l c_{k,l}^{\eta}(t)\, iK_{k,l}\, e^{iK_k x} e^{iK_l y}\right\}\right)^2\right), \quad (21)$$

$$\frac{\partial \eta(x, y, t)}{\partial t} = W\left(1 + \left(\mathscr{F}^{-1}\left\{\sum_k \sum_l c_{k,l}^{\eta}(t)\, iK_{k,l}\, e^{iK_k x} e^{iK_l y}\right\}\right)^2\right)$$
$$- \mathscr{F}^{-1}\left\{\sum_k \sum_l c_{k,l}^{\psi}(t)\, iK_{k,l}\, e^{iK_k x} e^{iK_l y}\right\}$$
$$\times \mathscr{F}^{-1}\left\{\sum_k \sum_l c_{k,l}^{\eta}(t)\, iK_{k,l}\, e^{iK_k x} e^{iK_l y}\right\}, \quad (22)$$

where $c_{k,l}^{\psi}(t)$ and $c_{k,l}^{\eta}(t)$ are the Fourier coefficients obtained by performing a Fourier transform on discrete values of ψ and η, respectively. Fig. 1 shows the flow chart of the HOS method during one time step.

3.2. Time integration

Time integration of Eqs. (21) and (22) is performed with the fifth-order Cash–Karp embedded Runge–Kutta scheme with error control and adjustable time-step size. For more details on time integration the reader is referred to Press et al. [18].

3.3. Initialization of the wave field in a HOS simulation

In order to initialize a HOS simulation, discrete values of $\psi(x, y, t = 0)$ and $\eta(x, y, t = 0)$ are needed. Initialization of HOS simulation is not trivial since linear initial conditions generally do not satisfy the free surface boundary conditions. As shown by Dommermuth [16], initializing the simulation with a linear solution leads to unstable simulation, since nonlinearities do not have the time to develop before the emergence of spurious high frequency standing waves. Dommermuth developed a time relaxation scheme to avoid this problem, enabling initialisation of HOS simulation with a linear solution. This adjustment scheme smooths out the natural emergence of nonlinear terms over time by relaxing

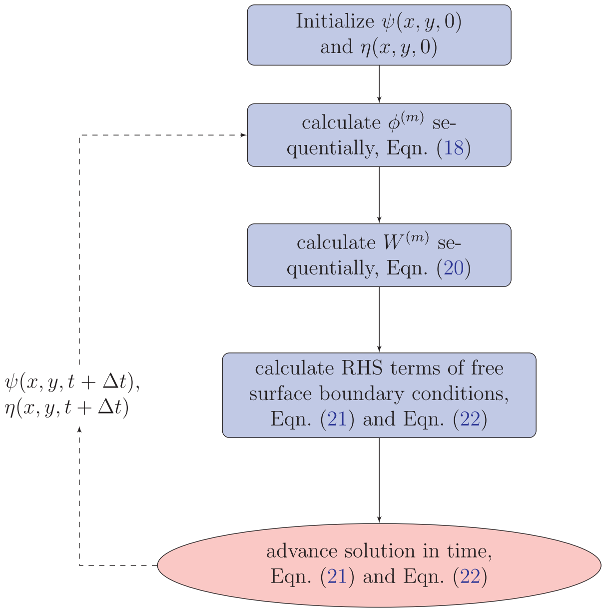

Fig. 1. Flow chart of the HOS algorithm.

the nonlinear RHS terms in free surface boundary conditions, Eqs. (4) and (5):

$$\frac{\partial\psi}{\partial t} + g\eta = G\left(1 - e^{-\left(\frac{t}{T_a}\right)^n}\right), \tag{23}$$

$$\frac{\partial\eta}{\partial t} - W^{(1)} = F\left(1 - e^{-\left(\frac{t}{T_a}\right)^n}\right), \tag{24}$$

where T_a is the relaxation time, and n is the relaxation exponent. According to Dommermuth [16], time relaxation period T_a should be at least as long as the period of the longest wave that can occur in the simulation. G and F are the nonlinear parts of dynamic and kinematic free surface boundary conditions, respectively:

$$G = -\frac{1}{2}\left(\frac{\partial\psi}{\partial x}, \frac{\partial\psi}{\partial y}\right)^2 + \frac{1}{2}W^2\left(1 + \left(\frac{\partial\eta}{\partial x}, \frac{\partial\eta}{\partial y}\right)^2\right), \tag{25}$$

$$F = -W^{(1)} - \left(\frac{\partial\psi}{\partial x}, \frac{\partial\psi}{\partial y}\right)\left(\frac{\partial\eta}{\partial x}, \frac{\partial\eta}{\partial y}\right) + W\left(1 + \left(\frac{\partial\eta}{\partial x}, \frac{\partial\eta}{\partial y}\right)^2\right). \tag{26}$$

Note that linear terms are not relaxed.

3.4. Dealiasing

In the HOS simulation, aliasing is inevitable since multiplication of periodic fields is performed in physical space instead of spectral space [19] for the products in the free surface boundary conditions, Eqs. (4) and (5), and for the products in sequential system of equations for ϕ and W, Eqs. (14) and (15). In this work, dealiasing is performed by extending the spectra using zero-padding [19]. Zero-padding is a technique where the wave number space is extended to the size of the physical mesh and the extended part of the wave number space is set to zero. More details can be found in Canuto et al. [19]. Number of modes that may be kept in wave number space is determined using the half rule:

$$N = \frac{M+1}{2}N_{\mathscr{F}}, \tag{27}$$

where $N_{\mathscr{F}}$ is the number of modes in wave number space, while N is the number of physical mesh nodes. M is the nonlinearity order used in the calculation. According to Eq. (27), to maintain the same number of alias-free wave numbers $N_{\mathscr{F}}$, for a high nonlinearity order M, larger physical mesh N should be used. This causes the simulation to be progressively slower with increasing order of nonlinearity M.

3.5. Coupling HOS and CFD

Decomposition model [7] based on SWENSE with implicit relaxation zones and implicitly redistanced Level Set method for interface capturing is used to achieve one way coupling of HOS and CFD. HOS solution in terms of velocity and surface elevation field is imposed into the CFD domain. The surface elevation in any point in time and space is provided by direct Fourier transform:

$$\eta(x,y,t) = \sum_k\sum_l c^{\eta}_{k,l}(t)e^{iK_kix}\,e^{iK_ly}. \tag{28}$$

The velocity field is not directly available, hence it is calculated from the velocity potential assuming the following shape function:

$$\phi(x,y,z,t) = \sum_k\sum_l c^{\psi}_{k,l}(t)\frac{\cosh\left(K_{k,l}(z+d)\right)}{\cosh(K_{k,l}d)}e^{iK_kx}\,e^{iK_ly}. \tag{29}$$

The velocity field is obtained by differentiating Eq. (29) in three Cartesian directions:

$$\begin{aligned}
v_x(x,y,z,t) &= \sum_k\sum_l c^{\psi}_{k,l}(t)iK_k\frac{\cosh\left(K_{k,l}(z'+d)\right)}{\cosh(K_{k,l}d)}e^{iK_kx}\,e^{iK_ly},\\
v_y(x,y,z,t) &= \sum_k\sum_l c^{\psi}_{k,l}(t)iK_l\frac{\cosh\left(K_{k,l}(z'+d)\right)}{\cosh(K_{k,l}d)}e^{iK_kx}\,e^{iK_ly},\\
v_z(x,y,z,t) &= \sum_k\sum_l c^{\psi}_{k,l}(t)K_{k,l}\frac{\sinh\left(K_{k,l}(z'+d)\right)}{\cosh(K_{k,l}d)}e^{iK_kx}\,e^{iK_ly},
\end{aligned} \tag{30}$$

where z' stands for the vertical coordinate modified using Wheeler correction:

$$z' = qz + d(q-1), \tag{31}$$

where $q = d/(d+\eta(x,y,t))$.

3.6. Viscous flow model

Governing equations of the incompressible, viscous, two-phase, and turbulent flow are shown in this section.

Conservation of mass is described with the following equation:

$$\nabla \cdot \mathbf{u} = 0, \tag{32}$$

where **u** stands for a velocity field in global coordinate system. Equation of momentum conservation for a moving computational grid reads:

$$\frac{\partial \mathbf{u}}{\partial t} + \nabla \cdot ((\mathbf{u} - \mathbf{u}_M)\mathbf{u}) - \nabla \cdot (\nu_e \nabla \mathbf{u}) = -\frac{1}{\rho}\nabla p_d, \tag{33}$$

where $\mathbf{u}_M$ represents the relative grid motion velocity according to the Space Conservation Law [20], ν_e is the effective kinematic viscosity taking into account the fluid kinematic viscosity and turbulent eddy viscosity, allowing general eddy viscosity turbulence models. ρ is the density field, while *pd* stands for dynamic pressure: $p_d = p - \rho\mathbf{g}.\mathbf{x}$, where p stands for total pressure, **g** is the gravitational acceleration, and **x** is the radii vector. In the present numerical model, the Ghost Fluid Method (GFM) is used to discretize free surface boundary conditions in the CFD model [21]. The GFM method takes into account the jump in density and pressure gradient on the interface, removing the spurious air velocities near the free surface. The reader is referred to Vukčević et al. [21] for more details on the GFM method.

The Level Set method is used for interface capturing with implicit redistancing [7]:

$$\frac{\partial \Psi}{\partial t} + \nabla \cdot (\mathbf{c}\Psi) - \Psi\nabla \cdot \mathbf{c} - b\nabla \cdot (\nabla\Psi) = b\frac{\sqrt{2}}{\epsilon}\tanh\left(\frac{\Psi}{\epsilon\sqrt{2}}\right), \tag{34}$$

where Ψ stands for the Level Set field, while b and ϵ are numerical parameters, diffusion coefficient and width parameter, respectively. **c** is the modified convective velocity. For further details regarding viscous flow model the reader is referred to Vukčević et al. [7].

4. Validation of the implemented HOS method

Three test cases are performed to validate the implemented HOS algorithm:

- Comparison of nonlinear monochromatic wave propagation with nonlinear analytical Stokes solution, following Dommermuth [16].
- Comparison of irregular sea state propagation with viscous, two-phase CFD study performed by Lupieri et al. [22].
- A qualitative comparison of Benjamin–Feir (BF) instability emergence with experimental results performed by Su et al. [23] and Lake et al. [24], and a quantitative comparison of induced BF instability emergence with analytic solution obtained by Stiassnie and Shemer [25].

4.1. Monochromatic wave train validation

Long time evolution of a progressive monochromatic wave train is conducted and compared with a nonlinear analytical Stokes solution following Dommermuth [16]. Linear solution is imposed as the initial condition from which a nonlinear solution up to 8th order is obtained.

Table 1
Comparison of HOS results and exact Stokes solution modal amplitudes.

Order	Modal amplitude, m		Relative error, %
	Analytical solution	HOS solution	
1	9.9870520×10^{-2}	9.9870524×10^{-2}	4.34×10^{-6}
2	5.0594125×10^{-3}	5.0594197×10^{-3}	1.43×10^{-4}
3	3.8584235×10^{-4}	3.8584342×10^{-4}	2.78×10^{-4}
4	3.4929691×10^{-5}	3.4929838×10^{-5}	4.20×10^{-4}
5	3.4769679×10^{-6}	3.4769678×10^{-6}	-3.26×10^{-6}
6	3.6763951×10^{-7}	3.6763189×10^{-7}	-2.07×10^{-3}
7	4.0531740×10^{-8}	4.0530830×10^{-8}	-2.24×10^{-3}
8	4.6076934×10^{-9}	4.6026818×10^{-9}	-1.09×10^{-1}

Dommermuth [16] presented a HOS simulation for a wave with intermediate steepness $Ka = 0.1$, showing convergence of modal amplitudes during the simulation. In this study, the wave number is set to $K = 1$, giving the wave amplitude of $a = 0.1$ m. Relaxation time is $T_a = 8T$, where T is the wave period, and the relaxation exponent is set to $n_a = 4$.

The wave train is propagated using HOS during 100 periods, yielding 200 s of simulated time, which required 80 s of CPU time on a single core of a Intel Core i5-3570K CPU at 3.40 GHz.

Table 1 presents the comparison of HOS simulation modal amplitudes with analytical solution in terms of relative errors defined as:

$$\epsilon = (c_{kHOS} - c_{kS})/c_{kHOS}, \tag{35}$$

where c_{kHOS} is the kth modal amplitude from the HOS simulation, while c_{kS} is the kth modal amplitude from the analytical Stokes solution. It can be seen that the relative errors are very small, being only $4.34 \times 10^{-6}\%$ for the first order. Relative error increases for higher orders; however it remains acceptably small: the largest being $\approx 0.1\%$ for 8th order with modal amplitude of $\approx 4.6 \times 10^{-9}$ m. Order-wise rate of convergence over time is compared with the solution obtained by Dommermuth [16] in Fig. 2. The convergence rates agree well with Dommermuth's results, indicating consistent and valid implementation. It should be noted that order consistency proposed by West et al. [13] is not used here since it produced inferior results. Instead, the formulation developed by Dommermuth and Yue [12] is employed for this particular test case.

4.2. Propagation of unidirectional wave spectrum

Lupieri et al. [22] presented a viscous, two-phase CFD simulation of uniformly steep uni-directional spectra. Wave components are focused to create a steep focused wave, and changes in each spectrum are observed due to nonlinear and viscous effects. Focusing technique [26] is used to obtain a positive superposition of components at a desired location, and the wave energy spectrum is calculated for various locations along the basin. In HOS, FFT is performed in the spatial domain, i.e. spatial signal is transformed into wave number space. Lupieri et al. performed FFT to transform a temporal

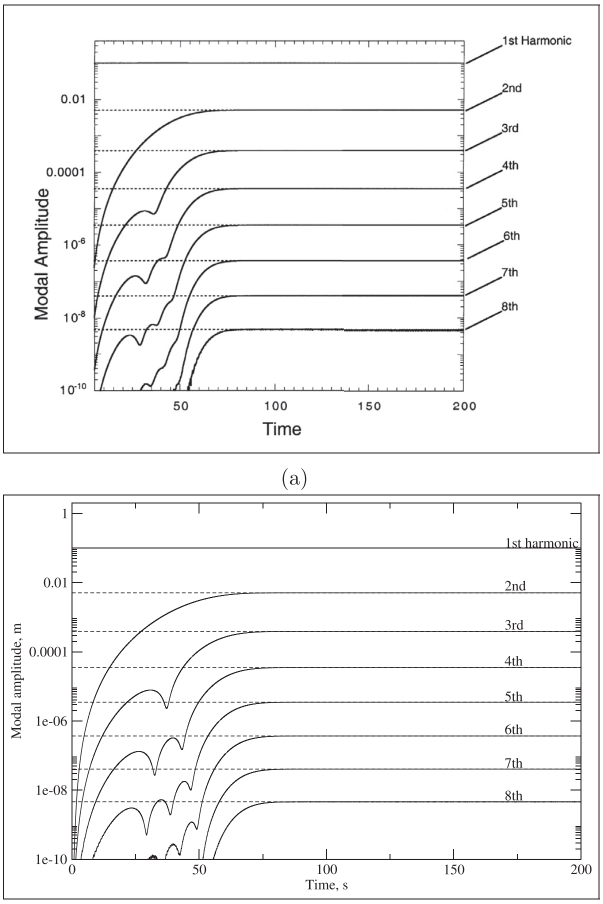

(a)

(b)

Fig. 2. Convergence rate of modal amplitudes, (a) Dommermuth [16], (b) present HOS result.

wave elevation signal into frequency domain. Although it is possible to perform a time spectral analysis of the wave elevation signal in HOS, it is not possible to achieve the same conditions of wave focusing. The reason for this is the time relaxation needed by HOS to initialize the simulation using a linear solution. As the relaxation time is several times longer than the propagation time of waves from the wave maker to the focusing location (used by Lupieri et al. [22]), HOS results are converted to the frequency domain $S_{\eta\eta}(\omega)$ from wavenumber spectrum $S_{\eta\eta}(K)$ using the dispersion relation.

Input spectra are constructed to have components with equal individual wave steepness. Four steepnesses are used: $H_i/\lambda_i = 1/715, 1/400, 1/300$ and $1/210$. Components are equidistantly spaced in the wavenumber space instead of the frequency space. Fig. 3 depicts the input spectrum with $H_i/\lambda_i = 1/715$.

For the first three cases with $H_i/\lambda_i = 1/715, 1/400, 1/300$, the spectra are calculated at $t = 37$ s while the focusing time is $T_f = 35$ s. In the case of the highest steepness $H_i/\lambda_i = 1/210$, relaxation time needs to be prolonged to $T_f = 80$ s due to higher nonlinearity of the spectrum, especially at focusing time. The time of focusing is increased to $T_f = 80$ s. The steeper the waves being simulated, the larger the difference between linear and non-linear solution. Thus, steeper waves demand higher relaxation time to permit stable development of the non-linear solution [16].

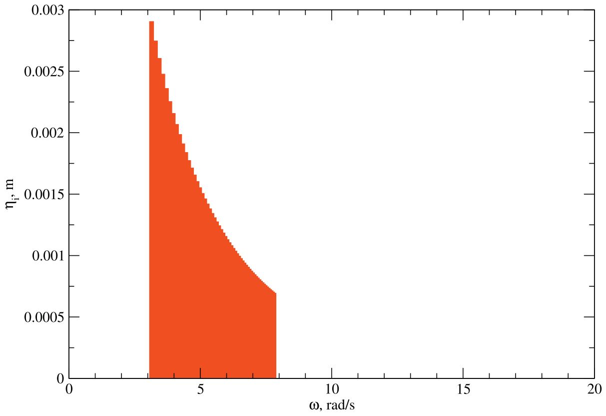

Fig. 3. Input spectrum for steepness $H_i/\lambda_i = 1/715$.

Table 2
HOS simulation parameters.

H_i/λ_i	1/715	1/400	1/300	1/210
N_x	1024	1024	1024	2048
M	6	6	6	10
T_a, s	25	25	25	60
T_f, s	35	35	35	80

HOS simulation parameters are summarized in Table 2 for each test case. N_x is the number of physical mesh points, M is the order of nonlinearity, T_a is the relaxation time, while T_f is the focusing time. Following Eq. (27), number of alias-free Fourier modes corresponds to $2N_x/(M+1)$. Length of the domain used in all simulations is 72.3 m, which corresponds to 18 wave lengths of the longest input wave. For the first three cases, 1.3 s of CPU time per one second of simulated time is required, while the last case took 5 s of CPU time per second on a single core of Intel Core i5-3570K CPU at 3.40 GHz. Results are shown in Figs. 4–7.

Results shows good agreement in all test cases comparing with viscous results. Magnitude of the highest spectrum peak corresponding to $\omega \approx 3.2$ rad/s is well predicted in all test cases. Furthermore, the rightmost smaller peak at $\omega \approx 8$ rad/s is well presented. In the case of highest steepness $H_i/\lambda_i = 1/210$ two peaks are present at the rightmost of the spectrum $(6 < \omega < 8$ rad/s), and both are well predicted in HOS calculation. For the first two cases with milder steepness, shape of the spectrum in the mid frequency range $(4 < \omega < 6$ rad/s) agrees well with the viscous results. According to Lupieri et al. [22], the lower frequency peaks $(0 < \omega < 2$ rad/s) in Figs. 4(a)–7(a) correspond to second sloshing mode of the CFD basin used in their simulation. These peaks are not present in HOS simulation due to

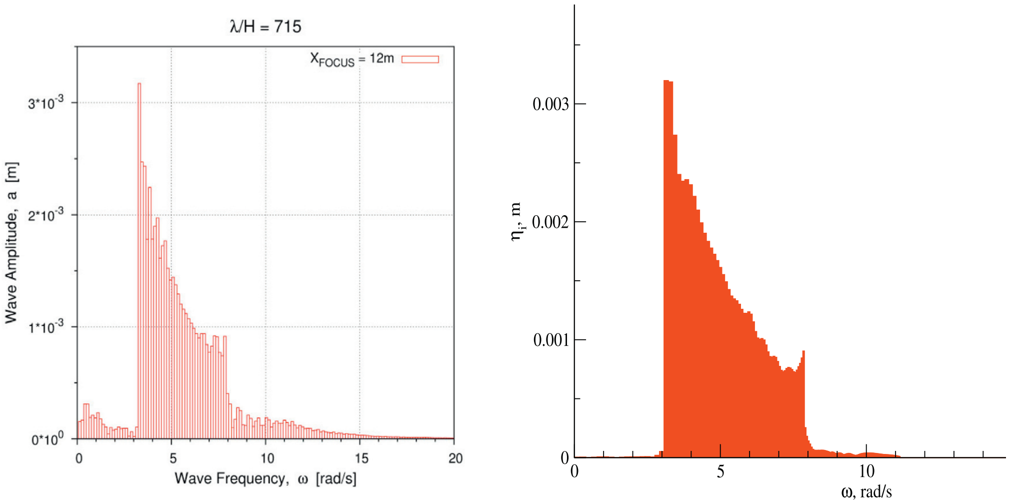

(a) (b)

Fig. 4. Spectrum comparison for $H_i/\lambda_i = 1/715, t = 37$ s, (a) Lupieri et al. [22], (b) present result.

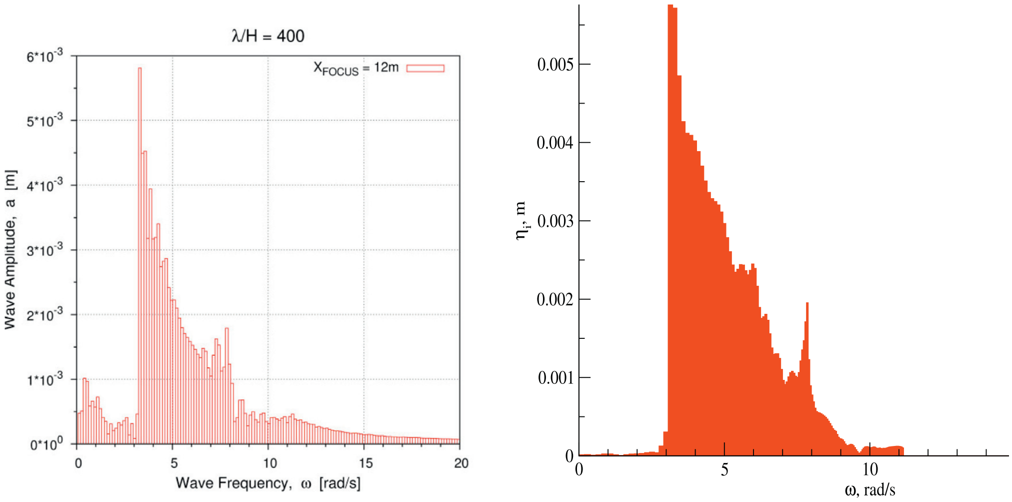

(a) (b)

Fig. 5. Spectrum comparison for $H_i/\lambda_i = 1/400, t = 37$ s, (a) Lupieri et al. [22], (b) present result.

unbounded periodic wave propagation. The cases for steepness $H_i/\lambda_i = 1/300$ and 1/210 correspond to wave breaking events at the focusing time, causing larger discrepancies in the mid frequency range ($4 < \omega < 6$ rad/s), which increase for larger steepness. HOS method is not able to capture wave braking events since η is a single valued function. When η has more than one solution (multi-valued function), the failure of convergence is caused by spurious high wave number components, which are truncated via filtering. In Figs. 4(b)–7(b), it can be seen that the frequency range is truncated at approximately 11 rad/s. This truncation enables HOS simulation to continue beyond the breaking event, causing energy loss. This is shown in Fig. 8, where computed energy over time is compared with the initial energy of the linear spectrum. This energy loss is present in the viscous study as well, however it is caused mainly by viscous dissipation in wave breaking mechanism. As expected, cases that correspond to wave braking events show larger energy loss after the focusing time.

4.3. Development of Benjamin–Feir instabilities

In their study, Benjamin and Feir [17] discovered an instability that occurs in monochromatic wave train. The instability was confirmed by numerous experiments, Feir [27] being the first. As shown by McLean et al. [28] and McLean [29],

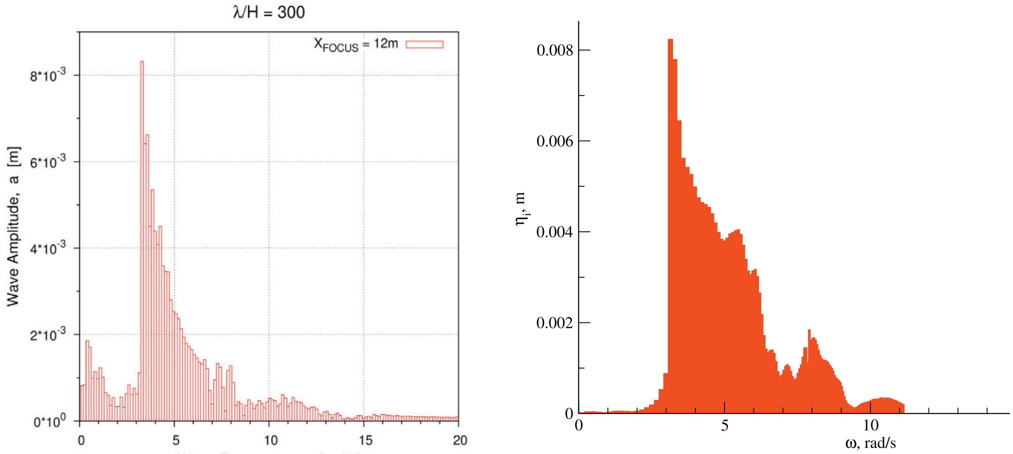

(a)　　(b)

Fig. 6. Spectrum comparison for $H_i/\lambda_i = 1/300, t = 37$ s, (a) Lupieri et al. [22], (b) present result.

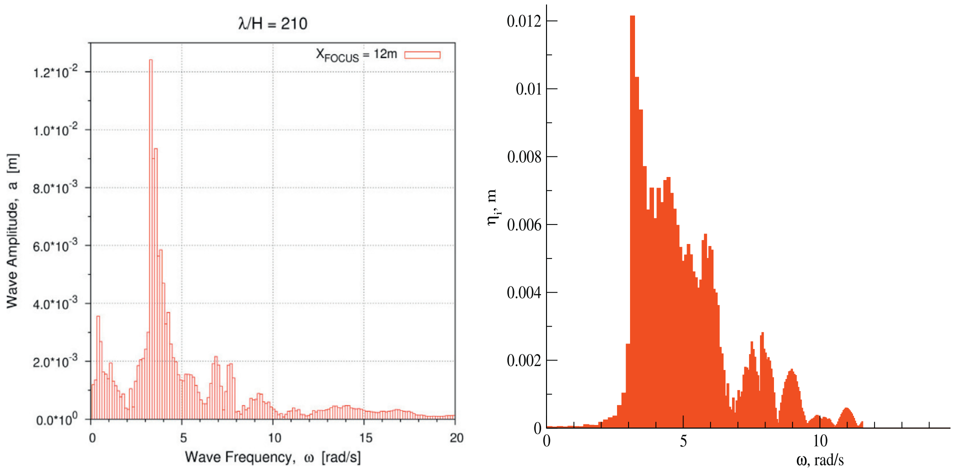

(a)　　(b)

Fig. 7. Spectrum comparison for $H_i/\lambda_i = 1/210, t = 84$ s, (a) Lupieri et al. [22], (b) present result.

there are two main types of instabilities in wave trains. Type I is the Benjamin–Feir instability, which occurs for waves of steepness $Ka < 0.38$, while type II occurs for $Ka > 0.4$. Only Benjamin–Feir instabilities will be considered in this section, which manifest as the emergence of nonlinear side bands whose amplitudes grow exponentially once they emerge. Side bands emerge near the carrier frequency and near higher order modes. The growth is initialized by an initial disturbance which is always present in nature and in numerical simulation (due to numerical errors), or it can be imposed. The growth of nonlinear sidebands occurring in HOS simulation is compared with theory and experiment.

First, a qualitative comparison is performed where the natural growth is observed, i.e. there is no imposed initial disturbance. Wave parameters used in the simulation and the HOS parameters are given in Table 3. HOS simulation is initialized using a linear solution. Simulation required ≈ 2 s of CPU time per one second of simulated time on a single core of Intel Core i5-3570K CPU at 3.40 GHz.

Time evolution of nonlinear side-bands in frequency domain is given in Fig. 9, and the dispersion relation is used to transform from the wave number to the frequency domain. Time domain Fourier analysis is difficult in HOS simulation since the occurrence of Benjamin–Feir instabilities is transient in time, and cannot be captured accurately by performing Fourier transform on the time elevation signal. The nonlinearities in HOS simulation evolve in time in the whole spatial domain, while in the experiment, nonlinearities evolve with waves propagating in space. A probe measuring elevation over time in the experiment will always be exposed to the

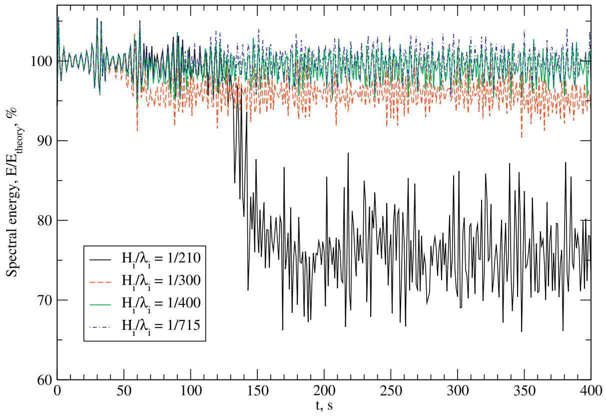

Fig. 8. Spectral energy computed in space during simulated time window.

Table 3
Wave and HOS simulation parameters.

Ka	K, rad/m	T, s	T_a, s	n_a	M	N_x
0.25	16.1	0.5	5	4	8	1024

same level of nonlinearity, since it is always equally distanced from the wave maker. This allows a time Fourier transform which produces spectrum in the frequency domain. Fig. 10(a) and (b) presents spectra for the corresponding wave steepness from the experimental studies of Su et al. [23] and Lake et al. [24], respectively.

According to Benjamin and Feir [17], the strongest instability growth is for $\delta = Ka$ where $\delta = \Delta f / f$. Δf is the frequency separation of the carrier frequency f and the frequencies of the higher and lower nonlinear side bands. It can be seen in Fig. 9 that the frequencies of the nonlinear side bands near the carrier frequency are approximately 9.7 and 14.8 rad/s. The carrier frequency is $\omega = 12.56$ rad/s which gives $\Delta\omega = 3.14$ rad/s. The frequencies of the fastest growing side bands are expected to be 9.4 and 15.7 rad/s, which is close to the obtained values. Part of the difference is caused by the use of linear dispersion relation.

A quantitative comparison is performed for a case where the initial instabilities are imposed. Following Stiassnie and Shemer [25] the initial solution comprises carrier Airy wave with $kA = 0.13$ and two sidebands harmonics with amplitudes 10% of the carrier wave, with $\pm 22\%$ wavenumber separation in respect to the carrier wave. Following Dommermuth and Yue [12] the carrier wavenumber is set to $K_c = 9$ rad/m to allow integral wavenumbers of sidebands; for the subharmonic $K_- = 7$ rad/m and for the superharmonic $K_+ = 11$ rad/m. In HOS simulation the order of nonlinearity is set to $M = 4$, while the number of grid points is $N = 128$. Time relaxation and order consistency are not used.

Time histories of the three harmonics obtained with HOS and by Stiassnie and Shemer are presented in Fig. 11, where η/η_0 is the wave amplitude normalised by carrier wave amplitude, and t/T_0 is the time scaled with carrier wave period. It can be seen that evolution of individual harmonics agrees well with the analytical solution. HOS simulation predicts the first minimum of the carrier mode near $t \approx 80T$, while the analytical solution predicts $t \approx 60T$. However, the distance between carrier mode minima is $\approx 85T$ for both HOS simulation and the analytical solution. It can be concluded that there is a delay in the nonlinearity development at the beginning of the simulation, but the time scale of nonlinear behaviour is well predicted.

5. Validation of coupling HOS and CFD

The coupling between HOS and CFD described in Section 3.6 is validated on a three hour irregular wave propagation. The validation is performed by comparing the wave energy spectrum obtained from HOS with the spectrum obtained in CFD measured at the same location. HOS simulation is initialised using JOSWAP spectrum with $H_s = 17$ m, $T_p = 15.5$ s and $\gamma = 2.6$. In the HOS simulation, $M = 3$ is used, $N_x = 2048$, and domain length is $L_x = 60,000$ m. Two-dimensional CFD simulation is carried out with domain 2160 m long, 100 m deep and 40 m high (above the calm free surface). Near the free surface the cells have the size of 0.5 × 0.5 m, while the grid counts 136,800 cells. Fixed time step of $\Delta t = 0.31$ s is used which corresponds to 50 time-steps per peak period of the spectrum. Inlet relaxation zone is 700 m long, while the outlet is 1000 m long, leaving 460 m of unaffected CFD domain. Long relaxation zones are necessary in order to prevent the reflection of the longest waves that can occur in the sea state, and to prevent standing waves corresponding to the natural frequency of the numerical wave tank. Given the small depth of the domain, the velocity field from HOS solution is imposed to the bottom boundary in order to mimic the rest of the fluid below the level of the bottom boundary. Fig. 12 shows the volume fraction field reconstructed from the level set variable in one time instant. The free surface is well preserved with very little smearing. The waves propagate from left to right.

As in the experimental wave basin test, the initial linear spectrum needs to be calibrated in order to obtain the imposed JONSWAP spectrum in the HOS realisation. Calibration of the initial HOS condition is performed by running at least ten three hour realisations of the target spectrum, and acquiring the average correction factors for the initial linear spectrum. In Fig. 13 the target spectrum is compared to the spectrum obtained before and after calibration.

The calibration coefficients are applied to the linear JONSWAP spectrum with random phase shifts used to initialise the HOS simulation coupled to the CFD simulation. Fig. 14 shows the comparison of wave energy spectrum obtained from the HOS simulation, and the spectrum measured in the corresponding CFD simulation. The damping of spectral wave energy is minimal, and the spectrum shape corresponds well. The agreement is better for lower frequencies, while higher frequencies ($\omega > 0.6$ rad/s) exhibit larger relative damping, which is caused by smaller spatial and temporal resolution relative to wave component height, length and period. In

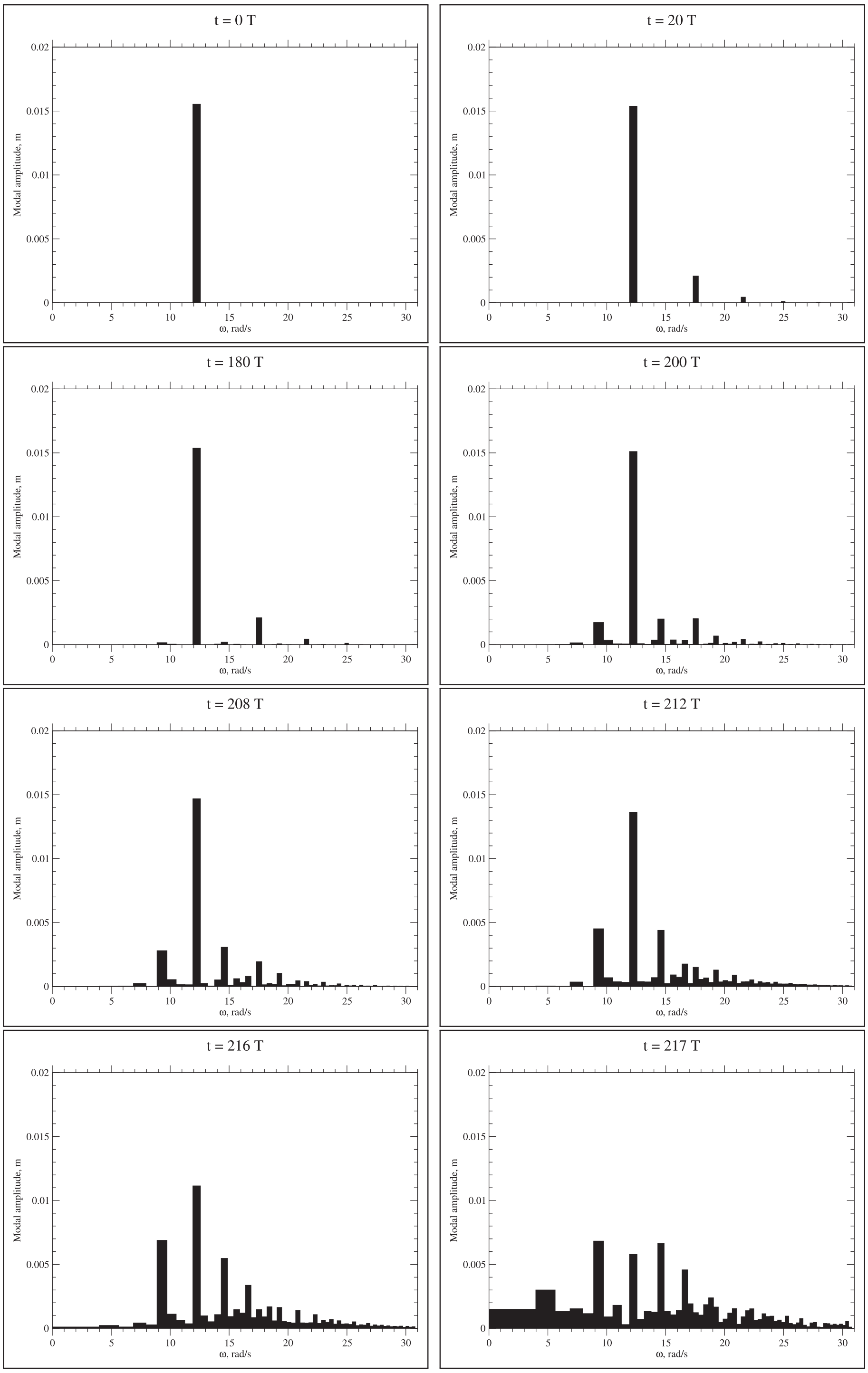

Fig. 9. Development of nonlinear side bands in HOS simulation.

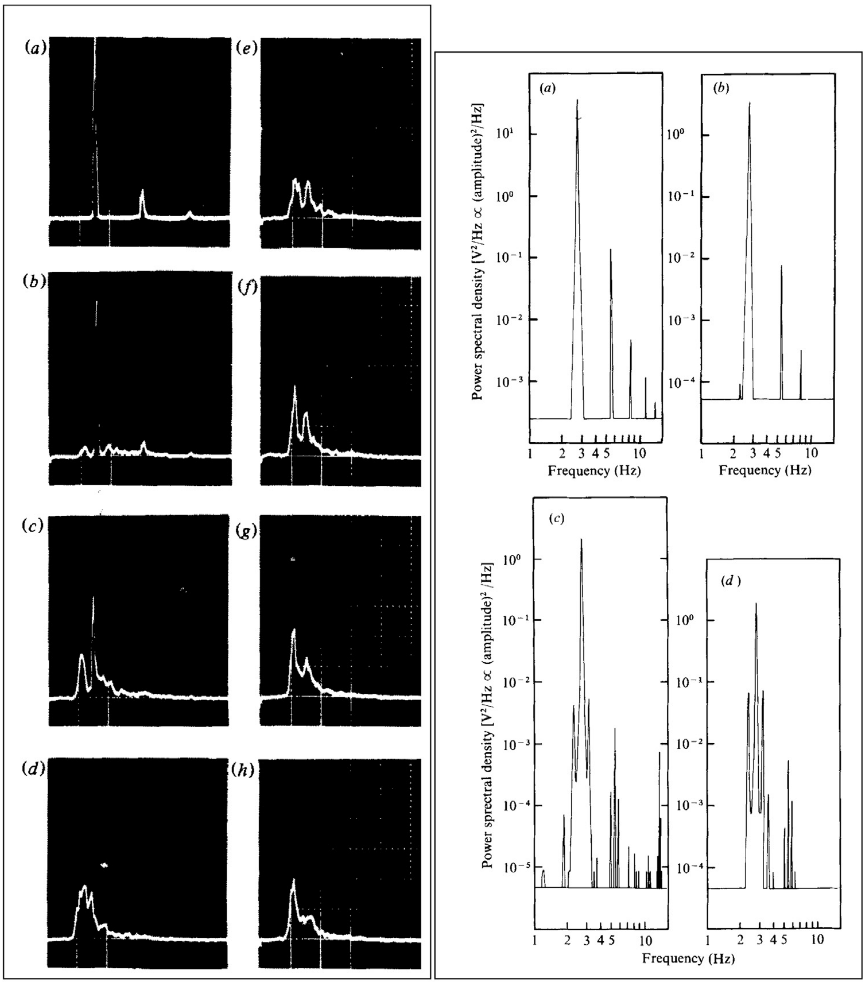

(a) (b)

Fig. 10. Experimental nonlinear side bands development, (a) Su et al. [23], (b) Lake et al. [24].

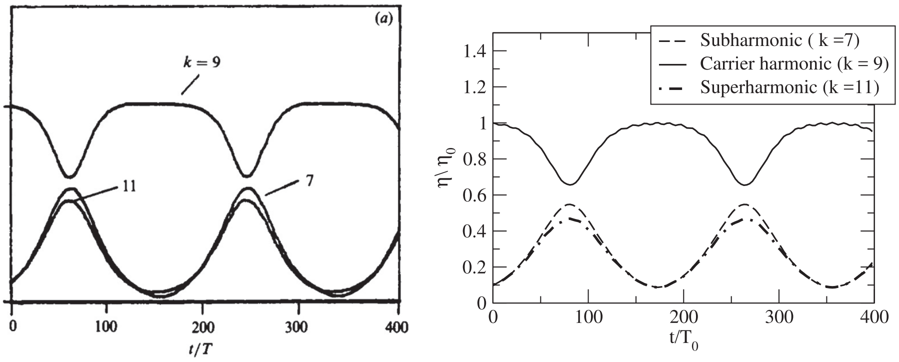

(a) (b)

Fig. 11. Time histories of the carrier, subharmonic and superharmonic wave amplitudes, (a) analytic solution by Stiassnie and Shemer [25], (b) present result.

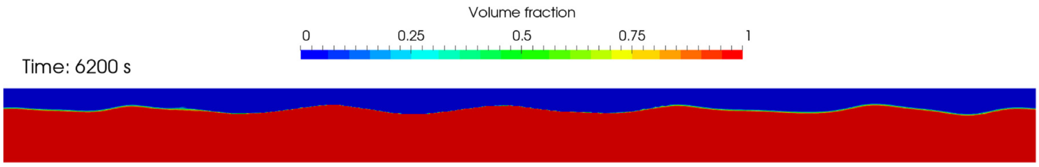

Fig. 12. Snapshot from the irregular wave propagation CFD simulation.

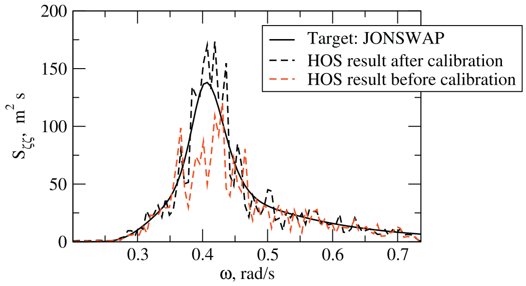

Fig. 13. Comparison of wave energy spectrum obtained with HOS before and after calibration.

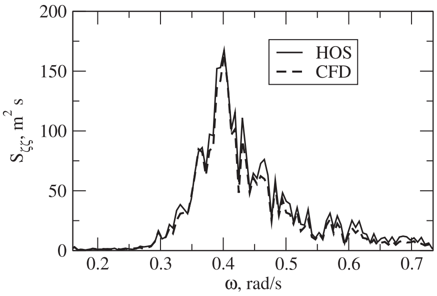

Fig. 14. Comparison of wave energy spectrum obtained with HOS and CFD.

Table 4
Quantitative comparison of wave energy spectrum obtained with HOS and CFD.

	H_s, m	T_p, s
HOS	17.12	12.76
CFD	16.13	13.11

Table 4 the two spectra are compared quantitatively, where H_s and T_p are compared. The significant wave height corresponds quite well, where damping in CFD results in 1 m smaller height corresponding to 5.8% difference. For the peak period the difference is smaller, being less than 2%. Note that the peak period differs significantly with respect to the theoretical value of 15.5 s. This is caused by the fact that the spectrum used in HOS is truncated for stability reasons, hence the theoretical expression for the peak period calculation derived based on the wave elevation distribution is not valid, however it enables a quantitative comparison.

6. CFD simulation of a 3D extreme wave encountering a full scale container ship

In this section a simulation of a 3D extreme wave encountering a freely floating full-scale container ship is presented. The hull form parameters of the KRISO Container Ship (KCS) are available at the Tokyo Workshop on CFD in Ship Hydrodynamics [30].

Unstructured grid with 1.2 million cells is used, mostly composed out of hexahedral cells (≈83%), the rest being polyhedral cells. At the hull surface, the grid is aligned with the hull surface with boundary layer refinement. The transition from the boundary layer cells to the surrounding background orthogonal grid is accomplished with polyhedral cells. Second order backward scheme is used for temporal discretisation in the momentum equation, while implicit first order upwind scheme is used for convection with second order, upwind biased deferred correction. Second order scheme with explicit limited non-orthogonal correction is used for the discretisation of the Laplace operator for the diffusion term in the momentum equation and the pressure. No turbulence modelling is used in this case since the ship has zero initial velocity, hence adverse pressure gradients can be expected near the hull in the wave field, rendering conventional eddy viscosity turbulence models non-valid.

A 3D extreme wave is obtained using HOS, where the HOS simulation is initialized using a linear directional spectrum. Directional spreading is modelled using the following expression [31]:

$$D(\theta) = \begin{cases} A(n)\cos^n\theta & \text{for } |\theta| \le \pi/2, \\ 0 & \text{for } |\theta| > \pi/2, \end{cases} \tag{36}$$

where $A(n)$ is the normalisation coefficient, θ is the dominant wave propagation direction, and n is the arbitrary directionality parameter. As the initial condition for HOS simulation, JONSWAP spectrum is used with significant wave height $H_s = 10.5$ m, peak period $T_p = 9.5$ s, and directionality constant $n = 8$. Dominant wave propagation direction is set to $\theta = 25^\circ$ with respect to longitudinal ship axis. Extreme wave occurred after $\approx 56T_p$ with wave height $H = 21.91$ m, as it can be seen on Fig. 15 at approximately $x = 900$ m and $y = 200$ m.

30 s of simulation took 132 h of CPU time on a Intel Core i7-4820K CPU at 3.70 GHz. Fig. 16 sequentially shows the encounter of the extreme wave on the KCS. At time zero, CFD simulation is initialized with the HOS solution corresponding to time $T_{HOS} = 526$ s. HOS simulation is then ran alongside the CFD simulation to produce the necessary

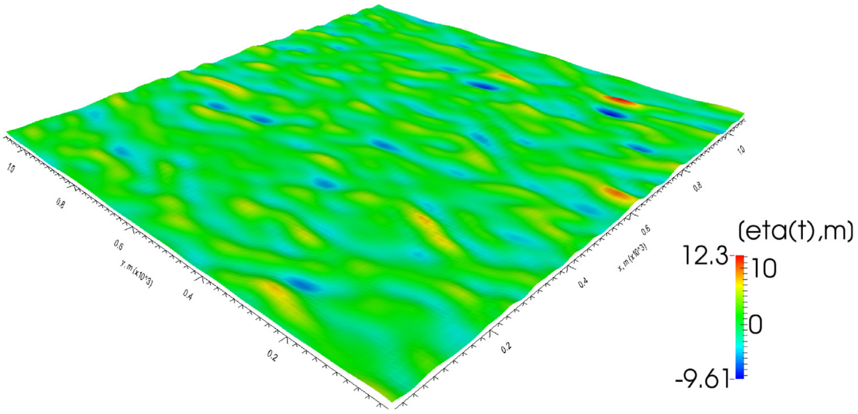

Fig. 15. Free surface elevation with freak wave event, $t = 532$ s.

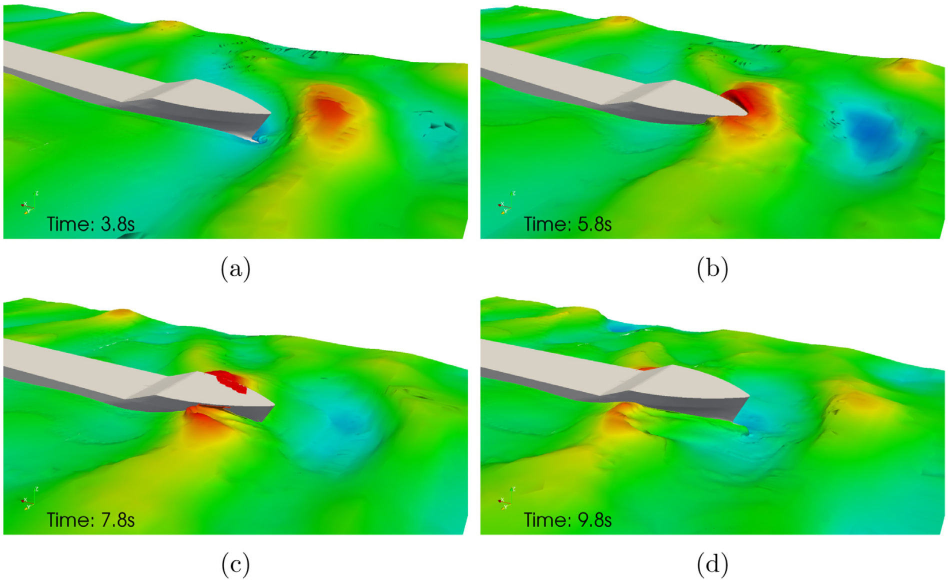

(a) (b) (c) (d)

Fig. 16. Three-dimensional freak wave encountering a full scale KCS. (The colour legend in this figure corresponds to Fig. 15).

blending results at the required time instances. At CFD simulation time $T = 5.8$ s the extreme wave encounters the bow of the container ship, while the green water event can be seen after the impact at $T = 7.8$ s. Fig. 17 shows the translational motion of the ship's centre of gravity during the simulation. It can be noticed that sway motion is greater than surge motion, due to the angle of dominant wave propagation direction. On Fig. 18 the rotation of the ship is shown, where significant roll angle can be seen.

Unfortunately, neither experimental nor numerical data are available for comparison today.

7. Summary

In this paper a framework for efficient irregular wave simulation using HOS and CFD coupling is presented. HOS is a pseudo-spectral, potential flow method for solving nonlinear free surface boundary conditions. It is primarily used to propagate arbitrary wave energy spectra, taking into account nonlinear wave-to-wave interaction and wave modulation. Among other applications, HOS can be used for low CPU cost extreme wave initialization for fully non-linear CFD simulations of wave impact and wave breaking.

The accuracy and validity of the implemented HOS model is assessed with three validation test cases. In the first test case, HOS solution of a propagating monochromatic wave train is considered, where modal amplitudes up to 8th order compare well with the analytical Stokes solution. The comparison verifies that given a linear initial condition, HOS can evolve the nonlinear solution accurately. Rate of convergence is also compared and shows good agreement with results obtained by Dommermuth [16].

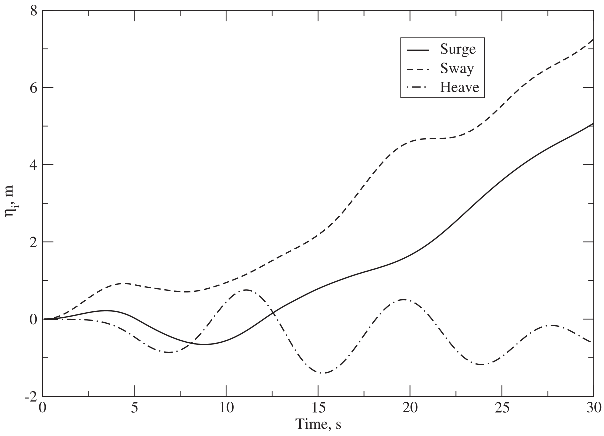

Fig. 17. Translational motion of the ship's centre of gravity during the extreme wave impact.

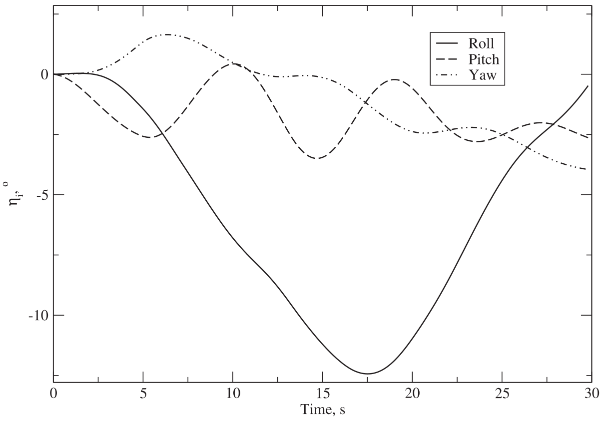

Fig. 18. Rotational motion of the ship around the centre of gravity during the extreme wave impact.

The second test case presents the propagation of four different uniformly steep, uni-directional input spectra where the solutions are compared with the viscous study performed by Lupieri et al. [22]. Results show good agreement, especially for wave spectra with smaller steepness.

The final validation case simulates the occurrence of Benjamin–Feir type instability in a propagating monochromatic wave train. Benjamin-Feir instability produced by HOS method agrees well with experimental and theoretical studies.

In order to test the precision of the HOS–CFD coupling, energy wave spectra obtained in HOS and corresponding CFD simulation is compared. The two spectra correspond well, indicating minor damping of wave energy.

Finally, an example CFD simulation is shown where the coupling of HOS and CFD is used to simulate a 3D directional extreme wave encountering a full-scale, freely floating container ship.

In future efforts the presented coupling will be utilised in order to calculate extreme response of naval objects such as green water, slamming and motion.

References

[1] W.R. Van Dalsem, J.L. Steger, in: Proceedings of AGARD Fluid Dynamics Panel Symposium on Application of CFD in Aeronautics, 1986.
[2] N.G. Jacobsen, D.R. Fuhrman, J. Fredsøe, Int. J. Numer. Methods Fluids 70 (9) (2012) 1073–1088, doi:10.1002/fld.2726.
[3] B.T. Paulsen, H. Bredmose, H.B. Bingham, Coast. Eng. 86 (2014) 57–76, doi:10.1016/j.coastaleng.2014.01.006.
[4] A.P. Engsig-Karup, H.B. Bingham, O. Lindberg, J. Comput. Phys. 228 (2009) 2100–2118, doi:10.1016/j.jcp.2008.11.028.
[5] B.T. Paulsen, H. Bredmose, H.B. Bingham, N.G. Jacobsen, J. Fluid Mech. 755 (2014) 1–3, doi:10.1017/jfm.2014.386.
[6] A. Pistidda, H. Ottens, in: Proceedings of the 18th Numerical Towing Tank Symposium, 2015, pp. 161–166.
[7] V. Vukčević, H. Jasak, S. Malenica, Ocean Eng. 121 (2016) 37–46, doi:10.1016/j.oceaneng.2016.05.022.
[8] P. Ferrant, L. Gentaz, D. Le Touzé, in: Proceedings of Numerical Towing Tank Symposium, NuTTS, 2002.
[9] C. Monroy, G. Ducrozet, A. Bonnefoy, A. Babarit, P. Ferrant, in: Proceedings of the 20th International Off-shore and Polar Engineering Conference, 2010, pp. 678–685.
[10] R. Marcer, C. Audiffren, C. Dassibat, C. de Jouette, P.E. Guillerm, in: Proccedings of 11$^{\text{éme}}$ Journées de l'Hydrodynamique, 2007, pp. 1–12.
[11] C. Kharif, E. Pelinovsky, Eur. J. Mech. B: Fluids 22 (2003) 603–634.
[12] D.G. Dommermuth, D.K.P. Yue, J. Fluid Mech. 184 (1987) 267–288.
[13] B.J. West, K.A. Brueckner, R.S. Janda, J. Geophys. Res. 92 (C11) (1987) 11803–11824.
[14] M. Tanaka, Fluid Dyn. Res. 28 (2001) 41–60.
[15] G. Ducrozet, F. Bonnefoy, D. Le Touzé, P. Ferrant, Nat. Hazards Earth Syst. Sci. 7 (2007) 109–122.
[16] D.G. Dommermuth, Wave Motion 32 (2000) 307–317.
[17] T. Benjamin, J.E. Feir, J. Fluid Mech. 27 (1967) 417–430.
[18] W.H. Press, S.A. Teukolsky, W.T. Vetterling, B.P. Flannery, Numerical Recipes in C++: The Art of Scientific Computing, Cambridge University Press, 2002.
[19] C. Canuto, M. Hussaini, A. Quarteroni, T. Zang, Spectral Methods in Fluid Dynamics, Springer, 1988.
[20] I. Demiridžić, M. Perić, Int. J. Numer. Methods Fluids 8 (1988) 1037–1050, doi:10.1002/fld.1650080906.
[21] V. Vukčević, H. Jasak, I. Gatin, Comput. Fluids 153 (2017) 1–19.
[22] G. Lupieri, T. Puzzer, G. Contento, in: Proceedings of the 21th Symposium Sorta, 2014.
[23] M. Su, M. Bergin, P. Marler, R. Myrick, J. Fluid Mech. 124 (1982) 45–72.
[24] B.M. Lake, H.C. Yuen, H. Rungaldier, W.E. Ferguson, J. Fluid Mech. 83 (1977) 49–74.
[25] M. Stiassnie, L. Shemer, J. Fluid Mech. 174 (1987) 299–312.
[26] J.R. Chaplin, Int. J. Offshore Polar Eng. 6 (2) (1996) 131–137.
[27] J.E. Feir, Proc. Roy. Soc. Lond. A 299 (1967) 54–58.
[28] J.W. McLean, Y. Ma, D. Martin, P. Saffman, H. Yuen, Phys. Rev. Lett. 46 (1981) 817–820.
[29] J.W. McLean, J. Fluid Mech. 114 (1982) 315–330.
[30] National Maritime Reasearch Inisitute (NMRI), in: Proceedings of Tokyo 2015: A Workshop on CFD in Ship Hydrodynamics, 2015. http://www.t2015.nmri.go.jp/ (Online; accessed 20.08.15).
[31] L.H. Holthuijsen, Waves in Oceanic and Costal Waters, Delft University of Techonlogy and UNESCO-IHE, 2007.

Statement of author contribution for PAPER 1

Inno Gatin is the main author of paper "A framework for efficient irregular wave simulations using Higher Order Spectral method coupled with viscous two phase model", published in Journal of Ocean Engineering and Science, 2017;2:253-267.

In this paper the implementation, validation and testing of the Higher Order Spectrum method were performed by Gatin. The paper was written by Gatin and reviewed by Jasak and Vukčević.

Co–authors:

Vuko Vukčević

Hrvoje Jasak

PAPER 2

Focused Wave Loading on a Fixed FPSO using Naval Hydro pack

Inno Gatin, Hrvoje Jasak and Vuko Vukčević
Faculty of Mechanical Engineering and Naval Architecture, University of Zagreb, Croatia
Wikki Ltd, London, United Kingdom

Steven Downie
Arup, London, United Kingdom

ABSTRACT

Validation of the Naval Hydro CFD software pack for focused wave loading on a fixed FPSO is presented in this paper. Naval Hydro is based on Finite Volume CFD software called foam–extend–4.0, and it is specialised for large–scale, two-phase surface flows encountered in naval hydrodynamics. Simulations are performed using SWENSE method (Spectral Wave Explicit Navier–Stokes Equations) for solution decomposition, while implicit relaxation zones are employed for wave initialisation and damping. Numerical results are submitted to a blind comparison with experimental results within the CCP–WSI Blind Test Workshop. Six cases are considered altogether where different incident waves and incident angles are considered. Pressure loads and free surface elevation are considered in this work.

KEY WORDS: Focused Wave Loads; FPSO; Wave Run–up; Naval Hydro Pack; CFD.

INTRODUCTION

Static naval objects such as Floating Production Storage and Offloading (FPSO) vessels are often exposed to severe weather conditions, where the operationality, life span, and structural integrity may be endangered. There is an ongoing effort in the scientific community aimed at the development, validation and certification of computational methods for predicting wave–body interaction. Finite Volume (FV) based Computational Fluid Dynamics (CFD) methods comprise one of the largest and most popular groups of computational methods for various problems, including naval hydrodynamics, and are more increasingly subjected to rigorous verification and validation in order to assure and promote their accuracy and applicability in modern marine industry. This paper presents a part of such an undertaking within the CCP–WSI Blind Test Workshop, where numerical results submitted by participants are compared to experimental measurements.

In this work Naval Hydro software pack is used to conduct simulations of focused wave loading on a static FPSO model. Naval Hydro pack is based on open–source, FV based CFD software called foam–extend–4.0, and it is specialised for large–scale, two phase flows with rigid body motion and wave generation. The discontinuities across the interface are taken into account with the Ghost Fluid Method (GFM) Vukčević, Jasak, and Gatin 2017, which imposes the free surface boundary conditions within the FV framework. For efficient wave propagation, SWENSE method Vukčević, Jasak, and Malenica 2016a; Vukčević, Jasak, and Malenica 2016b is employed, which is a solution decomposition approach where the flow field is decomposed into the incident portion arising from the potential wave theory, and diffracted component caused by inherent nonlinearities of Navier–Stokes equations. Surface waves are initialised and damped by using implicit relaxation zones Jasak et al. 2015, which are placed at the inlet and outlet of the computational domain, gradually blending the fully nonlinear CFD solution to the target incident wave field. The wave field is initialised with the NewWave theory Tromans et al. 1991.

Six cases are considered in total, divided in two parts: in Part 1 different focusing wave characteristics are used, with zero incident angle corresponding to head waves conditions. In Part 2, the same wave conditions are used with different incident angles. Pressure and surface elevation signals on several locations are reported. In addition to wave–body interaction simulations, the wave propagation is checked by performing empty–domain computations, where the signal is compared to the incident linear wave elevation signal and to the results of Higher Order Spectrum (HOS) nonlinear wave theory implemented in Naval Hydro Gatin et al. 2017. Using the data from the empty–domain simulations, the effect of fixed FPSO to the wave field is examined by comparing the two surface elevation data sets.

The paper is organised as follows: in the next section the numerical model is briefly presented, including GFM and SWENSE. Third section describes the test cases considered in the study, with geometry and wave field definitions. Next, the numerical set–up is presented, including computational domain geometry and discretisation details. In the fifth section results of empty–domain computations are presented with surface elevation comparison including experimental results, followed by wave load results. Finally, discussion and a brief conclusion are given.

NUMERICAL MODEL

This section briefly outlines the numerical methodology used in this work, including GFM and SWENSE.

Immiscible, two–phase, incompressible, viscous and turbulent flow model is governed by continuity and Navier-Stokes equations, which have the following form within SWENSE method Vukčević, Jasak, and Malenica 2016a:

$$\nabla \bullet \mathbf{u}_P = -\nabla \bullet \mathbf{u}_I, \tag{1}$$

$$\begin{aligned} \frac{\partial(\mathbf{u}_P)}{\partial t} &+ \nabla \bullet (\mathbf{u}\mathbf{u}_P) - \nabla \bullet (\nu_{eff} \nabla \mathbf{u}_P) = \\ &- \frac{\partial(\mathbf{u}_I)}{\partial t} - \nabla \bullet (\mathbf{u}\mathbf{u}_I) + \nabla \bullet (\nu_{eff} \nabla \mathbf{u}_I) - \frac{1}{\rho} \nabla p_d + \nabla \mathbf{u} \bullet \nabla \nu_{eff}, \end{aligned} \tag{2}$$

where indices P and I denote diffracted and incident components of the flow, respectively. The velocity field is denoted with U, ν_{eff} stands for effective kinematic viscosity, ρ is the fluid density, while p_d is the dynamic pressure defined as $p_d = p - \rho \mathbf{g} \bullet \mathbf{x}$. Here, p is total pressure, $\mathbf{g}$ denotes constant gravitational acceleration, while $\mathbf{x}$ stands for radii vector with respect to the origin of the coordinate system.

The interface is defined by using the Level Set method derived from the Phase Field equation Sun and Beckermann 2007; Sun and Beckermann 2008, which is more suitable for decomposition than the more popular Volume of Fluid (VOF) method. For more details on interface capturing and implementation of SWENSE method in Naval Hydro pack the reader is directed to Vukčević, Jasak, and Malenica 2016a.

In order for the above equations to be valid for both fluids (air and water), the discontinuities of pressure gradient, density and dynamic pressure must be taken into account. In the Naval Hydro pack, GFM is utilised for discretisation of the free surface boundary conditions Vukčević, Jasak, and Gatin 2017. The discontinuities are described by jump conditions, which state:

$$p_d^- - p_d^+ = -(\rho^- + \rho^+) \mathbf{g} \bullet \mathbf{x}\,, \tag{3}$$

$$\frac{1}{\rho^-} \nabla p_d^- - \frac{1}{\rho^+} \nabla p_d^+ = 0, \tag{4}$$

where superscripts + and - denote values infinitesimally close to the interface on the water and air side, respectively. The above equations stem from the dynamic free surface boundary condition, where the normal stress balance is satisfied exactly, while the tangential stress balance is approximated Vukčević, Jasak, and Gatin 2017.

FOCUSED WAVE LOADING ON FPSO

The considered test cases correspond to experimental studies from Mai et al. 2016, which are presented in this section. The geometry of the experimental program is shown in Figure 1, where three different FPSO models are shown. In this study, only the longest model is considered, label Model 3 in Mai et al. 2016. The dimensions of the wave basin are also indicated on the figure, as well as wave gauges (WG) and their positions. Front and side view of the bow of the vessel is shown in Figure 2, with indicated positions of pressure gauges. Schematic view of the experimental wave tank is shown in Figure 3. The working depth h is 2.93 m.

As mentioned above, six different cases are considered which are divided in two parts:

1. Part 1: three wave cases with different spectral characteristics, as shown in Table 1,
2. Part 2: three wave cases with different incident angles, as shown in Table 2.

In Table 1 and Table 2, a denotes the amplitude of the focused wave, T_p is the peak period of the JONSWAP spectrum, H_s is the significant wave height, ka denotes wave steepness, α stands for the incident angle, where zero degrees denotes head waves, and ϕ denotes the phase shift of individual wave components in the NewWave theory.

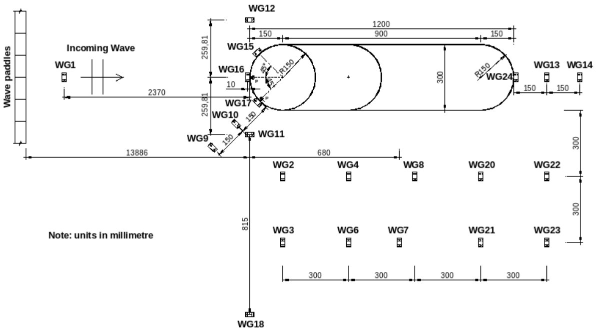

Fig. 1 Geometry of the experimental set–up A Collaborative Computational Project in Wave Structure Interaction n.d.

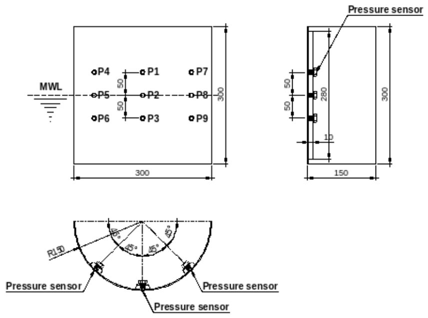

Fig. 2 Pressure gauges at the bow of the FPSO A Collaborative Computational Project in Wave Structure Interaction n.d.

Table 1 Wave parameters for test cases in Part 1

CCP–WSI ID	a, m	T_p, s	H_s ,m	ka	α, ^{o}	ϕ, rad
11BT1	0.069	1.456	0.077	0.13	0	π
12BT1	0.091	1.456	0.103	0.18	0	π
13BT1	0.094	1.362	0.103	0.21	0	π

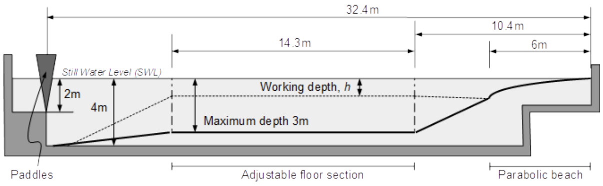

Fig. 3 Schematic view of the wave tankA Collaborative Computational Project in Wave Structure Interaction n.d.

Table 2 Wave parameters for test cases in Part 2

CCP–WSI ID	a, m	T_p, s	H_s ,m	ka	α, ^{o}	ϕ, rad
21BT1	0.089	1.456	0.103	0.17	0	π
22BT1	0.089	1.456	0.103	0.17	10	π
23BT1	0.089	1.456	0.103	0.17	20	π

SIMULATION SET–UP

In order to reduce the required computational time, computational domain is significantly reduced with respect to the dimensions of the physical wave tank. In order to avoid the influence of boundaries, implicit relaxation zones are placed next to outlet boundaries Jasak et al. 2015. Figure 4 shows the computational domain with the FPSO model. The relaxation zones are indicated with the red colour at the calm free surface. The blue portion of the free surface is the full CFD part of the domain. The domain is 20.7 m long, 7 m wide, and the depth is set to 2.93 m. The inlet boundary is set to 4.5 m in front of the FPSO, while the outlet is set 15 m behind the stern. In the experimental wave tank the bottom has variable depth, however given the depth of the wave tank and spectral wave characteristics the influence of the bottom on the wave field can be neglected. Hence, constant depth is set in the numerical domain, with depth that corresponds to the shallower part of the wave tank.

Three different computational grids are used in this work, one for each incident angle case with characteristics shown in Table 3. Grids are of hybrid type, containing structured and unstructured regions, where structured hexahedral cells prevail. In order to keep the direction of wave propagation parallel with the grid direction, grids for cases 22BT1 and 23BT1 are generated by rotating the FPSO model and fitting the computational mesh to the rotated model. Figure 5 shows the top view of the grid in the horizontal plane on the calm free surface. The finest grid level stretches from the FPSO model to the inlet boundary in order to allow the waves to propagate in uniform grid resolution until they reach the FPSO model. Cell size in the finest region corresponds to $\Delta x = 0.01$ m, $\Delta y = 0.02$ m and $\Delta z = 0.005$ m. Figure 6, Figure 7 and Figure 8 show discretised FPSO model for grids 1, 2 and 3, respectively. It can be seen that grids are very similar except for the orientation of the model.

Time–step is controlled in all simulations in order to maintain the Courant–Friedrich–Lewy (Co) number below 1. This results in time–steps ranging between 0.005 and 0.015 seconds. Second order backward scheme is used for time marching, and upwind biased scheme with second order differed correction is used for convection. All other operators and interpolations are performed using linear second order schemes. Conjugate Gradient linear solver is used for the pressure, momentum and free surface transport equations, with absolute tolerance set to 1E-7.

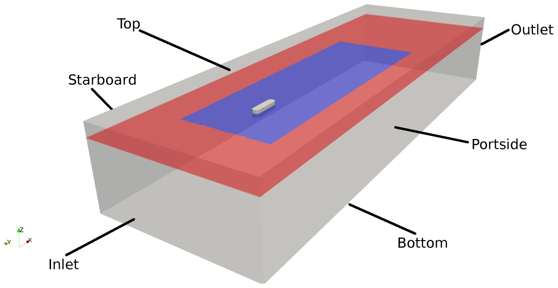

Fig. 4 Computational domain with relaxation zones (red colour).

Table 3 Computational grid characteristics

Grid ID	CCP–WSI ID	No. cells
1	11BT1, 12BT1, 13BT1, 21BT1	4 134 460
2	22BT1	4 138 516
3	23BT1	4 138 521

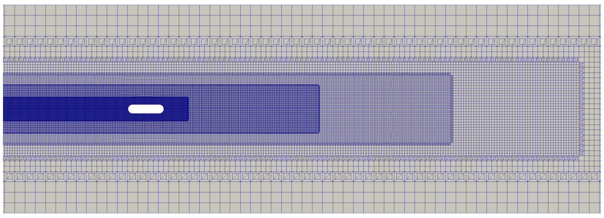

Fig. 5 Top view of grid 1 on the horizontal plane at the calm free surface. Inlet boundary is on the left hand side of the figure.

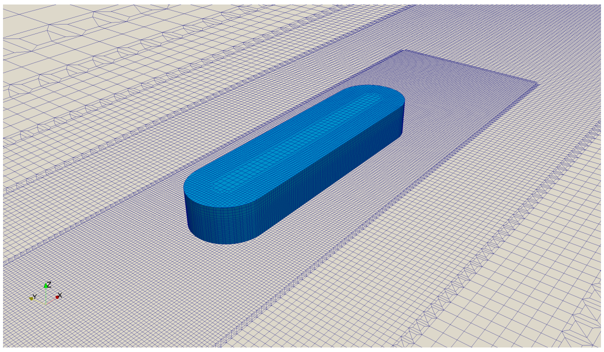

Fig. 6 View of the discretised FPSO model in grid 1.

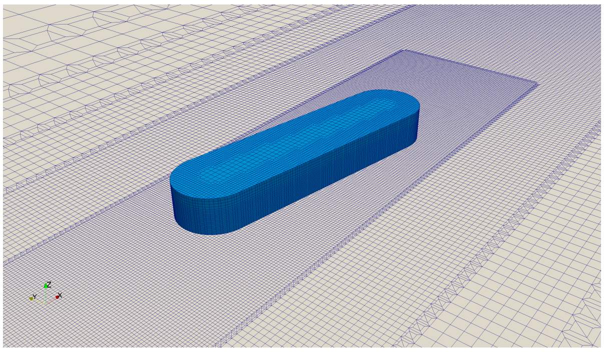

Fig. 7 View of the discretised FPSO model in grid 2.

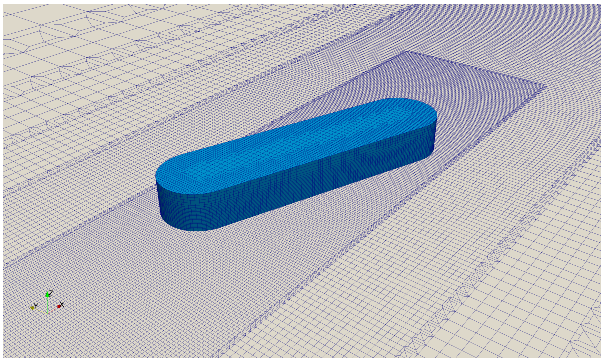

Fig. 8 View of the discretised FPSO model in grid 3.

WAVE PROPAGATION TESTS

Before moving on to wave loading simulations, wave propagation is checked in order to ensure valid incident wave group. Grids without the FPSO model is generated which corresponds exactly to grids 1, 2 and 3. Equivalent numerical settings are used described in the previous section.

The focused wave is generated by superimposing 244 linear wave components equidistantly spaced between 0.1 and 2 Hz A Collaborative Computational Project in Wave Structure Interaction n.d. Focusing point is set at the bow of the FPSO, at time $T = 10$ s. Free surface elevation is measured in time on locations indicated in Figure 1 corresponding to WG 16, 17 and 24. The measured surface elevation signal is compared to linear evolution and experimental results. The shorter domain which is used in CFD in front of the FPSO with respect to the experiment may cause a difference in the level of nonlinearity of the wave field at the focusing location since there is less time for nonlinear wave–to–wave interaction and wave modulation to develop. In order to asses the influence which different domain length may have on the wave field, and ultimately on wave loads, surface elevation signal from CFD is compared to fully nonlinear HOS method Gatin et al. 2017 which is based on the potential flow model. In HOS simulations, equivalent amount of time and space to the experiment is given for development of nonlinearities in the wave field.

For the sake of brevity, only the comparison for WG 16 will be shown here, which is located at the bow of the model. Figure 9 shows the surface elevation comparison for case 11BT1, where EFD stands for experimental results. The four signals correspond well, where the HOS signal shows higher wave crests surrounding the focused wave through. At the focused wave through CFD signal is more similar to HOS than to the linear solution, unlike the remained of the signal. Figure 10 shows signal comparison for case 12BT1, where similar behaviour is observed at the wave through. However, at the wave crest preceding the focusing wave through, CFD and HOS correspond better with respect to the linear solution indicating stronger nonlinearities in the wave field. This is expected since 12BT1 wave case is steeper than 11BT1. For case 13BT1 this behaviour is even more pronounced, as shown in Figure 11, since this is the steepest wave case. Cases 21BT1, 22BT1 and 23BT1 have the same spectral properties, giving equivalent wave fields. Hence, one graph is given for these three cases on Figure 12. Similar behaviour to case 12BT1 is exhibited, since the wave steepness is similar as well. All surface elevation signals correspond very well to experimental measurements.

Overall the surface elevation signals show reasonable correspondence between linear, CFD, HOS and experimental results, with some differences which should be kept in mind. Nonetheless, acceptably accurate wave loads should be obtained using these numerical settings.

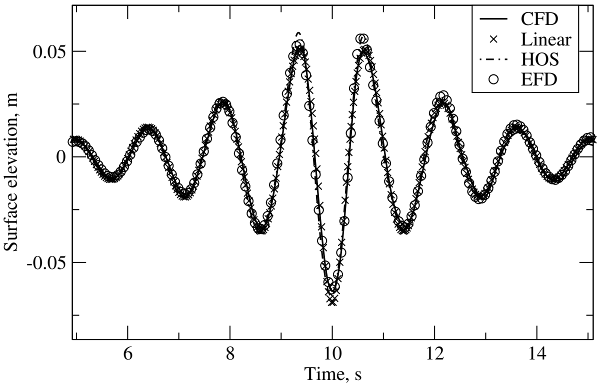

Fig. 9 Empty domain surface elevation comparison at WG 16 for case 11BT1.

WAVE LOADS RESULTS

In order to examine the effects of wave–body interaction, the surface elevation is compared for simulations with and without the FPSO model. Pressure signals are also reported, where only 1 to 6 pressure gauges are reported for cases 11BT1, 12BT1 and 13BT1 since the flow is symmetric. For case 21BT1 all pressure gauges (1 to 9) are reported in order to facilitate the comparison with 22BT1 and 23BT1 cases.
Figure 13 shows the top view of the wave field in the most severe case 13BT1, at the time of focusing. Figure 14 and Figure 15 show cases 22BT1 and 23BT1 where the difference in the incident angle can be observed.

The comparison of surface elevation signals at WG 16, 17 and 24 for case 11BT1 is given in Figure 16, where the incident elevation from the empty domain simulations is compared to the diffracted wave field

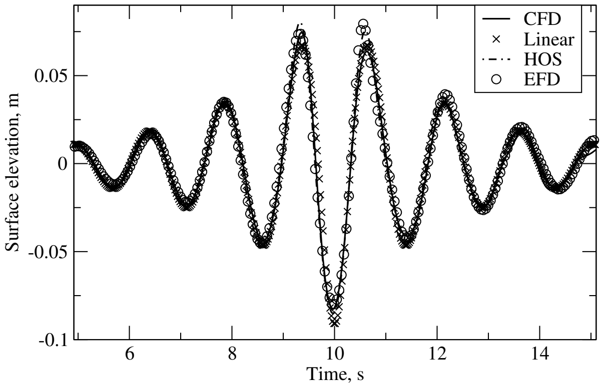

Fig. 10 Empty domain surface elevation comparison at WG 16 for case 12BT1.

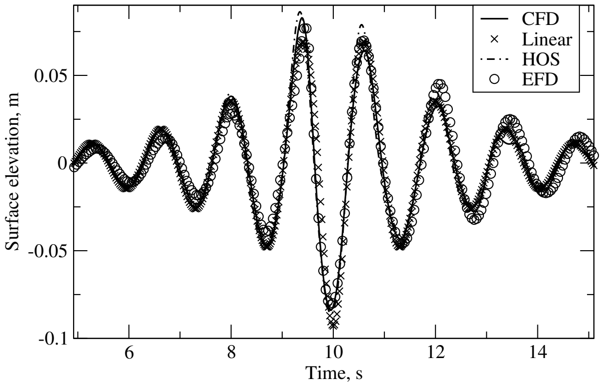

Fig. 11 Empty domain surface elevation comparison at WG 16 for case 13BT1.

in the presence of the FPSO model. For the two gauges in front of the bow, wave amplitudes are larger with respect to the incident wave field. As expected, at wave gauge behind the stern (WG 24) the amplitudes are smaller due to wave energy dissipation. Very similar behaviour is observed on Figure 17 and Figure 18 for cases 12BT1 and 13BT1, respectively. Since case 21BT1 is also a head wave condition, similar results to Part 1 cases are observed on Figure 19. For the oblique case 22BT1 shown in Figure 20 diffracted wave shows larger differences with respect to head wave cases. This is especially true for surface elevation gauge 17. Surprisingly, for larger incident angle (23BT1) the incident and diffracted wave fields show little difference for gauge 17, as shown in Figure 21.

As mentioned above, relative pressure is measured at the bow of the model, on positions indicated on Figure 2. Figure 22, Figure 23 and Figure 24 show relative pressure signals for cases 11BT1, 12BT1 and 13BT1, respectively. Gauges at the same vertical positions are grouped together on individual graphs for easier comparison. As expected, pressure is higher on the centreline with respect to gauges positioned at 45^o with respect to the centreline. On Figure 25, Figure 26 and Figure 27 pressure signals for cases 21BT1, 22BT1 and 23BT1 are presented, respectively. For case 21BT1 gauges positioned at symmetric positions with respect to the centreline show identical pressure signals, which is expected since the incident angle is 0^o for this case. For case 22BT1 shown on Figure 26 pressure measured on gauges P7, P8 and P9 is higher than pressure measured at the corresponding gauges on the opposite side (P4, P5 and P6) due to their position on the windward side. For case 23BT1 this effect is more pronounced, where the gauges on the windward side show very similar pressure values to gauges positioned at the centreline. However, no significant increase in maximum pressure peak is observed for different heading angles. Differences are smaller than 20 Pa.

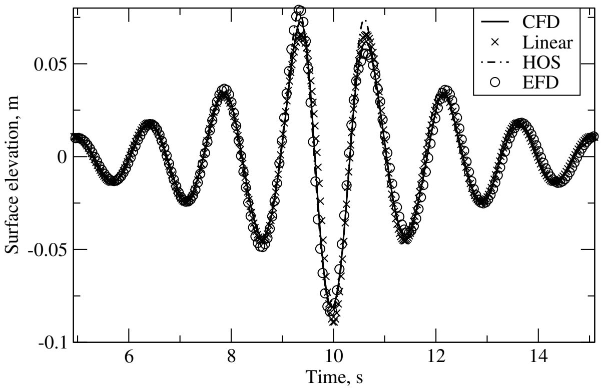

Fig. 12 Empty domain surface elevation comparison at WG 16 for case 21BT1.

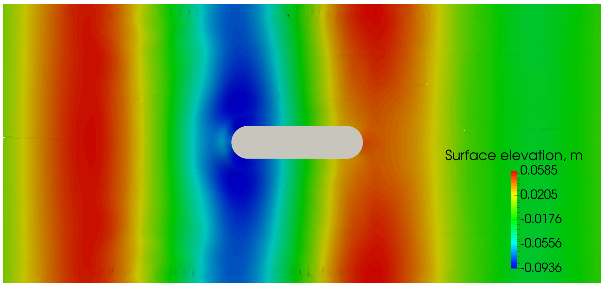

Fig. 13 Free surface elevation at the time of focusing for case 13BT1.

CONCLUSION

Wave loading of a simplified FSPO model is investigated in this work using numerical simulations. Naval Hydro software pack based on open–source software foam–extend–4.0 is used, which employs advanced numerical methods for simulating large–scale, incompressible and viscous two–phase flow. The study is performed for the CCP–WSI Blind Test Workshop A Collaborative Computational Project in Wave Structure Interaction n.d., where the numerical results of various participants will be compared to experimental values.

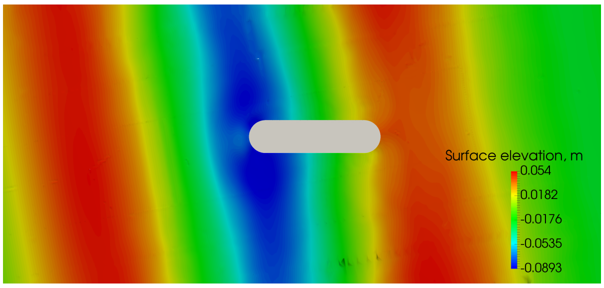

Fig. 14 Free surface elevation at the time of focusing for case 22BT1.

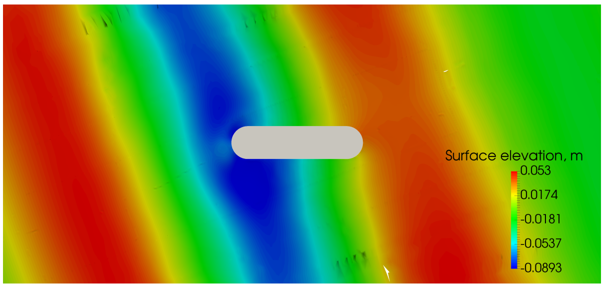

Fig. 15 Free surface elevation at the time of focusing for case 23BT1.

0

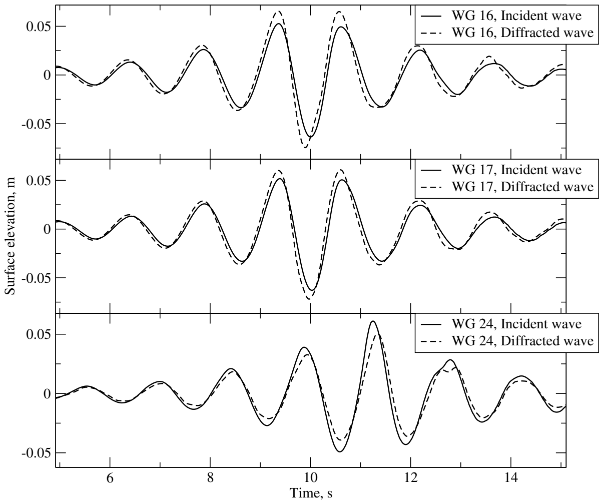

Fig. 16 Comparison of free surface elevation signals for WG 16, 17 and 24 (from top to bottom), for case 11BT1.

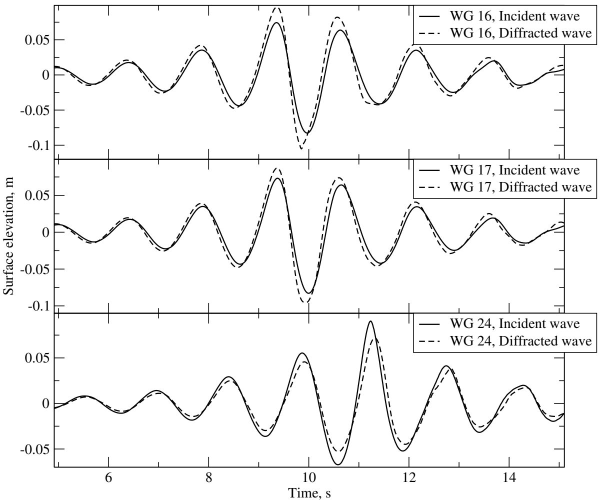

Fig. 17 Comparison of free surface elevation signals for WG 16, 17 and 24 (from top to bottom), for case 12BT1.

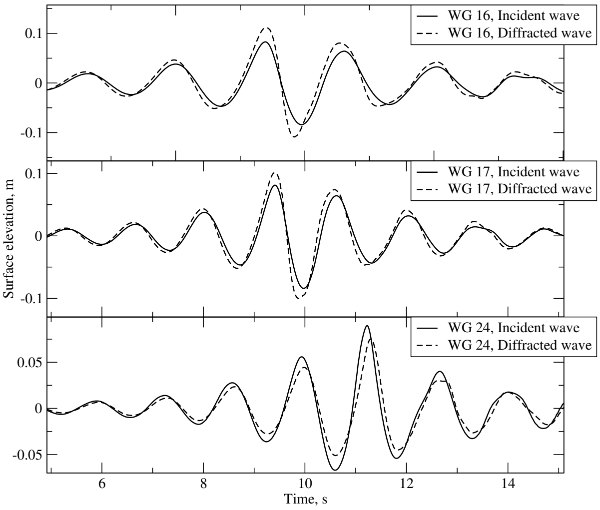

Fig. 18 Comparison of free surface elevation signals for WG 16, 17 and 24 (from top to bottom), for case 13BT1.

Irregular wave group defined with the NewWave theory is used for wave generation. Six different wave cases are examined, where four have zero incident angle, while two cases have 10 and 20 degrees wave incident angle with respect to the central plane of the FPSO model. Accuracy of wave propagation in the present CFD model is checked by performing simulations without the FPSO model and comparing the free surface elevation to the linear solution, nonlinear solution based on potential flow model, and experimental results. The comparison showed that small differences exist between the surface elevation measured in CFD

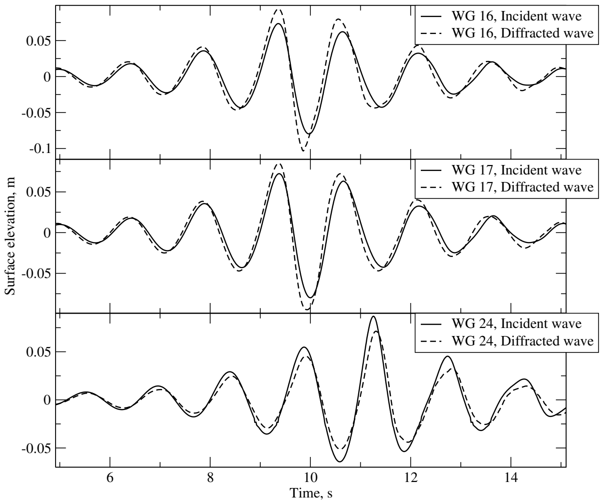

Fig. 19 Comparison of free surface elevation signals for WG 16, 17 and 24 (from top to bottom), for case 21BT1.

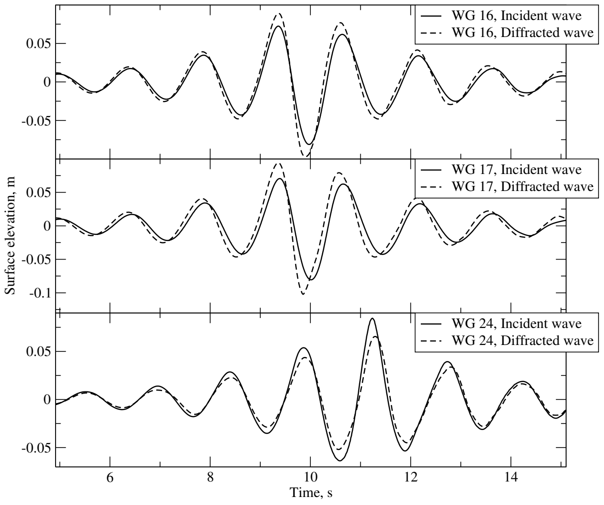

Fig. 20 Comparison of free surface elevation signals for WG 16, 17 and 24 (from top to bottom), for case 22BT1.

and the linear solution, while good correspondence is achieved with respect to experimental results.

Comparison of surface elevation signals between the simulations with and without the FPSO model showed reasonable trends, where the diffraction increased the elevation at the bow and lowered it at the stern of the vessel. Pressure measured at the bow at six locations for symmetrical cases and nine for asymmetrical is also presented, showing that no significant increase in pressure is caused by 10 and 20 degrees incident angle.

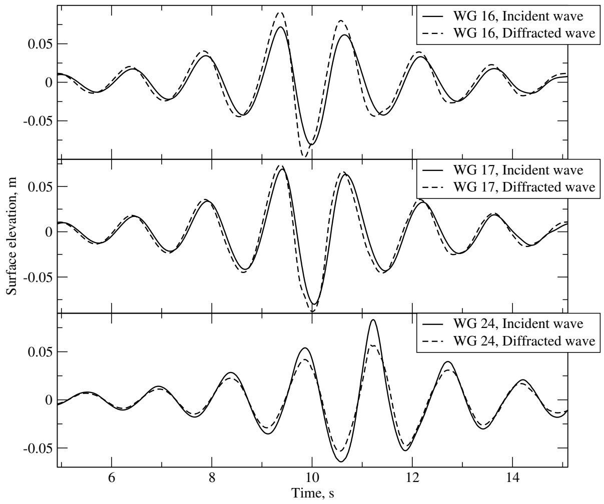

Fig. 21 Comparison of free surface elevation signals for WG 16, 17 and 24 (from top to bottom), for case 23BT1.

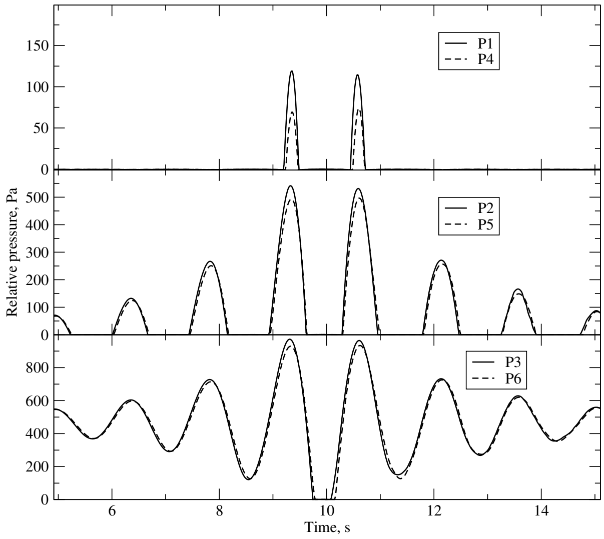

Fig. 22 Relative pressure signals for case 11BT1.

The study produced physical and consistent results, while the accuracy is yet to be determined in the scope of the CCP–WSI Blind Workshop by comparing all the presented results to experimental measurements.

REFERENCES

A Collaborative Computational Project in Wave Structure Interaction. `https://www.ccp-wsi.ac.uk/blind_test_series_1_focused_wave`.

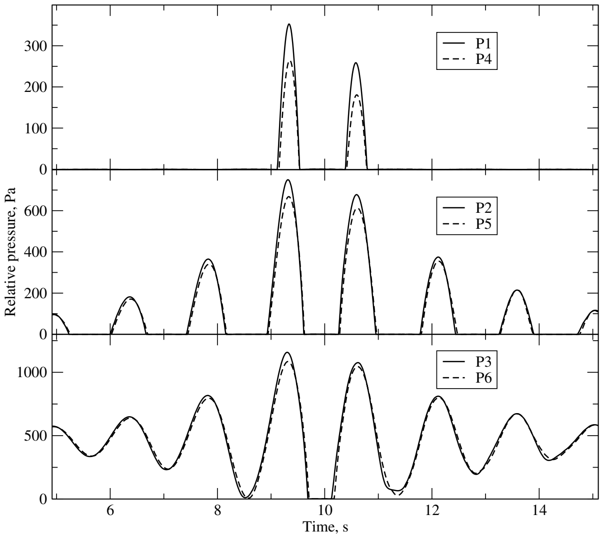

Fig. 23 Relative pressure signals for case 12BT1.

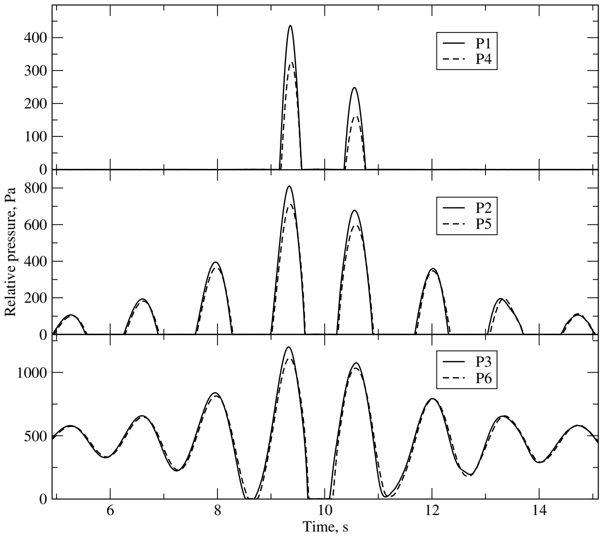

Fig. 24 Relative pressure signals for case 13BT1.

Gatin, I., Vukčević, V., and Jasak, H. (2017). “A framework for efficient irregular wave simulations using Higher Order Spectral method coupled with viscous two phase model”. In: *Journal of Ocean Engineering and Science* 2, pp. 253–267. ISSN: 24680133. DOI: `10.1016/j.joes.2017.09.003`.

Jasak, H., Vukčević, V., and Gatin, I. (2015). “Numerical Simulation of Wave Loads on Static Offshore Structures”. In: *CFD for Wind and Tidal Offshore Turbines*. Springer Tracts in Mechanical Engineering, pp. 95–105. ISBN: 978-3-319-16201-0.

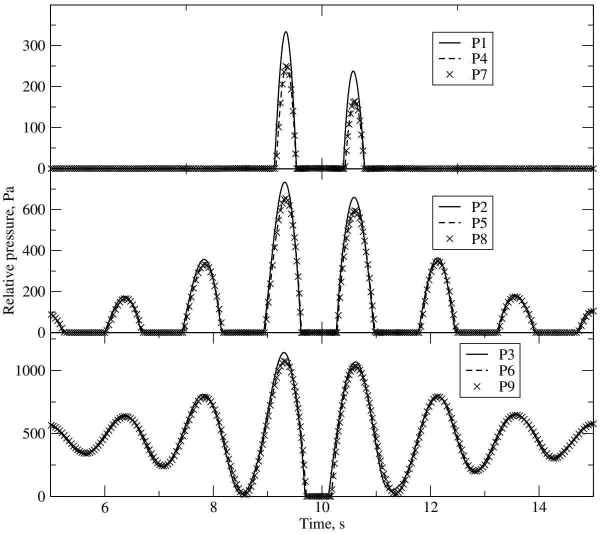

Fig. 25 Relative pressure signals for case 21BT1.

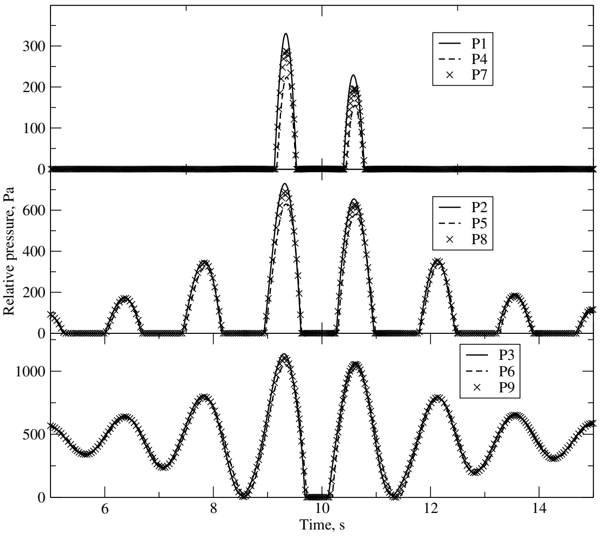

Fig. 26 Relative pressure signals for case 22BT1.

Mai, T., Greaves, D., Raby, A., and Taylor, P. H. (2016). “Physical modelling of wave scattering around fixed FPSO-shaped bodies”. In: *Applied Ocean Research* 61, pp. 115–129. ISSN: 01411187. DOI: `10.1016/j.apor.2016.10.007`.

Sun, Y. and Beckermann, C. (2007). “Sharp interface tracking using the phase–field equation”. In: *J. Comput. Phys.* 220, pp. 626–653.

– (2008). “A two–phase diffusive–interface model for Hele–Shaw flows with large property contrasts”. In: *Physica D* 237, pp. 3089–3098.

Tromans, P. S., Anatruk, A. R., and Hagemeijer, P. (1991). “New Model for the Kinematics of Large Ocean Waves Application as a Design

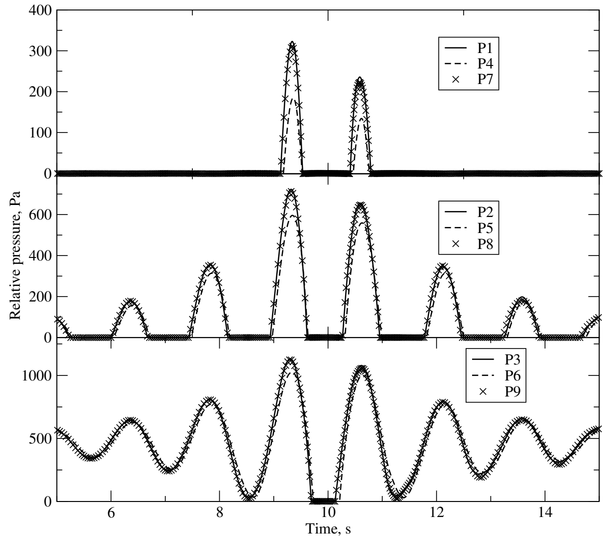

Fig. 27 Relative pressure signals for case 23BT1.

Wave". In: *Proceedings of the First International Offshore and Polar Engineering Conference* 8.August, pp. 64–71.

Vukčević, V., Jasak, H., and Malenica, S. (2016a). "Decomposition model for naval hydrodynamic applications, Part I: Computational method". In: *Ocean Eng.* 121, pp. 37–46. DOI: `10.1016/j.oceaneng.2016.05.022`.

– (2016b). "Decomposition model for naval hydrodynamic applications, Part II: Verification and validation". In: *Ocean Eng.* 121, pp. 76–88. DOI: `10.1016/j.oceaneng.2016.05.021`.

Vukčević, V., Jasak, H., and Gatin, I. (2017). "Implementation of the Ghost Fluid Method for free surface flows in polyhedral Finite Volume framework ". In: *Computers & Fluids* 153, pp. 1–19.

PAPER 3

Ocean Engineering 143 (2017) 295–304

Contents lists available at ScienceDirect

Ocean Engineering

journal homepage: www.elsevier.com/locate/oceaneng

Enhanced coupling of solid body motion and fluid flow in finite volume framework

Inno Gatin[a,*], Vuko Vukčević[a], Hrvoje Jasak[a,b], Henrik Rusche[b]

[a] University of Zagreb, Faculty of Mechanical Engineering and Naval Architecture, Ivana Lučića 5, Zagreb, Croatia
[b] Wikki Ltd, 459 Southbank House, SE1 7SJ London, United Kingdom

ARTICLE INFO

Keywords:
6–DOF rigid body motion
Motion–fluid coupling
Seakeeping
Naval hydrodynamics
Foam–extend

ABSTRACT

An enhanced coupling strategy for the resolution of 6–degrees–of–freedom rigid body motion and unsteady incompressible fluid flow in Finite Volume collocated arrangement using PIMPLE algorithm and rigid mesh motion is presented in this paper. The improved coupling is achieved by calculating the 6–degrees–of–freedom motion equations after each pressure correction step in the pressure–velocity PISO (Pressure Implicit With Splitting of Operators) algorithm. Solving the 6–degrees–of–freedom equations after each solution of the pressure equation of the PISO loop accelerates the convergence, leading to smaller number of nonlinear pressure–velocity iterations needed per time–step. The novel approach is verified and validated on a heaving decay case, while the achieved acceleration in terms of the number of PISO loops is demonstrated on seakeeping simulations of a container ship.

1. Introduction

Numerical simulations using Computational Fluid Dynamics (CFD) are frequently used in computational naval hydrodynamics for assessing wave induced loads and motions (Larsson et al., 2013, 2015a, 2015b). There are numerous reasons why wave induced loads and motions of floating objects are important in marine engineering. Fuel consumption of ships sailing in waves is one of them, due to the increase of oil price during the last couple of decades, as well as the increasingly rigorous regulations regarding harmful gas emission. Seakeeping characteristics of ships are important for safety and comfort of crew and passengers, as well as for assessing acceleration loads (e.g. heavy deck equipment, superstructures etc.).

CFD is proving to be a useful tool in predicting behaviour of ships in waves. Numerous publications (e.g. Orihara and Miyata, 2003; Carrica et al., 2008, 2011, 2012; Bhushan et al., 2009; Kim, 2011; Castiglione et al., 2011; Wu et al., 2011; Guo et al., 2012; Miyata et al., 2014; Mousaviraad et al., 2015; Sadat-Hosseini et al., 2013; Simonsen et al., 2013; Tezdogan et al., 2015) tend to depict the accuracy and potential of CFD for solving such problems, using different ways to couple 6–degrees–of–freedom (6–DOF) motion and fluid flow. The coupling of body motion and fluid flow is commonly performed on the level of the nonlinear pressure–velocity loop (SIMPLE or PIMPLE), i.e. after the flow solution rigid body motion equations are solved and the computational grid is moved accordingly. The procedure is then repeated within each time–step until convergence. This is the conventional strongly coupled approach, hereinafter referred to as conventional approach. The PIMPLE algorithm is comprised of multiple PISO pressure–velocity loops, where pressure is updated multiple times per one momentum equation–update (Issa, 1986).

The above mentioned, conventional approach has been verified in numerous publications. Orihara and Miyata (2003) use a predictor–corrector algorithm for the in–house code WISDAM–X, where they recalculate the entire flow field after every body motion correction. Castiglione et al. (2011) imply that the in–house code CFDShip-Iowa uses a similar approach, where the complete fluid flow solution is obtained in each body motion–fluid flow iteration. Wu et al. (2011) describe the execution sequence of the CFD code used in their study where a similar procedure is employed. To achieve convergence of the coupling, multiple body motion–fluid flow iterations are needed. Simonsen et al. (2013) and Vukčević and Jasak (2015) reported that a minimum of five pressure–velocity (PISO) loops were needed per time–step to ensure convergence. For the fluid flow itself to converge, smaller number of PISO loops is sufficient, typically two for wave related problems. Hence, the body motion–fluid flow coupling presents a considerable overhead in terms of CPU time.

A modified approach for coupling the rigid body motion equations and fluid flow is described, verified and validated in this paper. Pressure field and body motion are tightly coupled at the body boundary in large scale naval hydrodynamics problems. Pressure

---

* Corresponding author.
E-mail addresses: inno.gatin@fsb.hr (I. Gatin), vuko.vukcevic@fsb.hr (V. Vukčević), h.jasak@wikki.co.uk, hrvoje.jasak@fsb.hr (H. Jasak), h.rusche@wikki.co.uk (H. Rusche).

http://dx.doi.org/10.1016/j.oceaneng.2017.08.009
Received 6 December 2016; Received in revised form 13 June 2017; Accepted 7 August 2017

influences the body motion through the force acting on the body, while the moving body influences the flow through the change of body boundary velocity and relative grid motion fluxes (see Demirdžić and Perić, 1988). Rigid grid motion is used, i.e. the grid is not deformed when the body is moving. Enhancing the coupling between the pressure equation and the body motion equations has been proposed before for resolving the coupling of fluid flow and elastic bodies (Fernández et al., 2005), however no similar approach is encountered for a special case of rigid bodies that are modelled as boundaries of the fluid domain, where no volume discretisation of the body is present.

In this work the convergence of the body motion–fluid flow coupling is accelerated by further resolving the coupling via updated 6–DOF solutions after each pressure correction equation within the PISO loop in addition to the standard motion update after each PISO loop. The grid position is not updated between every pressure correction in order to save CPU time. This is allowed since relative flux caused by the grid motion does not influence the pressure equation due to its elliptic nature for incompressible flows. Furthermore, the influence of the new grid position is considered negligible since the motions are generally small within a time–step, even for large overall motions (e.g. manoeuvres). We stress that the grid motion and relative fluxes are updated after each PISO loop in a given time–step, correctly accounting for the complete 6–DOF–fluid flow coupling. Tighter coupling leads to a smaller number of PISO iterations needed to ensure body motion–fluid flow coupling convergence, which in turn reduces the overall CPU time.

The benefit of the presented approach over the conventional approach is the tighter coupling of the pressure equation and the 6–DOF equations which dictate the motion of the body, which in turn represents the boundary of the fluid domain. In the conventional approach, the 6–DOF equations are solved once per PISO loop, i.e once per pressure–velocity coupling. In the proposed approach, 6–DOF equations are solved a significantly larger number of times: in addition to the standard update in every pressure–velocity coupling loop, the 6–DOF equations are additionally solved every time the pressure equation is solved.

This paper is organised as follows. First, the numerical model of the enhanced approach for fluid flow–6–DOF coupling is described, comprising the governing equations, brief description of the numerical procedure and a detailed procedure of the novel algorithm. Second, a test case of a heaving cylinder is presented to verify and validate the novel approach by comparing the results with experimental and analytical results. Next, container ship seakeeping test cases are presented to demonstrate the improvement of convergence of rigid body motion–fluid flow coupling achieved with the new approach, accompanied by a discussion of the results. Finally a brief conclusion is given.

2. Numerical method

The enhanced 6–DOF–fluid flow coupling scheme is implemented in foam–extend (Jasak, 2009), a community driven fork of OpenFOAM open source software, which uses second–order accurate finite volume spatial discretisation with arbitrary polyhedral grid support (Jasak and Gosman, 2001). In this section a brief overview of the discretised governing equations for incompressible two–phase flow is given. The numerical procedure based on the PISO algorithm including the solution of 6–DOF rigid body motion equations is shown. Finally, the novel approach for coupling 6–DOF body motion equations with the pressure equation is presented.

2.1. Fluid flow governing equations

In free surface hydrodynamic problems, the incompressible two–phase flow is governed by the momentum equation, continuity equation and the free surface transport equation. Two phases are modelled with a single set of governing equations, where the discontinuity in pressure gradient and density at the interface is resolved using the Ghost Fluid Method (GFM) (Vukčević, 2016; Vukčević et al., 2017). The GFM imposes pressure jump conditions at the free surface ensuring a sharp transition of fluid properties. For incompressible fluids the conservation of mass is governed by:

$$\nabla \cdot \mathbf{u} = 0, \tag{1}$$

where $\mathbf{u}$ represents a continuous velocity field in the global coordinate system. For a moving computational grid the momentum equation reads:

$$\frac{\partial \mathbf{u}}{\partial t} + \nabla \cdot ((\mathbf{u} - \mathbf{u}_M)\mathbf{u}) - \nabla \cdot (\nu_e \nabla \mathbf{u}) = -\frac{1}{\rho}\nabla p_d, \tag{2}$$

where $\mathbf{u}_M$ is the relative grid motion velocity which stems from the Space Conservation Law (Demirdžić and Perić, 1988); ν_e is the effective kinematic viscosity comprising appropriate phase viscosity and turbulent eddy viscosity; ρ is the density field, and p_d stands for dynamic pressure: $p_d = p - \rho \mathbf{g} \cdot \mathbf{x}$. Note that due to the GFM, volumetric fluxes are used for convection instead of mass fluxes (see Vukčević et al., 2017 for details). Algebraic Volume of Fluid (VOF) (Rusche, 2002) method is used for interface capturing with additional convective term for interface compression:

$$\frac{\partial \alpha}{\partial t} + \nabla \cdot (\mathbf{u}\alpha) + \nabla \cdot (\mathbf{u}_r \alpha (1 - \alpha)) = 0, \tag{3}$$

where α is the volume fraction, and $\mathbf{u}_r$ stands for artificial compressive velocity field which is oriented in the normal direction towards the free surface (Weller, 2008). The third term is active only near the free surface due to the nonlinear term $\alpha(1-\alpha)$. The details on the evaluation of $\mathbf{u}_r$ can be found in Rusche (2002).

Detailed discretisation of temporal derivative, convection and diffusion in (2) in integral form can be found in Jasak (1996), while already discretised equations are used in the text below. The semi–discretised momentum equation for each cell reads:

$$a_P \mathbf{u}_P + \sum_f a_N \mathbf{u}_N = \mathbf{b} - \frac{1}{\rho}\nabla p_d, \tag{4}$$

where a_P stands for the diagonal coefficient, a_N for the off–diagonal coefficients, and subscripts P and N stand for values in the parent cell centre and neighbouring cell centres, respectively. Parent cell is the cell for which the equation is being solved for, and the neighbouring cells are all the cells which share a face with the parent cell (Jasak and Gosman, 2001). $\sum_f$ is the sum over all neighbouring faces f, and $\mathbf{b}$ stands for the source term. Following notation proposed by Jasak (1996), (4) can be written as:

$$\mathbf{u}_P = \frac{H(\mathbf{u}_N)}{a_P} - \frac{1}{a_P}\frac{\nabla p_d}{\rho}, \tag{5}$$

where $H(\mathbf{u}_N)$ presents an explicit operator:

$$H(\mathbf{u}_N) = -\sum_F a_N \mathbf{u}_N + \mathbf{b}. \tag{6}$$

The pressure equation is derived by interpolating (5) on cell faces and substituting into the discretised form of (1), yielding:

$$\sum_f \mathbf{s}_f \cdot \left(\frac{1}{a_P}\right)_f \left(\frac{1}{\rho}\nabla p_d\right)_f = \sum_f \mathbf{s}_f \cdot \frac{(\mathbf{H}(\mathbf{u}_N))_f}{(a_P)_f}, \tag{7}$$

where $\mathbf{s}_f$ stands for surface normal vector, and subscripts f denote values at face centres. For a detailed derivation of the pressure equation with the GFM, the reader is referred to Vukčević et al. (2017).

2.2. Numerical procedure

The solution of above equations is achieved in a segregated manner in a PIMPLE loop, a combination of SIMPLE and PISO algorithms, where the PISO loop is repeated multiple times per time–step. The pressure velocity coupling is resolved in the PISO manner, while the repetition of PISO multiple times per time step is specific to SIMPLE algorithm. Within the PISO loop, the momentum equation is solved once, while the pressure equation, (7), is solved multiple times. After each pressure correction step, the velocity field is updated explicitly using (5).

2.3. Coupling of fluid flow and 6–DOF body motion equations

In most naval hydrodynamic problems pressure forces acting on a moving body dominate over viscous forces, resulting in a strong coupling of 6–DOF body motion and pressure at the body boundary. The boundary velocity is determined by solving the 6–DOF body motion ODE, where the right hand side represents the excitation force **F** and moment **M**:

$$\mathbf{F} = \mathbf{F}_p + \mathbf{F}_v, \tag{8}$$

$$\mathbf{M} = \mathbf{M}_p + \mathbf{M}_v, \tag{9}$$

where indices p and v denote pressure and viscous parts, respectively. Pressure and viscous forces are calculated in the global inertial reference frame by integrating the pressure and shear stress on the body surface, respectively:

$$\begin{aligned} \mathbf{F}_p &= \sum_{bf} \mathbf{s}_{bf} p_{bf}, \\ \mathbf{F}_v &= \sum_{bf} \rho_{bf} \nu_{e,bf} \mathbf{s}_{bf} \cdot \mathbf{T}^*, \\ \mathbf{M}_p &= \sum_{bf} \mathbf{r}_{bf} \times \mathbf{s}_{bf} p_{bf}, \\ \mathbf{M}_v &= \sum_{bf} \mathbf{r}_{bf} \times (\rho_{bf} \nu_{e,bf} \mathbf{s}_{bf} \cdot \mathbf{T}^*), \end{aligned} \tag{10}$$

where index bf denotes face at the body boundary, $\mathbf{T}^*$ is the deviatoric part of the stress tensor $\mathbf{T}$ which is twice the symmetric part of the velocity gradient tensor $\nabla\mathbf{u}$. $\mathbf{r}$ is the radii vector of the face centre with respect to the centre of gravity. In the conventional approach used in PIMPLE algorithms, the pressure force F_p converges in an oscillatory manner in successive PISO loops during one time–step due to the elliptic nature of the pressure equation, while the viscous force exhibits smoother convergence. If the pressure forces are dominant, such oscillations deteriorate the convergence rate of body motion–fluid flow coupling.

The pressure equation and the rigid body motion equations are mutually coupled, where the pressure influences the 6–DOF equations through (10), while the body velocity solution influences the pressure equation through (6). The strong coupling between pressure and body boundary velocity is present even without moving the grid.

In this work an enhanced approach for 6–DOF–fluid flow coupling is proposed, in which 6–DOF body motion equations are solved after each pressure correction equation within the PISO loop, allowing tighter coupling with the pressure equation. After the solution of the pressure equation, the forces acting on the body are recalculated and body motion ODEs are solved:

$$\begin{aligned} \frac{\partial \mathbf{v}}{\partial t} &= \mathbf{F}/m, \\ \frac{\partial \boldsymbol{\omega}}{\partial t} &= \mathbf{I}^{-1} \cdot (\mathbf{M} - \boldsymbol{\omega} \times (\mathbf{I} \cdot \boldsymbol{\omega})), \end{aligned} \tag{11}$$

where $\mathbf{v}$ is the velocity of the centre of mass of the body, $\boldsymbol{\omega}$ is the rotational velocity with respect to the centre of mass, while $\mathbf{I}$ stands for the tensor of inertia of the body. Fifth-order Cash-Karp embedded Runge-Kutta scheme with error control and adjustive time-step size (Press et al., 2002) is used for integration of rigid body motion equations, while no under–relaxation is used.

The change of the body velocity is inserted in the pressure equation through (6) by updating the source term **b** for cells adjacent to the body boundary. The source can be decomposed into the contribution from the boundary condition at the moving body and the remaining part of the source:

$$\mathbf{b} = \mathbf{b}_r + \mathbf{b}(\mathbf{u}_{bf}), \tag{12}$$

where $\mathbf{u}_{bf}$ stands for the velocity of the body boundary faces, $\mathbf{b}(\mathbf{u}_{bf})$ is the part of the source term which is a function of the velocity at the body boundary, while $\mathbf{b}_r$ stands for the remaining portion of the source term (other boundary conditions, non–orthogonal correction of the diffusion term etc.). The body boundary velocity is calculated from the rigid body kinematics obtained from (11) as:

$$\mathbf{u}_{bf} = \mathbf{v} + \boldsymbol{\omega} \times \mathbf{r}_{bf}. \tag{13}$$

The body boundary, i.e. the grid, is not moved in the pressure loop to save CPU time. Instead, the grid is moved only once per PISO loop, to allow complete coupling with the velocity field and the free surface. Hence the 6–DOF equations are further resolved at the negligible expense of additional rigid body motion ODE solution per each pressure correction equation. The flow chart of the PIMPLE loop including the enhanced 6–DOF body motion coupling is shown in Fig. 1.

3. Decaying heave motion of a cylinder

In this section verification and validation of the proposed approach is presented on a case of 2D decaying heave motion of a cylinder. Verification is performed by refining the spatial and temporal resolution simultaneously, following Eça and Hoekstra (2008). Experimental and theoretical results published by Ito (1977) and Maskell and Ursell (1970) are used for validation, respectively.

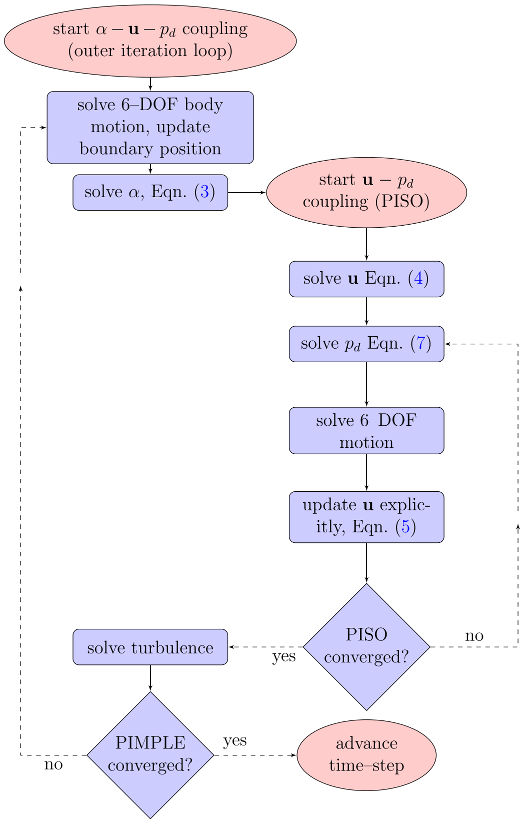

Fig. 1. Flow chart of the segregated solution algorithm.

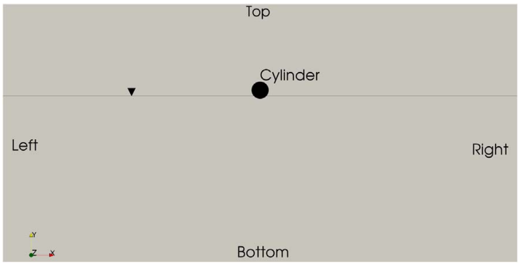

Fig. 2. Computational domain for the heaving cylinder test case.

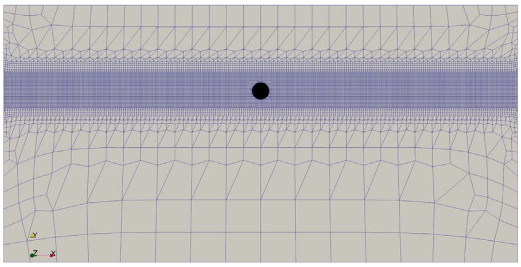

Fig. 3. Coarse computational grid corresponding to refinement level 1 for the heaving cylinder test case.

The experimental and theoretical data are given in dimensionless form, where the temporal and spatial scales are normalised with the initial displacement δ and with $\sqrt{g/R}$, respectively, where R denotes the cylinder radius. Hence, the cylinder dimensions are selected arbitrarily: $R = 1$ m, while the initial displacement is set to $\delta = 2/3R$ upward. The computational domain is 60 m wide, with a water depth of 20 m and 10 m height above the free surface. Fig. 2 shows the computational domain with boundaries and cylinder position with respect to the free surface. Implicit relaxation zones (Jasak et al., 2015) are positioned at the left and right boundary for wave absorption, and extend 15 m towards the cylinder. Wave velocity boundary condition is set on the left, right and bottom boundary, while zero gradient is set on the top boundary. Zero gradient pressure boundary condition is set on all boundaries except the top, where total pressure is prescribed.

Second order backward temporal discretisation scheme is used, while implicit upwind scheme with deferred second order correction is used to discretise the convection term in the momentum equation. Second order scheme with explicit limited non–orthogonal correction is used for the discretisation of the diffusion term. For the interface capturing equation second order scheme with deferred correction is used for the convection, while turbulence equations are convected with first order upwind scheme. Four PISO correctors are used per time–step for all simulations, where two pressure corrections per PISO loop are employed. All equations are solved to the tolerance of $O(-8)$ calculated with the L_1 norm, guaranteeing that the final residual does not exceed this value. However, the actual accuracy of the calculations is expressed via initial residual of all equations prior to the last solution in the time–step, and it will be shown for the below simulations. These residuals need to be sufficiently small to show that the pressure–velocity–free surface system has converged to a satisfactory level.

3.1. Verification

Verification procedure for unsteady flow from Eça and Hoekstra (2008 is adopted, where four grids are used in order to establish the total uncertainty arising from temporal and spatial discretisation errors. According to the recommendations of Eça and Hoekstra (2014), for complex flow cases at least four refinement levels are needed to get a reliable uncertainty assessment. Refinement ratio $r = 2$ is used which defines the ratio between the temporal resolution τ_i/τ_{i-1} and spatial resolution h_i/h_{i-1} of adjacent refinement levels i. Temporal and spatial resolution are refined simultaneously, i.e. $h_3/h_4 = \tau_3/\tau_4 = h_2/h_3 = \tau_2/\tau_3 = h_1/h_2 = \tau_1/\tau_2 = r$. The values for the coarsest level are set to: $h_1 = 0.125$ m, which is the vertical and horizontal dimension of a typical cell near the free surface; $\tau_1 = 0.05$ s. This results in 19 050, 72 554, 283 386 and 1 120 410 cells for grids corresponding to refinement levels 1, 2, 3, and 4, respectively. The corresponding time–steps are $\tau_1 = 0.05$ s, $\tau_2 = 0.025$ s, $\tau_3 = 0.0125$ s and $\tau_4 = 0.00625$ s. Since the time–step is fixed, the Courant–Friedrichs–Lewy (CFL) number varies between 0.5 and 2.5, with a mean of ≈ 1.1. Since the spatial and temporal resolution are refined simultaneously, the CFL number behaves similarly in all simulations. The computational grid is unstructured, composed mostly of hexahedral cells ($\approx$95%), and a minor portion of polyhedral cells ($\approx$5%). The coarsest grid is shown in Fig. 3, where it can be seen that the grid is refined in the vicinity of the free surface.

Eça and Hoekstra (2014) recommend using a least squares approach for discretisation error estimate when the flow field is complex and when unstructured grids are used, which will be summarized here for clarity. Evaluation of ith grid uncertainty for well behaved data sets with four or more refinement levels can be expressed as:

$$U_i = F_S \epsilon_i + \sigma + |\phi_i - \phi_{fit}|, \tag{14}$$

where U_i presents the grid uncertainty for grid i, $F_S = 1.5$ is the safety factor, ϵ_i is the discretisation error, σ is the standard deviation of the least squares fit, ϕ_i is the value of the observed simulation variable on grid i, and ϕ_{fit} is the corresponding value obtained from the least squares fit. The data is considered well behaved if the relation $\sigma < \Delta$ is fulfilled, where Δ defines a data range parameter defined as:

$$\Delta = (\phi_{max} - \phi_{min})/(N - 1), \tag{15}$$

where ϕ_{max} and ϕ_{min} denote maximum and minimum value of the variable obtained using different refinement levels. In cases when τ_i and h_i are simultaneously varied, ϵ_i is determined as (Eça and Hoekstra, 2008):

$$\epsilon_i = \alpha h_{i*}^p, \quad h_{i*} = (\tau_i h_i^2)^{1/3}, \tag{16}$$

where α is a constant that needs to be calculated, while p is the achieved order of accuracy. When more than three refinement level results are available, least squares method is used to obtain α and p by minimising the following function:

$$S(\phi_0, \alpha, p) = \sqrt{\sum_{i=1}^{N} (\phi_i - (\phi_0 + \alpha h_{*i}^p))^2}, \tag{17}$$

where ϕ_0 presents the estimate of the exact solution. The convergence is considered monotone if $0.5 \le p \le 2.1$. The standard deviation of the least squares fit is determined as:

$$\sigma = \sqrt{\frac{\sum_{i=1}^{N} (\phi_i - (\phi_0 + \alpha h_{*i}^p))^2}{N - 3}}. \tag{18}$$

Fig. 4 shows the heave signal in time for the four refinement levels, where z stands for the heave displacement. Fig. 5 shows the enlarged graph in order to see the analysed portion of the signal more clearly. The uncertainty analysis is performed on heave signal characteristics in temporal and frequency domain. In temporal domain, first two extrema of the signal are used, while in the frequency domain the mean value and harmonics with the largest magnitudes are analysed. The harmonic amplitudes are obtained by performing a Fast Fourier Transform on the first 10 s of the signal. Fig. 6 shows the initial residuals of the last solution in the time–step for pressure, momentum and interface capturing equations during the simulation for the finest refinement level. The residuals exhibit similar behaviour for all variables, maintaining at the level of $O(-5)$ or less during the simulation. Fig. 7 shows the spectrum of the heave signal for all refinement levels, where Z

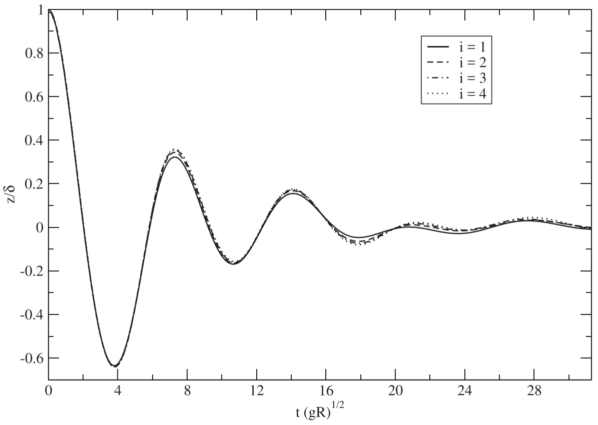

Fig. 4. Cylinder heave signals obtained using different temporal and spatial refinements.

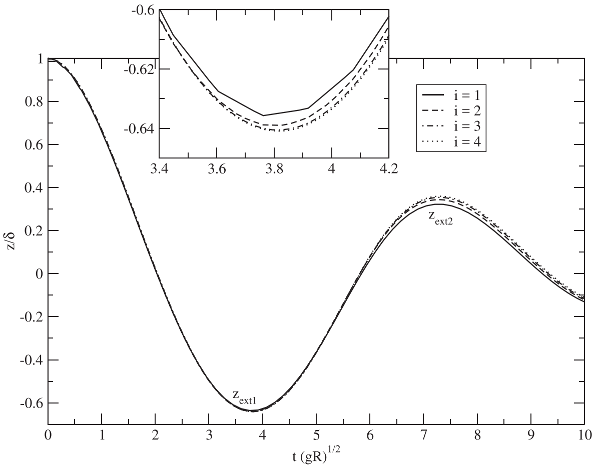

Fig. 5. Enlarged view of the analysed portion of the cylinder heave signal.

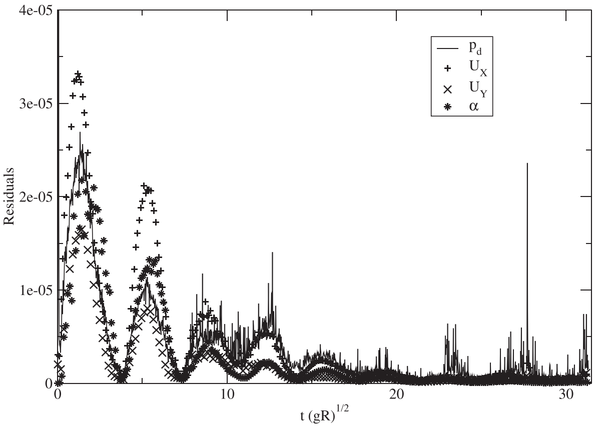

Fig. 6. Initial residuals of the equations before the last solution in the time–step, during the fine resolution simulation.

stands for the Fourier amplitude of the heave signal. Circles denote the amplitudes that are analysed.

Table 1 shows the complete verification data for two items in temporal domain: z_{ext1} and z_{ext2}, denoting the first and the second extrema of the heave signal; and three items in frequency domain: mean Z_0, first Z_1 and second Z_2 order amplitudes. The uncertainties are calculated for the finest grid, i.e. $i = 4$ in (14). Standard deviation σ is smaller than the data range parameter Δ for all items, hence the data is well behaved. Since $0.5 < p < 2.1$ for all items, monotone convergence is achieved. Order of convergence is between 1 and 2 for all items except the mean value. Uncertainties are acceptably small for all items ranging from 0.03% to 2.1%, except for the mean of heave motion Z_0 which exhibits 10% of uncertainty due to its small absolute value.

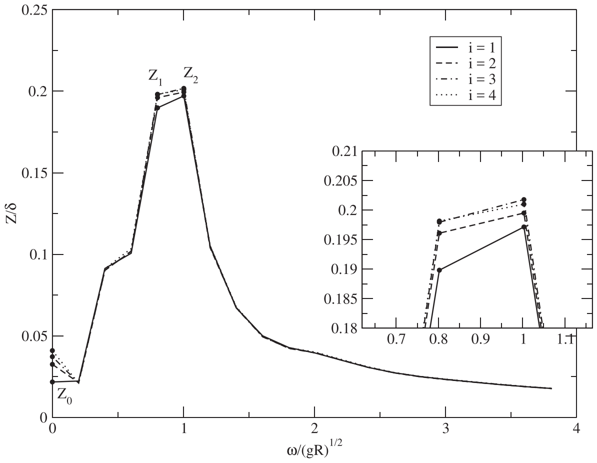

Fig. 7. Spectrum of cylinder heave oscillation.

Table 1
Verification results for the cylinder heave decay case.

Item	ϕ_0	p	σ	Δ	U_4, %
z_{ext1}/δ	−0.6414	1.2767	0.000132	0.00174	0.07
z_{ext2}/δ	0.3647	1.0104	0.000173	0.01247	2.09
Z_0/δ	0.0442	0.8980	0.000670	0.00641	10.20
Z_1/δ	0.1984	1.9306	0.000177	0.00278	0.03
Z_2/δ	0.2017	1.3634	0.000976	0.00154	0.28

3.2. Validation

Results obtained using the finest temporal and spatial discretisation are used for the validation including the uncertainties calculated in the previous section following (Eça et al., 2016), where they are compared against experimental data presented by Ito (1977) and theoretical results published by Maskell and Ursell (1970). The comparison is performed for the same items used in the verification study. Fig. 8 shows the comparison of dimensionless heave signals. The present result agrees with theory and experiment reasonably well, within the range set by the theoretical and experimental data. Comparison of temporal and spectral items between the theoretical, experimental and numerical results are presented in Table 2. Relative difference is calculated as $D_{a-b} = (\phi_a - \phi_b)/\phi_a$, where indices denote the corresponding method: E is experimental, T theoretical and C is the result of the present CFD method. The relative differences between the experimental and theoretical results are generally larger than the difference of the CFD result with either of them. It can be noticed that the CFD result corresponds better to the theoretical data, while larger differences occur with respect to the experimental results.

The result comparison including discretisation uncertainties are graphically presented in Fig. 9, where the uncertainties from Table 1 are used. Note that absolute values of corresponding items are shown for better visibility. The error bars, which present the discretisation uncertainty interval, are often very close together and visually form a single line. Generally the numerical results agree better with theoretical

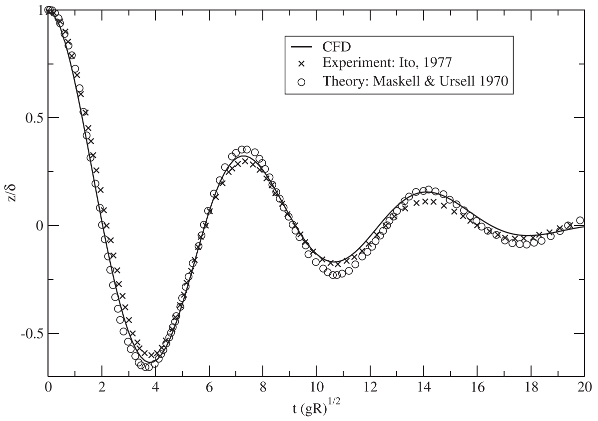

Fig. 8. Cylinder heave signal comparison.

Table 2
Validation results for the cylinder heave decay case.

Item	Experimental	Theory	CFD	D_{E-T}, %	D_{E-C}, %	D_{T-C}, %
z_{ext1}/δ	−0.6015	−0.6573	−0.6409	−9.28	−6.56	2.49
z_{ext2}/δ	0.2977	0.3521	0.3596	−18.26	−20.76	−2.11
Z_0/δ	0.0468	0.0366	0.0410	21.71	12.39	−12.02
Z_1/δ	0.1848	0.2103	0.1981	−13.83	−7.25	5.79
Z_2/δ	0.1971	0.2134	0.2010	−8.28	−1.98	5.81

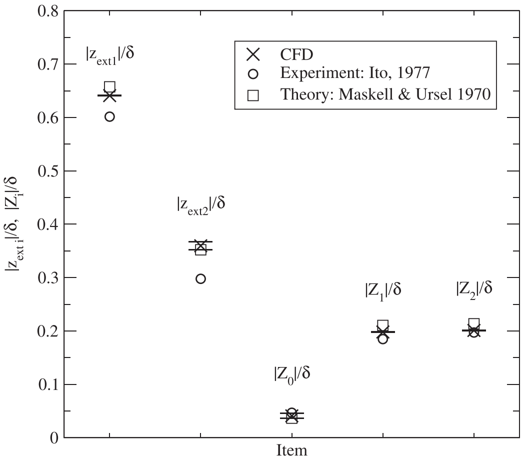

Fig. 9. Comparison of numerical, experimental and theoretical results including the numerical uncertainties.

results, especially for the temporal items, z_{ext1} and z_{ext2}.

4. Performance comparison on a seakeeping case

In this section a typical seakeeping case is considered in order to compare the enhanced approach with the conventional approach. The two methods are compared in terms of performance, including the 6–DOF–fluid flow coupling sensitivity study, where the number of PISO correctors per time–step is varied.

Seakeeping simulations of KRISO Container Ship (KCS) are performed to assess the acceleration achieved with the enhanced approach for 6–DOF–fluid flow coupling. Regular head waves are imposed at design Froude number $Fr = 0.261$, while the wave parameters are chosen to correspond to 2.10 C5 case from the Tokyo Workshop on CFD in Ship Hydrodynamics (2015) (National Maritime Reasearch Inistitute, 2015).

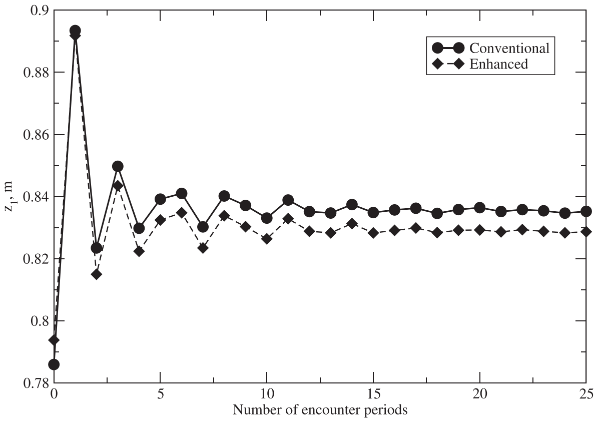

Fig. 10. Example of periodic convergence of first order amplitude of heave, obtained using the conventional and enhanced approach with 4 PISO correctors per time step.

In order to compare the two coupling strategies, all parameters of the simulations are the same in all cases except the number of PISO correctors per time–step. Simulations with 2, 4, 8, 10 and 14 PISO correctors are conducted with the conventional approach, while 2, 3, 4, 8 and 14 PISO correctors are used with the proposed approach. Four pressure correction steps are used per PISO corrector in all simulations. k–ω SST turbulence model is used (Menter, 1994) with wall functions, where the average y^+ on the hull is 50. Mean, first order and phase shift of the first order of resistance, heave and pitch are compared. Moving window Fourier transform for every encounter period is used to obtain frequency domain signals throughout successive periods. Fig. 10 shows an example of the moving window Fourier transform of the first order amplitude of heave. The periodic uncertainty is below 2% for all simulations, hence it is considered not to have a significant influence on the comparison below. More details on how the periodic convergence is attained can be found in Vukčević and Jasak (2015). The required CPU time per time step is also compared. A cluster with distributed memory is used with nodes: CPU2x Intel Xeon E5-2637 v3 4core, 3.5 GHz, 15 MB L3 Cache, DDR42133, with Infini–Band communication. Two nodes, i.e. eight cores are used for each simulation.

KCS model characteristics can be found at Tokyo 2015 CFD Workshop website (National Maritime Reasearch Inistitute, 2015). Heave and pitch motions are free, and half of the model is simulated using a symmetry boundary condition at the vertical centre plane. Inlet boundary is positioned at $1L_{PP}$ from the fore perpendicular, outlet at $2L_{PP}$ from the aft perpendicular, while the farfield boundary at the side of the ship is set at the distance of $1.5L_{PP}$ from the symmetry plane. The depth of the domain is set to $1.5L_{PP}$, while the top boundary is set to $1L_{PP}$ from the free surface. The velocity at the inlet, outlet, bottom and farfield is prescribed from the stream function wave theory, while the dynamic pressure boundary condition is set to zero gradient. Fixed pressure is set at the top boundary, with zero gradient on the velocity field. Wave height to cell height ratio is $H/\Delta z \approx 20$, while wave length to cell length ratio near the hull is $\lambda/\Delta x \approx 335$. Implicit relaxation zones (Jasak et al., 2015) are used in order to gradually impose the incident wave field into the computational domain and to damp the waves at the outlet boundary, in order to prevent reflection. Length of relaxation zones are $\lambda/2$ at the inlet and side boundary, and 1λ at the outlet. Fig. 11 shows the discretised hull surface, symmetry plane and a plane normal to the longitudinal direction on the main cross section. The rudder is fixed at zero angle, and the model is towed at constant carriage velocity corresponding to Froude number of 0.261. Same grid with 950,000 cells is used in all simulations, while the time step is set to $\Delta t = 0.0046$ s, which corresponds to 400 time–steps (Vukčević, 2016) per encounter wave period. At least 10 encounter periods are simulated

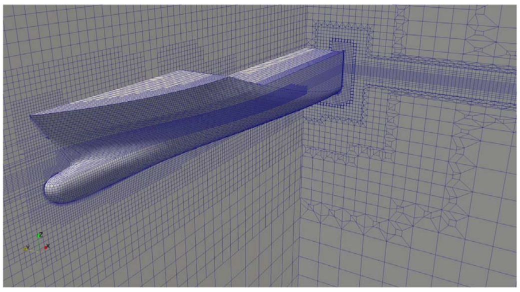

Fig. 11. Computational grid used in the KCS seakeeping simulations.

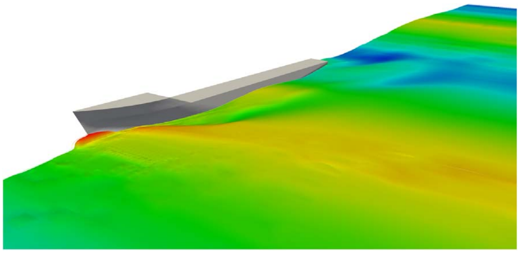

Fig. 12. View of free surface elevation in KCS seakeeping simulation for $t = 18.2$ s.

in all simulations. Fig. 12 shows one time instance from the simulation, where the incident, diffracted and radiated wave systems can be observed.

The results are compared in Fig. 13. The solution obtained using 14 PISO correctors with conventional approach is used as a reference (denoted by symbol ⋄). The conventional scheme result using two PISO correctors is far from the reference (converged) solution for all measured items. With the enhanced approach, two PISO correctors generally produce the solution which is close to the converged solution. It can also be seen that with the conventional approach at least four correctors are needed to obtain acceptable accuracy. In the following text results shall be analysed item by item.

In Fig. 13 the first row of graphs shows the comparison for total resistance R_T. For the zeroth order R_{T0} and first order R_{T1} of total resistance, the result obtained with the conventional approach using two PISO correctors is far from the converged solution. The enhanced approach achieves the solution which is close to the converged solution with fewer number of PISO correctors, while the solution does not change considerably with increasing number of PISO correctors, especially for the first order of total resistance.

The second row of graphs in Fig. 13 shows heave results. First order z_1 and phase shift γ_{z1} of heave confirm that two correctors with the enhanced approach produce the solution close to the reference solution. For the zeroth order z_0, the two methods exhibit different behaviour: the conventional approach diverges, while the enhanced approach converges after 8 PISO correctors. It should be noted that the first order and phase shift are more important for motions from a practical point of view compared to mean value, and that mean values of heave an pitch have significantly smaller absolute values.

The third row of graphs in Fig. 13 presents the result comparison for pitch motion. All three items show that the enhanced approach produces a solution close to the converged one with two PISO

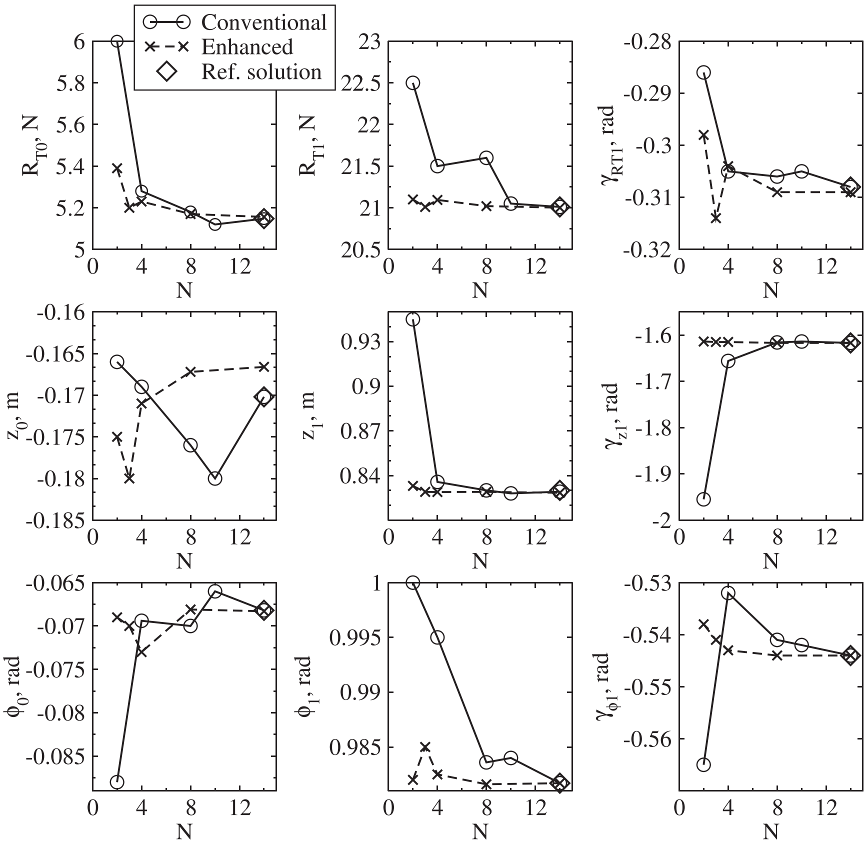

Fig. 13. Results comparison: R_T stands for total resistance, z for heave, ϕ for pitch. Index number 0 indicates zeroth Fourier series order (mean), while 1 stands for the first order of oscillation. γ is the phase shift of the item indicated in the index. N represents the number of PISO correctors per time–step.

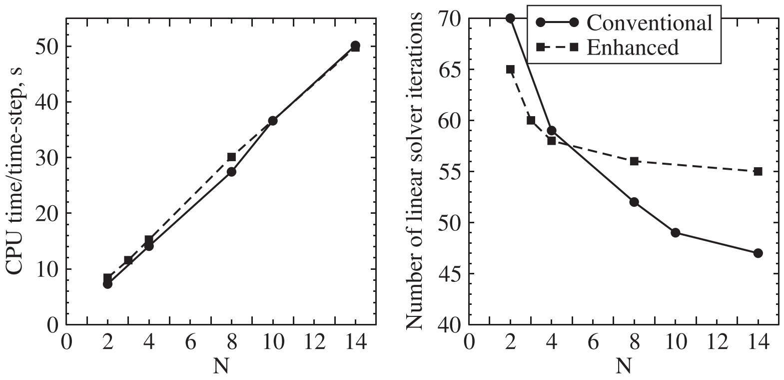

Fig. 14. Comparison of CPU time and the average number of pressure equation linear solver iterations per time–step for varying number of PISO correctors.

Table 3
Total CPU time for 20 encounter periods for individual seakeeping simulations.

N	2	3	4	8	10	14
Enhanced	19.0 h	11.5 h	34.6 h	68.0 h	N/A	112.5 h
Conventional	16.5 h	N/A	32.0 h	62.0 h	83.0 h	113.0 h

correctors, and that the result shows low dependence on the number of PISO correctors.

The main objective of this work is to reduce the required CPU time for transient simulations with body motion. Hence, a comparison of average CPU time per time–step for all simulations is shown in the first graph in Fig. 14. It can be noticed that two correctors with the enhanced approach require slightly more CPU time than two correctors with the conventional approach. This slight difference is caused by solving the motion equations once per each pressure correction equation. However, since smaller number of PISO correctors can be used with the enhanced approach (e.g. 2 instead of 4–8), a savings in CPU time of a factor of two and more can be achieved. Table 3 shows the total CPU time required for individual simulations.

As can be seen in Fig. 14, a different trend of the number of pressure equation linear solver iterations is exhibited by the two approaches, where the enhanced approach uses fewer number of iterations for small number of PISO correctors, however the conventional approach seems to converge to a smaller number of iterations. Nonetheless, the difference in the number of iterations is not significant in both cases. Krylov subspace Conjugate Gradient (CG) linear system solver with Cholesky preconditioner has been used in all simulations for the pressure equation.

Fig. 15 shows the comparison of the L_1 norm residuals of the last PISO corrector in the time–step, for velocity (4) and pressure (7) equations, averaged over all time–steps in the simulation. The residuals are shown with respect to the total number of PISO correctors used in the simulation. The velocity residuals represent the average of the component–wise time–step averaged residuals. For small number of PISO correctors, the residuals are lower for the enhanced approach, while both approaches converge to a similar value of $\approx 5\cdot 10^{-6}$ for pressure and $\approx 3\cdot 10^{-6}$ for velocity. The residuals of the 6–DOF motion equations are not shown here since they are few orders of magnitudes smaller than the fluid flow equations residuals, hence they are not relevant for the comparison.

4.1. Time–step sensitivity study

In order to determine the sensitivity of the results with respect to the number of time–steps per encounter wave period, a temporal resolution refinement study is performed. The sensitivity is investigated by using 25, 50, 100, 200, 400 and 800 time–steps per encounter wave period. Six PISO correctors and the coarse 600,000 cells grid is used in all simulations.

Fig. 16 shows heave, pitch and resistance amplitudes with respect to the number of time–steps per encounter period. All items converge with increasing temporal resolution, while first order amplitudes show smaller sensitivity then the mean values with respect to the temporal resolution. Hence, significant savings in computational time can be achieved by using coarse temporal resolution, while attaining reasonable accuracy. The difference in computational time between 25 and 800 time–steps per encounter period is 32 times. Fig. 17 shows the phases with respect to the number of time–steps per one encounter wave period. The phases are more sensitive to the temporal resolution, indicating that the dispersion error is higher than the dissipation error. Since phases are generally less important, especially in the early design stages, coarse temporal resolution presents an attractive option for quick estimation of seakeeping performance.

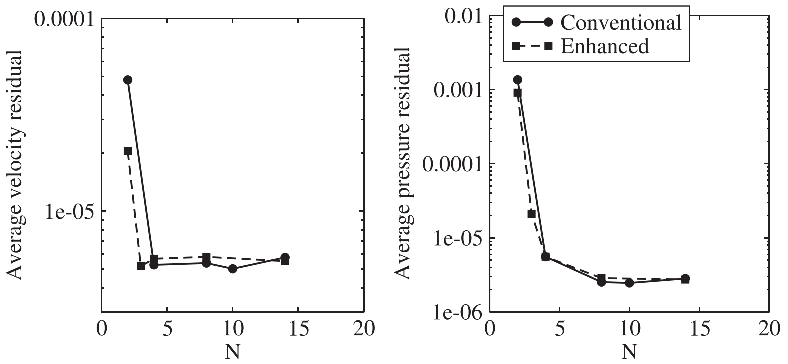

Fig. 15. Comparison of average time–step nonlinear residuals throughout the simulation for varying number of PISO correctors.

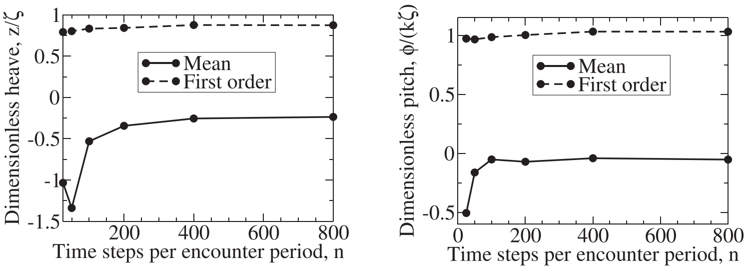

(a) Dimensionless heave amplitudes. (b) Dimensionless pitch amplitudes.

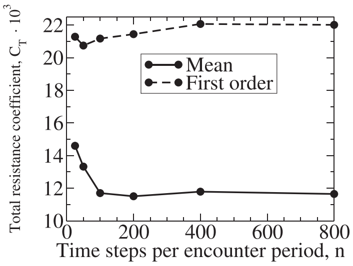

(c) Dimensionless resistance amplitudes.

Fig. 16. Convergence of heave, pitch and resistance amplitudes with increasing number of time steps per encounter period. Heave is normalised with wave amplitude ζ, and pitch with wave stepness $k\zeta$, where k stands for the wave number.

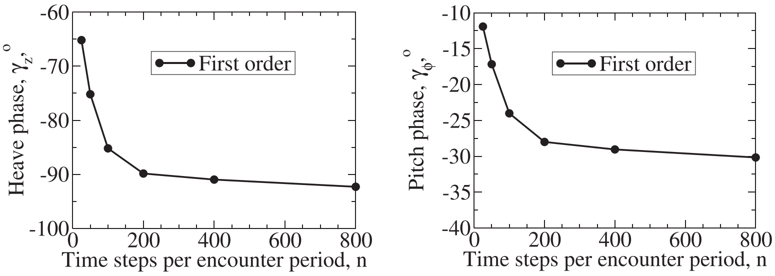

(a) Dimensionless heave phase. (b) Dimensionless pitch phase.

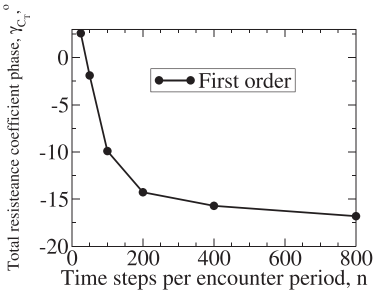

(c) Dimensionless resistance phases.

Fig. 17. Convergence of heave, pitch, and resistance phases with number of time steps per encounter period.

5. Conclusion

An enhanced method for coupling body motion and fluid flow in CFD simulations is presented, verified and validated in this paper. Along with the usual update of 6–DOF body motion equations after the converged pressure–velocity–free surface solution, 6–DOF motion equations are additionally solved after each pressure correction equation in the PISO loop, without moving the grid. The method accelerates the convergence of body motion–fluid flow coupling, reducing the number of PISO correctors per time–step while preserving the accuracy.

The present approach for coupling body motion and fluid flow is verified and validated on a heave decay simulation of a cylinder. The verification showed that the achieved order of accuracy is in accordance with the employed discretisation schemes, verifying the present method. The order of accuracy ranges from 0.89 to 1.93, while the uncertainties are reasonably small. Comparison with experimental and theoretical results of heave motion verified that accurate results are obtained, where the numerical results fall in the range between the experimental and theoretical data for majority of the quantities.

To test the acceleration which can be achieved using the enhanced scheme, simulations of a KCS model in regular head waves are performed using the conventional approach and the enhanced approach with varying number of PISO correctors. Mean, first order and phase shift of resistance, heave and pitch motions are compared.

The analysis of results showed that the proposed enhanced 6–DOF–fluid flow coupling approach takes less PISO correctors to reach convergence, whereas conventional approach demands four to eight PISO correctors to achieve satisfactory accurate solution. With the enhanced approach, two PISO correctors are sufficient to achieve satisfactory results for mean of resistance and first order amplitudes of motion, which are industrially relevant. Also, accurate prediction of phase shifts is obtained. Hence, significant savings of a factor of two and more in terms of CPU time can be achieved using the proposed approach, while retaining accuracy.

For future research, the issue of added mass instability will be addressed to investigate weather the proposed method enhances the stability of simulation in case of numerically unstable cases.

Acknowledgements

This research was sponsored by Bureau Veritas under the administration of Dr. Šime Malenica and Dr. Quentin Derbanne.

References

Bhushan, S., Xing, T., Carrica, P., Stern, F., 2009. Model- and full-scale URANS simulations of athena resistance, powering, seakeeping, and 5415 maneuvering. J. Ship Res. 53, 179–198.

Carrica, P.M., Paik, K.-J., Hosseini, H.S., Stern, F., 2008. URANS analysis of a broaching event in irregular quartering seas. J. Mar. Sci. Technol. 13, 395–407.

Carrica, P.M., Fu, H., Stern, F., 2011. Computations of self-propulsion free to sink and trim and of motions in head waves of the KRISO Container Ship (KCS) model. Appl. Ocean Res. 33, 309–320.

Carrica, P.M., Sadat-Hosseini, H., Stern, F., 2012. CFD analysis of broaching for a model surface combatant with explicit simulation of moving rudders and rotating propellers. Comput. Fluids 53, 117–132.

Castiglione, T., Stern, F., Bova, S., Kandasamy, M., 2011. Numerical investigation of the seakeeping behavior of a catamaran advancing in regular head waves. Ocean Eng. 38, 1806–1822. http://dx.doi.org/10.1016/j.oceaneng.2011.09.003.

Demirdžić, I., Perić, M., 1988. Space conservation law in finite volume calculations of fluid flow. Int. J. Numer. Methods Fluids 8 (9), 1037–1050.

Eça, L., Hoekstra, M., 2014. A procedure for the estimation of the numerical uncertainty of CFD calculations based on grid refinement studies. J. Comput. Phys. 262, 104–130. http://dx.doi.org/10.1016/j.jcp.2014.01.006.

Eça, L., Hoekstra, M., 2008. Code verification of unsteady flow solvers with the method of the manufactured solutions. Int. J. Offshore Polar Eng. 18(2).

Eça, L., Vaz, G., Koop, A., Pereira, F., Abreu, H., 2016. Validation: what, why and how. In: Proceedings of the ASME 35rd International Conference on Ocean, Offshore and Arctic Engineering. Vol. 2.

Fernández, M.A., Gerbeau, J.-F., Grandmont, C., 2005. A Projection Semi-implicit Scheme for the Coupling of an Elastic Structure with an Incompressible Fluid. Research Report RR-5700. INRIA.

Guo, B.J., Steen, S., Deng, G.B., 2012. Seakeeping prediction of KVLCC2 in head waves with RANS. Appl. Ocean Res. 35, 56–67.

Issa, R.I., 1986. Solution of the implicitly discretised fluid flow equations by operator-splitting. J. Comput. Phys. 62, 40–65.

Ito, S., 1977. Study of the Transient Heave Oscillation of a Floating Cylinder (M.S. Thesis). University of Tokyo, Japan.

Jasak, H., 1996. Error Analysis and Estimation for the Finite Volume Method with Applications to Fluid Flows (Ph.D. thesis). Imperial College of Science, Technology & Medicine, London.

Jasak, H., 2009. OpenFOAM: open source CFD in research and industry. Int. J. Nav. Archit. Ocean Eng. 1 (2), 89–94.

Jasak, H., Gosman, A.D., 2001. Residual error estimate for the finite-volume method. Numer. Heat Transf. Part B-Fundam. 39 (1), 1–19.

Jasak, H., Vukčević, V., Gatin, I. Numerical simulation of wave loads on static offshore structures. In: CFD for Wind and Tidal Offshore Turbines, Springer Tracts in Mechanical Engineering. pp. 95–105.

Kim, S., 2011. CFD as a seakeeping tool for ship design. Int. J. Nav. Archit. Ocean Eng. 3, 65–71.

Larsson, L., Stern, F., Visonneau, M., 2013. Numerical Ship Hydrodynamics: An Assessment of the Gothenburg 2010 Workshop. Springer. http://dx.doi.org/10.1007/978-94-007-7189-5.

Larsson, L., Stern, F., Visonneau, M., Hirata, N., Hino, T., Kim, J., 2015a. (Eds.). Tokyo 2015: A Workshop on CFD in Ship Hydrodynamics. Vol. 2, NMRI (National Maritime Research Institute), Tokyo, Japan.

Larsson, L., Stern, F., Visonneau, M., Hirata, N., Hino, T., Kim, J., 2015b (Eds.). Tokyo 2015: A Workshop on CFD in Ship Hydrodynamics, Vol. 3, NMRI (National Maritime Research Institute), Tokyo, Japan.

Maskell, S.J., Ursell, F., 1970. The transient motion of a floating body. J. Fluid Mech. 44 (2), 303–313. http://dx.doi.org/10.1017/S0022112070001842.

Menter, F.R., 1994. Two-equation eddy-viscosity turbulence models for engineering applications. AIAA J. 32 (8), 1598–1605.

Miyata, H., Orihara, H., Sato, Y., 2014. Nonlinear ship waves and computational fluid dynamics. Proc. Jpn. Acad. Ser. B-Phys. Biol. Sci. 90, 278–300. http://dx.doi.org/10.2183/pjab.90.278.

Mousaviraad, S.M., Wang, Z., Stern, F., 2015. URANS studies of hydrodynamic performance and slamming loads on high-speed planning hulls in calm water and waves for deep and shallow conditions. Appl. Ocean Res. 51, 222–240.

National Maritime Reasearch Inistitute (NMRI), 2015. Tokyo 2015: A Workshop on CFD in Ship Hydrodynamics. ⟨http://www.t2015.nmri.go.jp/⟩. (Online; Accessed 20 August 2015).

Orihara, H., Miyata, H., 2003. Evaluation of added resistance in regular incident waves by computational fluid dynamics motion simulation using an overlapping grid system. J. Mar. Sci. Technol. 8, 47–60. http://dx.doi.org/10.1007/s00773-003-0163-5.

Press, W.H., Teukolsky, S.A., Vetterling, W.T., Flannery, B.P., 2002. Numerical Recipes in C++: The Art of Scientific Computing. Cambridge University Press, New York, USA.

Rusche, H., 2002. Computational Fluid Dynamics of Dispersed Two-Phase Flows at High Phase Fractions (Ph.D. thesis). Imperial College of Science, Technology & Medicine, London.

Sadat-Hosseini, H., Wu, P.-C., Carrica, P.M., Kim, H., Toda, Y., Stern, F., 2013. CFD verification and validation of added resistance and motions of KVLCC2 with fixed and free surge in short and long head waves. Ocean Eng. 59, 240–273.

Simonsen, C.D., Otzen, J.F., Joncquez, S., Stern, F., 2013. EFD and CFD for KCS heaving and pitching in regular head waves. J. Mar. Sci. Technol. 18, 435–459. http://dx.doi.org/10.1007/s00773-013-0219-0.

Tezdogan, T., Demirel, Y.K., Kellett, P., Khorasanchi, M., Incecik, A., Turan, O., 2015. Full-scale unsteady RANS CFD simulations of ship behaviour and performance in head seas due to slow steaming. Ocean Eng. 97, 186–206. http://dx.doi.org/10.1016/j.oceaneng.2015.01.011.

Vukčević, V., 2016. Numerical Modelling of Coupled Potential and Viscous Flow for Marine Applications (Ph.D. thesis). Faculty of Mechanical Engineering and Naval Architecture, University of Zagreb, Zagreb, Croatia.

Vukčević, V., Jasak, H., 2015. Seakeeping validation and verification using decomposition model based on embedded free surface method. In: Proceeding of the Tokyo 2015: A Workshop on CFD in Ship Hydrodynamics.

Vukčević, V., Jasak, H., Gatin, I., 2017. Implementation of the Ghost Fluid Method for free surface flows in polyhedral Finite Volume framework. Comput. Fluids 153, 1–19.

Weller, H.G., 2008. A New Approach to VOF-based Interface Capturing Methods for Incompressible and Compressible Flow. Tech. Rep., OpenCFD.

Wu, C.-S., Zhou, D.-C., Gao, L., Miao, Q.-M., 2011. CFD computation of ship motions and added resistance for a high speed trimaran in regular head waves. Int. J. Nav. Archit. Ocean Eng. 3, 105–110. http://dx.doi.org/10.3744/jnaoe.2011.3.1.105.

Statement of author contribution for PAPER 3

Inno Gatin is the main author of paper "Enhanced coupling of solid body motion and fluid flow in finite volume framework", published in Ocean Engineering, 2017;143:295-304.

In this paper the implementation, verification and validation of the method were performed by Gatin. Vukčević and Rusche devised the coupling strategy. The paper was written by Gatin and reviewed by Jasak and Vukčević.

Co–authors:

Vuko Vukčević

Hrvoje Jasak

Henrik Rusche

PAPER 4

J. Marine Sci. Appl. (2017) 16: 375-381
DOI: https://doi.org/10.1007/s11804-017-1436-4

Monolithic Coupling of the Pressure and Rigid Body Motion Equations in Computational Marine Hydrodynamics

Hrvoje Jasak, Inno Gatin*[*] and Vuko Vukčević

Faculty of Mechanical Engineering and Naval Architecture, University of Zagreb, 10000 Zagreb, Croatia

Abstract: In Fluid Structure Interaction (FSI) problems encountered in marine hydrodynamics, the pressure field and the velocity of the rigid body are tightly coupled. This coupling is traditionally resolved in a partitioned manner by solving the rigid body motion equations once per nonlinear correction loop, updating the position of the body and solving the fluid flow equations in the new configuration. The partitioned approach requires a large number of nonlinear iteration loops per time–step. In order to enhance the coupling, a monolithic approach is proposed in Finite Volume (FV) framework, where the pressure equation and the rigid body motion equations are solved in a single linear system. The coupling is resolved by solving the rigid body motion equations once per linear solver iteration of the pressure equation, where updated pressure field is used to calculate new forces acting on the body, and by introducing the updated rigid body boundary velocity in to the pressure equation. In this paper the monolithic coupling is validated on a simple 2D heave decay case. Additionally, the method is compared to the traditional partitioned approach (*i.e.* "strongly coupled" approach) in terms of computational efficiency and accuracy. The comparison is performed on a seakeeping case in regular head waves, and it shows that the monolithic approach achieves similar accuracy with fewer nonlinear correctors per time–step. Hence, significant savings in computational time can be achieved while retaining the same level of accuracy.

Keywords: monolithic coupling, pressure equation, rigid body motion, computational fluid dynamics, marine hydrodynamics, seakeeping

Article ID: 1671-9433(2017)04-0375-07

1 Introduction

In computational marine hydrodynamics, the problems including Fluid Structure Interaction (FSI) involving floating bodies are often encountered. Furthermore, elasticity of the body can be neglected in most applications, modelling only six degrees of freedom for the rigid body motion. In majority of cases, the problem includes a body at the free surface, forced into motion by wave forces or initial non–equilibrium of mass and displaced volume. In either case, the oscillatory motion of the floating body is primarily a result of interplay of pressure forces acting on the body, and the gravitational force. Since the fluid is incompressible, the pressure field is sensitive to the change in the body velocity. For this reason, this paper focuses on the coupling of the pressure equation and rigid body motion equations. The coupling is performed monolithically, where the pressure equation and rigid body motion equations are solved simultaneously. The development is performed in Naval Hydro software pack based on foam–extend open–source software.

Monolithic solution strategy is well documented in the literature for FSI involving deformable bodies, where the fluid and the structure are modelled within the same spatial discretisation framework (Hachem *et al.*, 2013; Legay *et al.*, 2011), or on separate grids (Farah *et al.*, 2016; Hu *et al.*, 2016). Finite Element Method is mostly used to discretise the structure and fluid flow equations (Bna *et al.*, 2013; Farah *et al.*, 2016; Hachem *et al.*, 2013; Heil *et al.*, 2008; Jog and Pal, 2011; Langer and Yang, 2016; Legay *et al.*, 2011; Yang *et al.*, 2016), while FV is used in some publications (Eken and Sahin, 2016; Hu *et al.*, 2016). Some authors state that the monolithic FSI model with a discretised structure can calculate rigid body dynamics as a special case. Hachem *et al.* (2013) state that the rigid body can be modelled by imposing special conditions to the Navier–Stokes equations for the stencils inside the structure. Legay *et al.* (2011) and Robinson-Mosher *et al.* (2011) show that rigid body can be simulated within the presented model by substituting the structural system of equations with the rigid body motion equations.

The publications mentioned above discretise the structure in order to provide a general framework for deforming bodies. In case of rigid bodies, the discretisation of the body volume would present an unnecessary overhead. Integrating the rigid body motion equations only requires information of mass, angular inertia of the body, and relative position of the centre of gravity, which are constant.

The novelty of this work is in the monolithic approach to the pressure–rigid body motion coupling within the FV framework where the body is represented as a boundary of the fluid domain, while the volume inside the body is not discretised. The approach offers a more resolved solution of the coupling comparing to the widely used partitioned approach (Orihara and Miyata, 2003; Castiglione *et al.*, 2011;

Received date: 10-Jan-2017
Accepted date: 28-Jul-2017
[*]**Corresponding author Email:** inno.gatin@fsb.hr

Wu *et al.*, 2011; Simonsen *et al.*, 2013; Vukčević and Jasak, 2015a; Simonsen *et al.*, 2013; Tezdogan *et al.*, 2015; Miyata *et al.*, 2014), enabling a reduction of the number of nonlinear iterations per time–step. In the present approach, the pressure field and the solid body motion equations are coupled at the level of linear solver step of the pressure equation. After each linear solver iteration, the updated pressure field is used to calculate forces acting on the rigid body, which are in turn used to repeatedly integrate the solid body motion equations. The updated velocity of the solid body is then injected in the right hand side of the pressure equation as the change of volumetric flux at the body boundary.

The paper is organized as follows. First, the numerical model is presented, comprising the discretisation of the coupling of the pressure equation and the rigid body motion equations, followed by details regarding the linear solver and the Aitkens relaxation method. Next, validation of the present approach is performed on a 2D heave decay test case by comparing with the well established partitioned approach. In the fourth section the two methods are compared on a seakeeping case in regular head waves. Finally, an overview of results and conclusion are given.

2 Numerical model

In this section the mathematical and numerical formulation of the monolithic coupling of the pressure equation and rigid body motion equation is described.

The momentum equation or incompressible, two phase flow states (Vukčević *et al.*, 2016a):

$$\frac{\partial \boldsymbol{u}}{\partial t} + \nabla .((\boldsymbol{u} - \boldsymbol{u}_M)\,\boldsymbol{u}) - \nabla .(\nu_e \nabla \boldsymbol{u}) = -\frac{1}{\rho}\nabla p_d \tag{1}$$

where $\boldsymbol{u}$ stands for the velocity field, while $\boldsymbol{u}_M$ is the relative grid motion velocity accounting for the Space Conservation Law (Demirdžić and Perić, 1988). ν_e stands for the effective kinematic viscosity, ρ is the density, while p_d stands for the dynamic pressure: $p_d = p - \rho \boldsymbol{g}.\boldsymbol{x}$, where $\boldsymbol{g}$ denotes the gravitational constant, while $\boldsymbol{x}$ represents the radii vector.

The pressure equation is derived from the mass conservation law, which can be written in the following form for incompressible flow:

$$\nabla .\boldsymbol{u} = 0 \tag{2}$$

The change of the boundary velocity $\delta \boldsymbol{u}_b$ of the rigid body can be accounted for explicitly in the continuity equation as:

$$\nabla .\boldsymbol{u} + \nabla .(\delta \boldsymbol{u}_b) = 0 \tag{3}$$

The discretisation of Eq. (2) in the integral FV framework will be omitted for brevity, the reader is directed to Jasak (1996) for details. The discretisation of Eq. (2) yields the pressure equation, which can be written in the form:

$$\sum_f \boldsymbol{s}_f . \left(\frac{1}{a_P}\right)_f \left(\frac{\nabla p_d}{\rho}\right)_f = \sum_f \boldsymbol{s}_f . \frac{(\boldsymbol{H}(\boldsymbol{u}_N))_f}{(a_P)_f} \tag{4}$$

where f denotes the face index, $\boldsymbol{s}_f$ stands for the surface area vector: $\boldsymbol{s}_f = s_f\,\boldsymbol{n}$, where s_f stands for the area of the face, while $\boldsymbol{n}$ denotes the face unit normal vector. a_P is the diagonal coefficient from the discretised momentum equation, Eq. (1) (Jasak, 1996). $\boldsymbol{H}$ is a linear operator stemming from the discretisation of the momentum equation, which is a function of explicit neighbouring cell velocities $\boldsymbol{u}_N$. The discretisation of the divergence of change of the boundary velocity in integral form states:

$$\int_V \nabla .(\delta \boldsymbol{u}_b)\mathrm{d}V = \oint_S \boldsymbol{n}.\delta \boldsymbol{u}_b \mathrm{d}S = \sum_f \boldsymbol{s}_f .\delta \boldsymbol{u}_{bf} \tag{5}$$

where the Gauss's theorem is employed to transform the volume integral into a surface integral. The final discretised form of the pressure equation monolithically coupled with the rigid body motion states:

$$\begin{aligned} &\sum_f \boldsymbol{s}_f . \left(\frac{1}{a_P}\right)_f \left(\frac{\nabla p_d}{\rho}\right)_f = \\ &\sum_f \boldsymbol{s}_f . \frac{(\boldsymbol{H}(\boldsymbol{u}_N))_f}{(a_P)_f} - \sum_f \boldsymbol{s}_f .\delta \boldsymbol{u}_{bf} \end{aligned} \tag{6}$$

The last term on the right hand side of Eq. (6) provides the coupling between the pressure equation and the rigid body motion. Note that mathematically, u_{bf} presents a velocity field defined at face centres, with non–zero values only where only for faces at the rigid body boundary.

To obtain the change of velocity $\delta \boldsymbol{u}_b$, rigid body motion equations are integrated:

$$\begin{aligned} \frac{\partial \boldsymbol{v}}{\partial t} &= \boldsymbol{F}/m \\ \frac{\partial \boldsymbol{\omega}}{\partial t} &= \boldsymbol{I}^{-1} . (\boldsymbol{M} - \boldsymbol{\omega} \times (\boldsymbol{I}.\boldsymbol{\omega})) \end{aligned} \tag{7}$$

where $\boldsymbol{v}$ denotes the translational velocity of the centre of mass, $\boldsymbol{F}$ is the total exerted force on the body, while m stands for the mass of the body. $\boldsymbol{\omega}$ is the rotational velocity, $\boldsymbol{I}$ is the tensor of inertia, while $\boldsymbol{M}$ stands for the external moment acting on the body. The force and moment acting on the body are calculated as the sum of pressure and viscous forces:

$$\begin{aligned} \boldsymbol{F} &= \sum_{bf} \boldsymbol{s}_{bf} p_{bf} + \boldsymbol{F}_v \\ \boldsymbol{M} &= \sum_{bf} \boldsymbol{r}_{bf} \times \boldsymbol{s}_{bf} p_{bf} + \boldsymbol{M}_v \end{aligned} \tag{8}$$

where the summation is carried out on boundary faces denoted with index bf, while $\boldsymbol{F}_v$ and $\boldsymbol{M}_v$ denote the viscous portion of the force and moment, respectively. The pressure at the boundary face p_{bf} is calculated from the dynamic pressure as: $p_{bf} = p_{d,bf} + \rho \boldsymbol{g}.\boldsymbol{x}_{bf}$. Hence, it represents the cross coupling term with the pressure equation, Eq. (6). The change of the boundary velocity $\delta \boldsymbol{u}_{bf}$ is finally calculated as the change of the translational and rotational velocity of the boundary face bf in the two adjacent linear solver iterations:

$$\delta \boldsymbol{u}_{bf}^n = \boldsymbol{v}^n - \boldsymbol{v}^{n-1} + (\boldsymbol{\omega}^n - \boldsymbol{\omega}^{n-1}) \times \boldsymbol{x}_{bf} \tag{9}$$

where n denotes the linear solver iteration, while $\boldsymbol{x}_{bf}$ denotes the radii vector of the boundary face.

Eq. (6) to Eq. (9) present a closed system regarding the pressure–rigid body motion coupling. At linear solver iteration level the following algorithm is employed to conduct the coupling:

1) Initialize $\delta \boldsymbol{u}_{bf}$ to zero,
2) Perform one iteration of the linear solver for the dynamic pressure equation, Eq. (6),
3) Update the dynamic pressure p_d,
4) Calculate the new forces and moments, Eq. (8), while keeping the viscous portion of the force constant,
5) Integrate the rigid body motion equations, Eq. (7),
6) Calculate the change of the boundary velocity, Eq. (9).
7) Go to next linear solver iteration,
8) Repeat 2) to 7) until convergence.

A flow chart of the nonlinear corrector used in this work is shown on Fig. 1. Note that multiple pressure corrections are performed in one nonlinear corrector.

In the two phase flow solver, Ghost Fluid Method is used (Vukčević, 2016) to impose the free surface boundary conditions in the FV framework, while Spectral Wave Explicit Navier Stokes Equations (SWENSE) (Vukčević *et al.*, 2016a) is used to imposed the wave field in the CFD domain.

2.1 Linear solver and rigid body motion integration

In this work the discretised pressure equation is solved using a preconditioned Conjugate Gradient (Saad, 2003) method for sparse linear systems. Cholesky factorisation is used as a preconditioner.

Integration of rigid body motion equations is performed using Fifth-order Cash-Karp embedded Runge-Kutta scheme with error control and adjustive time-step size (Press *et al.*, 2002).

2.2 Aitkens relaxation

In order to stabilise the calculation of the rigid body motion, Aitken's adaptive relaxation (Irons and Tuck, 1969) is employed. Since the solution of the pressure can vary dramatically in the first several iterations of the linear solver, the coupling with the rigid body motion equations can be unstable. In order to circumvent the instability, a dynamic relaxation is needed to exert heavy relaxation at the beginning of the linear solution process, and gradually increase the relaxation factor as the pressure solution starts to converge.

Using Aitken's algorithm, the acceleration of translational and rotational motion is relaxed. Here, the algorithm will be presented only for translational acceleration $\boldsymbol{a}$ for brevity. Acceleration $\boldsymbol{a}_k$ of the kth iteration is obtained using the relaxation factor ω_k:

$$\boldsymbol{a}_k = (1-\omega_k)\,\widetilde{\boldsymbol{a}}_k + \omega_k \boldsymbol{a}_{k-1} \tag{10}$$

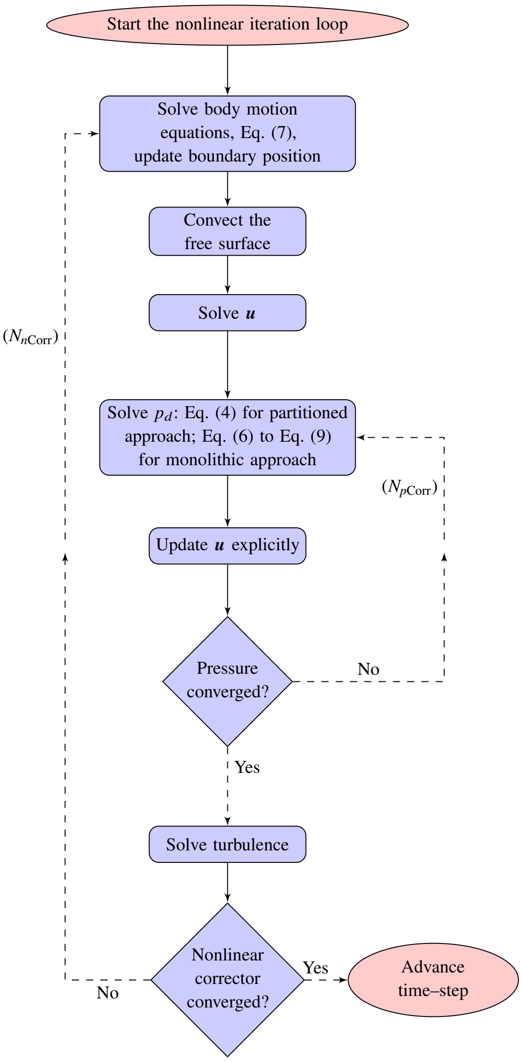

Fig. 1 Flow chart of the nonlinear corrector

where tilde denotes the calculated value. The relaxation factor is calculated based on the information from the previous iterations:

$$\omega_k = \omega_{k-1} + (\omega_{k-1}-1)\,\frac{(\Delta\boldsymbol{a}_{k-1}-\Delta\boldsymbol{a}_k)\,.\Delta\boldsymbol{a}_k}{(\Delta\boldsymbol{a}_{k-1}-\Delta\boldsymbol{a}_k)^2} \tag{11}$$

where $\Delta\boldsymbol{a}_k = \boldsymbol{a}_{k-1} - \boldsymbol{a}_k$, while $\Delta\boldsymbol{a}_{k-1} = \boldsymbol{a}_{k-2} - \boldsymbol{a}_{k-1}$.

3 Heaving barge test case

In this section the novel monolithic coupling of the pressure equation and rigid body motion is validated on 2D heave decay case of a barge. The results are compared with the partitioned approach, where the rigid body motion equations are updated once per nonlinear correction loop.

The 2D floating barge is set above the hydrostatic equilibrium position by 0.01 m at time zero to produce a heave decay motion. The mass of the barge is 0.32 kg, with height of 0.12 m, width of 0.2 m, and draught of 0.08 m. 32 160 cells are used for both the monolithic and

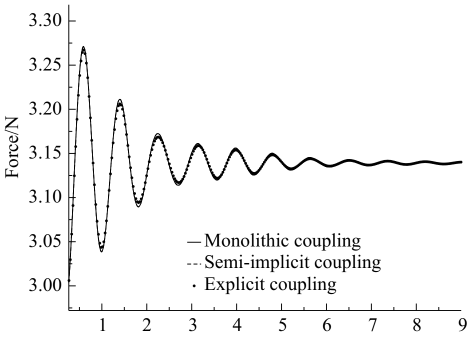

(a) Force

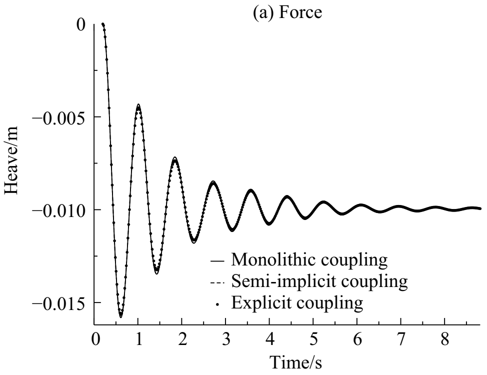

(b) Heave

Fig. 2 Comparison of the force signal and heave motion for the 2D heave decay case

partitioned simulation, while a fixed time step of 0.001 42 s is set corresponding to ≈ 400 time–steps per natural period of oscillation. The number of time–steps per period of oscillation is selected based on the authors experience, which can be found in Vukčević *et al.* (2016). The same number of nonlinear correctors is used per time–step, as well as the number of pressure corrections per nonlinear loop in every simulation. Eight nonlinear correctors per time–step and four pressure correctors per each nonlinear loop are used. The domain is 2 meters wide, 0.5 meters deep beneath the free surface and 0.5 meters high above the free surface. The computational grid is rigidly moving together with the moving body. Fixed zero value boundary condition for velocity is prescribed on the side boundaries and bottom, while a mixed fixed value and zero gradient boundary condition is placed at the top boundary. For pressure, zero gradient is placed on sides and bottom, while fixed value is set on the top boundary. For the VOF field, zero gradient boundary condition is placed on all boundaries.

For discretisation of the temporal term in the momentum equation backward second order scheme is used, while implicit upwind scheme with deferred second order correction is used for the convection term. The diffusion term in momentum equation, and the pressure equation are discretised using second order accurate scheme with explicit non–orthogonal correction. Same discretisation is used in all calculations performed for this study.

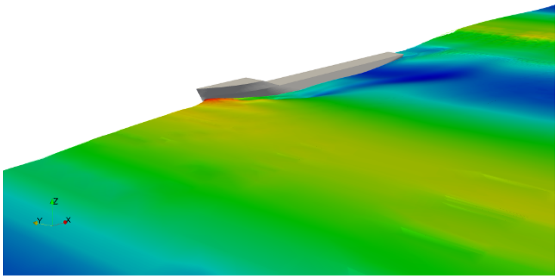

Fig. 3 Perspective view of the seakeeping simulation

The results are shown in Fig. 2, where the time signal of vertical force acting on the barge and heave motion are shown for the two simulations. Results of the monolithic coupling approach show good agreement with the partitioned approach, which validates the novel monolithic approach since the partitioned approach has been validated (Vukčević and Jasak, 2015a; Vukčević and Jasak, 2015b; Vukčević *et al.*, 2016b).

4 Seakeeping test case

A comparison of seakeeping simulation results is shown in this section for partitioned and novel monolithic approach. The convergence of the results with respect to the number of nonlinear correctors per time–step and the number of pressure correctors per each nonlinear corrector is compared, as well as computational demands.

Seakeeping simulation for the KRISO Container Ship (KCS) model in regular head waves is simulated (Fig. 3), where the simulation set–up corresponds to the C5 case from the Tokyo Workshop on CFD in Ship Hydrodynamics (Larsson *et al.*, 2015). Simulations are performed in model scale for Froude number $Fr = 0.261$, with length $L_{PP} = 6.05\,\mathrm{m}$, breadth $B = 0.85\,\mathrm{m}$ and drought $T = 0.285\,\mathrm{m}$. Regular incident wave is imposed with wave length $\lambda = 11.84\,\mathrm{m}$ and wave height $H = 0.196\,\mathrm{m}$. Relatively coarse grid is used with 600 000 cells to discretise half of the domain. Implicit relaxation zones Jasak *et al.*, (2015) are used to initialize the waves at the inlet boundary, and to damp the waves at the outlet. The inlet boundary is at a distance of $1L_{PP}$ in front of the bow, while the outlet is $2L_{PP}$ from the aft perpendicular. Side boundary is placed at $1.5L_{PP}$ from the centre line of the ship, while the depth of the domain is set to $1.5L_{PP}$ and height above the free surface to $1L_{PP}$. The ship is free to heave and pitch, while the surge velocity is set to a constant value. Eight simulations are performed altogether, where the number of nonlinear correctors per time–step and number of pressure correctors per nonlinear corrector in individual simulation are shown in the test matrix, Table 1.

Table 1 The test matrix showing the number of nonlinear correctors, $N_{n\mathrm{Corr}}$ per time–step and the number of pressure correctors, $N_{p\mathrm{Corr}}$ per each nonlinear corrector for each simulation

Simulation No.	$N_{n\mathrm{Corr}}$	$N_{p\mathrm{Corr}}$
1	2	2
2	2	4
3	2	8
4	4	4
5	6	4
6	8	4
7	10	4
8	14	4

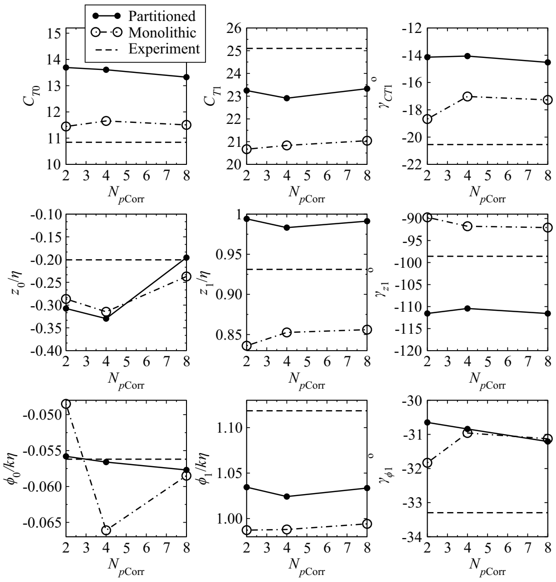

Fig. 4 Comparison of seakeeping results of partitioned and monolithic approach for coupling body motion and pressure equation, with respect to the number of pressure corrections $N_{p\mathrm{Corr}}$

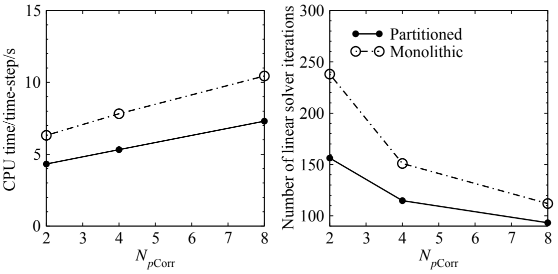

Fig. 5 Comparison of required computational time per time–step and the average number of pressure equation iterations with respect to the number of pressure corrections $N_{p\mathrm{Corr}}$

Fig. 4 shows the comparison of results of the two different coupling strategies with respect to the number of pressure corrections per nonlinear corrector, $N_{p\mathrm{Corr}}$ (see Fig. 1). The results correspond to simulations 1, 2 and 3 from Table 1. Hereafter, C_T stands for total resistance coefficient, z is heave, ϕ is pitch. η stands for wave amplitude, while k stands for the wave number. Mean values of harmonic oscillations in time are indicated with index 0, and first order amplitudes with 1. γ is the phase shift of the item indicated in the index. The first row of graphs shows, from left to right, the mean, first order amplitude and first order phase shift of the resistance coefficient. The second row shows the dimensionless heave motion, while the third shows the dimensionless pitch motion. Experimental data from Tokyo Workshop on CFD in Ship Hydrodynamics (Larsson *et al.*, 2015) is also included for reference, however the reader is referred to Vukčević and Jasak (2015a) and Vukčević and Jasak (2015b) for detailed validation of seakeeping with finer grids. The partitioned approach differs significantly from the monolithic approach for most items. The cause is that two nonlinear correctors per time–step are not sufficient for the partitioned approach to produce accurate results. This is further demonstrated on Fig. 6, where the partitioned approach exhibits a large variation in results obtained using 2, 4, 6, 8, 10 and 14 nonlinear correctors per time–step. The partitioned approach does not update the rigid body motion equations inside the pressure loop, *i.e.* the number of rigid body motion updates per time–step does not depend on $N_{p\mathrm{Corr}}$. Hence, the variation of results with changing number of $N_{p\mathrm{Corr}}$ is due to the unresolved fluid flow solution. For most items the results obtained using the partitioned approach show very little dependence on $N_{p\mathrm{Corr}}$, except for the mean value of heave, z_0. Hence, it can be concluded that the mean value of heave is sensitive to the accuracy of the pressure field solution. The monolithic approach shows dependence on $N_{p\mathrm{Corr}}$ for more items (γ_{CT1}, ϕ_0, $\gamma_{\phi1}$), since increasing the number of pressure corrections improves the coupling between the pressure force and rigid body motion. On Fig. 5 the average computational time per time–step is compared for the two approaches with respect to the number of pressure correctors per nonlinear corrector, as well as the average number of pressure equation linear solver iterations. As expected, the monolithic approach takes more computational time per time–step than partitioned approach, which is caused by solving the rigid body motion equations once per pressure linear solver iteration. Also, higher number of linear solver iterations is required, which can be prescribed to the fact that the source of the system of equations is changing throughout the solution process.

Fig. 6 shows the comparison of results for the two approaches with respect to the number of nonlinear correctors per time–step. The results correspond to simulations with indices 2 and 4 to 8 from Table 1. Again, experimental data is included for reference. Most items exhibit differences within 10%, while some exhibit higher differences. It should

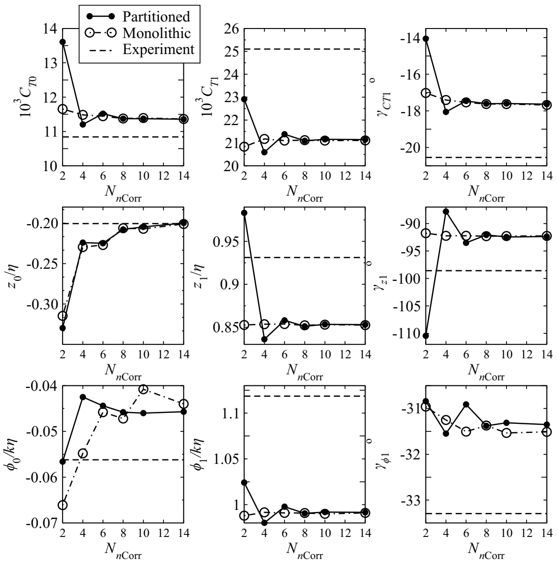

Fig. 6 Comparison of seakeeping results of partitioned and monolithic approach for coupling body motion and pressure equation, with respect to the number of nonlinear correctors per time–step $N_{n\mathrm{Corr}}$

be noted here that the focus of this paper is not on validation of seakeeping, rather on proving the benefits of the monolithic coupling. Hence, coarse spatial resolution is used since authors believe it is sufficient to show the advantages of the proposed approach. For detailed validation of the same test case the reader is referred to Vukčević and Jasak 2015a. For the partitioned approach the solution generally converges with 8 or more PISO correctors. For most items, the monolithic approach exhibits convergence with smaller number of correctors, and significantly smaller deviations between the solutions using 2, 4 and 6 correctors. For most items the monolithic approach achieves solution that is closed to the converged value with only 2 correctors. Hence, the monolithic approach shows smaller sensitivity to the number of nonlinear correctors per time–step. The most important items from the practical point of view (C_{T0}, z_1 and ϕ_1) are virtually insensitive to the number of nonlinear correctors. Hence, savings in computational time can be achieved while retaining the same level of accuracy for this items by using fewer nonlinear correctors per time–step. The items that showed larger sensitivity to the number of nonlinear correctors are the mean of heave z_0, mean of pitch ϕ_0 and phase shift of pitch $\gamma_{\phi 1}$. The variation of mean of heave with the varying number of nonlinear correctors is similar for partitioned and monolithic approach. It is likely that the accuracy of fluid flow solution influences the result more than the accuracy of the pressure–rigid body motion coupling, which is indicated in Fig. 4. Mean of pitch, ϕ_0, has a very small absolute value, hence the absolute differences between the partitioned and monolithic approach are not large. Again, Fig. 7 shows that it takes more computational time

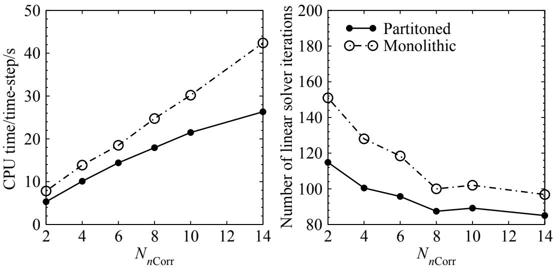

Fig. 7 Comparison of required computational time per time–step and the average number of pressure equation iterations with respect to the number of nonlinear correctors per time–step $N_{n\mathrm{Corr}}$

per time–step and more iterations of the pressure equation linear solver for the monolithic approach comparing to the partitioned approach.

Despite the fact that the monolithic approach requires more computational time per nonlinear corrector, significant savings can be achieved by using two instead of eight nonlinear correctors per time–step. According to Fig. 7, a reduction in overall computational time by a factor of 2.4 can be achieved in this manner.

5 Conclusions

Monolithic coupling of pressure equation and rigid body motion equations is shown in this paper for application in the field of computational marine hydrodynamics. The novel approach is first validated, and compared against the traditional partitioned approach in order to establish the validity and benefits of the method.

The validation is performed on a 2D heave decay simulation of a barge. The monolithic coupling approach is compared against the partitioned approach, showing very good agreement.

The performance of the two coupling methods is tested on a seakeeping case in regular head waves, where sensitivity to the number of pressure correctors per nonlinear corrector, as well as the number of nonlinear correctors per time step is investigated. Accuracy and computational time is compared for the two methods: monolithic coupling showed smaller sensitivity to the number of nonlinear correctors per time step, and it is shown that accurate results can be obtained with only two nonlinear correctors per time step. It is observed that the monolithic approach is computationally more expensive then the partitioned approach per nonlinear corrector, however it enables fewer nonlinear correctors to be used per time–step, offering a significant speed–up (by a factor of 2.4 for the given test case).

The developed monolithic coupling of pressure equation and rigid body motion is insensitive to the number of nonlinear correctors per time–step due to the better resolved coupling between the pressure equation and rigid body motion equations. The method offers significant savings in computational time and is applicable in a wide range of problems in the field of marine hydrodynamics.

Acknowledgements

This research was sponsored by Bureau Veritas under the administration of Dr. Šime Malenica.

References

Bna S, Manservisi S, Aulisa E, 2013. A multilevel domain decomposition solver for monolithic fluid-structure interaction problems. *11th International Conference of Numerical Analysis and Applied Mathematics 2013*, Pts 1 and 2, Vol. 1558. Rhodes, 871-874.
DOI: 10.1063/1.4825635

Castiglione T, Stern F, Bova S, Kandasamy M, 2011. Numerical investigation of the seakeeping behavior of a catamaran advancing in regular head waves. *Ocean Engineering*, **38**, 1806-1822.
DOI: 10.1016/j.oceaneng.2011.09.003

Demirdžić I, Perić M, 1988. Space conservation law in finite volume calculations of fluid flow. *International Journal for Numerical Methods in Fluids*, **8**(9), 1037-1050.

Eken A, Sahin M, 2016. A parallel monolithic algorithm for the numerical simulation of large-scale fluid structure interaction problems. *International Journal for Numerical Methods in Fluids*, **80**(12), 687-714.
DOI: 10.1002/fld.4169

Farah P, Vuong AT, Wall WA, Popp A, 2016. Volumetric coupling approaches for multiphysics simulations on non-matching meshes. *International Journal for Numerical Methods in Engineering*, **108**(12), 1550-1576.
DOI: 10.1002/nme.5285

Hachem E, Feghali S, Codina R, Coupez T, 2013. Immersed stress method for fluidstructure interaction using anisotropic mesh adaptation. *International Journal for Numerical Methods in Engineering*, **94**(9), 805-825.
DOI: 10.1002/nme.4481

Heil M, Hazel AL, Boyle J, 2008. Solvers for large-displacement fluid-structure interaction problems: segregated versus monolithic approaches. *Computational Mechanics*, **43**(1), 91-101.
DOI: 10.1007/s00466-008-0270-6

Hu Z, Tang WY, Xue HX, Zhang XY, 2016. A simple-based monolithic implicit method for strong-coupled fluid-structure interaction problems with free surfaces. *Computer Methods in Applied Mechanics and Engineering*, **299**, 90-115.
DOI: 10.1016/j.cma.2015.09.011

Irons BM, Tuck RC, 1969. A version of the Aitken accelerator for computer iteration. *International Journal for Numerical Methods in Engineering*, **1**, 275-277.
DOI: 10.1002/nme.1620010306

Jasak H, 1996. *Error analysis and estimation for the finite volume method with applications to fluid flows*. PhD thesis, Imperial College of Science, Technology & Medicine, London.

Jasak H, Vukčević V, Gatin I, 2015. Numerical simulation of wave loads on static offshore structures. *CFD for Wind and Tidal Offshore Turbines*, 95-105.

Jog CS, Pal RK, 2011. A monolithic strategy for fluid-structure interaction problems. *International Journal for Numerical Methods in Engineering*, **85**(4), 429-460.
DOI: 10.1002/nme.2976

Langer U, Yang HD, 2016. Robust and efficient monolithic fluid-structure-interaction solvers. *International Journal for Numerical Methods in Engineering*, **108**(4), 303-325.
DOI: 10.1002/nme.5214

Larsson L, Stern F, Visonneau M, Hirata N, Hino T, Kim J, 2015. *Tokyo 2015: A Workshop on CFD in Ship Hydrodynamics*. Vol. 3, NMRI (National Maritime Research Institute), Tokyo, Japan.

Legay A, Zilian A, Janssen C, 2011. A rheological interface model and its space-time finite element formulation for fluid-structure interaction. *International Journal for Numerical Methods in Engineering*, **86**(6), 667-687.
DOI: 10.1002/nme.3060

Miyata H, Orihara H, Sato Y, 2014. Nonlinear ship waves and computational fluid dynamics. *Proceedings of the Japan Academy Series B—Physical and Biological Sciences*, **90**, 278-300.
DOI: 10.2183/pjab.90.278

Orihara H, Miyata H, 2003. Evaluation of added resistance in regular incident waves by computational fluid dynamics motion simulation using an overlapping grid system. *Journal of Marine Science and Technology*, **8**, 47-60.
DOI: 10.1007/s00773-003-0163-5

Press WH, Teukolsky SA, Vetterling WT, Flannery BP, 2002. *Numerical Recipes in C++: The Art of Scientific Computing*. Cambridge University Press, Cambridge.

Robinson-Mosher A, Schroeder C, Fedkiw R, 2011. A symmetric positive definite formulation for monolithic fluid structure interaction. *Journal of Computational Physics*, **230**(4), 1547-1566.
DOI: 10.1016/j.jcp.2010.11.021

Saad Y, 2003. *Iterative methods for sparse linear systems*. 2nd edition, Society for Industrial and Applied Mathematics Philadelphia.

Simonsen CD, Otzen JF, Joncquez S, Stern F, 2013. EFD and CFD for KCS heaving and pitching in regular head waves. *Journal of Marine Science and Technology*, **18**, 435-459.
DOI: 10.1007/s00773-013-0219-0

Tezdogan T, Demirel YK, Kellett P, Khorasanchi M, Incecik A, Turan O, 2015. Full-scale unsteady RANS CFD simulations of ship behaviour and performance in head seas due to slow steaming. *Ocean Engineering*, **97**, 186-206.
DOI: 10.1016/j.oceaneng.2015.01.011

Vukčević V, 2016. *Numerical modelling of coupled potential and viscous flow for marine applications*. PhD thesis, Faculty of Mechanical Engineering and Naval Architecture, University of Zagreb.

Vukčević V, Jasak H, 2015a. Seakeeping validation and verification using decomposition model based on embedded free surface method. *Tokyo 2015: A Workshop on CFD in Ship Hydrodynamics*.

Vukčević V, Jasak H, 2015b. Validation and verification of decomposition model based on embedded free surface method for oblique wave seakeeping simulations. *Tokyo 2015: A Workshop on CFD in Ship Hydrodynamics*.

Vukčević V, Jasak H, Gatin I, Malenica S, 2016. Seakeeping sensitivity studies using the decomposition CFD model based on the ghost fluid method. *Proceedings of the 31st Symposium on Naval Hydrodynamics*, Monterey.

Vukčević V, Jasak H, Malenica S, 2016a. Decomposition model for naval hydrodynamic applications, Part I: Computational method. *Ocean Eng.*, **121**, 37-46.
DOI: 10.1016/j.oceaneng.2016.05.022

Vukčević V, Jasak H, Malenica S, 2016b. Decomposition model for naval hydrodynamic applications, Part II: Verification and validation. *Ocean Eng.*, **121**, 76-88.
DOI: 10.1016/j.oceaneng.2016.05.021

Wu CS, Zhou DC, Gao L, Miao QM, 2011. CFD computation of ship motions and added resistance for a high speed trimaran in regular head waves. *International Journal of Naval Architecture and Ocean Engineering*, **3**, 105-110.
DOI: 10.3744/jnaoe.2011.3.1.105

Yang P, Xiang J, Fang F, Pavlidis D, Latham JP, Pain CC, 2016. Modelling of fluid-structure interaction with multiphase viscous flows using an immersed-body method. *Journal of Computational Physics*, **321**, 571-592.
DOI: 10.1016/j.jcp.2016.05.035

PAPER 5

Ocean Engineering 148 (2018) 500–515

Contents lists available at ScienceDirect

Ocean Engineering

journal homepage: www.elsevier.com/locate/oceaneng

CFD verification and validation of green sea loads

Inno Gatin[a], Vuko Vukčević[a], Hrvoje Jasak[a,b,*], Jeonghwa Seo[c], Shin Hyung Rhee[c]

[a] University of Zagreb, Faculty of Mechanical Engineering and Naval Architecture, Ivana Lučića 5, Zagreb, Croatia
[b] Wikki Ltd, 459 Southbank House, SE1 7SJ, London, United Kingdom
[c] Research Institute of Marine Systems Engineering, Seoul National University, Gwanak-ro 1, Gwanak-gu, Seoul, 08826, South Korea

ARTICLE INFO

Keywords:
Green sea loads
Regular waves
CFD
Naval Hydro pack
VOF

ABSTRACT

An extensive verification and validation for green sea load simulations is presented. The calculations are performed using the Naval Hydro pack, a library based on foam–extend, which is an open source Computational Fluid Dynamics software. The geometric Volume of Fluid method is used for interface advection, while the Ghost Fluid Method is employed to discretise the free surface boundary conditions at the interface. Pressure measured at the deck of a fixed structure is compared to experimental data for nine regular waves. Verification is performed using four refinement levels in order to reliably assess numerical uncertainties. A detailed uncertainty analysis comprises both numerical and experimental data. Comparable uncertainties are exhibited in simulations and experiments, with good agreement of results.

1. Introduction

In the field of offshore and marine engineering, wave loading poses a wide range of different challenges which are important in the design process. One of the more difficult wave–related problems to describe and reliably estimate is the green sea load. Green sea, or water on deck, is a consequence of a highly nonlinear interaction between the floating structure and the free surface waves, which comprise incident, diffracted and radiated waves. The complex origin of the phenomenon renders the prediction of green sea occurrence challenging. Apart from that, violent two phase flow develops once the water is on the deck, which is difficult to predict via simplified flow theories. Green sea effect cause both local and global structural loads which can endanger the structural integrity, and therefore must be taken into account in the design process.

Given the complexity of the problem, experimental and numerical means are currently utilised to calculate green sea loads. According to Tamarel et al. (Temarel et al., 2016), both experimental and numerical methods available today are not mature to reliably assess green sea loads. Hence, further research is needed to establish confidence in both fields. As a result, a wide variety of methods have been developed and applied in recent years. Greco et al. (2012) used the numerical solver developed by Greco and Lugni (2012) to calculate wave loads on a patrol ship, including green sea loads with comparison to experiments. Lu et al. (2012) developed a time domain numerical method based on Finite Volume (FV) method used for green sea load simulations. Xu (2013) used Smoothed Particle Hydrodynamics to simulate breaking waves plunging onto a deck. Zhao et al. (2014) studied the influence of structure motion on the pressure loads due to green sea effects using a FV based method. Kim et al. (2013) used a linear method for assessing the ship motion, and a nonlinear viscous method to calculate green sea loads on a container vessel. Ruggeri et al. (2013) used WAMIT software based on the potential flow model and a viscous FV code StarCCM+ to devise guidelines for green sea load calculations. Joga et al. (2014) compared two viscous FV codes with experimental results of water ingress into open ship holds during green sea events. Pakozdi et al. (2014) coupled a potential flow based method and a viscous model to conduct simulations of green sea events. Zhu et al. (2009) conducted numerical simulations of green sea events for a Floating Production, Storage and Offloading (FPSO) vessel.

In this work, a detailed validation study of green sea loads on a static structure is conducted. Experimental results published by Lee et al. (2012) are used for the comparison. Nine regular wave cases are investigated, including the uncertainty analysis of numerical and experimental results. Naval Hydro software pack is used for numerical simulations, which is an extension of the collocated FV based CFD open source software foam–extend (Weller et al., 1998; Jasak, 2009). The Naval Hydro package is specialised for viscous, two phase, large scale flows. Nonlinear stream function regular wave theory by Rienecker and Fenton (1981) is used for wave generation. The potential wave flow and CFD are coupled

---

[*] Corresponding author. University of Zagreb, Faculty of Mechanical Engineering and Naval Architecture, Ivana Lučića 5, Zagreb, Croatia.
E-mail addresses: inno.gatin@fsb.hr (I. Gatin), vuko.vukcevic@fsb.hr (V. Vukčević), h.jasak@wikki.co.uk, hrvoje.jasak@fsb.hr (H. Jasak), thamjang@snu.ac.kr (J. Seo), shr@snu.ac.kr (S.H. Rhee).

https://doi.org/10.1016/j.oceaneng.2017.10.026
Received 5 June 2017; Received in revised form 29 August 2017; Accepted 16 October 2017

in a one–way fashion using implicit relaxation zones (Jasak et al., 2015) by imposing the wave solution at the boundaries of the domain and gradually transitioning to the nonlinear CFD solution towards the middle of the domain. The interface is captured using the Volume of Fluid (VOF) method where a novel geometric approach developed by Roenby et al. (2016) is employed, called isoAdvector. Free surface boundary conditions are discretised using the Ghost Fluid Method (GFM) (Vukčević, 2016), providing a infinitesimally sharp pressure and density gradient distribution at the interface.

The aim of this paper is to assess the accuracy and feasibility of a modern naval hydrodynamics CFD software for predicting green sea loads. In order to reduce the possible sources of error to a minimum, a simple static geometry is analysed with publicly available experimental results (Lee et al., 2012). Since numerical simulations of wave induced motions and loads have been validated using the Naval Hydro package in the past (Vukčević, 2016; Vukčević et al., 2015, 2016; Jasak et al., 2014), green sea load validation is the missing piece for conducting complete numerical simulations with moving bodies where green sea loads are calculated.

This paper is organised as follows: in the second chapter the numerical method is outlined. The third chapter gives basic information about experimental measurements that are used for comparison. In the fourth chapter the numerical simulations of green sea loads are described in detail, including the simulation set–up, uncertainty analysis procedure and comparison of the results with the experiments. Finally, a brief conclusion is given.

2. Numerical model

In this section the numerical model used in this work is presented. Governing equations describing two–phase, incompressible and viscous flow are:

$$\nabla\cdot\mathbf{u} = 0, \tag{1}$$

$$\frac{\partial \mathbf{u}}{\partial t} + \nabla\cdot(\mathbf{u}\mathbf{u}) - \nabla\cdot(\nu\nabla\mathbf{u}) = -\frac{1}{\rho}\nabla p_d, \tag{2}$$

where $\mathbf{u}$ denotes the velocity field, ν stands for the kinematic viscosity of the corresponding phase, ρ is the density, while p_d stands for dynamic pressure:

$$p_d = p - \rho\mathbf{g}\cdot\mathbf{x}. \tag{3}$$

Here, p is the absolute pressure, $\mathbf{g}$ is the gravitational acceleration, while $\mathbf{x}$ denotes the radii vector. Note that the momentum equation has been divided through by the density, assuming a two–phase free surface system of incompressible immiscible fluids. Eq. (1) and Eq. (2) are discretised in collocated FV fashion yielding the pressure and momentum equation (Vukčević et al., 2017), respectively. The equations are solved implicitly. Eq. (2) is valid for both phases, where the discontinuity of dynamic pressure and density at the interface is taken into account with the GFM (Vukčević, 2016; Vukčević et al., 2017). The dynamic pressure and density jump conditions are a consequence of normal stress balance at the free surface. The tangential stress balance is modelled approximately, while the surface tension is neglected. The two jump conditions arising from the normal stress balance are:

$$p_d^- - p_d^+ = -\left(\rho^- + \rho^+\right)\mathbf{g}\cdot\mathbf{x}\ , \tag{4}$$

$$\frac{1}{\rho^-}\nabla p_d^- - \frac{1}{\rho^+}\nabla p_d^+ = 0. \tag{5}$$

Superscripts "+" and "−" denote the water and air phase, respectively. Eq. (4) states that the jump of dynamic pressure across the interface is proportional to the jump in density, while Eq. (5) states that the jump of specific dynamic pressure gradient is zero. The jump conditions are introduced into the discretisation via specialised discretisation schemes, ensuring that Eq. (4) and Eq. (5) are satisfied. The reader is referred to Vukčević et al. (2017) for details.

In order to advect the interface, a geometric VOF method called isoAvector (Roenby et al., 2016) is used. Standard advection equation is used in order to transport the volume fraction variable α:

$$\frac{\partial \alpha}{\partial T} + \nabla\cdot(\alpha\mathbf{u}) = 0. \tag{6}$$

Written for a finite control volume P, and discretised in time using the first order accurate Euler method, Eq. (6) states:

$$\int_{V_P} \alpha_P(t+\Delta t) - \alpha_P(t) dV = -\int_t^{t+\Delta t} \oint_{S_P} \alpha\,\mathbf{n}\,\mathbf{u} dS\, d\tau, \tag{7}$$

where V_P is the volume of the control volume P, S_P is the closed boundary surface of the control volume, $\mathbf{n}$ is the unit normal vector of the boundary surface, while τ denotes the time integration variable. For a surface boundary discretised with a finite number of faces, the closed surface integral is replaced with a sum of surface integrals across the faces:

$$V_P(\alpha_P(t+\Delta t) - \alpha_P(t)) = -\sum_f \int_t^{t+\Delta t} \int_{S_f} \alpha\,\mathbf{n}_f\,\mathbf{u} dS_f\, d\tau, \tag{8}$$

where f denotes the face index. The volume integral of the temporal term is discretised assuming a second order accurate FV method (Jasak, 1996). Instead of evaluating the temporal and surface integrals in Eq. (8) by employing conventional discretisation schemes, in the isoAdvector method they are integrated explicitly directly from the information about the moving iso–surface of the volume fraction, representing the interface, through a polyhedral cell. In this way, sub–grid resolution is achieved for interface advection. This results in a sharp interface and bounded volume fraction field. The reader is directed to (Roenby et al., 2016) for more details on the isoAdvector method.

2.1. Wave modelling

Regular waves are imposed into the CFD domain via implicit relaxation zones (Jasak et al., 2015). Relaxation zones are regions in the computational domain where the theoretical wave solution is imposed by smoothly transitioning to the calculated CFD solution. The same method is used to dampen the waves at the outlet, where the CFD solution is gradually replaced by the imposed solution, the incident wave in this case. A stream function wave model (Rienecker and Fenton, 1981) is used which is fully nonlinear, permitting a shorter CFD domain since the wave nonlinearities are resolved outside of the CFD domain.

3. Green sea experiments

The experimental tests were performed in the towing tank of Seoul National University, with the details and results published in (Lee et al., 2012). A simplified model of a FPSO vessel is used, where three different bow shape configurations are tested. The computations in this work are performed for one of the geometries, called Rect0 in the original paper (Lee et al., 2012). The structure is static in order to reduce the number of possible sources of error when comparing the results. Ten pressure gauges are positioned at the deck of the model. The geometry of the model and position of pressure gauges are shown in Fig. 1. A vertical wall is positioned at the deck to simulate the breakwater. Pressure data is measured for nine incident wave cases, with wave parameters shown in Table 1. Pressure gauges are labelled as indicated in Fig. 1 in a separate figure for clarity.

In (Lee et al., 2012) detailed experimental results are presented for pressure peaks of individual gauges. The reported values are average

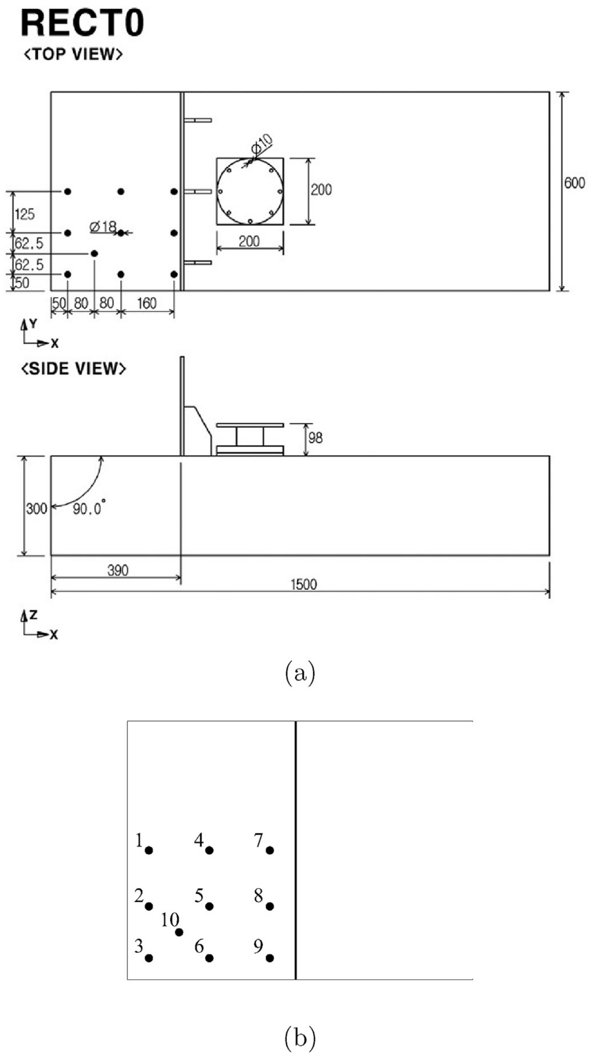

Fig. 1. Geometry of the FPSO model: a) model dimensions and pressure gauge positions (pressure gauges are indicated with black dots) (Lee et al., 2012), b) schematic of pressure gauges arrangement with labels.

pressure peaks over 35 incident wave periods. Maximum and minimum values of peaks are also reported, enabling the assessment of periodic uncertainty. However, from the elastic structural response point of view, the integral of force (i.e. pressure) is more relevant than extremely short force peaks. For that reason, additional post–processing of raw experimental data is performed in order to establish the average pressure time integral in one wave period, as well as maximum and minimum values.

Table 1
Incident wave parameters.

Wave ID	λ, m	a, m	ka
1	2.25	0.04500	0.126
2	2.25	0.05625	0.157
3	2.25	0.06750	0.188
4	3.00	0.06000	0.126
5	3.00	0.07500	0.157
6	3.00	0.09000	0.188
7	3.75	0.07500	0.126
8	3.75	0.09375	0.157
9	3.75	0.11250	0.188

The total experimental uncertainties are calculated as the superposition of measuring uncertainties: bias and precision limit of pressure gauges; and of periodic uncertainty of the pressure peak or pressure integral in time. The bias and precision limit are stated in (Lee et al., 2012). Periodic uncertainty is calculated as:

$$U_{EP} = \frac{\phi_{\max} - \phi_{\min}}{N_E}, \tag{9}$$

where ϕ denotes an arbitrary measured item in one wave period, such as pressure peak or pressure integral, while N_E stands for the number of periods included in the analysis. $\phi_{\max}$ and $\phi_{\min}$ are the maximum and minimum values measured during N_E periods. Total experimental uncertainty is then:

$$U_{ET} = \sqrt{U_{EM}^2 + U_{EP}^2}, \tag{10}$$

where U_{EM} stands for measuring uncertainties comprised of bias and precision limit of the pressure gauges.

4. Green sea simulations

In this section the simulations of green sea loading are presented. First, the simulation setup is described in detail, followed by a brief description of the numerical uncertainty analysis used in this work. Second, the results are shown, where first a sensitivity study is performed regarding domain size, in order to justify the reduction of the domain size described below. Next, the results are compared to experimental data, followed by a short discussion. Finally, another sensitivity study is performed regarding the interface capturing method, where the isoAdvector method is compared to the conventional algebraic VOF method (Rusche, 2002).

4.1. Simulation setup

Simulations have been performed for all wave cases for geometry Rect0 with vertical stem. Four grids are used for each wave case in order to establish the numerical uncertainty, while the results from the finest grid are used as reference results for the comparison. Fig. 2 shows the computational domain for wave 4 as an example, with indicated boundaries. The wall on the deck is simulated as a domain boundary, hence the deck of the model is not included beyond the wall. It is assumed that this simplification does not influence the flow on the deck. Despite the symmetry of the computational domain with respect to the longitudinal plane, the violent flow occurring on deck during the green water phenomenon is not necessarily symmetric. Hence, the full domain is simulated as opposed to only half. The characteristics of fine grids for

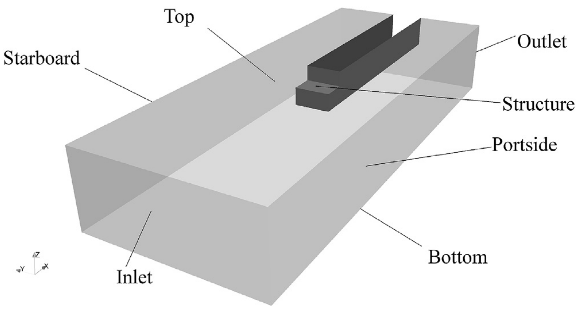

Fig. 2. Computational domain.

Table 2
Computational grid characteristics.

Wave ID	L, m	L_R, m	H, m	$\lambda/\Delta x$	$a/\Delta z$	Δz_{deck}, m
1	6.5	2.5	0.15	375	15.5	$5.84\cdot10^{-4}$
2	6.5	2.5	0.15	375	19.4	$5.84\cdot10^{-4}$
3	6.5	2.5	0.30	225	23.3	$1.36\cdot10^{-3}$
4	7.7	3.1	0.30	333	20.7	$1.34\cdot10^{-3}$
5	7.7	3.1	0.60	333	16.3	$3.92\cdot10^{-3}$
6	7.7	3.1	0.60	333	19.5	$7.91\cdot10^{-3}$
7	14.0	4.0	0.60	354	15.8	$2.24\cdot10^{-3}$
8	14.0	4.0	0.60	354	19.8	$2.24\cdot10^{-3}$
9	14.0	4.0	0.60	354	27.3	$4.28\cdot10^{-3}$

all wave cases are presented in Table 2. Here, L is the domain length, while L_R indicates the length of inlet and outlet relaxation zones. $\lambda/\Delta x$ and $a/\Delta z$ denote the number of cells per wave length and wave amplitude, respectively. H denotes the height of the domain above the deck in metres, where different heights are used depending on the wave amplitude and expected wave run–up against the wall. The freeboard height is 0.045 m above the free surface (Lee et al., 2012). Δz_{deck} denotes the height of the cell above the deck. At certain height from the deck, the cell height is linearly increased towards the top boundary in order to reduce the number of cells. Also, the cell size is reduced linearly in the horizontal direction from the inlet boundary towards the structure. Hence, $\lambda/\Delta x$ is measured next to the structure. Fig. 3 shows the computational grid in the longitudinal central plane and on the surface of the structure used for wave 4. Note that the coarse grid is presented for better visibility of grid lines. The simple geometry of the structure enables fully structured and orthogonal grids to be generated.

Depth and breadth of the domain are constant for all wave cases, where the depth is $D = 1$ m, and breadth $B = 3$ m. It should be noted here that the depth of the wave tank in the experiments was 3.5 m, however only 1 m is included in the simulation in order to save computational time. To avoid influence of this simplification, wave velocity from the stream function wave theory is prescribed at the bottom in order to make it transparent to the flow. This treatment assumes that the diffracted wave field is negligible at the depth of 1 m. Similarly, the breadth is also reduced from 8 to 3 m, with relaxation zones near the starboard and portside boundaries preventing reflection of the diffracted wave field.

Considering the violent free surface flows at the deck, and the explicit nature of the isoAdvector method, the time step is adjusted during the simulation to maintain a maximum fixed Courant–Fredrich–Lewy (CFL) number of $C_o = 0.75$. The same C_o is used in all simulations and on all grids, which results in consistent time step variation on different grids. For reference, average time–step for wave 1 on fine grid is 0.0006 s, while for wave 9 it is 0.001 s.

As indicated in Fig. 1, the circular pressure gauges are 18 mm in diameter. Cells used on the deck are rectangular, where the horizontal dimensions of the cell, which correspond to the spatial discretisation of the deck surface, ranges from 4 to 13 mm, depending on the grid. Hence, the deck surface discretisation resolution is always higher compared to the area of the pressure gauge used in the experiment. As stated in (Lee et al., 2012) the sampling rate of pressure gauges used in the experiment is 5 kHZ, corresponding to a time–step of 0.0002 s, which is comparable to time–steps used in the simulations.

No turbulence modelling is used in this work since it can be considered to have a negligible influence on pressure distribution at the structure. Moreover, the pressure and velocity gradients in the flow on deck are extremely violent, rendering standard single–phase, wall bounded models inapplicable. The influence of turbulence should, however, be investigated in the future.

4.2. *Uncertainty analysis*

The total numerical uncertainty is dominated by discretisation and periodic uncertainty, since the iterative uncertainty is kept low by using sufficient number of nonlinear correctors per time–step and converging linear systems to a tight tolerance ($\approx 10^{-9}$). In order to assess the discretisation uncertainty, a grid and time–step refinement uncertainty study is performed with the least squares approach developed by Eca & Hoekstra (Eça and Hoekstra, 2014). In case of unsteady flow, the time–step has to be varied as well as the grid resolution (Eça and Hoekstra, 2008). In this work the time–step is reduced simultaneously with the cell size by maintaining a fixed CFL number. For the least squares approach, at least four refinement levels are needed in order to calculate the uncertainty. Constant refinement ratio of $r = \sqrt{2}$ is used for all wave cases, which is defined as the ratio between spatial and temporal resolution between adjacent refinement levels: $r = h_{i-1}/h_i = \tau_{i-1}/\tau_i$, where h_i stands for the representative cell size of refinement level i, while τ_i stands for the time step. Since C_o changes linearly with the cell size, τ also varies linearly, hence the condition $r = \tau_{i-1}/\tau_i$ is satisfied. Table 3 lists the number of cells for all grids and wave cases. All simulations were performed on processors Intel Xeon E5-2637 v3 15M Cache 3.50 GHz. CPU time per wave period on eight cores for the coarse grid ranges between 1.3 and 1.9 h, while on the fine grid it ranges from 7.3 to 15.6 h, depending on the wave case.

According to Eca & Hoekstra (Eça and Hoekstra, 2014), the uncertainty assessment begins with assessing the error of discretisation:

$$\varepsilon_i = \alpha h_{i^*}^p\,, \quad h_{i^*} = \left(\tau_i h_i^2\right)^{1/3}, \tag{11}$$

using the least squares fit. Here, α is an unknown constant, and p is the obtained order of accuracy. The least squares fit is obtained by minimising the following function:

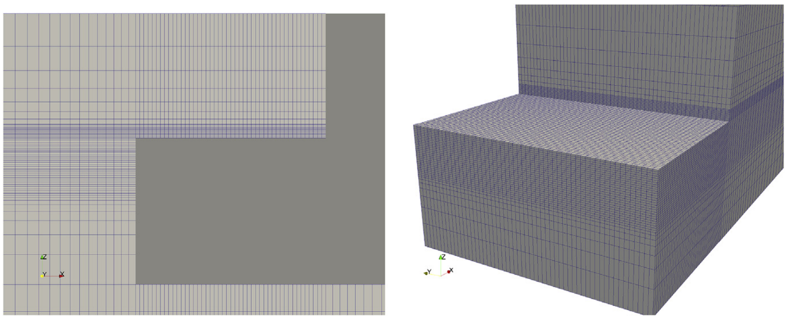

(a)

(b)

Fig. 3. Computational grid for wave 4 case: a) grid in the longitudinal central plane, b) surface grid of the structure.

Table 3
Grid sizes used in the uncertainty analysis.

Wave ID	Number of cells			
	Grid 1	Grid 2	Grid 3	Grid 4
1	498 720	948 780	1 969 077	3 928 939
2	498 720	948 780	1 969 077	3 928 939
3	276 699	518 476	1 077 515	2 181 103
4	291 546	546 952	1 140 179	2 299 683
5	319 035	603 876	1 236 052	2 509 667
6	238 617	453 796	934 552	1 887 253
7	627 009	1 181 376	2 313 248	4 561 172
8	627 009	1 181 376	2 313 248	4 561 172
9	484 674	905 268	1 754 384	3 454 682

$$S(\phi_0, \alpha, p) = \sqrt{\sum_{i=1}^{N} (\phi_i - (\phi_0 + \alpha h_{*i}^p))^2}, \tag{12}$$

where ϕ_0 denotes the estimate of the exact solution, while N denotes the number of refinement levels. Minimisation of Eq. (12) leads to a nonlinear system of equations, which needs to be solved iteratively. In case the observed order of accuracy p is larger than two, the first or second order terms are used, i.e. the following are solved:

$$\begin{aligned} \varepsilon_{1,i} &= \alpha h_{i*}, \\ \varepsilon_{2,i} &= \alpha h_{i*}^2, \end{aligned} \tag{13}$$

and the fit with smaller standard deviation is used. If $p < 0.5$, first and second order terms are retained in addition to Eq. (13):

$$\varepsilon_{12,i} = \alpha_1 h_{i*} + \alpha_2 h_{i*}^2, \tag{14}$$

where the fit with the smallest standard deviation is used. Standard deviation is calculated as:

$$\sigma = \sqrt{\frac{\sum_{i=1}^{N} (\phi_i - (\phi_0 + \alpha h_{*i}^p))^2}{N-3}}. \tag{15}$$

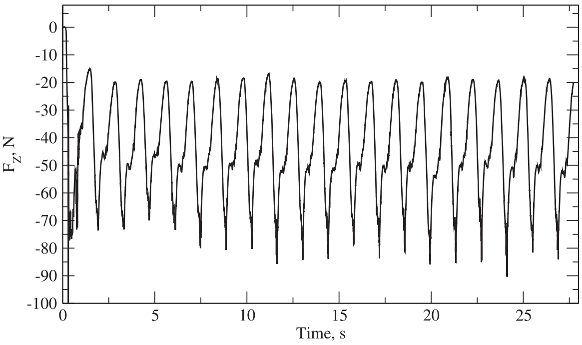

Fig. 4. Vertical force exerted on deck for wave 6.

Table 4
Discretisation uncertainties for vertical force peak and integral measured on the deck.

Wave ID	$F_{0,\max}$, N	$U_{CD,F}$, %	I_0, Ns	$U_{CD,I}$, %
1	21.83	8.8	22.02	0.4
2	37.45	15.0	36.27	11.4
3	62.25	5.3	59.45	8.5
4	39.56	12.7	42.21	20.7
5	61.09	2.2	61.03	4.4
6	163.27	35.8	105.95	16.0
7	72.07	1.4	71.66	0.3
8	159.93	0.2	115.61	0.03
9	284.39	8.2	166.02	1.9

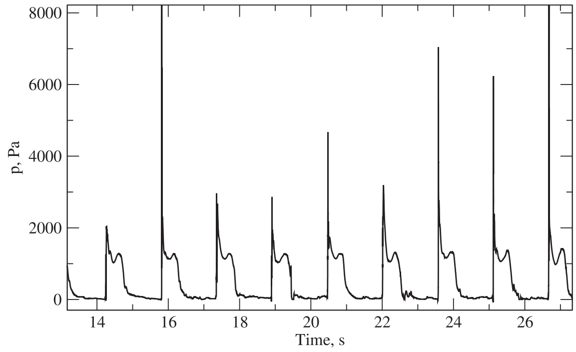

Fig. 5. Pressure signal at gauge 7 for wave 9.

Once ε, ϕ_0 and σ are known, the uncertainty of the result can be established. If the data is well behaved, the following expression is used for assessing the refinement uncertainty:

$$U_i = F_S \varepsilon_i + \sigma + |\phi_i - \phi_{fit}|, \tag{16}$$

where F_S is the safety factor, while ϕ_{fit} presents the least squares fitted value of the solution for grid i. The data is well behaved if $\sigma < \Delta$, where Δ expresses the data range:

$$\Delta = (\phi_{\max} - \phi_{\min})/(N-1), \tag{17}$$

where $\phi_{\max}$ and $\phi_{\min}$ represent the maximum and minimum value from all refinement levels. In case the data is not well behaved, i.e. $\sigma > \Delta$, the uncertainty is assessed as:

$$U_i = 3\frac{\sigma}{\Delta}(\varepsilon_i + \sigma + |\phi_i - \phi_{fit}|). \tag{18}$$

In this work the uncertainty is assessed for the finest refinement level, i.e. in the above expressions $i = 4$. Since the discretisation uncertainty study theoretically requires a smooth variable in time, the uncertainty is assessed for the vertical force exerted on the deck, i.e. the spatial integral of pressure, instead of the pressure measured at gauge locations.

Total computational uncertainty is assessed as the superposition of the discretisation and periodic uncertainty:

$$U_{CT} = \sqrt{U_{CD}^2 + U_{CP}^2}, \tag{19}$$

where U_{CD} denotes the discretisation uncertainty established using Eq. (16) or Eq. (18), while U_{CP} represents the periodic uncertainty calculated

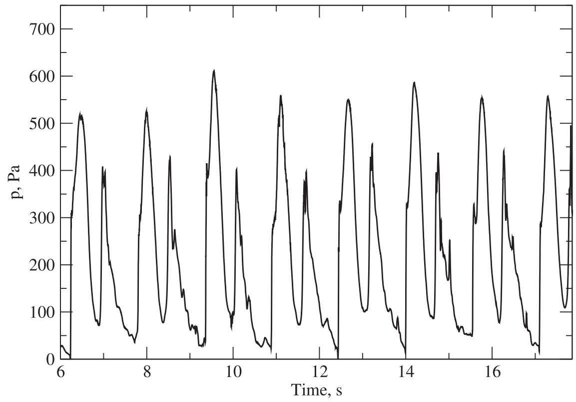

Fig. 6. Pressure signal at gauge 1 for wave 9.

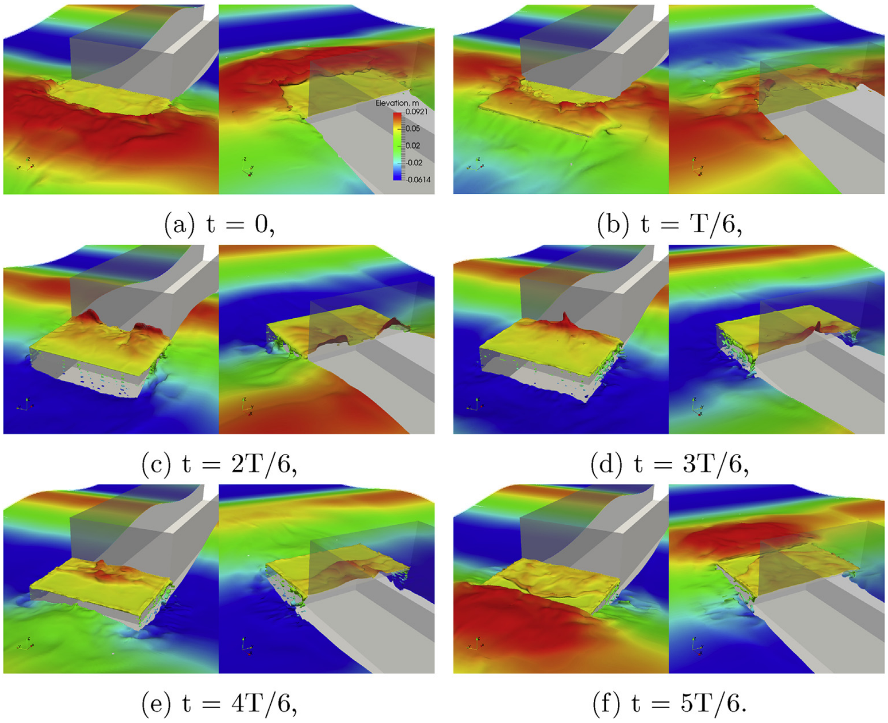

(a) t = 0, (b) t = T/6,

(c) t = 2T/6, (d) t = 3T/6,

(e) t = 4T/6, (f) t = 5T/6.

Fig. 7. Perspective view of the green sea event for wave 3.

in the same manner as for the experimental data:

$$U_{CP} = \frac{\phi_{\max} - \phi_{\min}}{N_C}, \tag{20}$$

where N_C denotes the number of periods included in the analysis. Fig. 4 shows the signal of vertical force acting on the deck for wave 6. For every wave case, 20 wave periods are simulated, where the last 14 are used in the analysis to avoid initial transient effects.

Numerical discretisation uncertainties calculated with the vertical force on deck are summarised in Table 4 for all wave cases, where $F_{0,\max}$ denotes the estimated exact solution (corresponding to ϕ_0 in Eq. (12)) of vertical force peak $F_{\max}$, while I_0 denotes the estimated exact solution for the force integral, i.e. force impulse. $F_{\max}$ and I are calculated as:

$$F_{\max} = \frac{\sum_{i=1}^{N_C} F_{i,\max}}{N_C}, \tag{21}$$

$$I = \frac{\sum_{i=1}^{N_C} \int_0^T F_i(t)dt}{N_C}, \tag{22}$$

where $F_{i,\max}$ denotes the force peak for period i, while T denotes the wave period. In Table 4, $U_{CD,F}$ and $U_{CD,I}$ denote the discretisation uncertainty for force peak $F_{\max}$ and force impulse I, respectively. Uncertainties show large differences from one wave case to another, however they remain below 10% for most items, and go as low as 0.03%. The outliers are wave 4 and 6 with uncertainties higher than 10%.

4.3. Results

As stated earlier, two sets of results are compared within this study:

- The average pressure peak during one period:

$$p_{\max} = \frac{\sum_{i=1}^{N_C} p_{i,\max}}{N_C}, \tag{23}$$

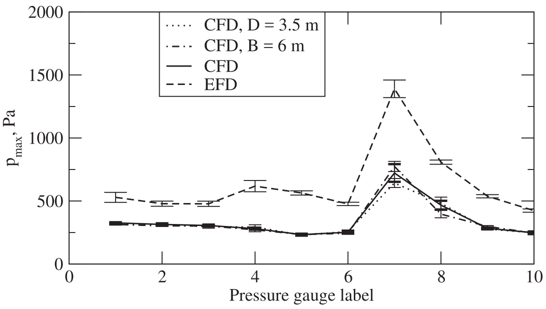

Fig. 8. Pressure peak comparison between different domain sizes for wave 7.

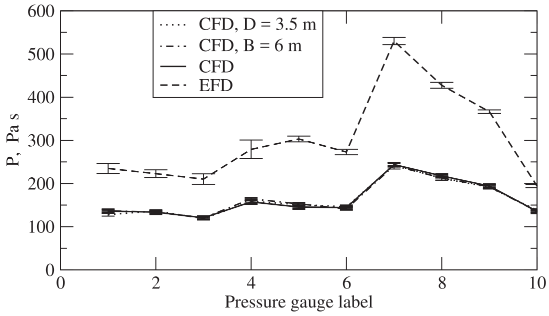

Fig. 9. Pressure integral comparison between different domain sizes for wave 7.

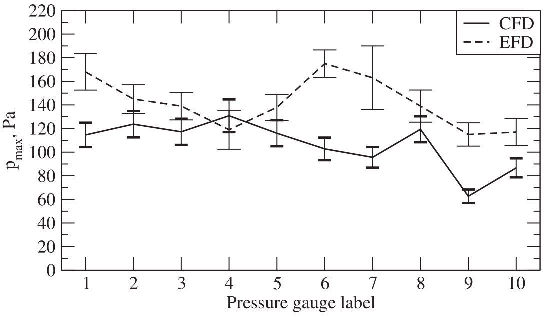

Fig. 10. Pressure peak results comparison for wave 1.

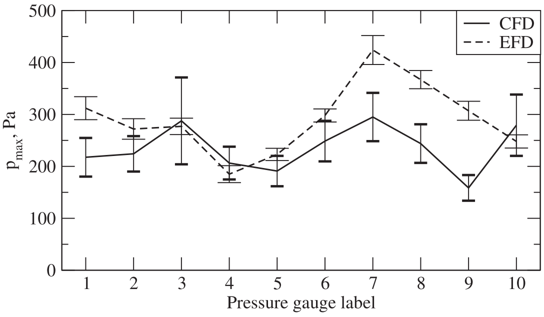

Fig. 11. Pressure peak results comparison for wave 2.

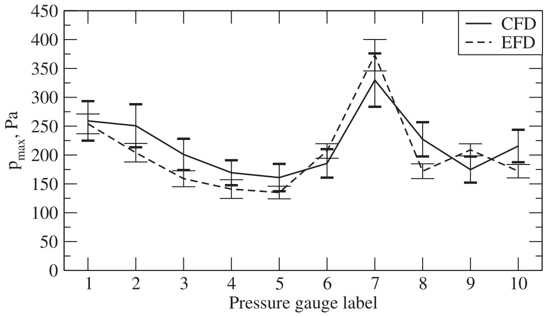

Fig. 13. Pressure peak results comparison for wave 4.

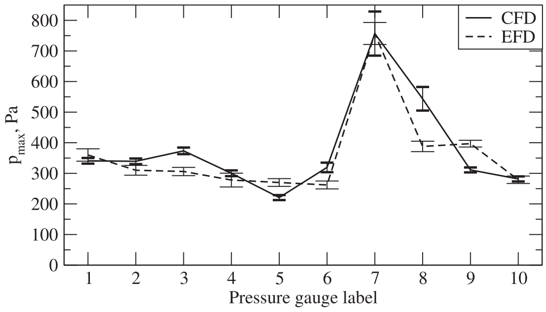

Fig. 14. Pressure peak results comparison for wave 5.

where $p_{i,\max}$ denotes the pressure peak during i-th wave period.

- The average pressure time integral over one wave period:

$$P = \frac{\sum_{i=1}^{N_C}\int_0^T p_i(t)dt}{N_C}\ . \tag{24}$$

Although the pressure peak that occurs during green sea event is an obvious quantity for comparison, it is not necessarily relevant for the structural response. If the pressure peak lasts a very short amount of time, it will not influence the structural response. On the other hand, it is a known fact that in numerical simulations, high pressure peaks can occur when a free surface impacts against a solid boundary. Hence, to provide a more complete comparison, the pressure integral in time is also compared. Fig. 5 shows an example of the pressure signal in time measured by gauge 7 for wave 9, where extremely transient pressure peaks can be seen. Large differences in pressure peaks increase the periodic pressure peak uncertainty, which is observed in the results shown below. However, the integral of pressure in time is not sensitive to high transient peaks. For gauges further away from the wall, pressure peaks are less prominent, as shown in Fig. 6 where gauge 1 pressure signal is shown for the same wave case.

In order to accurately capture the total pressure at the horizontal deck during a complete wave period, it is necessary to capture the thinnest layer of water that can occur during the wave recession from the deck. In order to achieve that, at least one cell centre is needed between the free surface and deck at all times. It can be observed in Table 2 that different cell sizes are used at the deck for different wave cases. The minimum depth of water on deck depends on wave amplitude and period. Waves with shorter period give a smaller amount of time for the water to pour down from the deck. Similarly, larger wave amplitude implies more water on deck. Fig. 7 sequentially shows one period of a green sea event for wave 3, where the thin layer of water can be seen after the collapse of water run–up against the wall.

4.3.1. *Influence of the domain size*

As stated earlier, breadth and depth of the domain were reduced with respect to experimental setup in order to reduce the number of cells. The

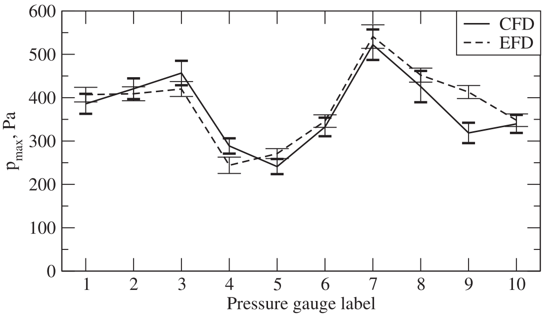

Fig. 12. Pressure peak results comparison for wave 3.

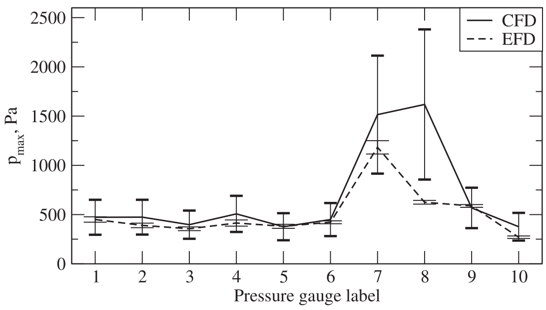

Fig. 15. Pressure peak results comparison for wave 6.

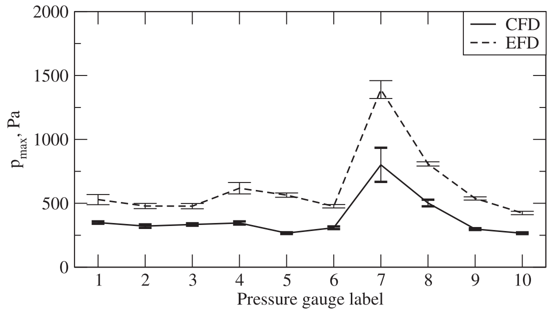

Fig. 16. Pressure peak results comparison for wave 7.

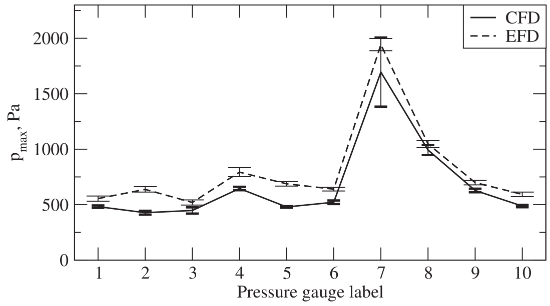

Fig. 17. Pressure peak results comparison for wave 8.

breadth was reduced from 8 to 3 m, while the depth of 1 m is used instead of 3.5 m. Depth was reduced by prescribing the incident wave velocity at the bottom boundary, hence the wave diffraction effects were neglected from this depth on. Breadth was reduced where similar boundary condition is imposed: relaxation zones were prescribed near the side boundaries in order to eliminate diffracted waves and prevent reflection.

In order to test the validity of these assumptions, and to assess their influence on pressure results, two additional tests are performed with different domain breadth and depth. Tests are performed for one wave only on the coarsest refinement level. Wave 7 case is used for this comparison for two reasons: it is in the group of longest waves, where limited depth could have the greatest influence, and because it exhibited poorest agreement with the experiment, as shown below. Hence, if these assumptions are not valid, an improvement in result quality should be exhibited.

The first test is performed by increasing the breadth of the computational domain from 3 to 6 m, while keeping the rest of the dimensions fixed. Side boundary conditions and size of the relaxation zones are not changed. In the second test the depth is increased from 1 m to 3.5 m, corresponding to the experimental setup. In this case the velocity boundary condition on the bottom is changed from incident wave velocity to non–slip, non–permeable wall boundary condition.

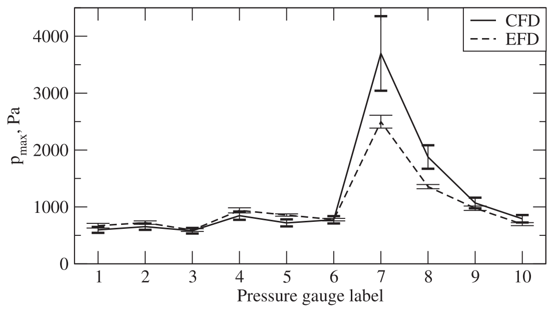

Fig. 18. Pressure peak results comparison for wave 9.

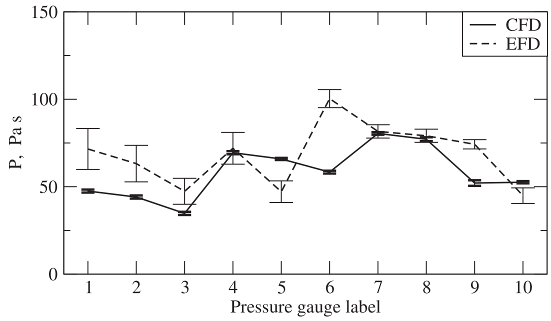

Fig. 19. Temporal pressure integral results comparison for wave 1.

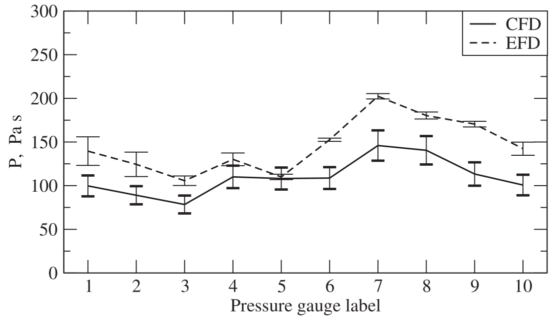

Fig. 20. Temporal pressure integral results comparison for wave 2.

Fig. 8 shows the comparison of the three CFD results and experimental results for pressure peaks. Results denoted with CFD correspond to the original setup used in this study, obtained on the coarsest refinement level. The remaining two CFD results are denoted with the changed dimension with respect to the original setup. The influence of the domain size is almost none for most wave gauges, except for gauge 7 and 8 where a very small change is observed.

Fig. 9 shows the comparison for pressure integrals. The variation of the domain size had a negligible influence on the pressure integrals for all gauges. Hence, the simplifications made to reduce the number of cells had no influence on the results, and are justified.

4.3.2. Pressure peaks

The comparison of pressure peak results with corresponding uncertainties are shown in Figs. 10–18. Complete results with uncertainties are given in tabular form in Sec. A.1. The average value of the pressure

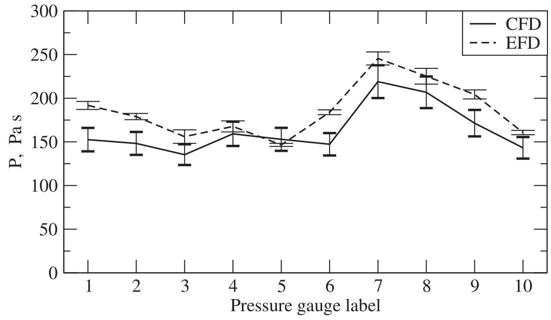

Fig. 21. Temporal pressure integral results comparison for wave 3.

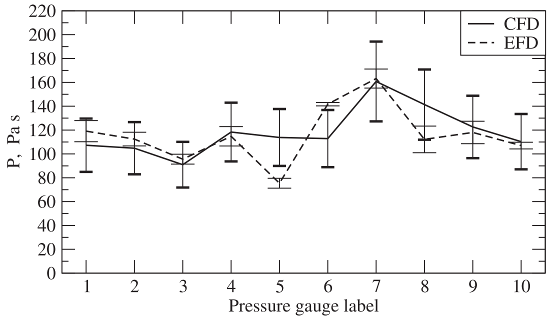

Fig. 22. Temporal pressure integral results comparison for wave 4.

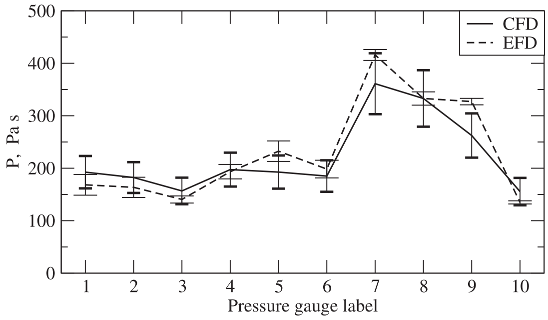

Fig. 24. Temporal pressure integral results comparison for wave 6.

peak is denoted on the y–axis while the x–axis denotes the index of the pressure gauge as indicated in Fig. 1. The error bars present the total numerical and experimental uncertainties, Eq. (19) and Eq. (10), respectively. CFD stands for the result obtained using the present numerical methods, while EFD stands for Experimental Fluid Dynamics.

Results for wave 1 are presented in Fig. 10. Relative differences between the results are considerable, however the absolute difference is not large since the pressure load for this case is small. The uncertainties are similar for most gauges, except for a few where experimental results exhibit higher uncertainties. This wave case has the smallest amplitude, requiring higher mesh resolution. Pressure peaks for wave 2 shown in Fig. 11 show similar agreement as wave 1, with slightly larger numerical uncertainties.

For wave 3, results in Fig. 12 show good agreement with experimental results. For eight out of nine gauges the uncertainty intervals overlap, and the trend is very well captured.

Wave 4 shows good agreement in Fig. 13, where uncertainty intervals overlap for all gauges, while the uncertainties are similar between the numerical and experimental result.

For wave 5, pressure peaks in Fig. 14 correspond well to experimental data, with gauge 8 and 9 showing larger discrepancies. Gauge 7, 8 and 9 are located close to the wall, where the most violent flow occurs, making the pressure in that area more challenging to predict and increasing the periodic uncertainties.

For wave 6, both experimental and numerical results shown in Fig. 15 predict considerably higher pressure peaks for gauge 7 near the wall than the gauges further from the wall. Results agree well for gauges further from the wall, however significant over–estimation is observed for gauges 7 and 8, as well as high uncertainties. The high uncertainties for gauges 7 and 8 are the consequence of extremely transient pressure peaks in the numerical result as shown in Fig. 5. For this case, numerical uncertainties are relatively large for all gauges due to high grid uncertainties, as shown in Table A6.

Unlike other cases, results for wave 7 show significant underestimation when comparing to the experimental data, as shown in Fig. 16. The trends, however, are well captured. The uncertainties are generally smaller than experimental uncertainties, except for gauges 7 and 8.

For wave 8 the results shown in Fig. 17 show good agreement with the experiment with low uncertainties, where gauge 7 stands out with higher uncertainties. In this case, as for wave 7, the pressure peaks are underestimated, but the difference is significantly smaller. As in majority of cases, the trend is well captured.

Wave 9 exhibits good agreement for gauges further from the wall as shown on Fig. 18, whereas gauges next to the wall show over–prediction with larger uncertainties originating mostly from periodic uncertainties (see Table A9). The over–prediction might also be related to compressibility effects, which will be investigated in the future.

4.3.3. Pressure integrals

The comparison of integrals of pressure in time for all wave cases is shown in Figs. 19–27. Complete results with uncertainties are given in tabular form in Sec. A.2. Same as for the pressure peaks, the x–axis on the graphs denotes the pressure gauge label, while integral of pressure P is shown on the y–axis.

The numerical results of pressure integrals for wave 1 shown in Fig. 19 exhibit very low uncertainties, while the agreement with experimental results is similar as for pressure peaks.

For wave 2, results in Fig. 20 show that the trend is well captured, while the values are somewhat underestimated. Numerical uncertainties are similar for all gauges.

In Fig. 21, pressure integrals for wave 3 show good agreement with the experiment, with smaller uncertainties for experimental measurements. For this wave case, pressure peaks show better agreement than the time integrals, which are generally underestimated.

For wave 4, good agreement is achieved as indicated in Fig. 22, with higher numerical uncertainties comparing to the experiment. The high numerical uncertainties originate from discretisation uncertainties, while periodic uncertainty has a minor contribution (see Table A13).

For wave 5, Fig. 23 shows good agreement with overlapping

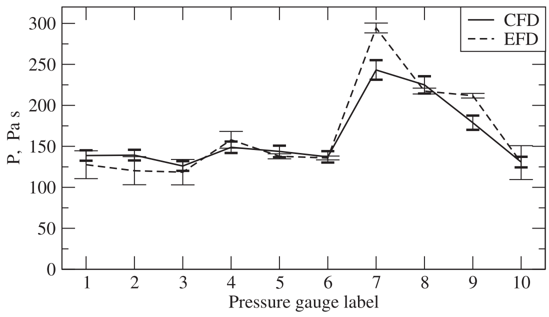

Fig. 23. Temporal pressure integral results comparison for wave 5.

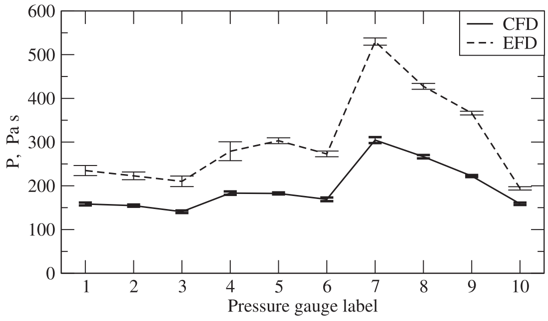

Fig. 25. Temporal pressure integral results comparison for wave 7.

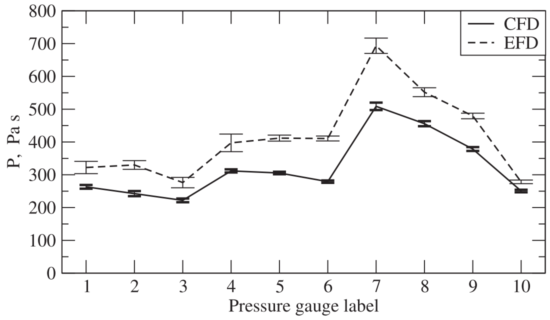

Fig. 26. Temporal pressure integral results comparison for wave 8.

uncertainty intervals, except for gauge 7 and 9. Numerical uncertainties are generally smaller than experimental for this case.

In Fig. 24 uncertainty intervals for wave 6 are overlapping for nine out of ten gauges, the only outlier being gauge 9. Same as for pressure peaks for this wave case, numerical uncertainties are larger than experimental due to large grid uncertainty.

As for pressure peaks, wave 7 exhibits considerable under–estimation for pressure integrals shown in Fig. 25, with small uncertainties and good prediction of the trend. The consistent underestimation of pressure in this case should be investigated from both numerical and experimental side. The difference might be caused by transversal reflection occurring in the experiment due to finite tank breadth, which is not present in the numerical simulation. Also, compressibility effects may influence the results, hence the effect of compressibility will be investigated in the future.

Wave 8 again shows good trend agreement and low uncertainties in Fig. 26, however the values are underestimated. Larger difference is observed in this case than for pressure peaks.

For wave 9 shown in Fig. 27 the trend is well captured with lower numerical uncertainties than experimental results. Unlike pressure peaks, here the values are underestimated for most gauges, except gauge number 10.

4.4. Discussion

Overall the results for both pressure peaks and integrals exhibit good agreement with the experimental data. Pressure peaks compare better with experiments for pressure gauges further from the wall, where the influence of water impingement is smaller. However, for waves 1 to 5 the peaks are well predicted even close to the wall with acceptable uncertainties, while waves 6 to 9 exhibit higher uncertainties and deviations for pressure gauge 7, which is next to the wall and at the centre line. Wave 6 shows very large deviation and uncertainty for gauge 8, which is an outlier in the results, and should be investigated. For long waves, i.e. 7 to 9, pressure peaks exhibit small uncertainties and well captured trends. The results agree well with the experimental data for wave 8 and 9, while wave 7 shows significant under–estimation.

Table 5
Overall result comparison.

Wave ID	E_{pmax}, Pa	E_{pmax}, %	E_P, Pas	E_P, %
1	37.21	25.61	15.20	22.65
2	68.75	21.91	36.33	24.13
3	30.56	8.46	23.73	12.61
4	34.58	18.64	13.44	13.04
5	48.90	14.76	14.65	7.89
6	172.52	29.82	25.63	11.14
7	251.12	39.10	109.96	34.59
8	130.79	17.31	93.31	21.88
9	229.60	15.84	71.80	13.99

Pressure integrals are predicted well for all gauges for waves 1 to 6, where the uncertainty intervals overlap. Trends agree with experiments as well, except for waves 1 and 4, where difference in trends is observed. For waves 7 to 9 the uncertainties are very low and the trends are captured accurately, however the values are significantly underestimated. The under–estimation is smaller for higher amplitudes, i.e. wave 7 shows the largest difference. This consistent underestimation of pressure for waves with $\lambda = 3.75$ m will be investigated in the future. The difference could indicate an inconsistency between the numerical simulations and experiments with regards to the wave elevation and reflection.

Regarding wave steepness in individual cases, no correlation can be seen in the graphs between trends of the curves, discrepancies and wave steepness. On the other hand, the trends show similarities between waves with the same wave length, while the wave height only influences the magnitude of pressure loads. Thus, it can be concluded that wave celerity has a larger influence on the character of the green water event than wave steepness in this case.

Overall summary of pressure peak and integral result comparison is given in Table 5. For each wave the average absolute and relative difference between numerical and experimental result across all pressure gauges is given. E denotes the difference of numerical and experimental result which is expressed in absolute values and in percentages relative to the experimental result, where the indices $p$max and P stand for pressure peak and integral, respectively. For pressure peaks, absolute difference ranges from 30 to 70 Pa for wave cases 1 to 5, while the difference increases for waves 6 to 9, ranging from 130 to 250 Pa. However the relative differences show smaller variation, except for wave 7 where larger discrepancies occur. Average relative difference for pressure peaks for all cases is 21%. Pressure integrals show smaller relative differences with the average difference across all wave cases of 18%. From the practical engineering point of view, the differences for small waves, 1, 2 and 3 are of smaller importance due to the small absolute value of pressure loads. On the other hand, larger differences for waves 6 and 7 should be investigated further since these would have a larger influence on the structural design due to higher absolute pressure loads.

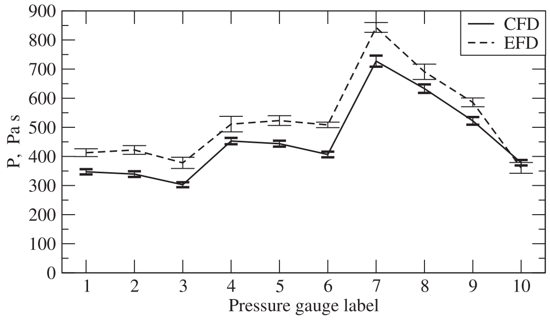

Fig. 27. Temporal pressure integral results comparison for wave 9.

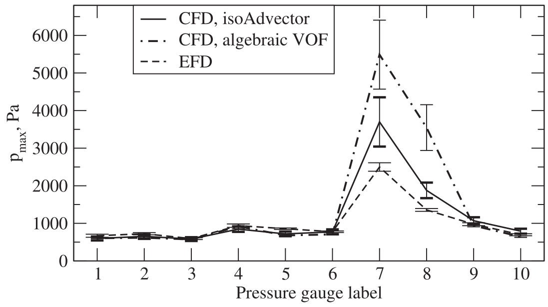

Fig. 28. Pressure peak comparison between the isoAdvector and the algebraic VOF method for wave 9.

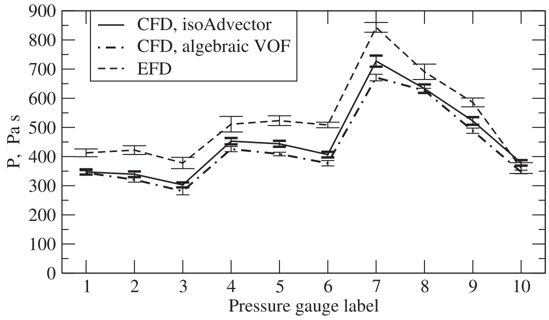

Fig. 29. Pressure integral comparison between the isoAdvector and the algebraic VOF method for wave 9.

4.5. *Influence of the interface advection method*

To compare the performance of the isoAdvector method for interface advection, an additional simulation is carried out for wave 9, where conventional algebraic VOF method is used with interface compression (Rusche, 2002). Fig. 28 shows the pressure peak results for wave 9 where in addition to experimental and numerical results, the numerical results with conventional algebraic VOF are given. Fig. 29 presents the comparison of the temporal integral of pressure. Note that in these graphs only the periodic uncertainty is included for numerical results, since the refinement study has not been performed with the algebraic VOF method. The results are similar for pressure peaks except for pressure gauges 7 and 8, where higher values are obtained with the algebraic VOF. Pressure integral results agree well between the two simulations, however the algebraic VOF exhibits slightly larger underestimation with respect to the experimental data. Fig. 30 sequentially shows a visual comparison of volume fraction field α for simulation where isoAdvector and algebraic VOF are used. With isoAdvector, the interface is confined within a single cell even when very violent free surface flow occurs. With algebraic VOF, the interface is smeared, and the geometry of the free surface is described less precisely.

Being a more complex method, isoAdvector requires a larger number of operations comparing to the algebraic VOF. Hence, an increase in CPU time is expected. Both simulations are performed using 24 cores on Intel Xeon Processor E5-2637 v3. Simulation with the algebraic VOF took 37.5 h, while the simulation using isoAdvector took 45 h to compute. Hence, an increased cost of 20% is exhibited in this case. Note that the increase in computational cost depends on the cost of the pressure–velocity coupling algorithm used in the solution procedure.

5. Conclusion

A comprehensive set of numerical simulations of green sea loads have been conducted using the FV based CFD software called Naval Hydro pack which is based on foam–extend. The Ghost Fluid Method is applied for discretisation of the free surface boundary conditions, while the geometric isoAdvector method is used for interface capturing.

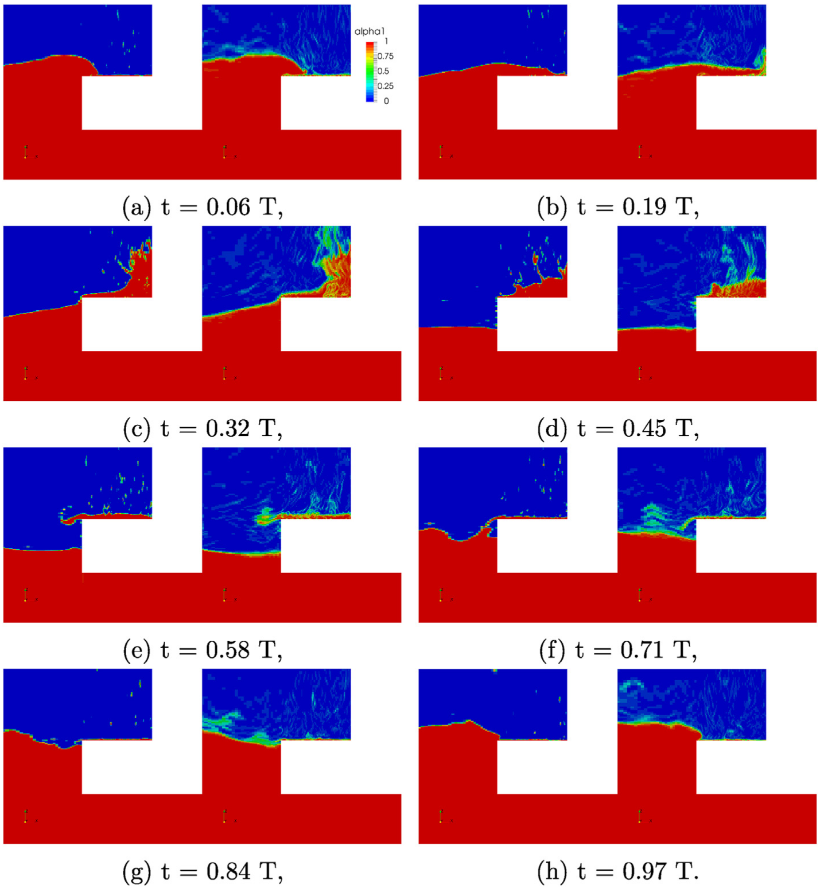

(a) t = 0.06 T,
(b) t = 0.19 T,
(c) t = 0.32 T,
(d) t = 0.45 T,
(e) t = 0.58 T,
(f) t = 0.71 T,
(g) t = 0.84 T,
(h) t = 0.97 T.

Fig. 30. Visual comparison of the volume fraction field α (denoted "alpha") in simulation where the isoAdvector (left) and the algebraic VOF method (right) are used.

All results are compared to experimental data in order to validate the present method for green sea load calculation. A case of a static, simplified FPSO model is used with a breakwater on deck, with regular incident waves. Nine wave cases are analysed with varying amplitude and steepness, where the pressure at ten locations on deck is measured. Uncertainties are assessed for both experimental and numerical data, yielding a comprehensive comparison. Detailed uncertainty analysis of numerical results is performed via grid and time–step resolution study, as well as periodic uncertainty analysis.

Compared pressure–related quantities are the average pressure peak and time integral of pressure during the wave period. Comparison of pressure peaks shows good overall agreement with comparable uncertainties between experimental and numerical data. Trends of peak pressure across pressure gauges agree well with experiments for seven out of nine wave cases, where the two smallest waves, wave 1 and 2 showed some discrepancy. Values and uncertainty intervals overlap for the majority of pressure gauges for waves 3, 4, 5, 6 and 9. Waves 1 and 2 show reasonable agreement, while waves 7 and 8 show underestimation of experimental results.

For temporal pressure integrals, trends are well captured for waves 2, 3, 5, 6, 7, 8 and 9, while waves 1 and 4 show slightly different trends. Values correspond well for waves 1, 3, 4, 5 and 6, while integrals for wave 2 and 9 are slightly underestimated. Waves 7 and 8 show larger underestimation which requires further investigation on both numerical and experimental side.

Overall, results show reasonable accuracy and high level of confidence. Comparable uncertainty between numerical and experimental results show that similar precision can be expected in terms of pressure on deck. Future work will involve prediction of realistic green sea loads for offshore objects in irregular waves.

Acknowledgement

The numerical research performed for this work was sponsored by Bureau Veritas under the administration of Dr. Šime Malenica and Dr. Quentin Derbanne.

Appendix. Results in tabular format

Complete results of both numerical and experimental studies are given in this section in tabular form, with break–down of numerical uncertainties.

A.1. Pressure peak results

Table A1
Pressure peak results for wave 1.

Gauge ID	$p_{\max,C}$, Pa	U_{CT}, Pa	U_{CD}, Pa	U_{CP}, Pa	$p_{\max,E}$, Pa	U_{ET}, Pa
1	114.63	10.35	10.10	2.25	168.00	15.41
2	123.69	11.15	10.90	2.33	145.00	12.06
3	117.26	11.08	10.33	4.00	139.00	11.67
4	130.84	13.85	11.53	7.68	119.00	16.49
5	116.03	11.01	10.23	4.09	138.00	10.97
6	102.78	9.60	9.06	3.17	175.00	11.60
7	95.63	8.70	8.43	2.18	163.00	26.99
8	119.38	10.96	10.52	3.06	139.00	13.61
9	62.66	5.71	5.52	1.47	115.00	9.87
10	86.69	8.04	7.64	2.51	117.00	11.30

Table A2
Pressure peak results for wave 2.

Gauge ID	$p_{\max,C}$, Pa	U_{CT}, Pa	U_{CD}, Pa	U_{CP}, Pa	$p_{\max,E}$, Pa	U_{ET}, Pa
1	217.51	37.26	32.55	18.15	312.00	22.15
2	224.13	34.16	33.54	6.48	272.00	19.81
3	287.62	83.59	43.04	71.66	277.00	15.76
4	206.41	31.54	30.89	6.39	185.00	16.31
5	190.97	29.22	28.58	6.09	223.00	11.74
6	248.64	39.06	37.20	11.89	298.00	12.60
7	295.03	46.53	44.15	14.69	424.00	27.91
8	243.91	37.13	36.50	6.85	367.00	17.55
9	158.58	24.65	23.73	6.69	307.00	18.26
10	279.21	59.03	41.78	41.70	248.00	12.75

Table A3
Pressure peak results for wave 3.

Gauge ID	$p_{\max,C}$, Pa	U_{CT}, Pa	U_{CD}, Pa	U_{CP}, Pa	$p_{\max,E}$, Pa	U_{ET}, Pa
1	385.93	23.06	20.30	10.94	407.00	16.81
2	420.63	23.84	22.12	8.88	409.00	16.12
3	456.87	28.15	24.03	14.66	420.00	17.15
4	288.67	17.66	15.18	9.02	244.00	18.89
5	241.12	17.49	12.68	12.04	271.00	11.44
6	332.49	21.39	17.49	12.32	346.00	14.50
7	522.20	35.21	27.46	22.04	541.00	27.18
8	425.62	36.13	22.38	28.36	452.00	16.12
9	318.71	23.54	16.76	16.53	413.00	15.04
10	339.52	20.77	17.86	10.61	348.00	14.53

Table A4
Pressure peak results for wave 4.

Gauge ID	$p_{\max,C}$, Pa	U_{CT}, Pa	U_{CD}, Pa	U_{CP}, Pa	$p_{\max,E}$, Pa	U_{ET}, Pa
1	259.10	34.24	32.78	9.89	254.00	17.11
2	250.67	37.25	31.71	19.54	204.00	16.01
3	201.02	27.07	25.43	9.26	159.00	13.87
4	169.31	21.62	21.42	2.95	141.00	16.17
5	160.91	23.66	20.36	12.05	135.00	10.90
6	185.47	24.70	23.46	7.72	207.00	12.64
7	329.82	46.27	41.73	19.99	373.00	27.21
8	227.19	29.67	28.74	7.36	172.00	12.84
9	174.71	22.55	22.10	4.47	209.00	10.54
10	215.57	28.11	27.27	6.80	172.00	11.61

Table A5
Pressure peak results for wave 5.

Gauge ID	$p_{\max,C}$, Pa	U_{CT}, Pa	U_{CD}, Pa	U_{CP}, Pa	$p_{\max,E}$, Pa	U_{ET}, Pa
1	340.91	9.28	7.63	5.29	360.00	20.15
2	339.31	9.19	7.59	5.18	310.00	16.01
3	373.49	10.82	8.36	6.88	306.00	13.42
4	300.17	9.41	6.72	6.59	278.00	22.48
5	220.82	8.12	4.94	6.44	270.00	12.78
6	319.33	15.67	7.14	13.95	262.00	12.99
7	756.78	72.07	16.93	70.06	757.00	35.95
8	543.68	38.66	12.16	36.70	388.00	17.11
9	311.14	8.13	6.96	4.21	397.00	11.08
10	281.68	8.27	6.30	5.36	279.00	12.08

Table A6
Pressure peak results for wave 6.

Gauge ID	$p_{\max,C}$, Pa	U_{CT}, Pa	U_{CD}, Pa	U_{CP}, Pa	$p_{\max,E}$, Pa	U_{ET}, Pa
1	472.46	177.72	169.35	53.92	450.00	27.14
2	473.75	176.85	169.81	49.39	390.00	23.25
3	397.45	143.55	142.46	17.66	356.00	18.60
4	507.24	183.41	181.81	24.12	414.00	31.39
5	376.76	137.54	135.05	26.06	381.00	20.42
6	449.28	167.66	161.04	46.65	422.00	14.67
7	1515.21	599.12	543.11	252.93	1183.00	67.99
8	1618.54	762.50	580.15	494.81	625.00	18.74
9	567.73	205.30	203.49	27.17	588.00	13.91
10	376.77	140.75	135.05	39.65	270.00	12.38

Table A7
Pressure peak results for wave 7.

Gauge ID	$p_{\max,C}$, Pa	U_{CT}, Pa	U_{CD}, Pa	U_{CP}, Pa	$p_{\max,E}$, Pa	U_{ET}, Pa
1	349.21	9.15	5.04	7.63	529.00	39.67
2	321.73	13.29	4.64	12.45	479.00	20.43
3	333.95	9.44	4.82	8.11	478.00	20.77
4	345.99	12.41	4.99	11.36	618.00	44.59
5	266.71	6.72	3.85	5.50	564.00	16.99
6	308.68	10.57	4.46	9.59	477.00	13.32
7	801.19	133.25	11.56	132.75	1390.00	69.72
8	502.13	25.91	7.25	24.87	808.00	16.73
9	298.24	6.79	4.30	5.26	538.00	12.65
10	265.99	6.59	3.84	5.36	424.00	13.20

Table A8
Pressure peak results for wave 8.

Gauge ID	$p_{\max,C}$, Pa	U_{CT}, Pa	U_{CD}, Pa	U_{CP}, Pa	$p_{\max,E}$, Pa	U_{ET}, Pa
1	482.15	11.23	1.11	11.17	555.00	23.30
2	427.90	17.32	0.99	17.29	638.00	24.35
3	448.10	28.21	1.03	28.19	520.00	23.09
4	645.67	15.46	1.49	15.39	793.00	40.47
5	479.41	6.84	1.11	6.75	688.00	20.56
6	522.08	16.02	1.20	15.98	640.00	16.65
7	1695.05	311.41	3.91	311.39	1943.00	55.10
8	992.93	45.14	2.29	45.08	1048.00	31.46
9	628.03	15.94	1.45	15.87	699.00	20.66
10	487.77	10.80	1.12	10.74	593.00	20.83

Table A9
Pressure peak results for wave 9.

Gauge ID	$p_{\max,C}$, Pa	U_{CT}, Pa	U_{CD}, Pa	U_{CP}, Pa	$p_{\max,E}$, Pa	U_{ET}, Pa
1	596.71	51.93	48.76	17.88	670.00	41.02
2	652.95	55.40	53.36	14.91	724.00	29.57
3	580.83	49.43	47.46	13.80	593.00	24.23
4	846.06	72.93	69.13	23.21	939.00	44.75
5	719.55	61.81	58.80	19.06	857.00	20.05
6	774.05	64.49	63.25	12.59	776.00	21.67
7	3697.68	655.71	302.15	581.94	2498.00	112.74
8	1877.29	206.91	153.40	138.86	1357.00	36.96
9	1069.49	92.66	87.39	30.79	977.00	38.47
10	791.68	65.44	64.69	9.84	697.00	26.35

A.2. Pressure integral results

Table A10
Pressure integral results for wave 1.

Gauge ID	P_C, Pa s	U_{CT}, Pa s	U_{CD}, Pa s	U_{CP}, Pa s	P_E, Pa s	U_{ET}, Pa s
1	47.52	0.85	0.17	0.84	71.57	11.68
2	44.09	0.89	0.16	0.88	63.22	10.42
3	34.75	0.91	0.13	0.90	47.37	7.43
4	69.44	0.87	0.25	0.84	71.96	9.10
5	65.86	0.59	0.24	0.54	47.15	6.18
6	58.34	0.80	0.21	0.77	100.35	5.16
7	80.47	0.72	0.29	0.66	81.61	3.83
8	77.13	1.12	0.28	1.08	79.12	3.75
9	52.09	1.59	0.19	1.58	74.26	2.65
10	52.57	0.64	0.19	0.61	44.88	4.45

Table A11
Pressure integral results for wave 2.

Gauge ID	P_C, Pa s	U_{CT}, Pa s	U_{CD}, Pa s	U_{CP}, Pa s	P_E, Pa s	U_{ET}, Pa s
1	99.74	11.96	11.39	3.62	139.56	16.38
2	89.01	10.40	10.17	2.16	124.41	13.97
3	78.44	10.25	8.96	4.97	105.65	5.44
4	110.06	12.87	12.57	2.77	130.15	7.31
5	108.17	12.59	12.36	2.43	110.00	3.08
6	108.69	12.49	12.42	1.37	152.58	1.83
7	145.92	17.36	16.67	4.84	202.38	3.08
8	140.51	16.26	16.05	2.57	180.32	4.02
9	113.34	13.41	12.95	3.50	170.46	3.22
10	100.72	11.77	11.51	2.48	142.34	7.51

Table A12
Pressure integral results for wave 3.

Gauge ID	P_C, Pa s	U_{CT}, Pa s	U_{CD}, Pa s	U_{CP}, Pa s	P_E, Pa s	U_{ET}, Pa s
1	152.55	13.42	12.96	3.48	191.71	4.59
2	148.23	13.11	12.60	3.62	178.96	3.55
3	135.35	11.85	11.50	2.86	156.00	7.72
4	159.21	13.94	13.53	3.37	167.67	6.32
5	152.89	13.16	12.99	2.08	146.54	1.76
6	147.28	12.81	12.52	2.73	183.92	2.75
7	218.97	18.80	18.61	2.68	245.51	7.48
8	206.77	18.10	17.57	4.33	225.16	9.04
9	171.43	15.15	14.57	4.14	204.30	5.15
10	143.22	12.35	12.17	2.07	160.71	2.46

Table A13
Pressure integral results for wave 4.

Gauge ID	P_C, Pa s	U_{CT}, Pa s	U_{CD}, Pa s	U_{CP}, Pa s	P_E, Pa s	U_{ET}, Pa s
1	107.27	22.37	22.24	2.42	119.08	8.85
2	104.79	21.90	21.72	2.79	112.43	5.74
3	90.96	19.15	18.86	3.35	95.59	4.13
4	118.34	24.64	24.53	2.32	114.77	8.10
5	113.80	23.85	23.59	3.55	75.41	4.15
6	112.86	23.98	23.40	5.27	141.68	1.41
7	160.76	33.46	33.32	2.96	163.19	8.00

Table A13 (*continued*)

Gauge ID	P_C, Pa s	U_{CT}, Pa s	U_{CD}, Pa s	U_{CP}, Pa s	P_E, Pa s	U_{ET}, Pa s
8	141.36	29.42	29.30	2.59	112.17	11.15
9	122.60	26.17	25.41	6.26	117.99	9.41
10	110.28	23.22	22.86	4.10	106.96	2.80

Table A14
Pressure integral results for wave 5.

Gauge ID	P_C, Pa s	U_{CT}, Pa s	U_{CD}, Pa s	U_{CP}, Pa s	P_E, Pa s	U_{ET}, Pa s
1	138.80	6.37	6.11	1.80	127.59	17.02
2	139.27	6.52	6.13	2.21	120.27	17.11
3	125.99	5.93	5.55	2.09	118.51	15.49
4	148.84	6.99	6.55	2.44	157.94	10.25
5	143.80	7.00	6.33	2.98	137.86	3.08
6	137.18	6.95	6.04	3.44	135.83	2.31
7	243.18	11.91	10.70	5.22	294.40	5.99
8	224.98	10.54	9.90	3.61	217.40	3.54
9	178.82	8.71	7.87	3.72	211.75	2.82
10	130.81	6.45	5.76	2.90	130.15	20.70

Table A15
Pressure integral results for wave 6.

Gauge ID	P_C, Pa s	U_{CT}, Pa s	U_{CD}, Pa s	U_{CP}, Pa s	P_E, Pa s	U_{ET}, Pa s
1	192.48	30.88	30.75	2.82	168.38	19.74
2	182.24	29.32	29.12	3.43	163.53	19.25
3	156.74	25.33	25.04	3.78	140.47	6.80
4	197.39	32.31	31.54	7.01	193.44	13.82
5	192.70	31.58	30.79	7.04	232.45	19.51
6	185.06	29.98	29.57	4.94	198.40	16.85
7	361.07	58.04	57.69	6.41	415.91	10.43
8	332.94	53.78	53.19	7.94	332.86	12.63
9	262.31	42.14	41.91	4.40	327.00	6.18
10	155.51	26.09	24.85	7.95	134.95	2.99

Table A16
Pressure integral results for wave 7.

Gauge ID	P_C, Pa s	U_{CT}, Pa s	U_{CD}, Pa s	U_{CP}, Pa s	P_E, Pa s	U_{ET}, Pa s
1	158.47	3.27	0.51	3.23	234.89	11.51
2	154.73	2.53	0.50	2.48	222.80	8.79
3	140.76	2.93	0.45	2.90	210.26	12.02
4	183.33	3.91	0.59	3.87	279.12	21.62
5	182.57	2.32	0.59	2.24	303.16	6.69
6	169.02	4.19	0.54	4.16	272.94	6.48
7	304.56	6.80	0.98	6.73	529.92	8.32
8	266.56	3.89	0.86	3.79	427.49	6.72
9	222.36	2.44	0.71	2.33	366.28	4.14
10	158.95	2.69	0.51	2.64	194.10	3.80

Table A17
Pressure integral results for wave 8.

Gauge ID	P_C, Pa s	U_{CT}, Pa s	U_{CD}, Pa s	U_{CP}, Pa s	P_E, Pa s	U_{ET}, Pa s
1	263.23	5.78	0.07	5.78	322.13	18.72
2	242.58	7.85	0.07	7.85	329.91	13.27
3	221.99	5.70	0.06	5.70	276.22	15.84
4	311.79	4.72	0.08	4.72	397.30	26.77
5	305.47	3.80	0.08	3.80	411.73	9.18
6	279.10	3.64	0.08	3.64	410.62	7.44
7	508.78	11.36	0.14	11.36	693.53	23.35
8	455.81	7.82	0.12	7.82	551.77	13.61
9	378.50	5.88	0.10	5.88	479.35	8.50
10	250.51	3.85	0.07	3.85	278.32	5.50

Table A18
Pressure integral results for wave 9.

Gauge ID	P_C, Pa s	U_{CT}, Pa s	U_{CD}, Pa s	U_{CP}, Pa s	P_E, Pa s	U_{ET}, Pa s
1	347.14	8.97	6.50	6.18	412.80	13.40
2	339.30	9.75	6.35	7.40	422.13	15.10
3	302.76	8.63	5.67	6.51	377.98	19.25
4	452.83	10.91	8.48	6.87	511.01	26.72
5	443.78	10.25	8.31	6.00	523.13	16.85
6	406.69	9.61	7.61	5.87	508.34	9.43
7	727.35	19.11	13.62	13.41	843.18	16.82
8	632.93	14.63	11.85	8.59	690.75	26.37
9	522.18	13.17	9.77	8.83	585.76	14.96
10	378.33	9.45	7.08	6.25	360.47	18.52

References

Eça, L., Hoekstra, M., 2008. Code verification of unsteady flow solvers with the method of the manufactured solutions. Int. J. Offshore Polar Eng. 18 (2).

Eça, L., Hoekstra, M., 2014. A procedure for the estimation of the numerical uncertainty of CFD calculations based on grid refinement studies. J. Comput. Phys. 262, 104–130. https://doi.org/10.1016/j.jcp.2014.01.006.

Greco, M., Lugni, C., 2012. 3-D seakeeping analysis with water on deck and slamming. Part 1: numerical solver. J. Fluids Struct. 33, 127–147. https://doi.org/10.1016/j.jfluidstructs.2012.04.005. GotoISI://WOS:000307413200008.

Greco, M., Bouscasse, B., Lugni, C., 2012. 3-D seakeeping analysis with water on deck and slamming. Part 2: experiments and physical investigation. J. Fluids Struct. 33, 127–147. https://doi.org/10.1016/j.jfluidstructs.2012.04.005. GotoISI://WOS:000307413200008.

Jasak, H., 1996. Error Analysis and Estimation for the Finite Volume Method with Applications to Fluid Flows. Ph.D. thesis. Imperial College of Science, Technology & Medicine, London.

Jasak, H., 2009. OpenFOAM: open source CFD in research and industry. Int. J. Nav. Archit. Ocean Eng. 1 (2), 89–94.

Jasak, H., Gatin, I., Vukčević, V., 2014. Numerical simulation of wave loading on static offshore structures. In: 11th World Congress on Computational Mechanics (WCCM XI), pp. 5151–5159.

Jasak, H., Vukčević, V., Gatin, I., 2015. Numerical Simulation of Wave Loads on Static Offshore Structures, in: CFD for Wind and Tidal Offshore Turbines. Springer Tracts in Mechanical Engineering, pp. 95–105.

Joga, R., Saripilli, J., Dhavalikar, S., Kar, A., 2014. Numerical simulations to compute rate of water ingress into open holds due to green waters. In: Proceedings of the 24th International Offshore and Polar Engineering Conference ISOPE, Busan, Korea.

Kim, S., Kim, C., Cronin, D., 2013. Green water impact loads on breakwaters of large container carriers. In: Proceedings of the 12th International Symposium on Practical Design of Ships and Other Floating Structures PRADS, Changwon, Korea.

Lee, H.-H., Lim, H.-J., Rhee, S.H., 2012. Experimental investigation of green water on deck for a CFD validation database. Ocean. Eng. 42, 47–60. https://doi.org/10.1016/j.oceaneng.2011.12.026.

Lu, H., Yang, C., Loehner, R., 2012. Numerical Studies of Green Water Impact on Fixed and Moving Bodies. International Society of Offshore and Polar Engineers, p. 22.

Pakozdi, C., Östman, A., Stansberg, C., Carvalho, D., 2014. Green water on FPSO analyzed by a coupled Potential-Flow-NS- VOF method. In: Proceedings of the 33rd International Conference on Ocean. Offshore and Arctic Engineering OMAE, San Francisco, USA.

Rienecker, M.M., Fenton, J.D., 1981. A Fourier approximation method for steady water waves. J. Fluid Mech. 104, 119–137.

Roenby, J., Bredmose, H., Jasak, H., 2016. A computational method for sharp interface advection. Open Sci. 3 (11) https://doi.org/10.1098/rsos.160405.

Ruggeri, F., Wata, R., Brisson, H., Mello, P., Sampaio Carvalho e Silva, C., Vieira, D., 2013. Numerical prediction of green water events in beam seas. In: Proceedings of the 12th International Symposium on Practical Design of Ships and Other Floating Structures PRADS, Changwon, Korea.

Rusche, H., 2002. Computational Fluid Dynamics of Dispersed Two - Phase Flows at High Phase Fractions. Ph.D. thesis. Imperial College of Science, Technology & Medicine, London.

Temarel, P., Bai, W., Bruns, A., Derbanne, Q., Dessi, D., Dhavalikar, S., Fonseca, N., Fukasawa, T., Gu, X., Nestegard, A., Papanikolaou, A., Parunov, J., Song, K.H., Wang, S., 2016. Prediction of wave-induced loads on ships: progress and challenges. Ocean. Eng. 119, 274–308.

Vukčević, V., 2016. Numerical Modelling of Coupled Potential and Viscous Flow for Marine Applications. Ph.D. thesis. Faculty of Mechanical Engineering and Naval Architecture, University of Zagreb.

Vukčević, V., Jasak, H., Malenica, S., 2015. Assessment of higher–order forces on a vertical cylinder with decomposition model based on swense method. In: Numerical Towing Tank Symposium.

Vukčević, V., Jasak, H., Gatin, I., Malenica, S., 2016. Seakeeping sensitivity studies using the decomposition CFD model based on the Ghost fluid method. In: Proceedings of the 31st Symposium on Naval Hydrodynamics.

Vukčević, V., Jasak, H., Gatin, I., 2017. Implementation of the Ghost fluid method for free surface flows in polyhedral finite volume framework. Comput. Fluids 153, 1–19.

Weller, H.G., Tabor, G., Jasak, H., Fureby, C., 1998. A tensorial approach to computational continuum mechanics using object oriented techniques. Comput. Phys. 12, 620–631.

Xu, H., 2013. Numerical Simulation of Breaking Wave Impact on the Structure. Ph.D. thesis. National University of Singapore, Singapore (.

Zhao, X., Ye, Z., Fu, Y., 2014. Green water loading on a floating structure with degree of freedom effects. J. Mar. Sci. Technol. 19, 302–313. https://doi.org/10.1007/s00773-013-0249-7.

Zhu, R.C., Miao, G.P., Lin, Z.W., 2009. Numerical research on FPSOs with green water occurrence. J. Ship Res. 53 (1), 7–18. GotoISI://WOS:000265900000002.

Statement of author contribution for PAPER 5

Inno Gatin is the main author of paper "CFD verification and validation of green sea loads" published in Ocean Engineering, 2017;148:500-515.

In this paper the verification and validation were performed by Gatin. Seo and Rhee post–processed and supplied the experimental data. The paper was written by Gatin and reviewed by Jasak and Vukčević.

Co–authors:

Vuko Vukčević

Hrvoje Jasak

Jeonghwa Seo

서정화

Shin Hyung Rhee

PAPER 6

Finite Volume Method for General Compressible Naval Hydrodynamics

Inno Gatin[a], Shengnan Liu[b], Vuko Vukčević[a], Hrvoje Jasak[a,c,*]

[a] University of Zagreb, Faculty of Mechanical Engineering and Naval Architecture, Ivana Lučića 5, Zagreb, Croatia
[b] University of Stavanger, Faculty of Science and Technology, Stavanger, Norway
[c] Wikki Ltd, 459 Southbank House, SE1 7SJ, London, United Kingdom

---

Abstract

An efficient, pressure–based segregated Finite Volume solution method for two–phase free surface flow simulations including compressibility effects is presented in this paper. Incompressible treatment of the heavier phase enables efficient long evolutions of wave fields without the need for a separate solver for handling wave field evolution. Air is treated as an ideal gas undergoing isentropic compression/expansion, removing the need for an additional energy equation, and related numerical difficulties. The discontinuity in properties at the free surface between the two phases is treated using the Ghost Fluid Method, correctly accounting for the abrupt change in density and compressibility.

Detailed verification and validation is conduced on three simple test cases comprising a liquid piston, free fall impact of a horizontal water column and a regular wave propagation to test the stability and accuracy for cases with and without significant compressibility effects. The present approach is compared with the incompressible formulation for industrial–grade simulations, showing that the same level of accuracy can be achieved without significant overhead in computational time. Finally, a compressible wave breaking impact from a large–scale experimental campaign is reproduced, showing that the method is capable of capturing trapped air cushioning effects with good

---

[*] Corresponding author.

Email addresses: `inno.gatin@fsb.hr` (Inno Gatin), `shengnan.liu@uis.no` (Shengnan Liu), `vuko.vukcevic@fsb.hr` (Vuko Vukčević), `h.jasak@wikki.co.uk` (Hrvoje Jasak), `hrvoje.jasak@fsb.hr` (Hrvoje Jasak)

Preprint submitted to Ocean Engineering *June 6, 2018*

accuracy where it is essential to account for compressibility of the gas phase.

Keywords: Compressible Two Phase Model, Finite Volume, Pressure Based, Validation, Wave Impact, Green Sea, Ghost Fluid Method.

1. Introduction

In the field of computational naval hydrodynamics the issue of compressible two phase flow presents a significant computational challenge. Application of Computational Fluid Dynamics (CFD) for resolving violent events where air compressibility plays an important role is becoming more popular, where the simulation objective is to assess structural loads of exposed structures. Typical problems involving air compressibility are sloshing, slamming and violent wave impacts. In such events, compressible behaviour of air entrained between the water and structure has an important influence in the overall structural loading [1, 2]. Thus, numerical methods have been developed in order to address this problem. Numerous approaches exist, with two most prominent groups being the Smoothed Particle Hydrodynamics (SPH) and the Finite Volume (FV) approach.

An abundance of SPH methods have been successfully applied to two–phase compressible flow, producing realistic and accurate results when compared to experimental and analytical data. Guilcher et al. [3] investigated scale effects on a wave impact against a wall with trapped air pockets, successfully applying the compressible SPH method. In another publication, Guilcher et al. [4] showed a validation of the approach on benchmark cases, namely the liquid piston case and free–falling water column, which will be used in this study as well. Luo et al. [5, 6] used a Consistent Particle Method to simulate wave breaking with trapped air pocket and sloshing in two connected tanks, showing good agreement with the experiment. Rostami and Ketabdari [7] validated their weakly compressible SPH method on a 2D dam break with horizontal column impact, However, no trapped air pockets were investigated. Lind et al. [8] showed a novel SPH method with a sharp interface treatment, validated on a dam break case with a trapped air pocket.

Despite the fact that SPH method can be used to effectively simulate aerated wave impacts and related phenomena, it remains computationally expensive for industrial applications. Furthermore, simulating complex geometries such as ships with superstructure becomes a problem, as well as accurate integration of 6–degrees–of–freedom motion of a floating object due to difficulties in treating of impermeable boundary conditions. For this reason the industry and research increasingly focuses their effort in developing FV based methods which are computationally more efficient for this type of application and allow consistent treatment of boundary conditions, while automatic grid generation tools provide body–fitted grids for the most intricate geometries. FV based methods have their respective challenges and problems which must be recognized. Treatment of an infinitesimally sharp interface between the two phases poses the most challenging issue. Nonetheless, there is an increasing number of publications dealing with development and application of FV methods for compressible two–phase flow in naval hydrodynamics.

Braeunig et al. [9] used a FV based numerical method to explore the possibility of exact scaling between model–scale and full–scale LNG sloshing and derived the gas properties that should be used in model scale to ensure good quality scaling. Dumbser [10] developed a pressure–based higher order WENO FV method for compressible two–phase flow. The method is validated on a number of dam–break cases comparing the results to experiments and shallow water flow theory. Plumerault et al. [11] developed a pressure–based two–phase compressible method that allows aerated water flow, which can be very important in highly violent wave impacts. The method is validated against experimental results for a wave impact against a wall with entrained air. Costes at al. [12] used a nonlinear potential flow based numerical method in conjunction with a compressible two–phase FV method to simulate wave impact with trapped air pocket. The potential flow solver is used to propagate the wave field, while the more expensive FV compressible method is used only in the vicinity of the structure. Miller et al. [13] developed a compressible pressure–based two–phase method specialised for simulating underwater explosions, where both air and water compressibility play an important role. Mixture–momentum formulation is used where compressibility properties are smeared across the interface using the VOF field. A three–dimensional shallow water explosion simulation is shown, where mass is not fully conserved. Ma et al. [14] developed a higher–order FV method for handling aerated two–phase wave impacts, where the dispersion of air in water is handled with the Volume of Fluid approach. The method proved accurate for fundamental cases as well as for a 2D wave impact case with trapped air pocket. The approach was also used to study rigid plate entry [15] where the influence of aeration was investigated experimentally and numerically, showing good agreement between the two sets of results. Furthermore, sloshing with trapped air effects is investigated in a de-pressurised tank with experimental comparison [16], showing once more the accuracy of the presented numerical approach. However, the drawback of higher–order numerical schemes is that they generally suffer from instabilities and are computationally more expensive. Calderón–Aánchez et al. [17] investigated a free fall of a horizontal water column with rectangular cross–section using OpenFOAM software, where the compressibility is explicitly accounted for. The ability of the code to capture compressible impact effects on this simple canonical case is demonstrated for various density ratios between the two phases. Zou et al. [18] used a commercial software FLUENT to investigate the effects of viscosity and air compressibility on violent sloshing events, concluding that lower impact pressures are obtained when a compressible air model is used as opposed to the incompressible model. Lyu et al. [19] investigated different interface capturing methods in a FV framework for simulating sloshing impacts, where both compressible and incompressible methods are used. They concluded that Volume of Fluid (VOF) based interface capturing is the most suitable to predict the motion of the liquid and pressure loads.

The objective of this study is to devise a two–phase flow model based on the FV method, where one phase is a compressible gas, while the other is an incompressible liquid, which could tackle industrial–grade simulations in terms of stability, efficiency and accuracy. The framework is designed in a way to provide a variety of computational features in a single program, to enable performing simulations that include wave propagation, rigid body motion of floating objects and compressible wave impact effects. In addition, in cases where compressibility effects are negligible, the method should perform equivalently to its incompressible counterpart [20]. In this manner, a single code can be applied to a wide variety of problems in naval hydrodynamics. It is for this reason that the present numerical framework will be tested on realistic 3D cases such as seakeeping of a container vessel in head seas, in addition to canonical cases which will be used for verification and validation of the method.

The numerical model presented in this paper is based on the two–phase, incompressible flow model developed by Vukčević et al. [20], which uses the Ghost Fluid Method (GFM) to implicitly discretise the free surface boundary conditions across the interface. The formulation provides a numerically sharp interface which handles the jump in pressure gradient and density across the interface. The approach offers a balanced treatment of pressure and density gradient terms in the momentum and the pressure equation, which removes the problem of spurious air velocities. Since air is considered compressible in this study, additional effort is employed to formulate a compressible GFM formulation in order to account for the abrupt change in compressibility of the two phases. The mathematical derivation and numerical implementation of the compressible GFM is described in detail in the two following sections. The gas phase is modelled as an isentropic ideal gas to produce a stable formulation of the pressure equation in low–Mach number regimes and removes the need to solve the conditional energy equation. This assumption is justified for the following reasons that are specific to naval hydrodynamics:

- Compressibility effects in naval hydrodynamics of interest here are related to volumetric compression of air by the liquid phase. This type of phenomena are highly transient, a few–hundred millisecond in duration [2], rendering any heat transfer between the trapped air pocket and the surrounding water negligible,
- Heat transfer rate between air and water is low for problems under consideration, thus a large temperature difference is needed to drive significant amount of heat from one fluid to the other. In the event of trapped air pocket, the temperature rise is not significant [16],
- In the event when there is sufficient time for significant heat transfer, there is no temperature difference between air and water to drive it, since in most naval hydrodynamic phenomena the temperature difference between air and water is small or zero.

The liquid phase is considered ideally incompressible, which facilitates the handling of mass conservation and avoids a plethora of numerical problems related to high speed of sound in liquids. The present approach is focused on volumetric compressibility effects that are important in naval hydrodynamics. Thus, pressure shock propagation in the liquid is not considered since it is not relevant for applications in this field. Furthermore, resolving pressure shocks requires temporal and spatial resolution that are prohibitive for everyday industrial use. The present numerical framework enables running the simulations at Courant numbers well above one, as will be demonstrated in

Sec. 5.2.

In the second and third section of the paper the mathematical and numerical model of the two–phase incompressible/compressible formulation is presented in detail. The derivation of the specialised interface–corrected discretisation schemes is shown in the FV framework. The fourth section is dedicated to verification and validation, where three canonical cases are conducted: i) liquid piston 1D case, testing the basic capability of the code to correctly account for compression of air and to conserve energy and mass; ii) a falling water column 2D case is performed with a high pressure impact in order to assure that the present approach can tackle violent compressibility effects; iii) in the third test case the accuracy and precision of the code to propagate a regular wave field is tested where no compressibility effects are present, including an extensive grid and time–step convergence study. The fifth section is dedicated to testing the numerical framework for more complex, three–dimensional cases that are more realistic in terms of industrial application. Two cases are considered here: a green sea loading case where pressure results are compared to experiments and to the solution of the incompressible solution; and a head waves seakeeping case of a containter vessel, comparing motion and total resistance to incompressible solution and experimental results. Computational time is also compared between compressible and incompressible formulation, showing no significant overhead. Finally, a compressible breaking wave impact is simulated where the results are compared to a large–scale experimental data. The paper is completed with an overview of the study and conclusions.

2. Mathematical Model

In this section the governing equations of viscous, turbulent, two–phase flow with compressible gas phase and incompressible liquid phase which are mutually immiscible are given. The equations governing both phases are combined into a single set of equations, where the Ghost Fluid Method (GFM) [21, 22, 23, 24, 25, 26, 27] is employed to account for the discontinuity of fluid properties across the interface. The mathematical model presented in this section represents an extension of the GFM for incompressible two–phase model shown in [20] to a special case where one phase is compressible and the other incompressible.

In the following text, governing equations for incompressible and compressible phase will be considered separately, followed by a description of the unified mathematical model for both phases. Finally, the mathematical formulation of the jump conditions at the free surface is given.

2.1. Incompressible phase

For single–phase, incompressible, viscous and turbulent flow used in this study the continuity equation reads:

$$\nabla\bullet\mathbf{u} = 0\,, \tag{1}$$

where $\mathbf{u}$ denotes the velocity field. Following Vukčević et al [20] the momentum equation can be written as:

$$\frac{\partial\mathbf{u}}{\partial t} + \nabla\bullet(\mathbf{u}\mathbf{u}) - \nabla\bullet(\mathbf{R}) = -\frac{1}{\rho_I}\nabla p + \mathbf{g}\,, \tag{2}$$

where $\mathbf{R}$ stands for the Reynolds stress tensor, accounting for general turbulence modelling. ρ_I is the constant density field of the incompressible fluid, $\mathbf{g}$ is gravitational acceleration while p stands for pressure field. For simulations in this study Reynolds Averaged Navier–Stokes model is used yielding the following momentum conservation equation:

$$\frac{\partial\mathbf{u}}{\partial t} + \nabla\bullet(\mathbf{u}\mathbf{u}) - \nabla\bullet\left(\nu_e\nabla\mathbf{u}\right) = -\frac{1}{\rho_I}\nabla p + \mathbf{g}\,, \tag{3}$$

where ν_e stands for effective cinematic viscosity, comprised of fluid kinematic viscosity and turbulent viscosity.

2.2. Compressible phase

For general compressible flow, the mass conservation equation states:

$$\frac{\partial\rho_c}{\partial t} + \nabla\bullet\left(\rho_c\mathbf{u}\right) = 0\,, \tag{4}$$

where ρ_c denotes the density field of the compressible fluid. 4 can be written in the following form:

$$\nabla\bullet\mathbf{u} = -\frac{1}{\rho_c}\left(\frac{\partial\rho_c}{\partial t} + \mathbf{u}\bullet\nabla\rho_c\right)\,. \tag{5}$$

Note that the right hand side of Eqn. 5 presents the difference between the compressible and incompressible conservation of mass. The momentum conservation equation for the compressible phase can be written as:

$$\frac{\partial\left(\rho_c \mathbf{u}\right)}{\partial t} + \nabla\bullet(\rho_c \mathbf{u}\mathbf{u}) - \nabla\mathbf{u}\bullet\nabla\mu_e - \nabla\bullet\left(\mu_e \nabla\mathbf{u}\right) = -\nabla p + \rho_c \mathbf{g}\,, \tag{6}$$

where μ_e stands for effective dynamic viscosity. Following Vukčević et al [20] pressure is decomposed into dynamic and static part:

$$p = p_d + \rho_c \mathbf{g}\bullet\mathbf{x}\,, \tag{7}$$

where $\mathbf{x}$ stands for the position vector. Introducing Eqn. 7 into Eqn. 6 reads:

$$\frac{\partial \rho_c \mathbf{u}}{\partial t} + \nabla\bullet(\rho_c \mathbf{u}\mathbf{u}) - \nabla\mathbf{u}\cdot\nabla\mu_e - \nabla\bullet\left(\mu_e \nabla\mathbf{u}\right) = -\nabla p_d - \nabla\rho_c \mathbf{g}\cdot\mathbf{x}\,. \tag{8}$$

By applying the chain rule on Eqn. 8, introducing Eqn. 5 and normalising with ρ_c the following form is obtained:

$$\begin{aligned} \frac{\partial \mathbf{u}}{\partial t} + \nabla\bullet(\mathbf{u}\mathbf{u}) - \frac{1}{\rho_c}\nabla\mathbf{u}\cdot\nabla\mu_e - \frac{1}{\rho_c}\nabla\bullet\left(\mu_e \nabla\mathbf{u}\right) - \mathbf{u}\nabla\bullet\mathbf{u} = \\ -\frac{1}{\rho_c}\nabla p_d - \frac{1}{\rho_c}\nabla\rho_c \mathbf{g}\bullet\mathbf{x}\,. \end{aligned} \tag{9}$$

In order to close the system of equations governing the compressible flow, i.e. Eqn. 5 and Eqn. 9, appropriate equation of state must be chosen. Since the compressible phase is gas in this application, ideal gas model is employed. Furthermore, to avoid an additional energy conservation equation, isentropic compression/expansion of the gas phase is assumed. In naval hydrodynamics CFD, this assumption is valid for the following reasons:

1. Compressibility effects in naval hydrodynamics are short–lived; the heat transfer between gas and liquid is negligible,
2. Heat transfer intensity between air and water, which are of interest in naval hydrodynamics, is small. Therefore, a large temperature difference between the phases would be needed to drive a significant heat transfer across the interface,
3. In a majority of problems related to naval hydrodynamics, air and water have the same temperature, thus no significant heat transfer exists between the non–compressed air and water.

Under these assumptions the equation of state for an ideal gas undergoing adiabatic pressure compression/expansion reads:

$$\frac{p}{\rho_c^{\gamma}} = a_c = const.\,, \tag{10}$$

where γ denotes the constant ratio of specific heats while a_c stands for isentropic constant.

Capturing compressible pressure waves is not of importance in naval hydrodynamics, instead the volumetric compressible events are of interest. Thus, the goal is to be able to capture air compressibility in events of trapped gas pockets, where the gas is compressed due to a reduction of volume under the influence of forces acting on its boundary. Having this in mind, a pressure based method is developed in this study, where pressure related operators in Eqn. 5 need to be reformulated in terms of pressure as a working variable. A total derivative of ρ_c is expressed as:

$$\frac{\partial \rho_c}{\partial p} = \frac{1}{a_c \gamma}\left(\frac{p}{a_c}\right)^{\frac{1-\gamma}{\gamma}}\,, \tag{11}$$

assuming isentropic compression/expansion of an ideal gas. Applying Eqn. 11 on Eqn. 5 yields:

$$\nabla\bullet\mathbf{u} = -\frac{1}{\rho_c}\frac{\partial \rho_c}{\partial p}\left(\frac{\partial p}{\partial t} + \mathbf{u}\bullet\nabla p\right)\,. \tag{12}$$

Substituting Eqn. 7 into Eqn. 12 results in the final form of the compressible mass conservation equation:

$$\nabla\bullet\mathbf{u} = -\frac{1}{\rho_c}\frac{\partial \rho_c}{\partial p}\left(\frac{\partial p_d}{\partial t} + \nabla\bullet(p_d\mathbf{u}) - p_d\nabla\bullet\mathbf{u} + \frac{\partial\left(\rho_c\mathbf{g}\bullet\mathbf{x}\right)}{\partial t} + \mathbf{u}\bullet\nabla\rho_c\mathbf{g}\bullet\mathbf{x}\right)\,. \tag{13}$$

2.3. Two–phase formulation

In order to model two–phase flow, above equations need to be combined into a single equation set. Volume of Fluid (VOF) method [28, 29] is employed to handle interface capturing, where volume fraction fields α_k are used to differentiate between individual phases. Here, k is the phase index (I for incompressible phase and c for compressible). The conservation of mass for both phases states:

$$\frac{\partial\left(\alpha_k\rho_k\right)}{\partial t} + \nabla\bullet\left(\alpha_k\rho_k\mathbf{u}\right) = 0\,. \tag{14}$$

By definition, α_k is 1 when the cell is fully occupied by fluid k, and 0 when no fluid k is present in the cell. For two–phase flow it follows that $\alpha_c = 1 - \alpha_I$. Thus, it is only necessary to convect one fraction field while the other is defined algebraically. In this study, only the incompressible phase fraction field α_I is convected since it ensures mass conservation because the convecting velocity satisfies Eqn. 1.

Applying Eqn. 1 and $\rho_I = const.$ to Eqn. 14 yields:

$$\frac{\partial \alpha_I}{\partial t} + \nabla\bullet\left(\alpha_I \mathbf{u}\right) = 0\,. \tag{15}$$

Finally the combined, two–phase equations are obtained by multiplying equations for two phases with corresponding volume fraction fields and superimposing them. The combined two–phase conservation of mass equation is obtained by combining Eqn. 1 and Eqn. 13:

$$\begin{aligned}\nabla\bullet\mathbf{u} = -\left(1-\alpha_I\right)\frac{1}{\rho_c}\frac{\partial \rho_c}{\partial p}\Bigg(&\frac{\partial p_d}{\partial t} + \nabla\bullet(p_d\mathbf{u})\\ &- p_d\nabla\bullet\mathbf{u} + \frac{\partial\left(\rho_c\mathbf{g}\bullet\mathbf{x}\right)}{\partial t} + \mathbf{u}\bullet\nabla\rho_c\mathbf{g}\bullet\mathbf{x}\Bigg)\,.\end{aligned} \tag{16}$$

Note that the velocity field is considered continuous across the interface, i.e. $\mathbf{u}_c = \mathbf{u}_I$. The momentum equation is obtained in the same manner, using Eqn. 3 and Eqn. 9:

$$\begin{aligned}\frac{\partial \mathbf{u}}{\partial t} + \nabla\bullet(\mathbf{u}\mathbf{u}) - \frac{1}{\rho}\nabla\mathbf{u}\bullet\nabla\mu_e - \frac{1}{\rho}\nabla\bullet\left(\mu_e\Delta\mathbf{u}\right) =\\ -\frac{1}{\rho}\nabla p_d - \left(1-\alpha_I\right)\left(\frac{1}{\rho_c}\nabla\rho_c\mathbf{g}\cdot\mathbf{x} - \mathbf{u}\nabla\bullet\mathbf{u}\right)\,,\end{aligned} \tag{17}$$

where $\rho = \alpha_I\rho_I + \left(1-\alpha_c\right)\rho_c$. Eqns. 16, 17, 15 and 10 make a closed system of equations which model a two–phase liquid incompressible/gas compressible fluid. In order for the model to be numerically stable and robust, the discontinuities at the interface need to be accounted for.

2.4. Interface discontinuities and jump conditions in the presence of phase compressibility

Across the interface ρ and $\partial\rho_c/\partial p$ have a discontinuity which is non–trivial for numerical treatment. In this study the discontinuities are taken into account by employing the GFM developed by Vukčević et al. [20], and extending the implemented method for treatment of a compressible gas phase. The discontinuities, or the jump conditions can be written as [23, 24]:

$$[\rho] = \rho^- - \rho^+ \,, \tag{18}$$

$$\left[\frac{\partial \rho}{\partial p}\right] = \left(\frac{\partial \rho}{\partial p}\right)^- - \left(\frac{\partial \rho}{\partial p}\right)^+ \,, \tag{19}$$

where "+" denotes values infinitesimally close to the interface at the liquid side and "−" at the gas side. Note that $\partial\rho/\partial p^+ = 0$ since the liquid phase is considered incompressible. In effect Eqn. 19 expresses the jump in compressibility across the interface. Although viscosity has a jump across the interface as well, it will be considered continuous across the interface as discussed in [20], which is justified for high Reynolds number flows that are of interest.

Apart from the discontinuities of fluid properties, additional jump conditions arise from kinematic and dynamic free surface boundary conditions. If the surface tension effects are neglected, dynamic free surface boundary condition states that pressure must be continuous across the interface:

$$[p] = 0 \,. \tag{20}$$

Since the governing equations are written in terms of dynamic pressure p_d, Eqns. 20, 18 and 7 are combined to yield:

$$[p_d] = -\,[\rho]\,\mathbf{g}{\bullet}\mathbf{x} \,. \tag{21}$$

The kinematic free surface boundary condition states that the velocity field must be continuous across the interface:

$$[\mathbf{u}] = \mathbf{u}^- - \mathbf{u}^+ = 0 \,. \tag{22}$$

In addition to the above jump conditions, additional conditions arise from the jump of governing equations themselves [23, 24, 30]. As shown by Vukčević et al. [20], by applying the jump operator on Eqn. 3 an additional jump condition is obtained:

$$\left[\frac{1}{\rho}\nabla p_d\right] = 0 \,, \tag{23}$$

which states that the dynamic pressure gradient divided with density must remain continuous across the interface. For the combined momentum equation (Eqn. 17) applying the jump operator yields:

$$\left[\frac{1}{\rho}\nabla p_d\right] = \left[-\nabla\!\bullet(\mathbf{u}\mathbf{u}) + \mathbf{u}\nabla\!\bullet\mathbf{u} - \frac{1}{\rho}\nabla\rho\mathbf{g}\cdot\mathbf{x}\right], \tag{24}$$

where viscous terms vanished due to the assumption mentioned above. The jump of temporal term reduces to zero since the velocity is continuous across the interface. Expanding the right hand side with the jump operator and taking into account that $\mathbf{u}\nabla\!\bullet\mathbf{u}^{+} = 0$ and $\nabla\rho_I = 0$, yields:

$$\left[\frac{1}{\rho}\nabla p_d\right] = \left[-\nabla\!\bullet(\mathbf{u}\mathbf{u})\right] + (\mathbf{u}\nabla\!\bullet\mathbf{u})^{-} - \frac{1}{\rho_c^{-}}\nabla\rho_c^{-}\mathbf{g}\cdot\mathbf{x}\,. \tag{25}$$

According to Eqn. 24 the gradient of dynamic pressure divided by the density has a discontinuity across the interface stemming from the compressibility of the gas phase. The third term on the right hand side represents the jump due to possible nonlinear hydrostatic pressure caused by non–zero density gradient in the gas phase. The second term is proportional to divergence in the gas phase, which is a measure of compressibility of gas. It is straightforward to prove that $\mathbf{u}\nabla\!\bullet\mathbf{u}^{-}$ is not zero, i.e. $(\mathbf{u}\nabla\!\bullet\mathbf{u})^{-} \neq (\mathbf{u}\nabla\!\bullet\mathbf{u})^{+}$: if the jump operator is applied on Eqn. 16 the following is obtained:

$$\nabla\!\bullet\mathbf{u}^{-} = -\frac{1}{\rho_c^{-}}\left(\frac{\partial\rho_c}{\partial t}^{-} + \mathbf{u}\bullet\nabla\rho_c^{-}\right). \tag{26}$$

Despite the fact that the velocity field is continuous across the interface, the divergence of velocity has a jump due to compressibility of the gas phase. Generally, convection jump in Eqn. 25 is non–zero as well, and must be taken into account. Dynamic pressure gradient, convection and divergence of velocity jumps are interdependent and have a nonlinear relationship. Thus, an iterative approach must be employed in order to resolve the free surface boundary problem. In this study, existing nonlinear loops used to couple equations Eqn. 17 and Eqn. 16 are also used to converge the jump conditions as well.

The above equations present a set of conditions that need to be imposed on the governing equations whenever a mathematical operation is performed which uses informations from both sides of the interface. In the following text, numerical implementation of the above jump conditions is shown.

3. Numerical model

In this section the complete numerical model developed in this study is presented. First, discretisation of governing equations will be outlined, creating a basis for further development of numerical operators which satisfy the jump conditions. Implementation of all operators requiring jump conditions is also described.

3.1. Discretisation of Governing Equations

Collocated, FV method is used to discretise governing equations, Eqns. 17, 16 and 14 [31]. The notation in the following text adheres to Vukčević et al. [20], as shown in Fig. 1: $\mathbf{s}_f$ is the surface area vector of a face, while $\mathbf{d}_f$ stands for the vector from cell centre P to cell centre N, where P and N represent two adjacent cells that share a face. Terms enclosed in curly braces $\{\cdot\}$ indicate that implicit FV discretisation is used, while explicit evaluation is used for the remaining terms. For details on FV discretisation used in `foam-extend`, the reader is directed to [32, 28].

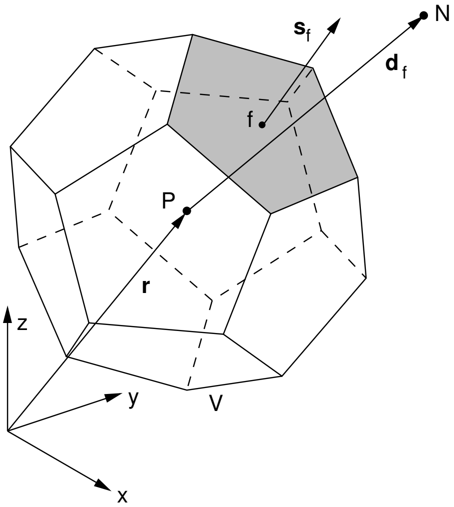

Fig. 1: Schematic representation of a polyhedral control volume P, which shares a face f with its immediate neighbour N.

The discretised form of Eqn. 17 states:

$$\begin{aligned} &\left\{\frac{\partial \mathbf{u}}{\partial t}\right\} + \{\nabla\bullet(\mathbf{u}\mathbf{u})\} - \left\{\frac{1}{\rho}\nabla\mathbf{u}\bullet\nabla\mu_e\right\} - \left\{\frac{1}{\rho}\nabla\bullet\left(\mu_e\nabla\mathbf{u}\right)\right\} = \\ &\qquad -\frac{1}{\rho}\nabla p_d - (1-\alpha_I)\left(\frac{1}{\rho_c}\nabla\rho_c\mathbf{g}\cdot\mathbf{x} - \{\mathbf{u}\nabla\bullet\mathbf{u}\}\right) . \end{aligned} \tag{27}$$

As stated in Sec. 2.4, temporal and viscous terms are continuous across the interface, and do not require special treatment. Convection, dynamic pressure gradient, density gradient and $\mathbf{u}\bullet\nabla\mathbf{u}$ terms require special treatment when calculated across the interface. For the conservation of mass, Eqn. 16, the discretised form can be written as:

$$\begin{aligned} \{\nabla\bullet\mathbf{u}\} &= -(1-\alpha_I)\frac{1}{\rho_c}\frac{\partial\rho_c}{\partial p}\left(\left\{\frac{\partial p_d}{\partial t}\right\} + \{\nabla\bullet(p_d\mathbf{u})\}\right. \\ &\qquad \left. - \{p_d\nabla\bullet\mathbf{u}\} + \frac{\partial\left(\rho_c\mathbf{g}\bullet\mathbf{x}\right)}{\partial t} + \mathbf{u}\bullet\nabla\rho_c\mathbf{g}\bullet\mathbf{x}\right) . \end{aligned} \tag{28}$$

Due to the discontinuities across the free surface, all terms in Eqn. 28 require special treatment. The pressure equation is obtained from Eqn. 28 following [32]. Discretised left hand side of conservation of mass, Eqn. 28, in integral form reads:

$$\int_{CV}\nabla\bullet\mathbf{u}\,\mathrm{d}V = \int_{\partial CV}\mathrm{d}\mathbf{s}\bullet\mathbf{u} = \sum_f \mathbf{s}_f\bullet\mathbf{u}_f\,, \tag{29}$$

where CV stands for the control volume, V is the cell volume, f is the control volume face index, $\mathrm{d}\mathbf{s}$ is the infinitesimal surface normal vector, while $\mathbf{s}_f$ stands for the face area vector. Cell–centred velocity is expressed by using the semi–discretised form of the momentum equation:

$$\mathbf{u}_P = \frac{\mathbf{H}(\mathbf{u}_N)}{a_P} - \frac{1}{\rho a_P}\left(\nabla p_d + \nabla\rho\mathbf{g}\bullet\mathbf{x}\right)\,, \tag{30}$$

where a_P denotes the summed diagonal coefficient for cell P, while $\mathbf{H}(\mathbf{u}_N)$ represents a linearised operator containing off–diagonal and source contribution resulting from the discretisation of implicit velocity operators. In order to substitute face centred velocity $\mathbf{u}_f$ using Eqn. 30, it must be interpolated to cell faces:

$$\mathbf{u}_f = \frac{\left(\mathbf{H}(\mathbf{u}_N)\right)_f}{\left(a_P\right)_f} - \left(\frac{1}{a_P}\right)_f\left(\frac{1}{\rho}\right)_{f_\Gamma}\left(\left(\nabla p_d\right)_{f_\Gamma} + \left(\nabla\rho\right)_{f_\Gamma}\mathbf{g}\bullet\mathbf{x}\right)\,, \tag{31}$$

where index f_Γ denotes terms that need special attention across the interface. By substituting Eqn. 31 into Eqn. 29, the discretised conservation of mass can be written as:

$$\begin{aligned}\sum_f \mathbf{s}_f \bullet \left(\frac{1}{a_P}\right)_f \left(\frac{1}{\rho}\right)_{f_\Gamma} (\nabla p_d)_{f_\Gamma} = & \\ \sum_f \mathbf{s}_f \bullet \left(\frac{(\mathbf{H}(\mathbf{u}_N))_f}{(a_P)_f} - \left(\frac{1}{\rho}\right)_{f_\Gamma} (\nabla \rho)_{f_\Gamma} \mathbf{g} \bullet \mathbf{x}\right) & \\ + \int_{CV} f_C\left(p_d, \rho\right) \mathrm{d}V \, , & \qquad (32)\end{aligned}$$

where

$$\begin{aligned}f_C\left(p_d, \rho\right) = & -\left(1 - \alpha_I\right) \frac{1}{\rho_c} \frac{\partial \rho_c}{\partial p} \left(\left\{ \frac{\partial p_d}{\partial t} \right\} + \left\{ \nabla \bullet (p_d \mathbf{u}) \right\} \right. \\ & \left. - \left\{ p_d \nabla \bullet \mathbf{u} \right\} + \frac{\partial \left(\rho_c \mathbf{g} \bullet \mathbf{x}\right)}{\partial t} + \mathbf{u} \bullet \nabla \rho_c \mathbf{g} \bullet \mathbf{x} \right) \, . \qquad (33)\end{aligned}$$

Below is a summary of all terms in Eqns, 27, 32 and 33, with comments on their treatment at the free surface:

1. From the momentum equation, Eqn. 27:
   - $\frac{\partial \mathbf{u}}{\partial t}$ is a cell–centred temporal derivative operator for the velocity field which is continuous across the interface. No special treatment is needed;
   - $\nabla \bullet (\mathbf{u}\mathbf{u})$ generally has a jump across the interface, as indicated in Eqn. 24, which needs to be taken into account;
   - $\frac{1}{\rho} \nabla \mathbf{u} \bullet \nabla \mu_e$ is continuous across the interface due to the assumptions made on the viscosity across the interface, except for the $1/\rho$ term. However, since the present method takes into account the discontinuity of ρ, the cell–centred value which is used in this term will be exact near the interface. Therefore, although this term has a jump, it requires no special attention in the numerical implementation of operators;
   - $\nabla \bullet \left(\mu_e \nabla \mathbf{u}\right)$ has no special treatment in this study due to assumptions of continuous viscosity field;

- $\frac{1}{\rho}\nabla p_d$ has a jump across the free surface as shown in Eqn. 24, which needs to be accounted for in the explicit operator;
- $\frac{1}{\rho_c}\nabla\rho_c\mathbf{g}\cdot\mathbf{x}$ is discontinuous since ρ has a discontinuity across the interface, and because the gradient of density is zero in the incompressible phase, while in the compressible phase it can be non–zero. Thus the explicit density gradient operator needs special treatment at the interface;
- $\mathbf{u}\nabla_\bullet\mathbf{u}$ is discontinuous across the interface since $\nabla_\bullet\mathbf{u}$ is discontinuous, as indicated in Eqn. 26.

2. From the conservation of mass, Eqn. 32:
    - $(1/a_P)_f$ is the inverse diagonal coefficient of the momentum equation interpolated on cell faces. It is continuous across the interface and can be interpolated using ordinary linear interpolation;
    - $(\frac{1}{\rho})_{f_\Gamma}$ is the inverse of the density field interpolated on faces. Due to discontinuity of density across the interface, interpolation cannot be performed linearly;
    - $(\nabla p_d)_{f_\Gamma}$ is an implicit surface normal gradient operator which requires special treatment across the interface due to the jump condition stated in Eqn. 24. This term is a part of the pressure Laplacian operator, and will be analysed in the remainder of the text;
    - $(\mathbf{H}(\mathbf{u}_N))_f$ arises from the off–diagonal and source contribution of terms in the momentum equation. Since $(\mathbf{H}(\mathbf{u}_N))_f$ is a function of velocity which is continuous across the interface, it requires no special attention during interpolation;
    - $(\nabla\rho)_{f_\Gamma}$ is an explicit surface normal gradient operator of density. Since neither density nor gradient of density are continuous across the interface, special attention is needed;
    - $f_C\,(p_d,\rho)$ contains $(1-\alpha_I)$ rendering it inactive in the incompressible phase. Thus, the entire term has a jump over the interface. In order to handle the jump consistently, the term is set zero for all cells where $\alpha_I < 0.5$, i.e. for all dry cells (Sec. 3.2), while the $(1-\alpha_I)$ term is removed. Even though the term is not active in the incompressible phase, operators within the term require compact stencil information, requiring special attention at the interface.

3. From Eqn. 33, which is active only in the compressible phase:
    - $\frac{\partial p_d}{\partial t}$ is a cell–centred operator, requiring no compact stencil information. However, due to the jump of p_d across the interface (Eqn. 21), the term requires special attention in the case when the interface crosses a cell centre in time, i.e. when an "incompressible cell" becomes "compressible". Note that the opposite case is not relevant, due to the multiplication of the whole term with $(1-\alpha_I)$;
    - $\nabla\bullet(p_d\mathbf{u})$ represents convection of dynamic pressure. Due to the jump of dynamic pressure across the interface, the term requires special treatment across the interface;
    - $p_d\nabla\bullet\mathbf{u}$ term contains a two–fold discontinuity at the interface: both p_d and $\nabla\bullet\mathbf{u}$ are discontinuous. However, p_d is a cell centred value, and since the present method resolves a sharp p_d field, no special attention is needed. $\nabla\bullet\mathbf{u}$ requires special attention, as indicated earlier;
    - $\frac{\partial(\rho_c\mathbf{g}\bullet\mathbf{x})}{\partial t}$ presents a temporal change of hydrostatic pressure. It requires special attention when an incompressible cell becomes compressible;
    - $\mathbf{u}\bullet\nabla\rho_c\mathbf{g}\bullet\mathbf{x}$ contains cell centred gradient of density, which needs special attention near the interface due to the discontinuity of density and density gradient.

In the following section the GFM interpolation is described, while Sec. 3.3 presents a detailed analysis of discretisation of terms requiring special attention at the interface, as listed above.

3.2. The Ghost Fluid Method

In GFM, mathematical operations for cells that are close to the interface are performed by extrapolating the fields to the cells across the interface. The computational stencil is never in two phases at once, which is achieved by treating the cells in the other phase as "ghost cells" of the same phase. This prevents the errors that occur when interpolation across the interface is performed using second or higher order accuracy, where the true shape of the gradient containing a step–change is not accounted for. The discontinuity of variables across the interface presents a singularity in the gradient, which is numerically difficult to treat.

Detailed description of the GFM is shown in [20], while the basic notation is repeated here for convenience. Since this study deals with a combination of an incompressible liquid and a compressible gas phase, the cells occupied by water will be referred as wet cells, while those occupied by air dry cells. Wet and dry cells are detected using the VOF liquid fraction field representing the incompressible phase: cell P is considered wet if $\alpha_I > 0.5$ and vice–versa. The second order accurate FV method which is used in this study is characterised by a compact computational stencil, meaning that only the cells sharing a face with cell P will be used to evaluate discretisation operators. Therefore, only the cells that are the closest to the interface will require special attention. A face between a wet and a dry cell is called interface face. Any interpolation on the interface face requires special treatment if the interpolated field contains a discontinuity.

In this study, dynamic pressure and density fields are extrapolated using the GFM, while the jump in velocity operators is taken into account through volumetric flux discontinuity (see Sec. 3.3.7). Two scenarios need to be covered when extrapolating a general scalar variable ϕ using GFM: first, when the owner cell P is wet and neighbour cell N is dry, and second, when the owner cell P is dry and N is wet. Rxtrapolation starts by assessing the values on both sides of the interface, denoted as ϕ^+ and ϕ^-, which are governed by the jump conditions. Once ϕ^+ and ϕ^- are calculated, they are used to extrapolate cell–centred values across the interface with the following expressions [20]:

- P is wet and N is dry:

$$\phi^+_{N_\Gamma} = \phi^+ + \frac{1-\lambda}{\lambda}\left(\phi^+ - \phi_P\right) \, , \tag{34}$$

$$\phi^-_{P_\Gamma} = \phi^- + \frac{\lambda}{1-\lambda}\left(\phi^- - \phi_N\right) \, . \tag{35}$$

- P is dry and N is wet:

$$\phi^-_{N_\Gamma} = \phi^- + \frac{1-\lambda}{\lambda}\left(\phi^- - \phi_P\right) \, , \tag{36}$$

$$\phi^+_{P_\Gamma} = \phi^+ + \frac{\lambda}{1-\lambda}\left(\phi^+ - \phi_N\right) \, . \tag{37}$$

Here, $\phi^+_{N_\Gamma}$ indicates the extrapolated value in cell N of the variable ϕ on the liquid side $(+)$. It will be used to interpolate values at the interface face between cells P and N when performing the operations for wet cell P. $\phi^-_{P_\Gamma}$, $\phi^-_{N_\Gamma}$ and $\phi^+_{P_\Gamma}$ have analogue meanings. λ stands for a dimensionless distance between cell centre P and location of the interface along vector $\mathbf{d}_f$ connecting the two cell centres (for details see [20]). In the VOF framework it is calculated as:

$$\lambda = \frac{\alpha_P - 0.5}{\alpha_P - \alpha_N}\,. \tag{38}$$

In this study, extrapolation of dynamic pressure using GFM described in [20] is extended by taking into account the altered jump conditions expressed by the right hand side of Eqn. 25. In the following text, the GFM extrapolation derived in [20] is repeated for convenience, followed by the extension for incompressible/compressible two–phase flow.

3.2.1. Dynamic pressure extrapolation for incompressible flow

In order to extrapolate the dynamic pressure to cell centres across the interface unsing Eqn. 36 and 37, values p_d^+ and p_d^- must first be determined. Discretising Eqn. 23 and using Eqn. 21, expressions for p_d^+ and p_d^- are obtained (see [33] for full derivation):

- P is wet and N is dry:

$$p_d^+ = \frac{\lambda\beta^-}{\overline{\beta}_w} p_{dN} + \frac{(1-\lambda)\beta^+}{\overline{\beta}_w} p_{dP} - \frac{\lambda\beta^-}{\overline{\beta}_w}\mathcal{H}\,, \tag{39}$$

$$p_d^- = \frac{\lambda\beta^-}{\overline{\beta}_w} p_{dN} + \frac{(1-\lambda)\beta^+}{\overline{\beta}_w} p_{dP} + \frac{\lambda\beta^+}{\overline{\beta}_w}\mathcal{H}\,, \tag{40}$$

- P is dry and N is wet:

$$p_d^+ = \frac{\lambda\beta^+}{\overline{\beta}_d} p_{dN} + \frac{(1-\lambda)\beta^-}{\overline{\beta}_d} p_{dP} - \frac{\lambda\beta^-}{\overline{\beta}_d}\mathcal{H}\,, \tag{41}$$

$$p_d^- = \frac{\lambda\beta^+}{\overline{\beta}_d} p_{dN} + \frac{(1-\lambda)\beta^-}{\overline{\beta}_d} p_{dP} + \frac{\lambda\beta^+}{\overline{\beta}_d}\mathcal{H}\,, \tag{42}$$

where the following substitutions are used to adhere to Vukčević et al. [20]:

$$\beta = \frac{1}{\rho}\,, \tag{43}$$

$$\mathcal{H} = [p_d] = p_d^- - p_d^+ = (\rho^+ - \rho^-)\mathbf{g}\bullet\mathbf{x}_\Gamma\,, \tag{44}$$

$$\overline{\beta_w} = \lambda\beta^- + (1-\lambda)\beta^+\,, \tag{45}$$

$$\overline{\beta_d} = \lambda\beta^+ + (1-\lambda)\beta^-\,, \tag{46}$$

where $\mathbf{x}_\Gamma$ denotes the radii vector of the intersection of vector $\mathbf{d}_f$ and the free surface, see Fig. 2. Substituting Eqns. 39–42 to Eqns. 34–37, extrapolated dynamic pressure values can be expressed in terms of cell–centred values:

- P is wet and N is dry:

$$p^+_{dN_\Gamma} = \frac{\beta^-}{\overline{\beta_w}} p_{dN} + \left(1 - \frac{\beta^-}{\overline{\beta_w}}\right) p_{dP} - \frac{\beta^-}{\overline{\beta_w}}\mathcal{H}\,, \tag{47}$$

$$p^-_{dP_\Gamma} = \frac{\beta^+}{\overline{\beta_w}} p_{dP} + \left(1 - \frac{\beta^+}{\overline{\beta_w}}\right) p_{dN} + \frac{\beta^+}{\overline{\beta_w}}\mathcal{H}\,, \tag{48}$$

- P is dry and N is wet:

$$p^-_{dN_\Gamma} = \frac{\beta^+}{\overline{\beta_d}} p_{dN} + \left(1 - \frac{\beta^+}{\overline{\beta_d}}\right) p_{dP} + \frac{\beta^+}{\overline{\beta_d}}\mathcal{H}\,, \tag{49}$$

$$p^+_{dP_\Gamma} = \frac{\beta^-}{\overline{\beta_d}} p_{dP} + \left(1 - \frac{\beta^-}{\overline{\beta_d}}\right) p_{dN} - \frac{\beta^-}{\overline{\beta_d}}\mathcal{H}\,. \tag{50}$$

Extrapolated values defined by Eqns. 47 to 50 are used in the discretisation of dynamic pressure gradient for cells next to the interface, which will be shown in detail later. They are used in following cases [20]:

- $p^+_{dN_\Gamma}$ - used when P is wet (N is dry) for the discretisation of cell P;
- $p^-_{dP_\Gamma}$ - used when P is wet (N is dry) for the discretisation of cell N;
- $p^-_{dN_\Gamma}$ - used when P is dry (N is wet) for the discretisation of cell P;
- $p^+_{dP_\Gamma}$ - used when P is dry (N is wet) for the discretisation of cell N.

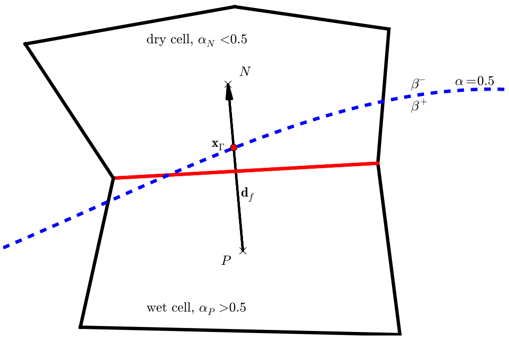

Fig. 2: Compact computational stencil near the free surface. Interface face shared by cells P and N is marked with a red line. $\mathbf{x}_\Gamma$ is the location of the free surface for this interface face [20].

3.2.2. Dynamic pressure extrapolation for incompressible/compressible flow

In Sec. 3.2.1 expressions for the GFM interpolation of the dynamic pressure across the interface are given for the case when both phases divided by a sharp interface are incompressible. These expressions will serve as a basis for the numerical model developed in this study, where the liquid phase is considered incompressible, while the gas phase is considered compressible. In order to derive the expressions for the dynamic pressure for incompressible/compressible two–phase model, Eqn. 25 is discretised and combined with Eqn. 21 to obtain p_d^+ and p_d^- values near the interface. The derivation is performed in the same fashion as for the incompressible mixture shown in [20, 33]. The resulting expressions are as follows:

- P is wet and N is dry:

$$
\begin{aligned}
p_d^+ = \frac{\lambda\beta^-}{\overline{\beta_w}} p_{dN} + \frac{(1-\lambda)\beta^+}{\overline{\beta_w}} p_{dP} - \frac{\lambda\beta^-}{\overline{\beta_w}} \mathcal{H} \\
+ \mathbf{d}_f \bullet \frac{\lambda\,(1-\lambda)}{\overline{\beta_w}} \left([\nabla \bullet (\mathbf{u}\mathbf{u})] - (\mathbf{u}\nabla \bullet \mathbf{u})^- \right) \\
+ \frac{\lambda\beta^-}{\overline{\beta_w}} \left(\rho_N - \rho^- \right) \mathbf{g} \bullet \mathbf{x}\,, \qquad (51)
\end{aligned}
$$

$$\begin{aligned}p_d^- = \frac{\lambda\beta^-}{\overline{\beta_w}} p_{dN} &+ \frac{(1-\lambda)\beta^+}{\overline{\beta_w}} p_{dP} + \frac{\lambda\beta^+}{\overline{\beta_w}}\mathcal{H} \\ &+ \mathbf{d}_f\bullet\frac{\lambda\,(1-\lambda)}{\overline{\beta_w}}\left([\nabla\bullet(\mathbf{uu})] - (\mathbf{u}\nabla\bullet\mathbf{u})^-\right) \\ &+ \frac{\lambda\beta^-}{\overline{\beta_w}}\left(\rho_N - \rho^-\right)\mathbf{g}\bullet\mathbf{x}\,, \end{aligned} \tag{52}$$

- P is dry and N is wet:

$$\begin{aligned}p_d^+ = \frac{\lambda\beta^+}{\overline{\beta_d}} p_{dN} &+ \frac{(1-\lambda)\beta^-}{\overline{\beta_d}} p_{dP} - \frac{\lambda\beta^-}{\overline{\beta_d}}\mathcal{H} \\ &- \mathbf{d}_f\bullet\frac{\lambda\,(1-\lambda)}{\overline{\beta_d}}\left([\nabla\bullet(\mathbf{uu})] - (\mathbf{u}\nabla\bullet\mathbf{u})^-\right) \\ &- \frac{(1-\lambda)\,\beta^-}{\overline{\beta_d}}\left(\rho^- - \rho_P\right)\mathbf{g}\bullet\mathbf{x}\,, \end{aligned} \tag{53}$$

$$\begin{aligned}p_d^- = \frac{\lambda\beta^+}{\overline{\beta_d}} p_{dN} &+ \frac{(1-\lambda)\beta^-}{\overline{\beta_d}} p_{dP} + \frac{\lambda\beta^+}{\overline{\beta_d}}\mathcal{H} \\ &- \mathbf{d}_f\bullet\frac{\lambda\,(1-\lambda)}{\overline{\beta_d}}\left([\nabla\bullet(\mathbf{uu})] - (\mathbf{u}\nabla\bullet\mathbf{u})^-\right) \\ &- \frac{(1-\lambda)\,\beta^-}{\overline{\beta_d}}\left(\rho^- - \rho_P\right)\mathbf{g}\bullet\mathbf{x}\,. \end{aligned} \tag{54}$$

Additional terms occurring in Eqns. 51–54 are proportional to effects of compressibility in the gas phase. The term $[\nabla\bullet(\mathbf{uu})]$ represents the jump in the convection term from the momentum equation, which is intentionally left under the jump operator $[\bullet]$ since it is calculated indirectly using volumetric flux jump (see Sec. 3.3.7). The term $(\mathbf{u}\nabla\bullet\mathbf{u})^-$ represents transport of velocity divergence on the compressible side of the interface. It will be shown later that first order assumption is made in evaluation of this term, where the value calculated at the dry cell centre will be used. The last term is proportional to the gradient of hydrostatic pressure caused by the change of density of the compressible phase in space. All three additional terms vanish in case when compressibility effects are negligible, which renders the method effective in low Mach conditions without volumetric compressibility effects. Without these three terms, Eqns. 51–54 correctly reduce to their incompressible counterparts, Eqns. 39–42. As shown later in the paper, this permits running complex flow simulations including large time–scale wave evolution and small time–scale volumetric compressibility effects in a single run, without the need of interchanging incompressible and compressible flow models.

Substituting Eqns. 51–54 into Eqns. 34–37, extrapolated dynamic pressure values are expressed in terms of cell–centred values:

- P is wet and N is dry:

$$\begin{aligned} p^{+}_{dN_\Gamma} = {} & \frac{\beta^-}{\overline{\beta}_w} p_{dN} + \left(1 - \frac{\beta^-}{\overline{\beta}_w}\right) p_{dP} - \frac{\beta^-}{\overline{\beta}_w}\mathcal{H} \\ & + \mathbf{d}_f \boldsymbol{\cdot} \frac{(1-\lambda)}{\overline{\beta}_w} \left([\nabla\boldsymbol{\cdot}(\mathbf{uu})] - (\mathbf{u}\nabla\boldsymbol{\cdot}\mathbf{u})^- \right) \\ & + \frac{\beta^-}{\overline{\beta}_w} \left(\rho_N - \rho^-\right) \mathbf{g}\boldsymbol{\cdot}\mathbf{x}\,, \end{aligned} \tag{55}$$

$$\begin{aligned} p^{-}_{dP_\Gamma} = {} & \frac{\beta^+}{\overline{\beta}_w} p_{dP} + \left(1 - \frac{\beta^+}{\overline{\beta}_w}\right) p_{dN} + \frac{\beta^+}{\overline{\beta}_w}\mathcal{H} \\ & + \mathbf{d}_f \boldsymbol{\cdot} \frac{\lambda}{\overline{\beta}_w} \left([\nabla\boldsymbol{\cdot}(\mathbf{uu})] - (\mathbf{u}\nabla\boldsymbol{\cdot}\mathbf{u})^- \right) \\ & + \frac{\lambda\beta^-}{(1-\lambda)\,\overline{\beta}_w} \left(\rho_N - \rho^-\right) \mathbf{g}\boldsymbol{\cdot}\mathbf{x}\,, \end{aligned} \tag{56}$$

- P is dry and N is wet:

$$\begin{aligned} p^{-}_{dN_\Gamma} = {} & \frac{\beta^+}{\overline{\beta}_d} p_{dN} + \left(1 - \frac{\beta^+}{\overline{\beta}_d}\right) p_{dP} + \frac{\beta^+}{\overline{\beta}_d}\mathcal{H} \\ & - \mathbf{d}_f \boldsymbol{\cdot} \frac{(1-\lambda)}{\overline{\beta}_d} \left([\nabla\boldsymbol{\cdot}(\mathbf{uu})] - (\mathbf{u}\nabla\boldsymbol{\cdot}\mathbf{u})^- \right) \\ & - \frac{(1-\lambda)\,\beta^-}{\lambda\overline{\beta}_d} \left(\rho^- - \rho_P\right) \mathbf{g}\boldsymbol{\cdot}\mathbf{x}\,, \end{aligned} \tag{57}$$

$$
\begin{aligned}
p^{+}_{dP_{\Gamma}} = \frac{\beta^-}{\overline{\beta}_d} p_{dP} + \left(1 - \frac{\beta^-}{\overline{\beta}_d}\right) p_{dN} - \frac{\beta^-}{\overline{\beta}_d} \mathcal{H} \\
- \mathbf{d}_f \mathbin{\bullet} \frac{\lambda}{\overline{\beta}_d} \left([\nabla \mathbin{\bullet} (\mathbf{u}\mathbf{u})] - (\mathbf{u} \nabla \mathbin{\bullet} \mathbf{u})^- \right) \\
- \frac{\beta^-}{\overline{\beta}_d} \left(\rho^- - \rho_P \right) \mathbf{g} \mathbin{\bullet} \mathbf{x} \,.
\end{aligned} \tag{58}
$$

Cell–centred extrapolation of dynamic pressure expressed with Eqns. 55–58 is used for discretisation in the same manner as for the incompressible two–phase flow. Depending on whether P is dry or wet, and from which cell the discretisation is being carried out, the corresponding expression is used (see Sec. 3.2.1).

3.2.3. Density extrapolation for incompressible/compressible flow

Apart from dynamic pressure extrapolation, the density field must also be extrapolated using the GFM in order to correctly evaluate the discontinuous gradient of density. In order to extrapolate the density field using Eqns. 34–37, values close to the interface in both phases (ρ^- and ρ^+) must be determined. Since the liquid phase is considered incompressible, its density is constant in space and time, i.e. $\rho^+ = \rho_I = const.$ On the other hand, density in the gas phase is not known and must be calculated.

Pressure and density of the gas phase are related by Eqn. 10; if p^- is known, ρ^- can easily be calculated as:

$$
\rho^- = \left(\frac{p^-}{a_c} \right)^{\frac{1}{\gamma}} = \left(\frac{p^-_d + \rho^- \mathbf{g} \mathbin{\bullet} \mathbf{x}}{a_c} \right)^{\frac{1}{\gamma}} , \tag{59}
$$

where Eqn. 7 is employed to substitute p^-. Note that Eqn. 59 is nonlinear with respect to ρ^-. The nonlinearity can be avoided by remembering that $p^- = p^+$ (Eqn. 20):

$$
\rho^- = \left(\frac{p^+}{a_c} \right)^{\frac{1}{\gamma}} = \left(\frac{p^+_d + \rho^+ \mathbf{g} \mathbin{\bullet} \mathbf{x}}{a_c} \right)^{\frac{1}{\gamma}} , \tag{60}
$$

where ρ^+ is constant. In order to calculate ρ^-, p^+_d must first be evaluated using Eqn. 51 or Eqn. 53, depending on whether cell P is wet or dry. Note that Eqns. 51 and 53 depend on ρ^- themselves, requiring a nonlinear loop in order to converge.

Once ρ^- is determined, it can be used to extrapolate the density of the gas phase across the interface to the wet cell centre using Eqns. 35 and 36. Extrapolating density of the liquid phase is not necessary, since $\rho_I = const.$

3.3. Interface Corrected Discretisation Schemes

In Sec. 3.1 implications of the jump conditions on individual terms from the governing equations are analysed. In this section, discretisation of each of these terms that require special attention on the interface is presented. There are three distinct groups of operators that need to be addressed:

1. Temporal terms: when a cell switches to compressible from incompressible from one time–step to another, special treatment needs to be applied in order to prevent unphysically large temporal change;
2. Scalar gradient terms: both cell–centred and face–normal gradients of dynamic pressure and density need to be addressed, where GFM extrapolation shown in Sec. 3.2 will be used. While cell–centred gradients are explicit, face–normal gradient of dynamic pressure is implicit since it is a part of the implicit pressure Laplacian operator. Special attention will be given to this term;
3. Velocity operators: convection and divergence of velocity are handled using volumetric flux jump that arises from the pressure equation. Both implicit and explicit versions of the convection operator need to be devised, while the divergence operator is always explicit.

3.3.1. Dynamic Pressure Temporal Derivative Discretisation

Temporal derivative of density and dynamic pressure contain a singularity for cells that change phase due to the motion of the interface within a time–step. Since both terms exist only in the compressible phase, only the scenario when the cell changes from the incompressible to compressible phase needs to be addressed. In the opposite case, the temporal change is simply zero due to incompressibility.

Temporal derivative of dynamic pressure can be discretised using the implicit first order Euler method as:

$$\frac{\partial p_d}{\partial t} = \frac{p_d^n - p_d^o}{\Delta t}\,, \tag{61}$$

where n stands for the current time–step value and o for the old time–step value. For cells that were wet in the old time step, and are dry in the current (termed new dry cells hereafter), dynamic pressure jump (Eqn. 21) needs to be added to the old time–step value:

$$\left(\frac{\partial p_d}{\partial t}\right)_\Gamma = \frac{p_d^n - \left(p_d^o + \left(\rho_I - \rho_c\right)\mathbf{g}\bullet\mathbf{x}\right)}{\Delta t}\,. \tag{62}$$

The new dry cells are marked using the following criteria:

$$\left(\alpha_I^o - \alpha_I^n\right) > 0.5\,. \tag{63}$$

Note that the density from the compressible phase is not present in the previous time step, and current time–step value is used instead. Since the density difference between air and water, which are relevant for marine applications, is four or more orders of magnitude larger than the temporal change in air density, this assumption has a negligible influence on accuracy.
In order to achieve second order accuracy in time, backward scheme is used:

$$\frac{\partial p_d}{\partial t} = \frac{1}{\Delta t}\left(\frac{3}{2}p_d^n - 2p_d^o + \frac{1}{2}p_d^{oo}\right)\,, \tag{64}$$

where p_d^{oo} stands for the dynamic pressure from the second last time–step before the current one. In this case, there are three possible combinations that require special treatment due to conditions in the dynamic pressure:

- n corresponds to a dry cell, while o and oo correspond to a wet cell. In this case, a jump must be added in dynamic pressure for both o and oo values of dynamic pressure:

$$\left(\frac{\partial p_d}{\partial t}\right)_\Gamma = \frac{1}{\Delta t}\left(\frac{3}{2}p_d^n - 2\left(p_d^o + \left(\rho_I - \rho_c\right)\mathbf{g}\bullet\mathbf{x}\right) + \frac{1}{2}\left(p_d^{oo} + \left(\rho_I - \rho_c\right)\mathbf{g}\bullet\mathbf{x}\right)\right)\,. \tag{65}$$

- n and o correspond to a dry cell, while oo correspond to a wet cell. In this case dynamic pressure value from oo must be corrected:

$$\left(\frac{\partial p_d}{\partial t}\right)_\Gamma = \frac{1}{\Delta t}\left(\frac{3}{2}p_d^n - 2p_d^o + \frac{1}{2}\left(p_d^{oo} + \left(\rho_I - \rho_c\right)\mathbf{g}\bullet\mathbf{x}\right)\right)\,. \tag{66}$$

- n and oo correspond to a dry cell, while o corresponds to a wet cell. Here, p_d^o needs to be corrected:

$$\left(\frac{\partial p_d}{\partial t}\right)_\Gamma = \frac{1}{\Delta t}\left(\frac{3}{2}p_d^n - 2\left(p_d^o + \left(\rho_I - \rho_c\right)\mathbf{g}\bullet\mathbf{x}\right) + \frac{1}{2}p_d^{oo}\right) . \tag{67}$$

In the case when p_d^n corresponds to a wet cell, no special treatment is necessary since the temporal change of dynamic pressure is not assessed for the incompressible phase. Also, if the cell has been dry during the last three time–steps, no special treatment is needed since no jump in dynamic pressure occurred.

3.3.2. Density Temporal Derivative Discretisation

Another temporal derivative term that needs special treatment is the rate of change of ρ in time. For the incompressible phase, this term is zero and requires no special attention. In cases when a wet cell becomes a dry, special treatment is needed. In order to asses the temporal change of density in cells for which old time–step density values are not available, Eqn. 5 is utilised:

$$\left(\frac{\partial \rho}{\partial t}\right)_\Gamma = -\rho\nabla\bullet\mathbf{u} - \mathbf{u}\bullet\nabla\rho\,, \tag{68}$$

where terms on the right hand side are evaluated using the jump conditions, as described in the following text. Eqn. 68 can be used in this manner since ρ is not implicitly solved for. Instead, it is calculated using the equation of state, Eqn. 10.

3.3.3. Discretisation of Dynamic Pressure Gradient Term

Explicit, cell–centred gradient operator for dynamic pressure can be written in the following form using the Gauss theorem [34]:

$$\nabla p_d = \frac{1}{V_P}\int_{CV}\nabla p_d\,\mathrm{d}V = \frac{1}{V_P}\oint_{\partial CV} p_d\,\mathrm{d}\mathbf{S} = \frac{1}{V_P}\sum_f \mathbf{s}_f\bullet p_{df}\,, \tag{69}$$

where p_{df} stands for the face interpolated dynamic pressure, which requires special attention at the interface. By using a central differencing interpolation, dynamic pressure gradient for cell P reads:

$$\nabla p_{dP} = \frac{1}{V_P}\sum_f \mathbf{s}_f\left(f_x p_{dP} + (1-f_x)p_{dN}\right)\,, \tag{70}$$

where f_x is the interpolation weight for central differencing defined as $f_x = \overline{fN}/\overline{PN}$, where $\overline{fN}$ denotes a vector from cell centre P to face centre f, while $\overline{PN}$ is the vector connecting the two cell centres. $\sum_f$ denotes summation over cell faces. For interface cells, the sum over cell faces need to be separated for ordinary and interface faces, since interface faces require special attention:

$$\begin{aligned}(\nabla p_{dP}) =& \frac{1}{V_P}\sum_{f\not\Gamma} \mathbf{s}_f \left(f_x p_{dP} + (1-f_x) p_{dN}\right)\\ &+ \frac{1}{V_P}\sum_{f\Gamma} \mathbf{s}_f \left(f_x p_{dP} + (1-f_x) p^{+/-}_{dN_\Gamma}\right) ,\end{aligned} \tag{71}$$

where $\sum_{f\not\Gamma}$ denotes the sum over ordinary faces, while $\sum_{f\Gamma}$ stands for the sum over interface faces. $p^{+/-}_{dN_\Gamma}$ presents the extrapolated dynamic pressure value obtained using Eqn. 55 or 57, depending on whether P is wet or dry, respectively. For the gradient calculated in the neighbour cell N across the interface, equivalent expression is used where extrapolated values for $p^{+/-}_{dP_\Gamma}$ are used instead.

3.3.4. Discretisation of the Density Gradient Term

Interface corrected, explicit, cell–centred density gradient is discretised in the same manner as the dynamic pressure gradient shown in Sec. 3.3.3:

$$\begin{aligned}(\nabla \rho)_{P_\Gamma} =& \frac{1}{V_P}\sum_{f\not\Gamma} \mathbf{s}_f \left(f_x \rho_P + (1-f_x) \rho_N\right)\\ &+ \frac{1}{V_P}\sum_{f\Gamma} \mathbf{s}_f \left(f_x \rho_P + (1-f_x) \rho^{-}_{N_\Gamma}\right) .\end{aligned} \tag{72}$$

Note that $\rho^{-}_{N_\Gamma}$ is used instead of $\rho^{+/-}_{N_\Gamma}$ since the GFM extrapolation will be used only from the dry side, as the gradient of density is zero in the incompressible phase. $\rho^{-}_{N_\Gamma}$ is determined using Eqn. 36 in conjunction with Eqn. 60. When discretising terms for a dry cell N, Eqn. 35 is used to determine $\rho^{-}_{P_\Gamma}$.

3.3.5. Discretisation of the Pressure Laplacian Term

The term on the left hand side of Eqn. 32 represents the pressure Laplacian term and requires special attention. For incompressible two–phase flow, the implicit treatment is achieved by extrapolating the dynamic pressure values with respect to cell centred values using Eqns. 47–50. It is shown by Vukčević et al. [20] that for incompressible two phase–flow the pressure equation remains symmetric notwithstanding the jump conditions. For the incompressible/compressible mixture, the extrapolated values have additional terms (see Eqns. 55–58) which are explicit with respect to dynamic pressure, while the implicit portion remains unchanged. Thus, the implicit, interface corrected pressure Laplacian developed by Vukčević et al. [20] is supplemented with the explicit sources due to jump of compressibility across the interface. The implicit portion of the jump conditions remains symmetric, however the pressure equation is no longer symmetric due to implicit treatment of dynamic pressure convection. The explicit compressible jump conditions are also not symmetric, which leads to a jump in the source of the pressure Laplacian, as shown below.

The pressure Laplacian (left hand side of Eqn. 32) is discretised as:

$$\begin{aligned}\sum_f \mathbf{s}_f \bullet \left(\frac{1}{a_P}\right)_f (\beta)_{f_\Gamma} (\nabla p_d)_{f_\Gamma} &= \sum_f \left(\frac{1}{a_P}\right)_f (\beta)_{f_\Gamma} |\mathbf{s}_f| \frac{(p_{dN} - p_{dP})_\Gamma}{|\mathbf{d}_f|} \\ &+ \sum_f \mathbf{k} \bullet \left(\frac{1}{a_P}\right)_f (\beta \nabla p_d)_f^o \,,\end{aligned} \tag{73}$$

where **k** stand for the non–orthogonal correction vector, which is obtained using the over–relaxed approach [32]. The second term on the right hand side is explicit, and contributes to the source of the pressure Laplacian and the respective conservative flux. The first term is implicit face normal gradient contribution, which requires special treatment due to jump conditions. Note that Eqn. 73 holds no assumptions on the compressibility of either of the phases, thus it is identical to the expressions in [20]. For a wet interface cell P, the first term on the right hand side can be divided into two sums:

$$\begin{aligned}\sum_f \left(\frac{1}{a_P}\right)_f (\beta)_{f_\Gamma} |\mathbf{s}_f| \frac{(p_{dN} - p_{dP})_\Gamma}{|\mathbf{d}_f|} = \\ = \sum_{f\not\Gamma} \left(\frac{1}{a_P}\right)_f (\beta)_f |\mathbf{s}_f| \frac{p_{dN} - p_{dP}}{|\mathbf{d}_f|} \\ + \sum_{f\Gamma} \left(\frac{1}{a_P}\right)_f (\beta)_{f_\Gamma} |\mathbf{s}_f| \frac{p^+_{dN_\Gamma} - p_{dP}}{|\mathbf{d}_f|} \,.\end{aligned} \tag{74}$$

To examine the contribution of one interface face for the mixture of compressible and incompressible fluid, the second sum is expanded by substituting $p^+_{dN_\Gamma}$ with Eqn. 55:

$$\begin{aligned}\left(\frac{1}{a_P}\right)_f (\beta)_{f_\Gamma} |\mathbf{s}_f| \frac{p^+_{dN_\Gamma} - p_{dP}}{|\mathbf{d}_f|} &= \\ \left(\frac{1}{a_P}\right)_f \frac{|\mathbf{s}_f|}{|\mathbf{d}_f|} \frac{\beta^+\beta^-}{\overline{\beta_w}} &\cdot \\ \left(p_{dN} - p_{dP} - \mathcal{H} + \mathbf{d}_f \bullet \frac{(1-\lambda)}{\beta^-} \left([\nabla\bullet(\mathbf{uu})] - (\mathbf{u}\nabla\bullet\mathbf{u})^-\right) + \left(\rho_N - \rho^-\right) \mathbf{g}\bullet\mathbf{x}\right)&,\end{aligned} \tag{75}$$

where $(\beta)_{f_\Gamma}$ is replaced with β^+, since the density in the liquid phase is constant. The last two terms in Eqn. 75 arise from the compressible jump conditions, while the first three correspond to the implicit jump condition and the explicit hydrostatic jump condition, which are the same as for the incompressible two–phase flow. The treatment and matrix contribution of the implicit and hydrostatic jump conditions is shown in details by Vukčević et al. [20], and will not be repeated here. Instead, only the source contribution from the compressible portion of the jump condition will be examined in detail. The compressible portion of the source contribution for a wet P cell can be written as:

$$\begin{aligned}S_P = \left(\frac{1}{a_P}\right)_f \frac{|\mathbf{s}_f|}{|\mathbf{d}_f|} \frac{\beta^+\beta^-}{\overline{\beta_w}} &\cdot \\ \left(\mathbf{d}_f \bullet \frac{(1-\lambda)}{\beta^-} \left([\nabla\bullet(\mathbf{uu})] - (\mathbf{u}\nabla\bullet\mathbf{u})_N\right) + \left(\rho_N - \rho^-\right) \mathbf{g}\bullet\mathbf{x}\right)&.\end{aligned} \tag{76}$$

As mentioned earlier, the term $[\nabla\bullet(\mathbf{uu})]$ is the jump in the convection term, which is calculated using the volumetric flux jump (see below). The term $(\mathbf{u}\nabla\bullet\mathbf{u})^-$ is replaced with $(\mathbf{u}\nabla\bullet\mathbf{u})_N$, i.e. first order accurate evaluation of this term is used.

By writing the equivalent of Eqns. 74 – 76 for the neighbouring dry cell N, and employing Eqn. 56 the source contribution for cell N is expressed as:

$$\begin{aligned}S_N = \left(\frac{1}{a_N}\right)_f \frac{|\mathbf{s}_f|}{|\mathbf{d}_f|} \frac{\beta^+\beta^-}{\overline{\beta_w}}& \\ \cdot \left(\mathbf{d}_f \bullet \frac{\lambda}{\beta^-} \left([\nabla\bullet(\mathbf{uu})] - (\mathbf{u}\nabla\bullet\mathbf{u})_N\right) + \frac{\lambda}{(1-\lambda)} \left(\rho_N - \rho^-\right) \mathbf{g}\bullet\mathbf{x}\right)&,\end{aligned} \tag{77}$$

where $(\beta)_{f\Gamma}$ is replaced with β^-, assuming first order accuracy since $\beta^- \neq$ *const*. Unlike the implicit and hydrostatic part of the pressure Laplacian, the compressible jump conditions result in asymmetric source terms, since $S_P \neq S_N$. In other words, interface cells P and N will have a different source contribution from the same face. Equations for a dry P and wet N cell can be derived analogously to above equations, and will be omitted for sake of brevity.

3.3.6. Discretisation of Surface Normal Density Gradient Term

As described in Sec. 3.1, Eqn. 32 requires explicit evaluation of the surface normal density gradient on cell faces. Ordinary, second order accurate discretisation of this term assuming orthogonal grid reads:

$$(\nabla \rho)_f = \frac{\rho_N - \rho_P}{|\mathbf{d}_f|}\,. \tag{78}$$

For non–orthogonal grids an explicit correction is applied similarly as described in Sec. 3.3.5. For interface faces, GFM extrapolation is used in order to correct for the jump in density. For a wet cell P the following expression is used:

$$(\nabla \rho)_{f\Gamma} = \frac{\rho^-_{N_\Gamma} - \rho_P}{|\mathbf{d}_f|}\,, \tag{79}$$

while for a dry cell N the surface gradient reads:

$$(\nabla \rho)_{f\Gamma} = \frac{\rho_N - \rho^-_{P_\Gamma}}{|\mathbf{d}_f|}\,. \tag{80}$$

Here, $\rho^-_{N_\Gamma}$ and $\rho^-_{P_\Gamma}$ are determined as described in Sec. 3.3.4.
Above expressions take into account the jump in density when evaluating surface normal gradient of the density field. However, the jump in the gradient itself is handled through the discretisation of the pressure Laplacian, due to the third term on the right hand side of Eqn. 25 (see Sec. 3.3.5 for details). In other words, the surface normal density gradient is not unique for interface faces, instead wet and dry cells will get different contributions from this term. Wet cells will have no equivalent contribution since the density gradient is zero in the incompressible phase, while the dry cell contribution can be non–zero.

3.3.7. Volumetric Flux Jump

Using Eqn. 31 volumetric flux for face f can be written as:

$$F_f = \mathbf{s}_f \bullet \mathbf{u}_f = \mathbf{s}_f \bullet \frac{(\mathbf{H}(\mathbf{u}_N))_f}{(a_P)_f} - \mathbf{s}_f \bullet \mathbf{n}_f \left(\frac{1}{a_P} \right)_f (\beta)_{f_\Gamma} \left((\nabla p_d)_{f_\Gamma} + (\nabla \rho)_{f_\Gamma} \mathbf{g} \bullet \mathbf{x} \right) , \tag{81}$$

where $\mathbf{n}_f$ denotes face normal vector. Evaluation of volumetric flux must be corrected at the interface since both face normal dynamic pressure and density gradients in Eqn. 81 are discontinuous. Looking from the wet cell P side, the volumetric flux on an interface face reads:

$$(F_f)_{\Gamma_P} = \mathbf{s}_f \bullet \mathbf{u}_f = \mathbf{s}_f \bullet \frac{(\mathbf{H}(\mathbf{u}_N))_f}{(a_P)_f} - \mathbf{s}_f \bullet \mathbf{n}_f \left(\frac{1}{a_P} \right)_f \beta^+ \left(\frac{p^+_{dN_\Gamma} - p_{dP}}{|\mathbf{d}_f|} + \cancelto{0}{\frac{\rho^+_{N_\Gamma} - \rho_P}{|\mathbf{d}_f|}} \mathbf{g} \bullet \mathbf{x} \right) , \tag{82}$$

where the density gradient vanishes due to incompressibility of the liquid phase. Substituting $p^+_{dN_\Gamma}$ with Eqn. 55 yields:

$$\begin{aligned}(F_f)_{\Gamma_P} = {}& \mathbf{s}_f \bullet \frac{(\mathbf{H}(\mathbf{u}_N))_f}{(a_P)_f} - \mathbf{s}_f \bullet \mathbf{n}_f \left(\frac{1}{a_P} \right)_f \frac{\beta^+ \beta^-}{\overline{\beta_w}} \frac{1}{|\mathbf{d}_f|} \Bigg(p_{dN} - p_{dP} - \mathcal{H} \\ & + \mathbf{d}_f \bullet \frac{(1-\lambda)}{\beta^-} \left([\nabla \bullet (\mathbf{u}\mathbf{u})] - (\mathbf{u} \nabla \bullet \mathbf{u})^- \right) + \left(\rho_N - \rho^- \right) \mathbf{g} \bullet \mathbf{x} \Bigg) .\end{aligned} \tag{83}$$

Looking from the dry cell N side, the volumetric flux on an interface face reads:

$$(F_f)_{\Gamma_N} = \mathbf{s}_f \bullet \mathbf{u}_f = \mathbf{s}_f \bullet \frac{(\mathbf{H}(\mathbf{u}_N))_f}{(a_P)_f} - \mathbf{s}_f \bullet \mathbf{n}_f \left(\frac{1}{a_P} \right)_f \beta^+ \left(\frac{p_{dN} - p^-_{dP_\Gamma}}{|\mathbf{d}_f|} + \frac{\rho_N - \rho^-_{P_\Gamma}}{|\mathbf{d}_f|} \mathbf{g} \bullet \mathbf{x} \right) . \tag{84}$$

Substituting $p^-_{dP_\Gamma}$ with Eqn. 56 and $\rho^-_{P_\Gamma}$ with Eqn. 36 yields:

$$
\begin{aligned}
(F_f)_{\Gamma_N} = \\
&\mathbf{s}_f \bullet \frac{(\mathbf{H}(\mathbf{u}_N))_f}{(a_P)_f} - \mathbf{s}_f \bullet \mathbf{n}_f \left(\frac{1}{a_P} \right)_f \frac{\beta^+ \beta^-}{\overline{\beta_w}} \frac{1}{|\mathbf{d}_f|} \Big(p_{dN} - p_{dP} - \mathcal{H} \\
&- \mathbf{d}_f \bullet \frac{\lambda}{\beta^-} \left([\nabla \bullet (\mathbf{u}\mathbf{u})] - (\mathbf{u} \nabla \bullet \mathbf{u})^- \right) + \left(\rho_N - \rho^- \right) \mathbf{g} \bullet \mathbf{x} \Big) \ . \qquad (85)
\end{aligned}
$$

Comparing Eqns. 83 and 85, it follows that the flux on the same face has a different magnitude depending on whether the discretisation is performed from the side of cell P or cell N. This means that there is a volumetric flux jump equal to:

$$
\begin{aligned}
[F_f] = (F_f)_{\Gamma_P} - (F_f)_{\Gamma_N} = \\
&-\mathbf{s}_f \bullet \mathbf{n}_f \left(\frac{1}{a_P} \right)_f \frac{\beta^+}{\overline{\beta_w}} \frac{\mathbf{d}_f}{|\mathbf{d}_f|} \bullet \left([\nabla \bullet (\mathbf{u}\mathbf{u})] - (\mathbf{u} \nabla \bullet \mathbf{u})^- \right) \ . \qquad (86)
\end{aligned}
$$

The jump of volumetric flux should be taken into account in convection and divergence terms by correcting the face interpolated fluxes with Eqn. 86. Note that the jump in flux is present only numerically across the interface face, since the ghost cells change the actual phase of the opposing cell. Physically, the flux jump across the interface is zero due to Eqn. 22. Consequently, the velocity itself has no jump for cell–centred operations.

In order to clarify the meaning of the volumetric flux jump, Fig. 3 shows a schematic representation of a one–dimensional liquid piston case discretised with five control volumes (cells). There is no mass or heat flux through domain boundaries. The bottom two cell centres are denoted with P and N. The vertical piston is divided into three layers, where two pockets of air (top and bottom) are separated by a layer of water. The water moves downwards under the influence of gravity, compressing the bottom air pocket while expanding the top one. At the bottom part of the piston, the interface is located somewhere between cell centre P and face f_2. The interface, denoted by Γ in the figure, moves with velocity $\mathbf{u}_f$. Since water is modelled as incompressible, velocity at face f_1 must be equal to the interface velocity to satisfy the continuity equation. For cell P the continuity equation can be discretised as:

$$
\begin{aligned}
(\nabla\bullet\mathbf{u})_P &= \frac{1}{V_P}\int_{CV}\nabla\bullet\mathbf{u}\,\mathrm{d}V = \frac{1}{V_P}\int_{\partial CV}\mathbf{n}\bullet\mathbf{u}\,\mathrm{d}S \\
&= \frac{1}{V_P}\sum_f S_f\mathbf{n}_f\bullet\mathbf{u}_f = \frac{1}{V_P}\left(S_{f1}\mathbf{n}_{f1}\bullet\mathbf{u}_{f1} + S_{f2}\mathbf{n}_{f2}\bullet\mathbf{u}_{f2}\right) = 0\,, \qquad (87)
\end{aligned}
$$

where the remaining faces of cell P have no contribution since the flux is zero. The above equation yields the following condition:

$$u_{f1} = u_{f2}\,, \tag{88}$$

since

$$
\begin{aligned}
S_{f1} &= S_{f2}\,, && (89)\\
\mathbf{n}_{f1} &= -\mathbf{n}_{f2}\,, && (90)\\
\mathbf{n}_{f1}\bullet\mathbf{u}_{f1} &= u_{f1}\,, && (91)\\
\mathbf{n}_{f2}\bullet\mathbf{u}_{f2} &= u_{f2}\,. && (92)
\end{aligned}
$$

Eqn. 88 states that the velocity (i.e. volumetric flux) on face f_2 must be equal to the one on f_1 in order to satisfy the continuity equation for cell P. However, from the physical point of view the flux through the imaginary face f_2 is not equal to the flux across f_1 due to the compression of air phase between the interface and face f_2. The jump in flux described by Eqn. 86 handles this difference, by applying a correction which is proportional to the divergence of velocity in the air phase. The correction fills the space between the interface and face f_2 with water, as well as cell N. Looking from the air side, a similar correction is applied, filling the space between the interface and face f_1 with air, in order to correctly calculate the flux on face f_2. Note that the magnitude of the correction is affected by the actual position of the interface due to term $\beta^+/\overline{\beta_w}$ in Eqn. 86. The closer the interface to cell P, the larger the correction.

3.3.8. Discretisation of the Dynamic Pressure Convection Term

Convection of dynamic pressure in Eqn. 33 is implicit with respect to dynamic pressure. It has a two–fold discontinuity across the interface due to the discontinuity of the convective flux (see Sec. 3.3.7) and the discontinuity

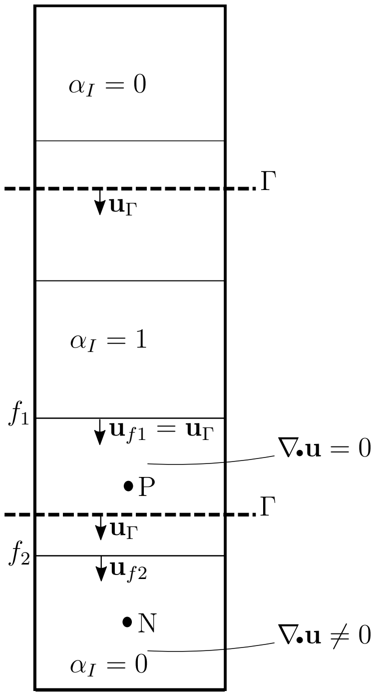

Fig. 3: A schematic representation of a one–dimensional liquid piston case. Γ denotes the position of the interface which is moving downwards with velocity $\mathbf{u}_\Gamma$. There is neither mass or heat flux through domain boundaries. Air in the top pocket is being expanded, while air in the bottom is getting compressed.

in dynamic pressure prescribed with Eqn. 21. Ordinary second order accurate discretisation for cell P using Gauss theorem states:

$$\begin{aligned}\nabla\bullet(\mathbf{u}p_d)_P &= \frac{1}{V_P}\int_{CV}\nabla\bullet\mathbf{u}p_d\,\mathrm{d}V = \frac{1}{V_P}\oint_{\partial CV} p_d\,\mathrm{d}\mathbf{S}\bullet\mathbf{u}\\ &= \frac{1}{V_P}\sum_f \mathbf{s}_f\bullet\mathbf{u}_f p_{df} = \frac{1}{V_P}\sum_f F_f p_{df}\,,\end{aligned}\tag{93}$$

where F_f denotes volumetric face flux. Dividing the sum over all cell faces for interface cells yields:

$$\begin{aligned}\nabla\bullet(\mathbf{u}p_d)_{P_\Gamma} &= \frac{1}{V_P}\sum_{f\not{\Gamma}} F_f\left(f_x p_{dP} + (1-f_x)p_{dN}\right)\\ &+ \frac{1}{V_P}\sum_{f\Gamma}(F_f)_{P_\Gamma}\left(f_x p_{dP} + (1-f_x)p^-_{dN_\Gamma}\right)\,,\end{aligned}\tag{94}$$

where $(F_f)_{P_\Gamma}$ stands for the interface face volumetric flux that contains the jump arising from jump conditions in Eqn. 25 (see Eqn. 83)). For cell N, $(F_f)_{P_\Gamma}$ is used instead. Note that convection of dynamic pressure term is active only in the compressible gas phase, rendering extrapolation from the incompressible phase unnecessary. Therefore, $p^-_{dN_\Gamma}$ is used instead of $p^{+/-}_{dN_\Gamma}$ in the above expressions.

3.3.9. Discretisation of Velocity Convection Term

Velocity convection term in the momentum equation (Eqn. 17) is treated implicitly. Ordinary FV discretisation states:

$$\begin{aligned}\nabla\bullet(\mathbf{uu})_P &= \frac{1}{V_P}\int_{CV}\nabla\bullet(\mathbf{uu})\,\mathrm{d}V = \frac{1}{V_P}\oint_{\partial CV}\mathbf{n}\bullet\mathbf{uu}\,\mathrm{d}S\\ &= \frac{1}{V_P}\sum_f \mathbf{s}_f\bullet\left(\mathbf{u}_f\mathbf{u}_f\right) = \frac{1}{V_P}\sum_f F_f\mathbf{u}_f\,.\end{aligned}\tag{95}$$

Dividing the sum over all cell faces for interface cells yields:

$$\begin{aligned}\nabla\bullet(\mathbf{uu})_{P_\Gamma} &= \frac{1}{V_P}\sum_{f\not{\Gamma}} F_f\left(f_x\mathbf{u}_P + (1-f_x)\mathbf{u}_N\right)\\ &+ \frac{1}{V_P}\sum_{f\Gamma}(F_f)_{P_\Gamma}\left(f_x\mathbf{u}_P + (1-f_x)\mathbf{u}_N\right)\,.\end{aligned}\tag{96}$$

Apart from the implicit convection term, the explicit interface jump $[\nabla \bullet (\mathbf{u}\mathbf{u})]$ of convection also needs to be defined. For an interface face dividing cell P and cell N, the jump can be written as:

$$\begin{aligned}[\nabla \bullet (\mathbf{u}\mathbf{u})] =& \frac{1}{V_P} \left(F_f\right)_{P_\Gamma} \left(f_x \mathbf{u}_P + (1 - f_x)\mathbf{u}_N\right) - \frac{1}{V_N} \left(F_f\right)_{N_\Gamma} \left(f_x \mathbf{u}_P + (1 - f_x)\mathbf{u}_N\right) \\ =& \left(\frac{1}{V_P} \left(F_f\right)_{P_\Gamma} - \frac{1}{V_N} \left(F_f\right)_{N_\Gamma} \right) \left(f_x \mathbf{u}_P + (1 - f_x)\mathbf{u}_N\right) \,, \end{aligned} \tag{97}$$

where $\left(F_f\right)_{P_\Gamma}$ and $\left(F_f\right)_{N_\Gamma}$ are defined by Eqns. 83 and 85. Note that $[\nabla \bullet (\mathbf{u}\mathbf{u})]$ and the volumetric flux jump are interdependent and require nonlinear interations to converge. Since the jump also depends on the solution of the pressure equation, the algorithm relies on the segregated solution procedure to couple the pressure and momentum equations and to converge the jump conditions.

3.3.10. Discretisation of the Velocity Divergence Term

Divergence of velocity is discretised as:

$$\begin{aligned}\nabla \bullet \mathbf{u}_P &= \frac{1}{V_P} \int_{CV} \nabla \bullet \mathbf{u} \, \mathrm{d}V = \frac{1}{V_P} \oint_{\partial CV} \mathrm{d}\mathbf{S} \bullet \mathbf{u} \\ &= \frac{1}{V_P} \sum_f \mathbf{s}_f \bullet \mathbf{u}_f = \frac{1}{V_P} \sum_f F_f \,. \end{aligned} \tag{98}$$

For interface cells the sum is divided for internal and interface faces:

$$\nabla \bullet \mathbf{u}_{P_\Gamma} = \frac{1}{V_P} \sum_{f \not\Gamma} F_f + \frac{1}{V_P} \sum_{f\Gamma} \left(F_f\right)_{P_\Gamma} \,, \tag{99}$$

where $\left(F_f\right)_{N_\Gamma}$ is used for the neighbouring interface cell N.

4. Verification and Validation

Three verification and validation cases are presented in this section. The first test case consists of a 1D liquid piston where the basic capability of the approach to simulate compression of the air phase is tested. In the second test case a free–falling horizontal water column impact is simulated where impact pressures are compared to other numerical methods in the literature. The third test case verifies that the approach can be used for regular wave propagation with negligible compressibility effects.

4.1. Liquid Piston

The liquid piston case is a basic test for compressible two–phase flow solvers. The test corresponds to Fig. 3: it is a one–dimensional problem where the layer of water is suspended between two air pockets. The water oscillates under the influence of interchanging gravitational energy and internal energy of the air phase. If the domain boundaries permit no mass or heat flux, and if both fluids are considered inviscid, the process is adiabatic. Thus, the oscillation of the water column should persist indefinitely. This test case was used as a benchmark by Ma et al. [14] and Guilcher et al. [4], and the results of this implementation will be compared to theirs for validation. The schematic representation of the test case with dimensions is shown in Fig. 4. The density of water is set to 1000 kg/m^3, density of air to 1 kg/m^3, while the initial pressure of air is set to p = 1 bar. Both phases are considered inviscid. Second order temporal scheme is used for all temporal derivatives. For convection of velocity and dynamic pressure, second order linear scheme is used. For interface convection a second order accurate van Leer bounded scheme is used with deferred correction.

Verification study is performed by systematically varying spatial and temporal resolution, where the procedure suggested by Eça & Hoekstra [35, 36] for unsteady flows is employed. A code based on these procedures is used which is freely available [37]. The convergence study is performed with respect to the maximum pressure value during the first period of oscillation on the bottom boundary (see Fig. 6). Table 1 shows the results for the entire test matrix used for the verification, where the number of cells and time–step size are marked. Note that the result for 240 cells with 0.04 s time–step is not available since the simulation diverged due to a large Courant number. The output of the uncertainty calculation code is presented in Tab. 2

The case is validated against results obtained by Ma et al. [14] and Guilcher et al. [4]. Comparison of pressure on the bottom boundary in time is shown on Fig. 5. The three signals are in good agreement without notable differences.

To check the conservation of energy, a 10 seconds simulation time is performed. Figs. 6 and 7 show pressure and density time signals at the top and bottom boundary, respectively. Pressure and density oscillationn does not decay in time, proving that the conservation of energy is achieved.

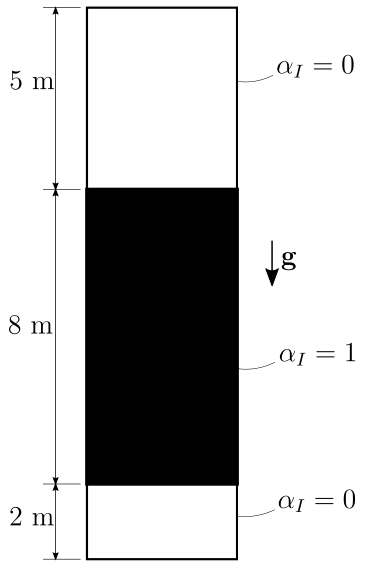

Fig. 4: A schematic representation of a one–dimensional liquid piston case.

Table 1: Test matrix results for the liquid piston test case. The values denote the peak pressure of the first oscillation period in Pa.

N_{Cells} \ Δt, s	0.04	0.02	0.01	0.005	0.0025
15	297288.98	303836.10	305526.95	305787.79	304039.69
30	284618.65	290061.17	292051.66	293511.72	295654.25
60	277320.55	284783.39	287491.17	287494.11	287930.21
120	277409.95	283421.45	285358.84	285850.38	286060.13
240	N/A	283801.79	285392.08	285743.46	285994.18

4.2. Free fall of a water column

In this test case a free fall impact of a horizontal square cross–section water is simulated, where impact pressure against a horizontal impermeable wall is measured. Fig. 8 shows the schematic representation of the case. Same initial pressure, air and water properties are used as in the liquid piston case. Initial velocity field in the entire domain is set to zero. First order Euler temporal scheme is used for time–integration, while velocity and dy-

Table 2: Verification results for the liquid piston test case. The notation follows Eça & Hoekstra [35]: ϕ_0 denotes the extrapolated exact solution, ϕ_1 denotes the finest level solution, q denotes the achieved accuracy in space, while p denotes achieved accuracy in time. p_{peak} denotes the peak pressure.

Item	ϕ_0, Pa	ϕ_1, Pa	U_ϕ	p	q
p_{peak}	285780.00	285994.18	0.2%	2.00	2.00

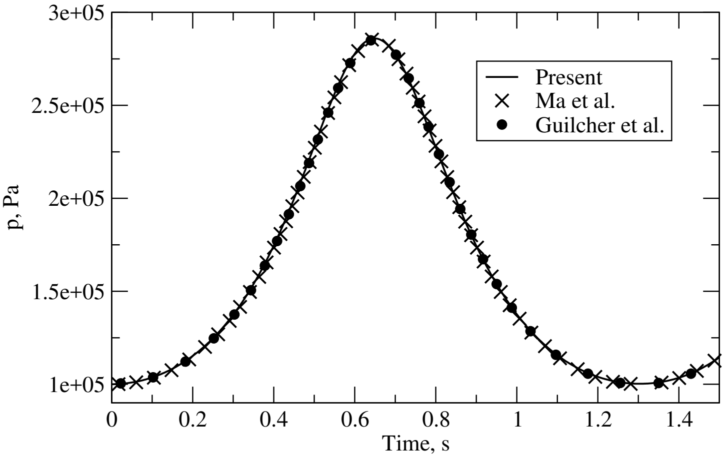

Fig. 5: Comparison of pressure at the bottom boundary of the liquid piston case against results obtained by Ma et al. [14] and Guilcher et al. [4]

namic pressure convection are discretised using first order upwind scheme. For interface convection a second order accurate van Leer bounded scheme is used as in the previous test case. The domain is discretised using 200 cells in the horizontal direction and 1 200 cells in the vertical direction. A fixed Courant number of 0.9 is maintained during the simulation by varying the time–step size. The time–step varied between 0.005 seconds at the beginning of the simulation, reducing to 2.5×10^{-4} during the impact.

Pressure measured at the bottom boundary at the centre of the domain is compared to results obtained by Braeunig et al. [9], Ma et al. [14] and Guilcher et al. [4]. The comparison of pressure signals is presented in Fig. 9. The peak of the pressure signal obtained with the present approach cor-

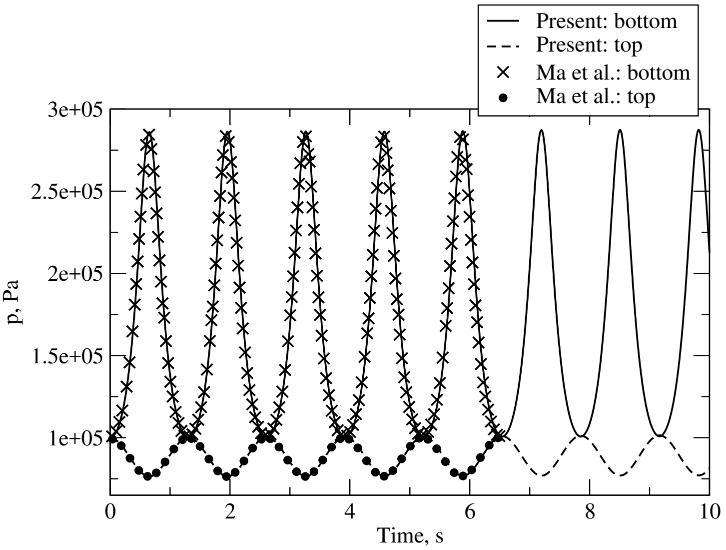

Fig. 6: Comparison of pressure at the bottom and top boundary of the liquid piston case during 10 seconds.

responds well with the results obtained by Guilcher et al. The coarse grid result by Ma et al. and the result obtained by Braeunig et al. predict lower pressure values, while the fine grid result by Ma et al. gives a significantly larger pressure peak of 34 bars. Comparing to the remaining results which range between 22.6 to 25.4 bars this is an outlier.

Fig. 10 shows the variation of the air density entrained in the cavity. The geometry of the free surface with visualisation of the velocity and pressure fields is shown in Figs. 11 and 12 for several time instances. After the first impact shown on Fig. 11c, a pocket of air gets entrained underneath the water column. The cavity fist expands as seen in Figs. 11d and e, and then compresses as visible in Figs. 11f, 12a and b. Then, the cavity expands again as shown in Figs. 12c and d. The oscillation can be seen in the complete pressure signal shown in Fig. 13.

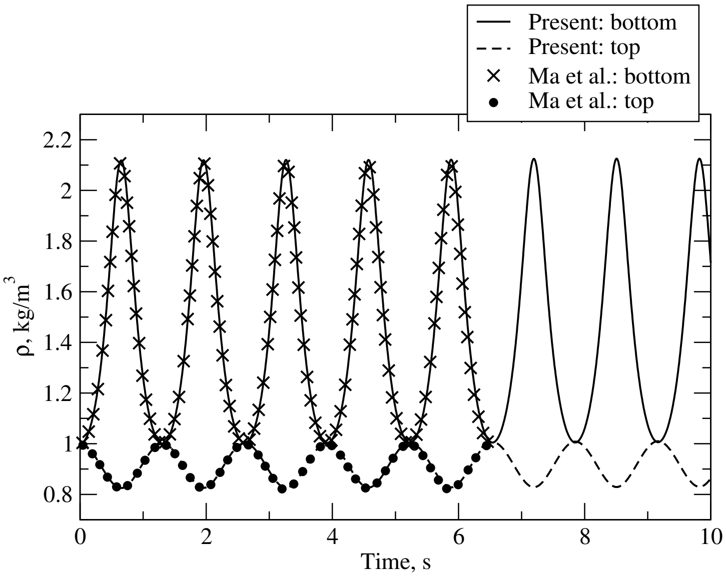

Fig. 7: Comparison of density at the bottom and top boundary of the liquid piston case during 10 seconds.

4.3. Regular Wave Propagation

The goal of this study is to devise a compressible two–phase flow model that can be applied to a large variety of problems in the field of naval hydrodynamics. For that end, it is important to assure that wave propagation can be handled accurately and efficiently , when phase compressibility effects are negligible. In this section, a detailed verification and validation is performed for propagation of a regular wave. The regular wave is initialised using the stream function wave theory with a period $T = 3$ s, height $H = 0.1$ m and wave length $\lambda = 13.93$ m. A two–dimensional domain is 60 m long, 6 m deep and 0.3 m high above the free surface. Inlet and outlet implicit relaxation zones [38] are placed at the edges of the domain, with a length of 22 m, leaving 16 m of unaffected length in the middle of the domain. Fig. 14 shows the velocity field in the simulation, where the black vertical lines indicate the end of the inlet and outlet relaxation zones. The waves propagate from left to right. Same discretisation schemes are used as in the liquid piston case, thus second order accuracy is expected. All simulations are performed for 10 wave

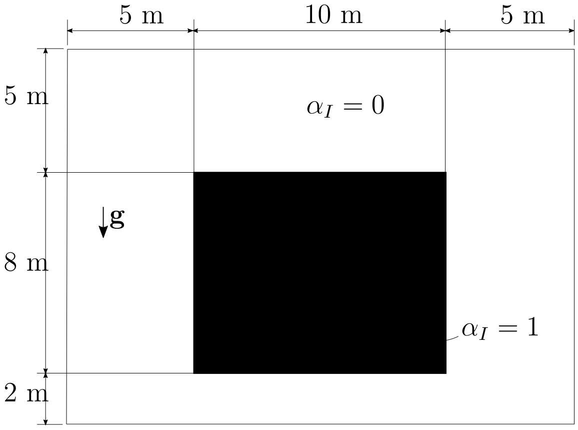

Fig. 8: A schematic representation of falling water column test case. A horizontal water column with a rectangular cross–section is suspended in air at time zero. Under the influence of gravity the column impacts the bottom horizontal surface.

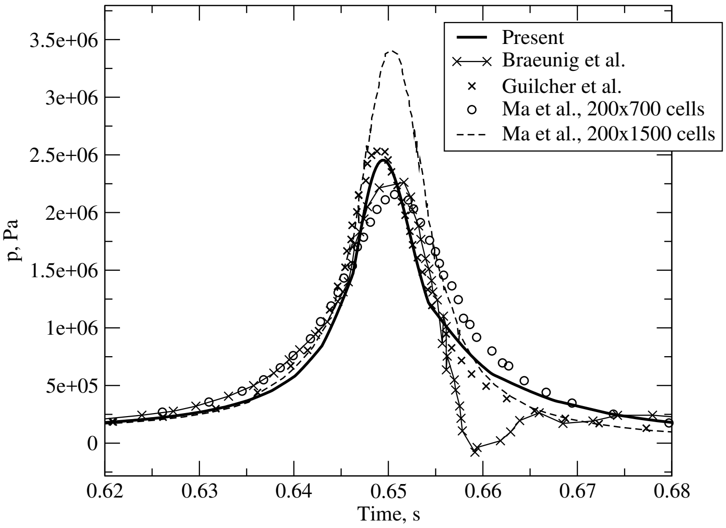

Fig. 9: Pressure signal comparison during the impact of the falling water column. Pressure measured at the center of the bottom boundary is compared to Braeunig et al. [9], Ma et al. [14] and Guilcher et al. [4].

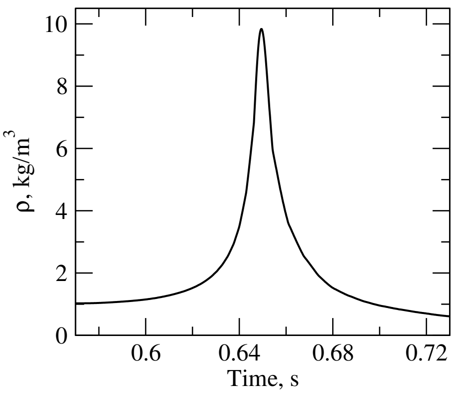

Fig. 10: Air density variation in the air cavity during the impact of the falling water column.

periods, i.e. for 30 seconds. For verification and validation, surface elevation signal measured in the middle of the domain (denoted with a white vertical line in Fig. 14) is used. First and second order harmonic amplitudes, η_1 and η_2 are obtained by using Fast Fourier Transform of the surface elevation measured in the last wave period (i.e. from $t = 27$ to $t = 30$). Fig. 15 shows the time evolution of the surface elevation.

Verification is performed using the same procedure as in Sec. 4.1 by systematically varying spatial and temporal resolution. The grid is non–uniformly distributed along the vertical and horizontal axis in order to optimise the number of cells. In the vertical direction, uniform cell size is used 0.1 m above and below the free surface, while linear grading is applied outside, by enlarging the cells towards the bottom and the top boundary. Similar is applied in the horizontal direction, where uniformly distributed cells are placed in the middle of domain extending 8 m to each side, while linear grading is applied from that point towards the inlet and outlet boundaries. The verification test matrix with results for the first order amplitude is presented in Table 3, where the number of cells corresponds to the number of cells in the vertical direction in the uniformly distributed region around the interface. The number of cells in the horizontal direction in the central uniformly distributed region is obtained by multiplying this number with 1.5. Results

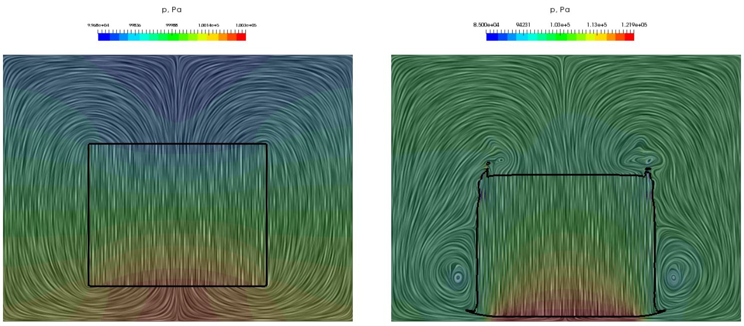

(a) $t = 0.05$ s,

(b) $t = 0.60$ s,

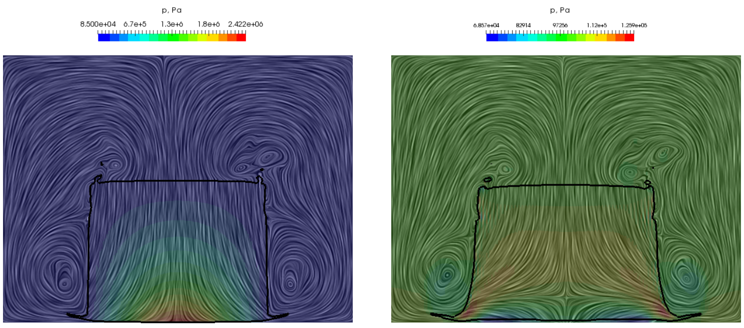

(c) $t = 0.65$ s,

(d) $t = 0.70$ s,

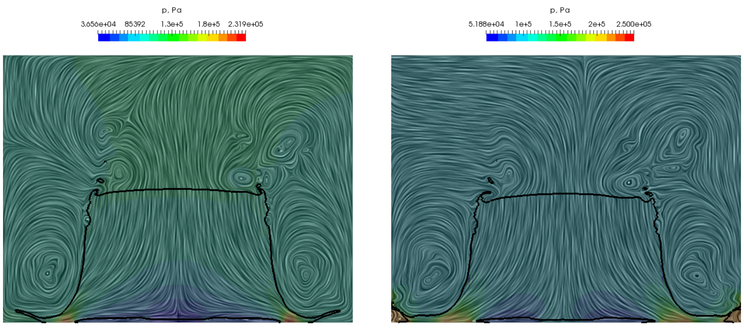

(e) $t = 0.75$ s,

(f) $t = 0.80$ s,

Fig. 11: Evolution of the interface, velocity and pressure field in the free fall of the water column. Part 1.

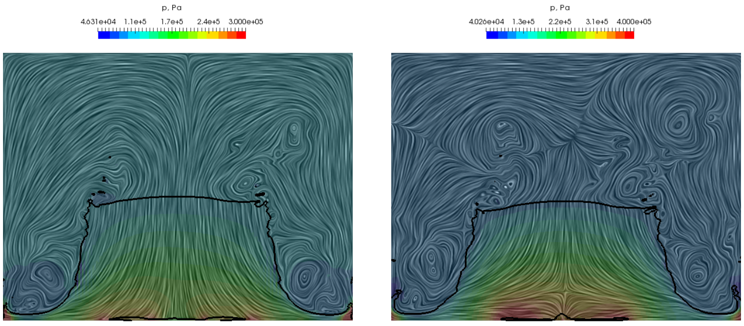

(a) $t = 0.85$ s, (b) $t = 0.90$ s,

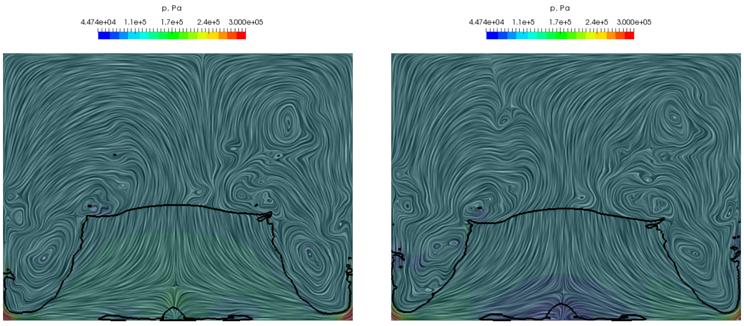

(c) $t = 0.95$ s, (d) $t = 1.00$ s,

Fig. 12: Evolution of the interface, velocity and pressure field in the free fall of the water column. Part 2.

for second order harmonic amplitude are shown in Table 4. Note that the second order amplitude is two orders of magnitude smaller comparing to the first order amplitude due to a relatively linear wave.

The output of the numerical uncertainty analysis is shown in Table 5. Second order accuracy in space is achieved for η_1, while the order of convergence in time of 1.61 is achieved. For η_2, second order accuracy in space is achieved as well, while first and second order exponents are used in time [36]. The grid uncertainty for η_1 is low being 0.4%, while for second order it is relatively higher, i.e. 10.9%. The second order amplitude is only 0.5 mm, while the cell height on the finest grid is $\Delta z = 0.2/64 = 0.003$ m, i.e. 3 mm.

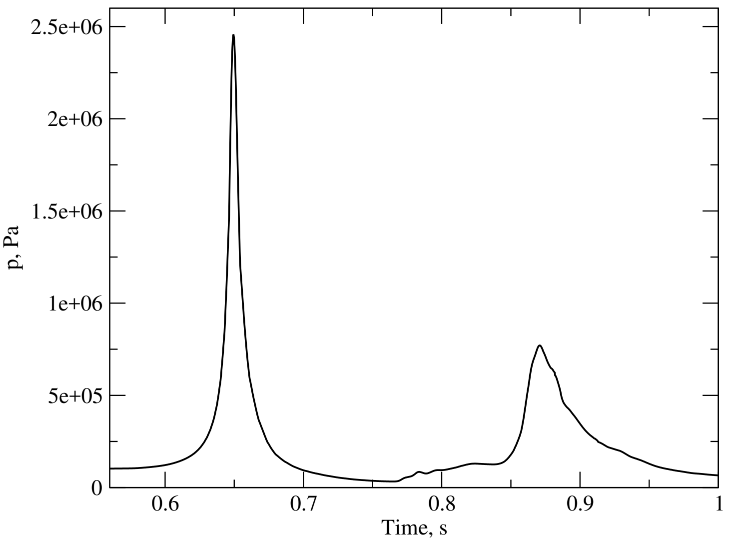

Fig. 13: Pressure signal measured during the free fall of the water column.

Thus, given that the second order amplitude is six times smaller than the finest cell, the obtained uncertainty is acceptable.

Numerical results are validated against the solution of the stream function wave theory. Comparison of surface elevation signals are shown in Fig. 15, while the harmonic amplitudes are compared in Tab. 6. The error between the stream function solution and numerical results is calculated as $E_{rr} = (\eta_{SF} - \eta_{CFD}) / \eta_{SF}$. For the first order amplitude, the error is 0.25%, while the second order amplitude exhibited relative error of 8.7%, which is acceptable considering the magnitude of η_2 compared to the cell height. Overall, this test case proves that the present model is capable of simulating wave propagation accurately and precisely.

In order to compare the computational efficiency with the counterpart incompressible numerical model, two simulations are carried out with equivalent settings on the same computer: a single core of a Intel Core i7-4820K CPU (3.70GHz). It took 785 seconds of wall–clock time to finish 30 seconds of simulation with 11 700 cells grid using the compressible solver, while it took 760 seconds with the incompressible. Thus, the two approaches are almost equivalent in terms of computational efficiency.

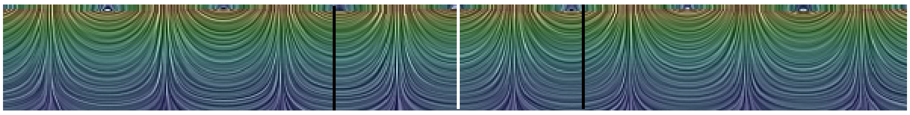

Fig. 14: Regular wave propagation case. The colour represents the magnitude of the velocity, the black vertical lines denote the ends of inlet and outlet relaxation zones, while the white vertical line denotes the location of the wave probe.

Table 3: Test matrix results for the wave propagation test case. The values denote the first order harmonic amplitude (η_1) of free surface elevation in meters.

Δt, s N_{Cells}	0.02	0.01	0.005	0.0025
16	0.048422	0.048882	0.049179	0.049199
32	0.049681	0.049822	0.049918	0.049981
64	0.049995	0.050027	0.050049	0.050079

Table 4: Test matrix results for the wave propagation test case. The values denote the second order harmonic amplitude (η_2) of free surface elevation in meters.

Δt, s N_{Cells}	0.02	0.01	0.005	0.0025
16	0.000560	0.000586	0.000533	0.000557
32	0.000603	0.000585	0.000565	0.000536
64	0.000530	0.000548	0.000537	0.000534

5. Industrial Cases: Validation

Validation of industrially relevant cases is performed in this section, where numerical results are compared to experimental data. Additionally, numeri-

Table 5: Verification results for the wave propagation test case. The notation follows Eça & Hoekstra [35]: ϕ_0 denotes the extrapolated exact solution, ϕ_1 denotes the finest level solution, p denotes the achieved accuracy in space, while q denotes achieved accuracy in time. η_1 and η_2 denote first and second order harmonic amplitudes of the free surface elevation, respectively.

Item	ϕ_0	ϕ_1	U_ϕ	p	q
η_1, m	5.01×10^{-2}	5.01×10^{-2}	0.4%	2.00	1.61
η_2, m	5.12×10^{-4}	5.34×10^{-4}	10.9%	2.00	$*^{1,2}$

$*^{1,2}$ Fit was made using first and second order exponents

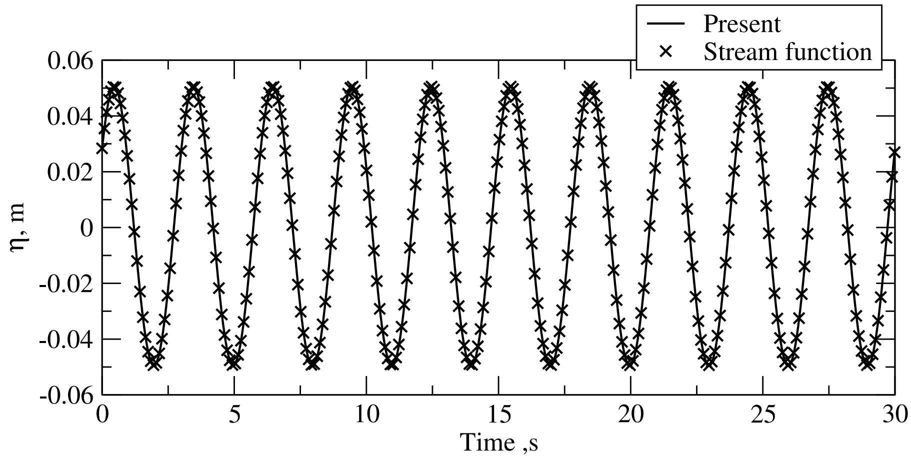

Fig. 15: Time signal of surface elevation in the wave propagation case. Comparison between the present result obtained with $N_{Cells} = 64$ and $\Delta t = 0.0025$ from Tab. 3 and 4, and the Stream function wave theory solution.

Table 6: Validation results for the wave propagation test case. Numerical results correspond to the solution obtained with $N_{Cells} = 64$ and $\Delta t = 0.0025$ from Tab. 3 and 4.

Item	Stream function	Numerical result	E_{rr}, %
η_1, m	0.049952	0.050079	-0.25%
η_2, m	0.000585	0.000534	8.7%

cal results obtained with the present approach are compared to the its counterpart incompressible formulation [20] in terms of accuracy and performance. Two test cases are considered: a green sea loading case and a seakeeping case of a container vessel in regular head waves.

5.1. Green Sea Loading

Wave on deck or green sea phenomenon can often include violent wave impacts against vertical structures such as breakwaters. It is important to ensure that the present model can be used to accurately predict such loads. In this section a benchmark case is used to validate the method against experimental data published by Lee et al. [39]. A detailed verification and validation of the incompressible framework has been performed in the past [40] using the same experimental data, where nine different incident regular waves are considered. However, only the most severe incident wave will be considered here, where the result will be compared to the experimental data and numerical results from Gatin et al. [40] in order to study the influence of compressibility on the results. The incident wave corresponds to wave ID 9 from [40], with wave length $\lambda = 3.75$ m, amplitude $a = 0.1125$ m, with a resulting wave steepness of $ka = 0.188$, where k denotes the wave number. A simplified, fixed model of a FPSO (Floating Production, Storage and Offloading) vessel termed "RECT0" [39] is considered, with geometry shown in Fig. 16a. Pressure probes are positioned at ten locations on the horizontal deck, arranged as shown in Fig. 16b.

Computational domain used in the simulation is shown in Fig. 17. Implicit relaxation zones are placed on the inlet, outlet, starboard and portside boundaries in order to facilitate the wave generation and to prevent wave reflection. The regular wave is generated using the stream function theory. A computational grid with 3.45 million cells was used, corresponding to the finest grid level in [40]. Grid characteristics are shown in Tab. 7, where L denotes the domain length, L_R indicates the length of inlet and outlet relaxation zones, while $\lambda/\Delta x$ and $a/\Delta z$ denote the number of cells per wave length and wave amplitude, respectively. H stands for the height of the domain above the deck in metres. Note that the freeboard height is 0.045 m above the free surface [39]. Δz_{deck} stands for the height of the cell above the deck. In order to provide a fair comparison, same numerical settings are used for the simulation with the present compressible model with respect to the incompressible simulation performed in [40]. A geometric interface capturing

VOF method called isoAdvector [41] is employed to provide a sharp interface definition. A fixed Courant number of $C_o = 0.75$ is used, resulting in average time–step of around 0.001 s.

Following [40], the compared items are average pressure peak p_{max} and average pressure integral over one wave period P, which are calculated as:

$$p_{max} = \frac{\sum_{i=1}^{N_C} p_{i,max}}{N_C}\,, \tag{100}$$

$$P = \frac{\sum_{i=1}^{N_C} \int_0^T p_i\left(t\right) dt}{N_C}\,, \tag{101}$$

where $p_{i,max}$ denotes the pressure peak during i-th wave period, while N_C stands for the number of wave periods. Additionally, periodic uncertainty is calculated for both items as:

$$U_{CP} = \frac{\phi_{max} - \phi_{min}}{N_C}\,, \tag{102}$$

where ϕ denotes either p_{max} or P. Comparison of average pressure peaks between experimental and compressible and incompressible numerical results is shown in Fig. 18. The differences between incompressible and compressible two–phase models are negligible, which draws two conclusions: first, the compressibility effects such as trapped air are not present in this case, and second, the compressible formulation gives equivalent results to the incompressible model when no compressibility effects are present. Gatin et al. [40] assumed that the large overestimation of the pressure peak with respect to experimental results for pressure gauge ID 7 could be a consequence of compressibility effects which are not accounted for in the numerical model. Here, that assumption is proved to be wrong. Another reason that might cause the overshooting of the pressure peak is the fact that the breakwater is considered perfectly rigid in the simulation, while in the experiment a plexiglas wall is used. The dynamic response of the plexiglas could have an influence on the reduction of the pressure peak. Further efforts will be employed to detect the source of discrepancy. Nonetheless, for the remaining pressure gauges the comparison is acceptably accurate. The comparison of pressure integrals in time is shown in Fig. 19, where a similar agreement between the incompressible and compressible results are achieved as for pressure peaks.

In terms of computational time, the incompressible simulation took 45.7 hours using 32 cores of a Intel Xeon Processor E5-2637 v3 (15M Cache, 3.50 GHz), while the compressible took 27.7 hours on 64 cores of the same processor, showing comparable computational requirements.

Table 7: Computational grid characteristics for the green sea loading case.

L, m	L_R, m	H, m	$\lambda/\Delta x$	$a/\Delta z$	Δz_{deck}, m
6.5	2.5	0.15	375	15.5	$5.84 \cdot 10^{-4}$

5.2. Seakeeping

A ship sailing in waves can be subjected to compressible wave loading effects due to slamming and green water phenomena. In order to be able to effectively predict such loading the motion of the ship in waves must be accurately calculated. To that end a seakeeping simulation is performed in this section where a KRISO Container Ship (KCS) model is considered sailing in regular head waves. Wave characteristics, ship speed and scale correspond to the C5 case from the Tokyo Workshop on CFD in Ship Hydrodynamics [42], where experimental results can be found as well. Model length is $L_{PP} = 6.05$ m, breadth $B = 0.85$ m and draught $T = 0.285$ m. A regular incident wave with wave length $\lambda = 11.84$ m and wave height $H = 0.196$ m is imposed using the stream function wave theory. Unstructured computational grid is used with 950 000 cells, shown in Fig. 20. k–ω SST turbulence model is used in this simulation. Fluid–structure interaction occurring between the wave field and the ship is resolved using an enhanced coupling algorithm [43]. Wave generation and absorption is performed using implicit relaxation zones which are placed at the inlet and outlet boundaries. The inlet relaxation zone has a length of $\lambda/2$, while the outlet has a length of λ. The domain boundaries are positioned $1L_{PP}$ in front of the fore perpendicular, $2L_{PP}$ from the aft perpendicular, and $1.5L_{PP}$ from the side. A fixed time–step is used resulting in 400 time–steps per encounter wave period, i.e. $\Delta t = 0.0046$ seconds. During the simulation the maximum Courant number ranges between 9 and 18.

The time signal of heave motion is shown in Fig. 21, where incompressible and compressible formulations are compared. In order to provide a quantitative comparison, the last period of heave, pitch and total resistance signals

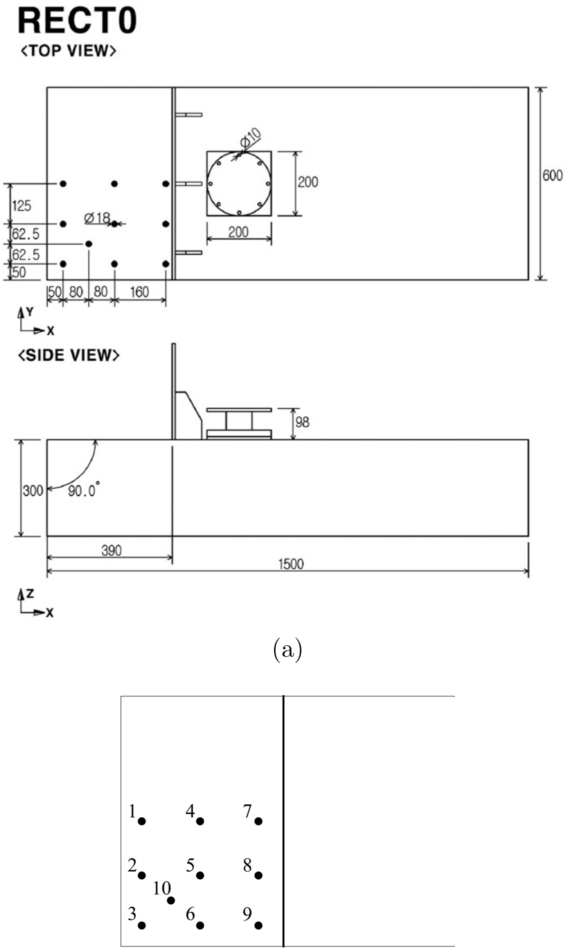

(a)

(b)

Fig. 16: Geometry of the FPSO model: a) model dimensions and pressure gauge positions (pressure gauges are indicated with black dots) [39], b) schematic of pressure gauges arrangement with labels.

are transformed into frequency space via FFT.

Table 8 shows the comparison of zeroth and first order harmonic ampli-

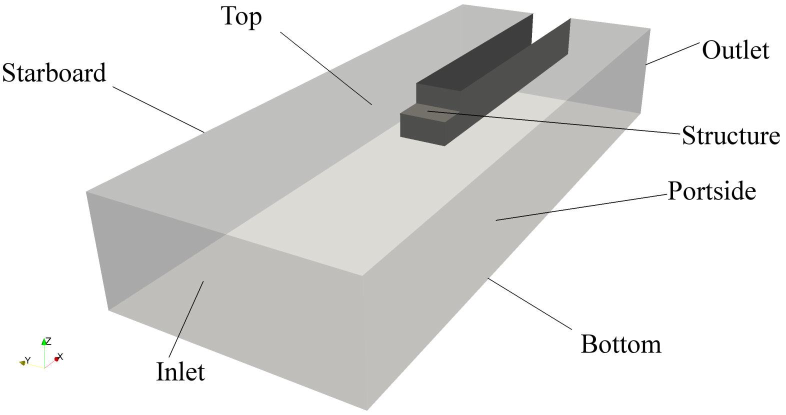

Fig. 17: Computational domain for the green sea loading case.

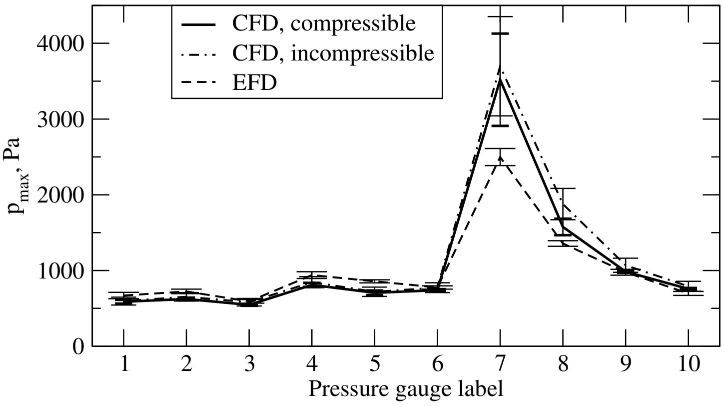

Fig. 18: Comparison of pressure average pressure peaks for the green sea loading case.

tudes, and phase shift of the first order harmonic for heave z, pitch ϕ and total resistance coefficient C_T. The present compressible and its counterpart incompressible models give very similar results, confirming that the two models are equivalent when the compressibility effects are absent. Both results compare well to experimental results, showing under 1.5% error for total resistance, and up to 5.5% error for first order amplitudes of motion. Note that relative errors are not presented for phase shifts, since they depend on the

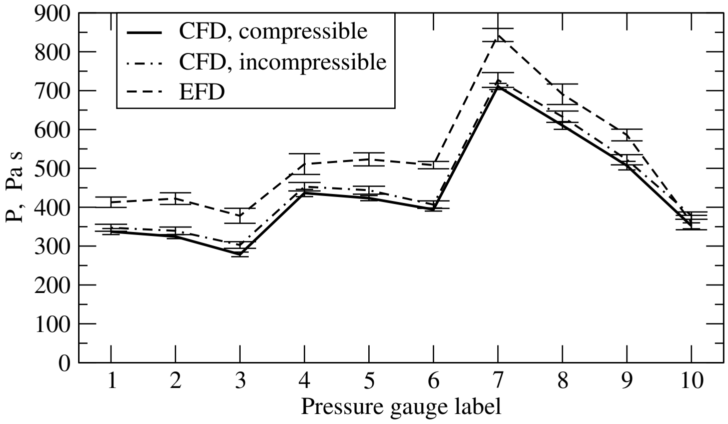

Fig. 19: Comparison of pressure average pressure integral in time for the green sea loading case.

arbitrary choice of the incident wave phase shift. The phase shifts differences range from 0.8^o for heave motion to 4^o for pitch motion.

In order to establish the overhead resulting from the compressible formulation, the computational time is compared for the two approaches. Both simulations were carried out on desktop computers: the incompressible simulation was performed on a Intel Core i5-3570K CPU at 3.40GHz, while the compressible one was performed on Intel Core i7-4820K CPU at 3.70GHz. It takes 4.7 hours of computational time per one wave period with the incompressible version, while it takes 3.6 hours with the compressible formulation. Note that the computer used for the compressible simulations has superior processor characteristics. Thus, the required computational resources are comparable between two formulations, rendering the present approach relevant for industrial applications.

6. Breaking wave impact with a trapped air bubble

This section presents the final test for the present model: a violent breaking wave impact with a trapped air bubble presented by Bullock et al. [2]. An extensive experimental campaign was conducted where large scale regular wave impacts against a vertical and inclined wall were measured. For this comparison, a wave with height $H = 1.25$ m, period of $T = 8$ s at calm

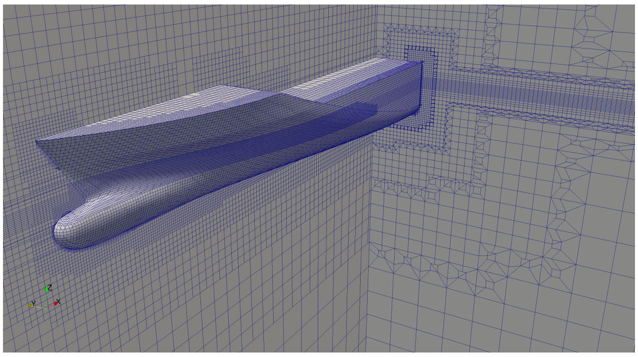

Fig. 20: Computational grid used in the KCS seakeeping simulation.

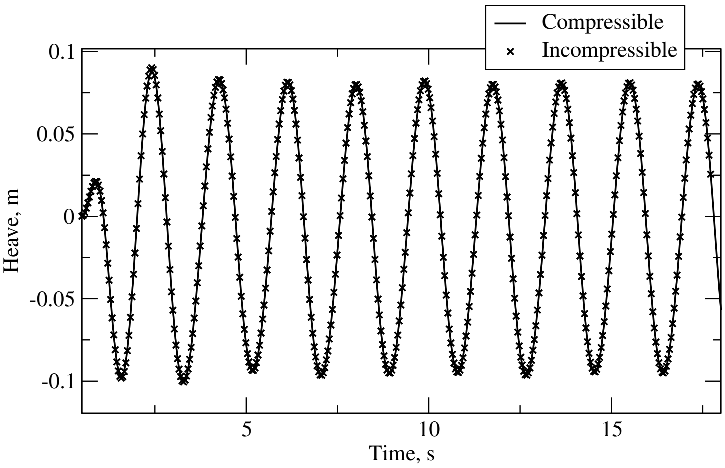

Fig. 21: Heave signal comparison in the seakeeping case.

water level depth of $d_c = 1$ m is selected, which results in a high–aeration impact [2] where a large air bubble is trapped between the wave front and the vertical wall. The experiments were conducted in a 350 m long, 5 m wide and 7 m deep Grosser Wellenkanal at the Forschungszentrum Küste in Hannover, Germany.

Simulation is conduced in a 2D domain that included 121 meters in front of the vertical wall, where the first 50 meters are the inlet relaxation zone

Table 8: Comparison of 0th and 1st order harmonic amplitudes and phase shift of 1st harmonic of heave z, pitch ϕ and total resistance C_T for the seakeeping case. γ denotes the phase shift of the first harmonic.

	Experimental	Compressible	Incompressible
$C_{T,0}$	5.421	5.495	5.447
$E_{rr,C_{T,0}}$,	N/A	-1.37	-0.48
$C_{T,1}$	25.101	23.447	23.329
$E_{rr,C_{T,1}}$, %	N/A	6.59	7.06
γ_{C_T}, ^{o}	-20.543	-16.766	-16.102
z_1/a	0.9312	0.8993	0.9004
E_{rr,z_1}, %	N/A	3.43	3.31
γ_z, ^{o}	-98.579	-98.462	-97.793
ϕ_1/ka	1.1185	1.0626	1.0572
E_{rr,ϕ_1}, %	N/A	5.00	5.48
γ_ϕ, ^{o}	-33.295	-29.128	-29.141

where the regular waves are initialised. Another 54 m of the domain is included behind the wall to provide comparable conditions to the experiment, where the wave was spilling over the wall. The height of the domain is 8 meters, corresponding to the depth of the wave tank. The bottom is placed at $z = 0$ m, while the undisturbed free surface level is at $z = 4$ m. The depth $d_c = 1$ m refers to water depth in front of the vertical wall, i.e. on the top of the mound. Fig 22 shows the view of the simulation domain where the vertical wall and the slope are indicated. The domain is discretised using 127 120 cells, with refinement near the vertical wall, presented on Fig. 23. `isoAdvector` method is used for interface capturing [41]. Nonlinear stream function wave theory is used to initialise the wave field and impose the oncoming waves at the domain inlet relaxation zone. The initial condition of the free surface is shown in Fig. 24, where a considerable asymmetry of the surface elevation around the calm free surface can be seen due to the shallow water condition. A fixed Courant number of 0.9 is used in order to resolve the violent wave impact. Three wave periods are simulated where the third one resulted in a breaking event with a trapped air bubble. It takes two wave periods for the reflected wave against the wall to interact with the oncoming waves creating a breaking event in front of the wall. Equivalent event was selected in the experimental results, i.e. the first period that resulted in a breaking event with trapped air bubble. Due to the longer domain, it took 5 periods in the experiment to obtain a breaking wave.

Pressure acting on the vertical wall is measured at positions corresponding to the experimental set–up. The vertical positions in meters of pressure gauges at the wall with respect to the bottom of the wave tank are: 3.49, 3.65, 3.74, 3.90, 4.04, 4.20, 4.39, 4.55, 4.70, 4.74, 4.90, 4.94, 5.10, 5.14, 5.30, 5.54, 5.70, and 5.89. In order to smooth out the noise present in pressure signals both in experiments and simulations, the integral of pressure is compared. The integral is calculated using the trapezoidal integration rule, where pressure values from the pressure gauges are assumed to be constant in the transversal direction.

Figs. 25 and 26 show the impact of the breaking wave with trapped air in the simulation. The initial air bubble separates into two parts, where one travels upwards while the second remains trapped in the bottom corner during the impact. After the impact, the run–up collapses creating a second breaking event travelling against incoming waves. Fig. 27 shows the comparison of the force acting on the vertical wall during the impact against the measured force in the experiment. The first peak after the impact agrees well with experimental measurements, as well as the first pressure drop, where sub–atmospheric pressure is recorded resulting in a negative force. From that point onwards (around $t = 11.32$ s), the force measured in the experiments damps within another period of oscillation, while in the simulation the pressure oscillation continues for another 7-8 periods. There are several possible reasons for discrepancy in energy loss of the oscillating air bubble:

- The simulation is 2D, thus any 3D effects are not influencing the impact. However, from the report and videos of the experimental campaign it can be concluded that 3D effects did not play a significant role in the first impact,

- In the simulation the wall and the surrounding structure are considered perfectly rigid, i.e. no energy transfer is possible from the fluid to the structure. According to Bullock et al. [2] a significant structural response was noticed during the experiment where the impacts generated "*forces that caused both the caisson and the reinforced-concrete walls of the channel to vibrate*" (page 605). The transfer of energy from the

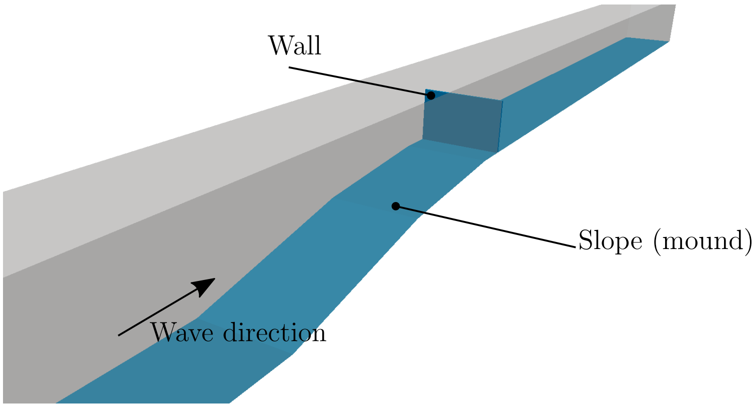

Fig. 22: Numerical domain for the wave impact test case. The vertical wall is placed on a two–segment inclined slope which is covered with gravel in the experiment.

wave to the caisson and the channel walls could be responsible for the damping of the bubble oscillation,

- In the experiment the vertical wall had equally spaced holes bored through the entire thickness of the wall to permit the water level to equalise on both sides of the wall. There were six columns of holes with three holes in each, where the holes had a circular cross–section with a diameter of around 10 cm. Fig. 28 shows a photograph of the vertical wall where the holes are visible. In an event of a breaking wave impact with trapped air, the air could escape from the bubble through the holes due to the large pressure difference. The escaping air would deflate the trapped bubble reducing the subsequent pressure oscillations. The effect of holes will be examined in future studies by performing a 3D simulation with the exact geometry of the wall including holes.

From the structural response point of view, the first force peak and through are more important than the force tail since they carry a large amount of energy due to high values acting on a large surface over an extended amount of time [2]. Thus, the present approach proves to be accurate with this respect, and can be used to accurately assess compressible wave impact loads.

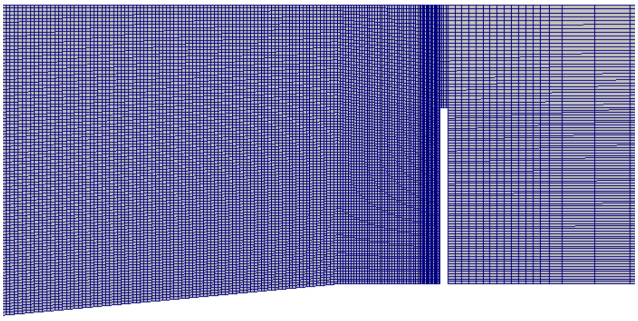

Fig. 23: View of the computational grid in front of the vertical wall in the wave impact simulation.

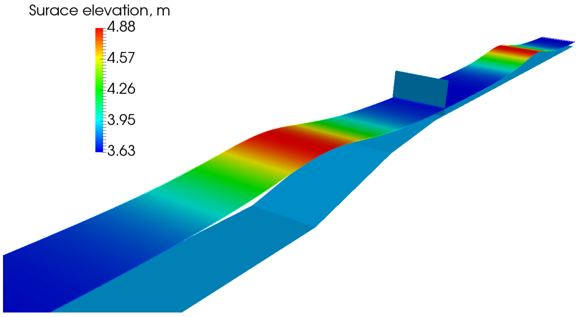

Fig. 24: Initial condition of the free surface elevation in the wave impact case.

7. Conclusion

A two–phase flow model with incompressible liquid and a compressible gas phase based on FV method intended primarily for various applications in marine engineering is presented in this paper. The implementation is performed in the Naval Hydro Pack software library based on foam–extend CFD software. The sharp change in fluid properties across the free surface is taken into account using the Ghost Fluid Method where specialised discretisation schemes are developed for arbitrary polyhedral unstructured grids. In this study the GFM is extended to take into account the jump in compressibility of the two phases, allowing the liquid phase to be considered incompressible

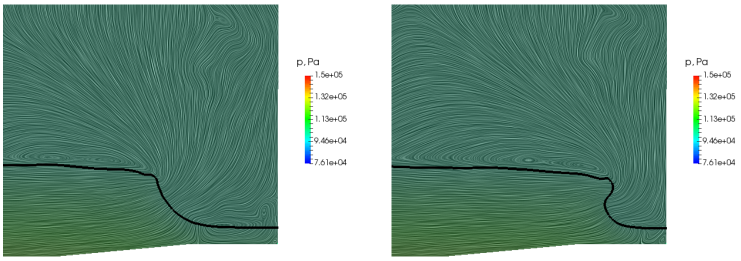

(a) $t = 18.25$ s, (b) $t = 18.50$ s,

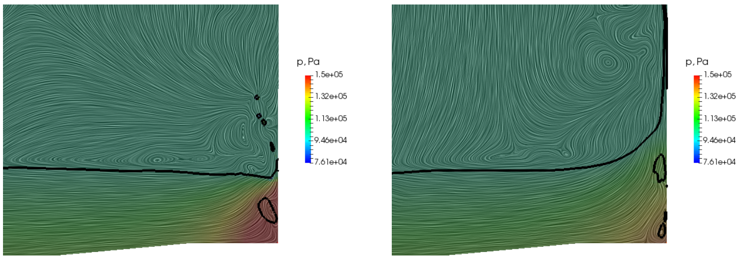

(c) $t = 18.75$ s, (d) $t = 19.00$ s,

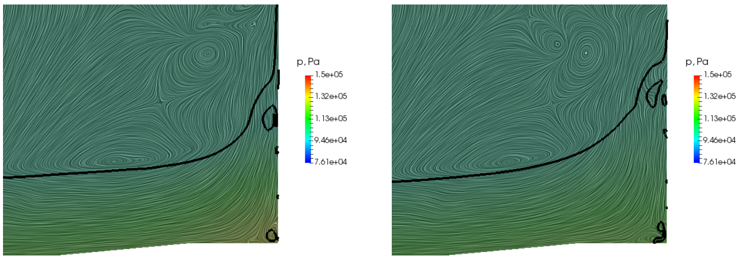

(e) $t = 19.25$ s, (f) $t = 19.50$ s.

Fig. 25: Evolution of the interface, velocity and pressure field in breaking wave impact event with trapped air. Part 1.

which avoids problems related with high speed of sound in water making the approach computationally inexpensive.

Verification and validation of the present approach is conducted on a 1D liquid piston case, a free fall impact of a horizontal water column, and regular wave propagation. The method proved to be accurate in capturing air compression and expansion effects, compressible impacts and simple wave

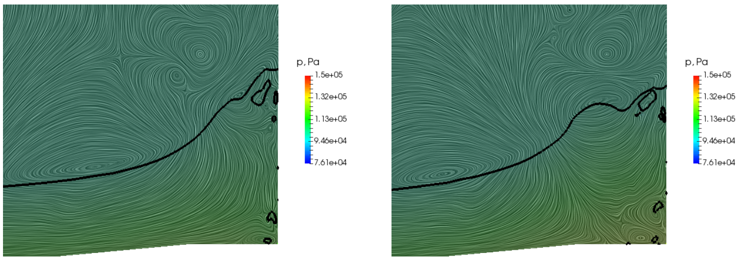

(a) $t = 19.75$ s, (b) $t = 20.00$ s,

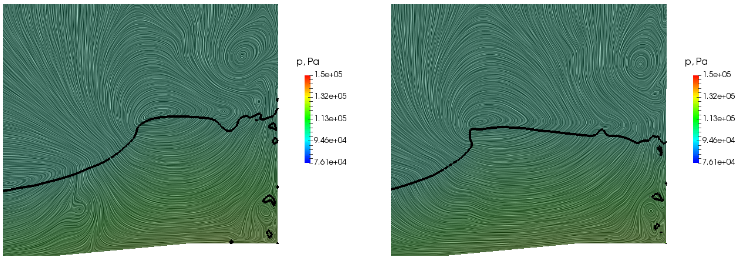

(c) $t = 20.25$ s, (d) $t = 20.50$ s.

Fig. 26: Evolution of the interface, velocity and pressure field in breaking wave impact event with trapped air. Part 2.

propagation where compressibility effects are negligible.

The aspect of industrial application of the method is tested on two test cases: a green water loading case and container vessel seakeeping in regular head waves. The method shows good correspondence with experimental results for both cases, while showing equivalent computational demands to its incompressible counterpart.

Finally, the ability of the method to capture wave impacts with trapped air effects is tested by comparing the simulation results to a large–scale experimental campaign. The present approach managed to reproduce the force peak exerted on a vertical wall, whereas the force oscillation after the first peak is overestimated. The possible reasons for the underestimated energy dissipation of the trapped air bubble oscillation will be studied in the future, where the most likely cause of discrepancy are the holes in the vertical wall present in the experiment, which were not modelled in the simulation. The

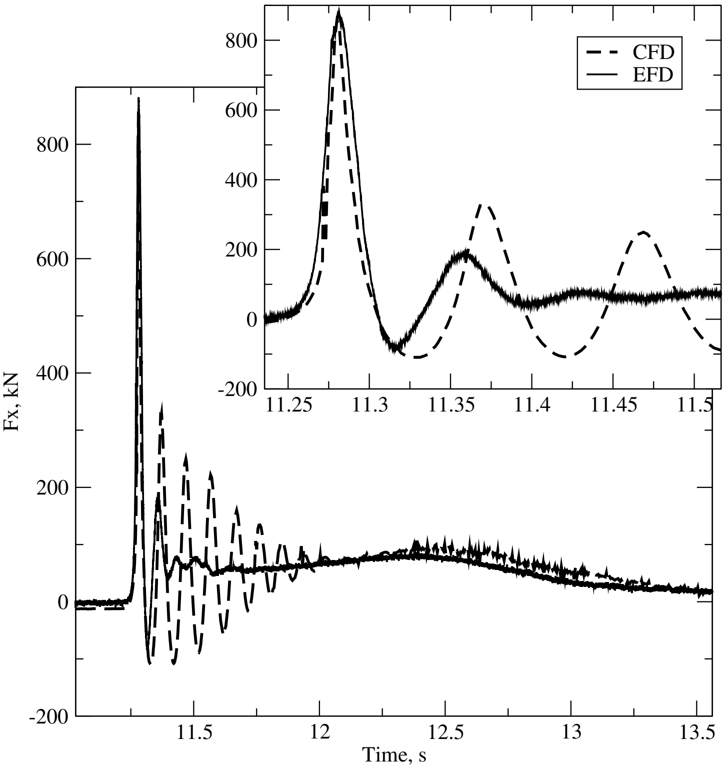

Fig. 27: Force signal comparison for the breaking wave case.

air bubble can deflate through these holes, damping the pressure oscillation.

Overall the present approach accurately and precisely models compressibility effects in two–phase flows characteristic for marine engineering. The method also proved to be applicable to realistic industrial cases with unstructured body–fitted grids and wave induced body motion, without an overhead in computational time. Future study will be focused on studying compressible breaking wave impacts in more details.

Fig. 28: Photograph of the vertical wall from the breaking wave impact experiment [2].

8. Acknowledgement

The numerical research performed for this study was sponsored by Bureau Veritas under the administration of Dr. Šime Malenica and Dr. Quentin Derbanne. The authors would like to acknowledge Prof. C. Obhrai from University of Stavanger, Norway, for providing access to experimental data related to breaking wave impacts.

References

[1] C. Obhrai, G. Bullock, G. Wolters, G. Muller, H. Peregrine, H. Bredmose, J. Grune, Violent Wave Impacts on Vertical and Inclined Walls: Large Scale Model Tests, Coastal Engineering (2004) 4075–4086.

[2] G. N. Bullock, C. Obhrai, D. H. Peregrine, H. Bredmose, Violent breaking wave impacts . Part 1 : Results from large-scale regular wave tests on vertical and sloping walls, Coastal Engineering 54 (2007) 602–617. `doi:10.1016/j.coastaleng.2006.12.002`.

[3] P. M. Guilcher, N. Couty, L. Brosset, D. Le Touzé, Simulations of breaking wave impacts on a rigid wall at two different scales with a two-phase fluid compressible SPH model, International Journal of Offshore and Polar Engineering 23 (4) (2013) 241–253.

[4] P. M. Guilcher, G. Oger, E. Jacquin, L. Brosset, N. Grenier, D. L. Touzé, Simulation of liquid impacts with a Two-Phase Parallel SPH model, International Journal of Offshore and Polar Engineering 24 (1) (2014) 11–20.

[5] M. Luo, C. G. Koh, W. Bai, M. Gao, A particle method for two-phase flows with compressible air pocket, International Journal for Numerical Methods in Engineering 108 (7) (2016) 695–721. `arXiv:1010.1724`, `doi:10.1002/nme.5230`.

[6] M. Luo, C. G. Koh, Shared-Memory parallelization of consistent particle method for violent wave impact problems, Applied Ocean Research 69 (2017) 87–99. `doi:10.1016/j.apor.2017.09.013`.

[7] M. Rostami V., M. J. Ketabdari, Application of the Modified Weakly Compressible SPH Method to the 3D Turbulent Wave Breaking Impact, Transactions of FAMENA 40 (1) (2016) 69–86.

[8] S. J. Lind, P. K. Stansby, B. D. Rogers, Incompressible-compressible flows with a transient discontinuous interface using smoothed particle hydrodynamics (SPH), Journal of Computational Physics 309 (2016) 129–147. `doi:10.1016/j.jcp.2015.12.005`.

[9] J.-P. Braeunig, L. Brosset, F. Dias, J.-M. Ghidaglia, Phenomenological Study of Liquid Impacts through 2D Compressible Two-fluid Numerical Simulations, in: 19th International Offshore and Polar Engineering Conference, Vol. 1, 2009, pp. 21–29.

[10] M. Dumbser, A simple two-phase method for the simulation of complex free surface flows, Computer Methods in Applied Mechanics and Engineering 200 (9-12) (2011) 1204–1219. `doi:10.1016/j.cma.2010.10.011`.

[11] L. R. Plumerault, D. Astruc, P. Maron, The influence of air on the impact of a plunging breaking wave on a vertical wall using a mul-

tifluid model, Coastal Engineering 62 (2012) 62–74. doi:10.1016/j.coastaleng.2011.12.002.

[12] J. Costes, F. Dias, J. M. Ghidaglia, A. Mrabet, Simulation of Breaking Wave Impacts on a Flat Rigid Wall by a 2D Parallel Finite Volume Solver with Two Compressible Fluids and an Advanced Free Surface Reconstruction, Proceedings of 23rd International Offshore and Polar Engineering Conference (ISOPE) 9 (2013) 880653.

[13] S. T. Miller, H. Jasak, D. A. Boger, E. G. Paterson, A. Nedungadi, A pressure-based, compressible, two-phase flow finite volume method for underwater explosions, Computers and Fluids 87 (2013) 132–143. doi:10.1016/j.compfluid.2013.04.002.
URL http://dx.doi.org/10.1016/j.compfluid.2013.04.002

[14] Z. H. Ma, D. M. Causon, L. Qian, C. G. Mingham, H. B. Gu, P. M. Ferrer, A compressible multiphase flow model for violent aerated wave impact problems, Proceedings of the Royal Society A: Mathematical, Physical and Engineering Sciences 470 (2172) (2014) 20140542–20140542. doi:10.1098/rspa.2014.0542.
URL http://rspa.royalsocietypublishing.org/cgi/doi/10.1098/rspa.2014.0542

[15] Z. H. Ma, D. M. Causon, L. Qian, C. G. Mingham, T. Mai, D. Greaves, A. Raby, Pure and aerated water entry of a flat plate, Physics of Fluids 28 (1). doi:10.1063/1.4940043.

[16] Z. H. Ma, D. M. Causon, L. Qian, C. G. Mingham, P. Martínez Ferrer, Numerical investigation of air enclosed wave impacts in a depressurised tank, Ocean Engineering 123 (2016) 15–27. doi:10.1016/j.oceaneng.2016.06.044.

[17] J. Calderón-Sánchez, D. Duque, J. Gómez-Goñi, Modeling the impact pressure of a free falling liquid block with OpenFOAM, Ocean Engineering 103. doi:10.1016/j.oceaneng.2015.04.060.

[18] C. F. Zou, D. Y. Wang, Z. H. Cai, Effects of boundary layer and liquid viscosity and compressible air on sloshing characteristics, International Journal of Naval Architecture and Ocean Engineering 7 (4) (2015) 670–690. doi:10.1515/ijnaoe-2015-0047.

[19] W. Lyu, O. el Moctar, R. Potthoff, J. Neugebauer, Experimental and numerical investigation of sloshing using different free surface capturing methods, Applied Ocean Research 68 (2017) 307–324. doi:10.1016/j.apor.2017.09.008.

[20] V. Vukčević, H. Jasak, I. Gatin, Implementation of the Ghost Fluid Method for free surface flows in polyhedral Finite Volume framework , Computers & Fluids 153 (2017) 1 − 19.

[21] R. P. Fedkiw, T. Aslam, S. Xu, The ghost fluid method for deflagration and detonation discontinuities, J. Comput. Phys. 154 (2) (1999) 393–427.

[22] M. Kang, R. P. Fedkiw, X.-D. Liu, A boundary condition capturing method for multiphase incompressible flow, J. Sci. Comput. 15 (3) (2000) 323–360.

[23] O. Desjardins, V. Moureau, H. Pitsch, An accurate conservative level set/ghost fluid method for simulating turbulent atomization, J. Comput. Phys. 227 (18) (2008) 8395–8416.

[24] J. Huang, P. M. Carrica, F. Stern, Coupled ghost fluid/two–phase level set method for curvilinear body–fitted grids, Int. J. Numer. Meth. Fluids 44 (2007) 867–897. doi:10.1002/fld.1499.

[25] W. Bo, J. W. Grove, A volume of fluid method based ghost fluid method for compressible multi-fluid flows, Comput. Fluids 90 (2014) 113–122.

[26] M. Kaneda, T. Haruna, K. Suga, Ghost-fluid-based boundary treatment in lattice boltzmann method and its extension to advancing boundary, Applied Thermal Engineering 72 (1) (2014) 126–134.

[27] B. Lalanne, L. R. Villegas, S. Tanguy, F. Risso, On the computation of viscous terms for incompressible two-phase flows with level set/ghost fluid method, J. Comput. Phys. 301 (2015) 289–307.

[28] H. Rusche, Computational fluid dynamics of dispersed two - phase flows at high phase fractions, Ph.D. thesis, Imperial College of Science, Technology & Medicine, London (2002).

[29] C. Hirt, B. Nicholls, Volume of fluid method for dynamics of free boundaries, J. Comput. Phys. 39 (1981) 201–221.

[30] P. Queutey, M. Visonneau, An interface capturing method for free–surface hydrodynamic flows, Comput. Fluids 36 (2007) 1481–1510. doi:10.1002/j.compfluid.2006.11.007.

[31] H. Jasak, A. D. Gosman, Residual error estimate for the finite-volume method, Numerical Heat Transfer Part B-Fundamentals 39 (1) (2001) 1–19.

[32] H. Jasak, Error analysis and estimation for the finite volume method with applications to fluid flows, Ph.D. thesis, Imperial College of Science, Technology & Medicine, London (1996).

[33] V. Vukčević, Numerical modelling of coupled potential and viscous flow for marine applications, Ph.D. thesis, Faculty of Mechanical Engineering and Naval Architecture, University of Zagreb, PhD Thesis (2016).

[34] H. Jasak, Error analysis and estimation for the finite volume method with applications to fluid flows, Ph.D. thesis, Imperial College of Science, Technology & Medicine, London (1996).

[35] L. Eça, M. Hoekstra, Code Verification of Unsteady Flow Solvers with the Method of the Manufactured Solutions, International Journal of Offshore and Polar Engineering 18 (2).

[36] L. Eça, M. Hoekstra, A procedure for the estimation of the numerical uncertainty of CFD calculations based on grid refinement studies, J. Comput. Phys. 262 (2014) 104–130. doi:10.1016/j.jcp.2014.01.006.

[37] ReFRESCO:A community based open-usage and open-source CFD code for the Maritime World., http://www.refresco.org/verification-validation/utilitiesvv-tools/, [Online; accessed January 2018].

[38] H. Jasak, V. Vukčević, I. Gatin, Numerical Simulation of Wave Loads on Static Offshore Structures, in: CFD for Wind and Tidal Offshore Turbines, Springer Tracts in Mechanical Engineering, 2015, pp. 95–105.

[39] H.-H. H. Lee, H.-J. J. Lim, S. H. Rhee, Experimental investigation of green water on deck for a CFD validation database, Ocean Engineering 42 (2012) 47–60. doi:10.1016/j.oceaneng.2011.12.026.

[40] I. Gatin, V. Vukčević, H. Jasak, J. Seo, S. H. Rhee, CFD verification and validation of green sea loads, Ocean Engineering 148 (2018) 500–515. doi:10.1016/j.oceaneng.2017.10.026.

[41] J. Roenby, H. Bredmose, H. Jasak, A computational method for sharp interface advection, Open Science 3 (11). doi:10.1098/rsos.160405.

[42] L. Larsson, F. Stern, M. Visonneau, N. Hirata, T. Hino, J. Kim (Eds.), Tokyo 2015: A Workshop on CFD in Ship Hydrodynamics, Vol. 3, NMRI (National Maritime Research Institute), Tokyo, Japan, 2015.

[43] I. Gatin, V. Vukčević, H. Jasak, H. Rusche, Enhanced coupling of solid body motion and fluid flow in finite volume framework, Ocean Engineering 143 (December 2016) (2017) 295–304. doi:10.1016/j.oceaneng.2017.08.009.

PAPER 7

Ocean Engineering 171 (2019) 554–564

Contents lists available at ScienceDirect

Ocean Engineering

journal homepage: www.elsevier.com/locate/oceaneng

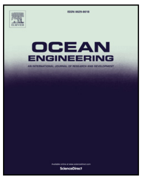

Green sea loads in irregular waves with Finite Volume method

Inno Gatin[a,*], Nikola Vladimir[a], Šime Malenica[b], Hrvoje Jasak[a,c]

[a] *University of Zagreb, Faculty of Mechanical Engineering and Naval Architecture, Ivana Lučića 5, Zagreb, Croatia*
[b] *Bureau Veritas Marine & Offshore, Departement Recherche, Le Triangle de l'Arche, 8 Cours du Triangle - CS 50101, 92937, Paris La Defense Cedex, France*
[c] *Wikki Ltd, Studio 459 China Works, 100 Black Prince Road, London, United Kingdom*

ARTICLE INFO

Keywords:
Green sea loads
Equivalent Design Wave
Compressible two phase model
Finite Volume
Ghost Fluid Method

ABSTRACT

Extreme green sea loads upon a vertical deck structure of an Ultra Large Container Ship are calculated in this paper using Finite Volume based CFD simulations in full scale, where two different approaches for the definition of the Equivalent Design Wave are used. Linear frequency–domain method is used to calculate the long–term response in terms of Relative Wave Elevation, which in turn is used to define a deterministic Equivalent Design Wave which is then used in the CFD simulation. The simulations are conducted using a newly developed flow model that takes into account air compression in violent free–surface phenomena. Regular Equivalent Design Wave and Response Conditioned Wave approaches are used and compared in terms of loads exerted on the deck structure and required computational resources. Some differences in loads are found between the methods, whilst similar computational resources are required. The Regular Equivalent Design Wave gives larger loads, making it a safer choice. However, the Response Conditioned Wave takes into account the relevant ocean wave conditions as well as the response of the ship, resulting in smaller loads which would enable smaller structural scantlings and cost savings.

1. Introduction

Assessing realistic green water loads is a challenging task where the statistics related to the operational profile of the ship needs to be translated into a deterministic load. Linear frequency–domain methods provide the essential tool for defining the statistical description of ship response with respect to the operational profile. In case of green sea loads, motion response of the ship is used together with the statistical description of the wave field to produce the Relative Wave Elevation (RWE) distribution. However, linear methods do not offer means of assessing loads resulting from green sea events, where a high fidelity method must be included. Recently, Finite Volume (FV) Computational Fluid Dynamics (CFD) methods are being increasingly used for deterministic green sea simulations based on long–term distributions of green sea events. These simulations require a deterministic description of the wave field which in some way represents the statistical description of the ship response and sea state.

A number of publications successfully applied FV based CFD to calculate green sea loads on marine structures. Kudupudi and Datta (2009) calculated green sea loads on a moving vessel where the motion is calculated with a panel method software where comparable results are obtained with respect to experimental measurements. Silva et al. (2017a) conducted an experimental campaign with oblique waves green sea events upon a FPSO. The tested wave field settings are selected based on the frequency domain linear method, while experimental measurements are used to detect the absolute maximum RWE, which is reproduced using CFD in the subsequent publication (Silva et al., 2017b). The simulation includes rigid body motion and it successfully reproduces the experimental measurements, while a tremendous amount of computational resources was necessary to produce the result: 12 days on 480 cores to simulate 30 s of real time in full scale, for a computational grid discretised with 40 million cells. Pakozdi et al. (2016) used CFD in order to predict green water loads on a Tension Leg Platform in a 10 000 year extreme event. They used an approach that is equivalent to the regular Equivalent Design Wave; however the selection of regular wave characteristics are based on crest height and free surface elevation rise velocity based on irregular wave measurements in a wave tank, instead of a long–term statistical distribution. The authors state that this approach reduces the required computational time since it does not require irregular wave propagation in CFD. The drawback of this approach is that it requires experimental measurements to detect the irregular extreme events in order to measure the steepness and rise time.

In order to reduce the overall computational time for assessing

---

[*] Corresponding author.
E-mail addresses: inno.gatin@fsb.hr (I. Gatin), nikola.vladimir@fsb.hr (N. Vladimir), sime.malenica@bureauveritas.com (Š. Malenica), h.jasak@wikki.co.uk, hrvoje.jasak@fsb.hr (H. Jasak).

https://doi.org/10.1016/j.oceaneng.2018.10.061
Received 19 July 2018; Received in revised form 21 September 2018; Accepted 24 October 2018

green water loads, Pakozdi et al. (2014) developed a framework where a potential theory based method is coupled with CFD in order to minimise the size of the CFD domain and the duration of the simulated time. A reasonable comparison with experimental measurements is achieved. Joga et al. (2014) compared two commercial CFD codes in assessing water ingress into open cargo holds of a container ship during green sea events in irregular beam seas. Both codes predicted motion with reasonable accuracy. The authors concluded that assessing volume of shipped water poses a greater challenge.

In this study a specialised CFD software library called the Naval Hydro Pack, based on foam–extend, is used to investigate two different approaches for assessing green sea loads in full scale for a deck structure of an Ultra Large Container Ship (ULCS). The two tested approaches for defining the Equivalent Design Wave are (Hauteclocque et al., 2012):

- Regular Equivalent Design Wave: regular incident wave,
- Response Conditioned Wave: irregular focused wave.

To the authors best knowledge, no similar comparison has been published where CFD is used to evaluate individual approaches. The present numerical framework has been verified and validated by Gatin et al. (2018) for assessing green water pressure loads. Here, a novel numerical formulation where water is incompressible and air is compressible which is described, verified and validated in an upcoming publication, is applied to the problem of wave–body interaction. During wave impacts against large–flare bows such as the ones present in container ships, a volume of air can get trapped between the wave and the structure, which then redistributes the impact energy in time and space. In general, the air pocket will prolong the duration of high pressure loads and increase the surface area upon which they act (Obhrai et al., 2004; Bullock et al., 2007), intensifying the energy transfer between the wave and the structure. For this reason, and for reasons of numerical stability, it is important to encompass air compression in simulations where it may occur. The present method introduces air compression effects without significant computational overhead, rendering the numerical framework more general. Linear frequency domain method is used in order to calculate the long–term distribution of the RWE, where the dynamic coefficients needed for the analysis are calculated using HYDROSTAR software. Equivalent Design Wave is determined based on the long–term distribution of the RWE. Head wave condition is analysed since it represents the most critical heading for the observed deck structure: a vertical transversally positioned wall–type breakwater at the bow. Two CFD simulations are conducted corresponding to the two design wave definitions: a regular wave simulation where the Regular Equivalent Design Wave is used, and a focused irregular wave train based on Response Conditioned Wave theory. The two simulations are compared in terms of pressure loads on the breakwater and computational time.

This paper is organised as follows. The second section briefly outlines the numerical model presenting the two–phase compressible/incompressible approach. In the third section basic information regarding the analysed container ship are given, including the linear frequency domain analysis data. The fourth section is dedicated to the CFD simulations, where the two different design wave definition approaches are used, including a discussion and the comparison. Additionally, to validate the linear and CFD approach a comparison against experimental data is performed for a model–scale KRISO Container Ship (KCS). Finally, a brief conclusion is given.

2. Numerical model

The numerical model behind the FV based method is briefly presented in this section. The flow model assumes incompressible water phase and a compressible air phase. The Ghost Fluid Method (GFM) is employed to resolve field discontinuities at the interface, including the abrupt change in phase compressibility.

Two–phase, viscous and turbulent flow with incompressible liquid phase and a compressible air phase is modelled with the following momentum conservation equation:

$$\frac{\partial \mathbf{u}}{\partial t} + \nabla\cdot(\mathbf{u}\mathbf{u}) - \nabla\cdot(\mathbf{R}) = -\frac{1}{\rho}\nabla p_d - \left(\frac{1}{\rho}\nabla\rho\mathbf{g}\cdot\mathbf{x} - \mathbf{u}\nabla\cdot\mathbf{u}\right) , \tag{1}$$

where $\mathbf{u}$ stands for the velocity field, ρ is the discontinuous density field and $\mathbf{R}$ is the Reynolds stress tensor, allowing general turbulence modelling. p_d denotes the dynamic pressure calculated as $p_d = p - \rho\mathbf{g}\cdot\mathbf{x}$, where p stands for static pressure, $\mathbf{g}$ is the gravity vector, while $\mathbf{x}$ denotes the radii vector. Conservation of mass for two phase flow used in this study states:

$$\nabla\cdot\mathbf{u} = -\frac{1}{\rho}\frac{\partial\rho}{\partial p}\left(\frac{\partial p_d}{\partial t} + \nabla\cdot\left(p_d\mathbf{u}\right) - \left(p_d\nabla\cdot\mathbf{u} + \frac{\partial(\rho\mathbf{g}\cdot\mathbf{x})}{\partial t} + \mathbf{u}\cdot\nabla\rho\mathbf{g}\cdot\mathbf{x}\right)\right) . \tag{2}$$

In the above equations, the GFM is employed to provide a sharp evaluation of the gradient and divergence operators where specialised discretisation schemes are used for computational cells near the interface. Thus, in water the right hand side of Eqn. (2) reduces to zero since $\partial\rho/\partial p = 0$ for incompressible fluid, while in cells occupied by air the term is active. Similarly, the last term on the right hand side of Eqn. (1) also reduces to zero for cells occupied by water since $\nabla\rho = 0$ and $\nabla\cdot\mathbf{u} = 0$. In this study, air is considered to be an isentropic ideal gas, where the following holds:

$$\frac{\partial\rho}{\partial p} = \frac{1}{a_c\gamma}\frac{p}{a_c}^{\frac{1-\gamma}{\gamma}}, \tag{3}$$

where γ denotes the constant specific heats ratio while a_c stands for the isentropic constant. In this paper values of $\gamma = 1.4$ and $a_c = 100\,000$ are used.

The free surface is modelled with the Volume of Fluid (VOF) interface capturing method with an additional interface compression term (Rusche, 2002):

$$\frac{\partial\alpha}{\partial t} + \nabla\cdot(\mathbf{u}\alpha) + \nabla\cdot(\mathbf{u}_r\alpha(1-\alpha)) = 0 \, , \tag{4}$$

where α denotes the volume fraction, while $\mathbf{u}_r$ stands for compressive velocity field which is oriented in the normal direction towards the free surface (Weller). A Courant number–sensitised formulation is used in this study as described by Jasak et al. (2014).

The GFM acts by extrapolating the values from cells next to the interface onto cells across the interface making the ”ghost cells”. In that way, standard FV interpolation schemes can be used without creating the interpolation error due to large differences in fields on different sides of the interface. For example, when evaluating the density gradient for a cell occupied by air next to the interface, density is extrapolated to the cell occupied by water on the other side of the interface, and standard gradient scheme is applied where the extrapolated value is used instead of the actual value that corresponds to density in water. In order to extrapolate different fields across the interface, it is necessary to determine physical jump conditions which govern the change of properties across the interface. Dynamic free surface boundary condition dictates that the static pressure must be equal on both sides of the interface:

$$[p] = p^- - p^+ = 0, \tag{5}$$

where $[\cdot]$ denotes the jump operator, + and − indices denote the value infinitesimally close to the interface from the water side and air side, respectively. The above equation can be written in terms of dynamic pressure as:

$$[p_d] = -[\rho]\mathbf{g}\cdot\mathbf{x} \, . \tag{6}$$

Eqn. (6) states that dynamic pressure has a jump across the interface, which can be used to extrapolate dynamic pressure from water to air and vice–versa. The kinematic free surface boundary condition states that the velocity must be continuous across the interface:

$$[\mathbf{u}] = \mathbf{u}^- - \mathbf{u}^+ = 0\,. \tag{7}$$

Further jump conditions arise from the governing equations (Desjardins et al., 2008; Huang et al., 2007; Queutey and Visonneau, 2007). The jump condition arising from the momentum equation (Eqn. (1)) states:

$$\left[\frac{1}{\rho}\nabla p_d\right] = \left[-\nabla\cdot(\mathbf{uu}) + \mathbf{u}\nabla\cdot\mathbf{u} - \frac{1}{\rho}\nabla\rho\mathbf{g}\cdot\mathbf{x}\right]\,, \tag{8}$$

which in effect states that dynamic pressure gradient divided with the discontinuous density field has a jump that depends on the compressibility of air. In case when compressibility effects are negligible, the right hand side reduces to zero, which in turn reduces the equation to the form shown by Vukčević et al. (2017) for incompressible two phase flow.

Eqns. (6) and (8) are used to extrapolate the dynamic pressure and correct the dynamic pressure gradient. They are also used for extrapolation of the density field from the air side, where the density field is not constant. The jump condition for the density field states:

$$[\rho] = \rho^- - \rho^+\,, \tag{9}$$

where ρ^+ is constant, while ρ^- needs to be calculated. Since air is considered as an adiabatic ideal gas, the following holds:

$$\rho^- = \left(\frac{p^-}{a_c}\right)^{\frac{1}{\gamma}} = \left(\frac{p_d^- + \rho^-\mathbf{g}\cdot\mathbf{x}}{a_c}\right)^{\frac{1}{\gamma}}\,. \tag{10}$$

The above set of equations close the system for a two–phase flow model where water is considered incompressible while air is treated as an ideal gas. Details regarding the implementation of numerical schemes and other will be published in a separate paper dedicated to the verification and validation of the model. The reader is also referred to Vukčević et al. (2017) for more details on the implementation of the GFM for incompressible two–phase flow, which forms a basis for the present approach.

3. SkyBench container ship

The ship considered in this work is an Ultra Large Container Ship (ULCS) belonging to the so called "SkyBench" design, see Fig. 1. Ship characteristics are shown in Table 1, where L_{OA} stands for length over all, L_{PP} is the length between perpendiculars, B is the breath of the ship, H is ship height, T draught, Δ stands for displacement in tons and V is ship speed in knots. I_{yy} stands for longitudinal moment of inertia, LCG is the longitudinal position of centre of gravity with respect to the aft perpendicular, and VCG is the vertical position of centre of gravity with respect to the calm free surface level. The large length of the ship results in high relative motion of the ship bow, rendering the bow structure and cargo vulnerable to green water loads. To mitigate this risk, a breakwater is positioned at the bow, whose structural design should take into account possible loads due to water on deck. In order to calculate design loads that can be exerted on the breakwater, a design wave field must first be defined based on the definition of the operational profile. Definition of a relevant design wave is not trivial, since it must represent a realistic maximum load that can be expected during the life time of the ship.

Table 1
General ship characteristics of the SkyBench ULCS.

L_{OA}, m	400.0
L_{PP}, m	383.0
B, m	58.6
H, m	30.5
T, m	14.5
Δ, t	212913.0
V, kt	23.0
I_{yy}, kg m^2	2.04×10^{12}
LCG, m	184.2
VCG, m	12.9

3.1. Ship response calculation

Definition of the design wave or irregular wave field is based on the selected Dominant Load Parameter (DLP). In this case, Relative Wave Elevation (RWE) is selected as DLP since the objective of this work is to assess maximum design loads of a breakwater structure at the ship's bow due to green water. RWE is the vertical distance between the free surface and a point fixed on the ship, e.g. deck at the bow. For a point positioned at the fore perpendicular on the deck level, negative RWE indicates water on deck, i.e. a green water event. The statistical description of ship motion with respect to relevant sea states (wave spectra) is calculated by using linear seakeeping theory based on the potential flow model. First, hydrodynamic coefficients need to be assessed for the relevant frequency range, i.e. the Response Amplitude Operator (RAO).

In this work, HYDROSTAR software is used to calculate the hydrodynamic coefficients. Fig. 2 shows the surface mesh of the underwater part of the ship used in HYDROSTAR. Since the head wave condition poses the greatest risk with respect to green water impacts on the breakwater, only this heading is considered, while the long–term analysis takes into account all relevant headings. With the calculated hydrodynamic coefficients, RAO-s for heave, pitch and RWE are calculated, as shown in Figs. 3 and 4. RWE is calculated with respect to the point defined with the intersection of the fore perpendicular F_P and the

Fig. 1. SkyBench ULCS.

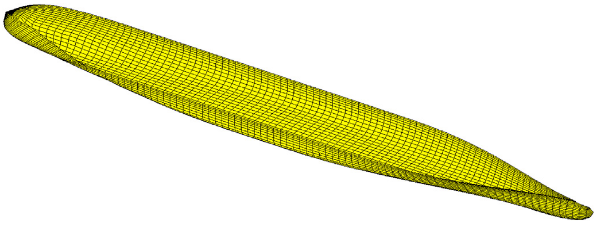

Fig. 2. Surface mesh used in the HYDROSTAR software.

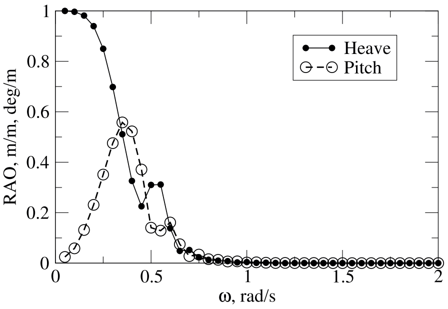

Fig. 3. Response Amplitude Operator for heave and pitch motion.

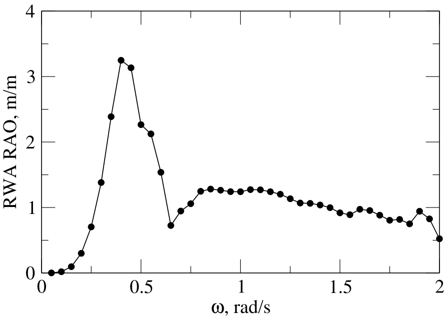

Fig. 4. Response amplitude operator for relative wave amplitude.

calm free surface in the ship's reference frame, i.e. for point defined with vector (196.3, 0,0).

3.2. Design wave definition

Two design wave approaches are tested in this work: Regular Equivalent Design Wave and Response Conditioned Wave (irregular waves with non–random phase shifts). Both are based on a long–term distribution of the DLP based on the operational profile of the ship. In this case the wave scatter diagram for North Atlantic from IACS Recommendation No. 34 is used for the long–term distribution analysis for the 25 year life–time of the ship. The ship is assumed to sail with 5 kt speed according to the rules from classification societies.

Obtained design wave characteristics are as follows:

1. Regular Equivalent Design Wave: wave amplitude $a = 10.6$ m, wave frequency $\omega = 0.4$ rad/s. The wave characteristics are defined using the long–term RWE value corresponding to a probability of 10^{-8}, which equals $\mathrm{RWE}_{long} = 34.45$ m. The amplitude is simply calculated by using the maximum RAO value $\mathrm{RAO}_{RW\ A,max}$ from Fig. 4 which is 3.25 m/m as (Hauteclocque et al., 2012):

$$a = \frac{\mathrm{RWE}_{long}}{\mathrm{RAO}_{RW\ A,max}} = 10.6. \tag{11}$$

The frequency of the wave is determined simply by using the frequency corresponding to $\mathrm{RAO}_{RW\ A,max}$, i.e. $\omega = 0.4$ rad/s.

2. Response Conditioned Wave: based on the Pierson–Moskowitz sea spectrum with $H_s = 14.5$ m and $T_p = 16.2$ s, where Relative Wave Amplitude RAO is used as described in (Hauteclocque et al., 2012). The wave spectrum characteristics are chosen in a way to correspond to the wave condition that has the largest contribution in the long–term RWE response. Fig. 5 shows the relative contributions of individual wave spectra to the long–term RWE value. The details regarding the definition of wave component amplitudes and phase sifts are given in Sec. 5.2.

4. KCS seakeeping in regular waves

Before moving on to performing green sea simulations for the SkyBench container ship, the CFD and linear approach are compared to experimental data in order to establish possible differences for this type of ship. Due to lack of experimental data for the SkyBench ship, the comparison study is performed for a KCS model, a similar ship that is

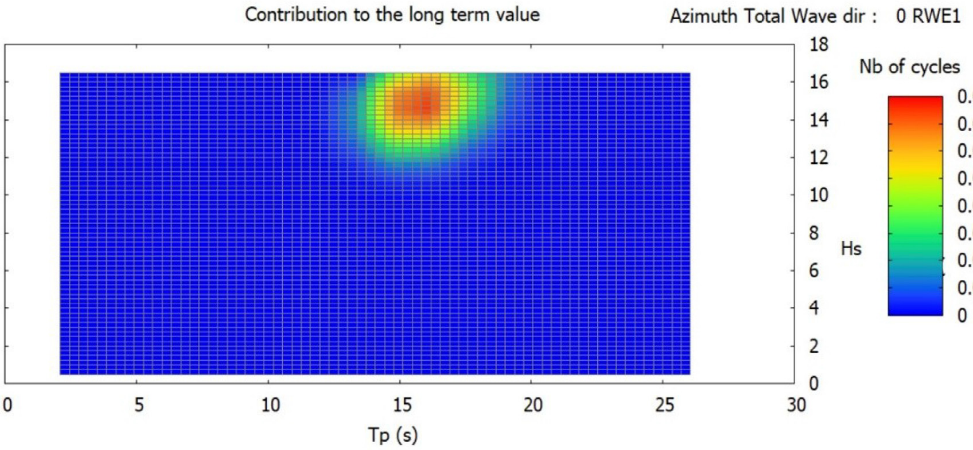

Fig. 5. Relative contribution of the different sea states to the RWE long–term value.

Table 2
General ship characteristics of the KCS model.

λ_M	37.89
L_{PP}, m	6.07
B, m	0.85
T, m	0.285
Δ, kg	956
Fr	0.261
I_{yy}, kg m^2	2236.5
LCG, m	3.13
VCG, m	0.093

Table 3
Incident wave characteristics used in the KCS seakeeping study in model scale.

λ, m	3.949	5.164	6.979	8.321	11.840
H, m	0.062	0.078	0.123	0.149	0.196
ω, rad/s	3.951	3.455	2.972	2.722	2.282

used as a benchmark hull on a number of workshops for CFD validation (Larsson et al., 2015). KCS model particulars are shown in Table 2, where Fr stands for the Froude number and λ_M the scale of the model. Note that the values in the table are given in model scale. First order amplitudes of heave and pitch motion are compared for five different wave frequencies, with model–scale wave characteristics shown in Table 3. Note that full scale wave frequencies correspond to a range between 0.37 and 0.64 rad/s, which covers the frequencies used in this study as shown in Sec. 3.2. Further details regarding CFD simulations can be found in (Vukčević and Jasak, 2015; Vukčević et al., 2016; Vukčević, 2016).

Comparison of heave amplitudes is presented in Fig. 6, where good general agreement is observed between the three sets of results. The CFD results is in notably better agreement with the experimental data than the linear results for the lowest and third wave frequency, while very good agreement is observed for high wave frequencies between the three methods. Fig. 7 shows the comparison of pitch motion amplitudes, where significant disagreement can be seen between experimental data and the linear solution, while CFD results agree quite well. Similar to heave results, the three results are in good agreement for higher frequencies where motions are smaller. Overall it can be concluded that some differences can be expected between the CFD result and linear solution for a container vessel, especially for pitch motion for lower frequencies. The reasons for this disagreement is likely to be related to inherent simplifications included in the linear frequency–-domain method.

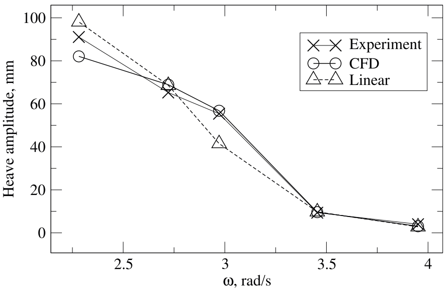

Fig. 6. Comparison of heave amplitude for KCS in regular waves.

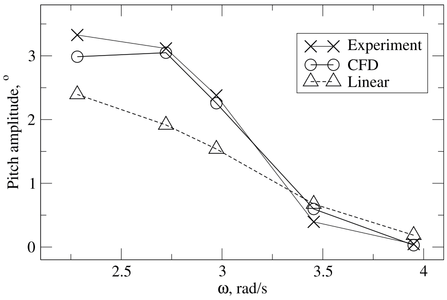

Fig. 7. Comparison of pitch amplitude for KCS in regular waves.

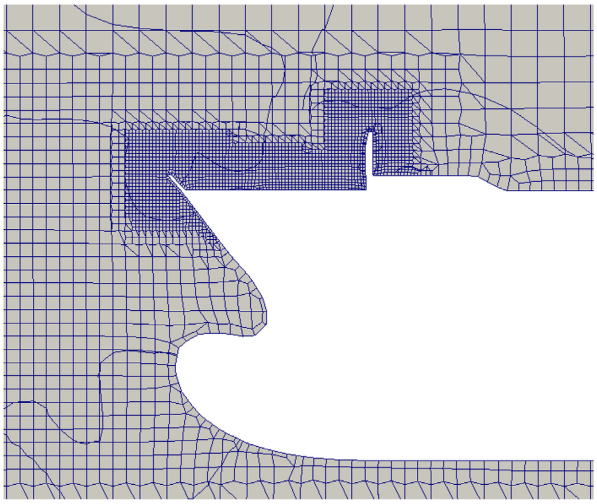

Fig. 8. Side view of the grid refinements at the bow of the ship.

5. Green sea CFD simulations for the SkyBench ship

In this section the two design wave approaches listed above are used to calculate the green sea loading on the breakwater of the SkyBench container ship in full scale using CFD. The methods are compared in terms of loading exerted on the structure and computational time required to perform the simulation.

Both simulations are simulated using the same computational grid generated using cfMesh software (JuretićcfMesh, 2017). The grid is unstructured containing 2 374 416 cells, which are mostly hexahedral (97.8%). Additional refinement is applied at the bow deck near the breakwater and the front bulwark in order to capture green water effects. A view of the grid in the central longitudinal plane near the breakwater is shown on Fig. 8, while the surface grid of the ship is shown in Fig. 9. The cells on the deck are cubic with sides of 0.375 m. The grid resolution is considered sufficient based on previous similar studies (e.g. (Gatin et al., 2017)). The computational domain is 1 330 m long, 635 m wide, 343 m deep and 152 m high above the calm free surface level. The size of the computational domain is based on the main ship dimensions according to the authors experience. Length is equivalent to roughly $3.5L_{PP}$, breadth to $11B$, depth to $1L_{PP}$ and height to $1/2L_{PP}$. The computational domain with domain boundaries is shown in Fig. 10. The origin of the coordinate system is at the calm free surface level, midship, at the longitudinal central plane. The positive x direction is oriented towards the bow of the ship, positive y direction is facing portside while positive z axis is directed upwards. Waves are introduced using implicit relaxation zones (Jasak et al., 2015), which are indicated with red colour at the calm free surface in Fig. 10. In the relaxation zones, a gradual transition is made between the incident wave field prescribed with an arbitrary wave solution (linear or nonlinear potential flow solution) and the CFD solution. Wave velocity field and surface elevation from the analytical wave theory are introduced into the momentum and VOF equation (Eqn. (1) and (4)), where a

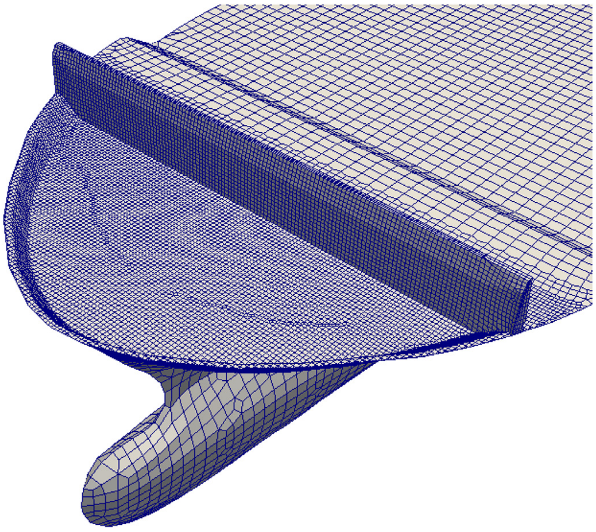

Fig. 9. Surface discretisation of the ship bow in the CFD computational grid.

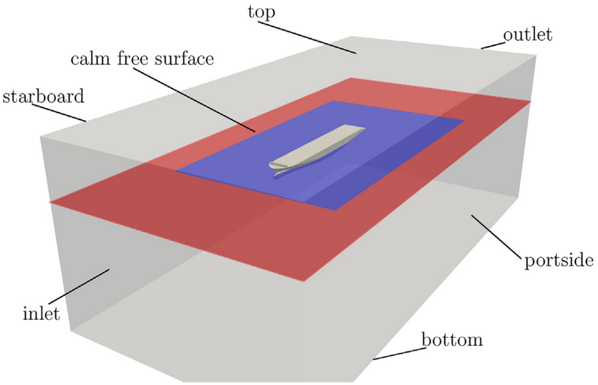

Fig. 10. View of the CFD compuational domain. The relaxation zones are indicated with red colour on the calm free surface. The blue colour indicates undisturbed CFD solution region. (For interpretation of the references to colour in this figure legend, the reader is referred to the Web version of this article.)

weighting factor is used to allow gradual blending between the solution of respective equations and the analytical solution. The reader is referred to Jasak et al. (2015) for more details on the implementation of the relaxation zones. The relaxation zones also serve as absorption zones for radiated and diffracted waves. Inlet, outlet, portside and starboard boundaries have zero–gradient boundary condition for pressure, while the VOF and the velocity field are evaluated using linear wave field solution. The bottom boundary also has a zero–gradient condition for pressure, while VOF is fixed to 1, and the velocity is also evaluated using the linear wave solution. In this way, the bottom boundary acts as a infinite depth boundary condition. The top boundary is set to a fixed value pressure boundary condition where $p = 100\,000$ Pa, VOF field is set to zero, while zero gradient is used for the velocity field.

Second order backward temporal discretisation scheme is used for all temporal derivatives, while second order upwind biased convection scheme with deferred correction is used for velocity and pressure convection terms. The coupling of the rigid body motion equations and the fluid flow is performed using an enhanced approach where the rigid body motion equations are solved once per pressure–corrector step (Gatin et al., 2017), where a geometric method is used for integration of rigid body motion equations (Müller and Terze, 2016). Two degrees of freedom are considered: heave and pitch, while the remaining are constrained, since vertical plane motion is dominantly relevant with respect to green water occurrence in head waves condition.

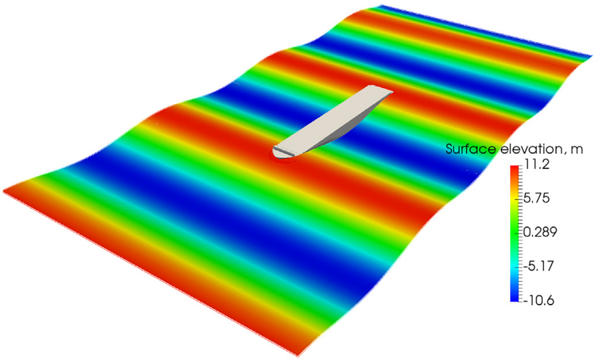

Fig. 11. Initial condition of the free surface elevation in the Regular Equivalent Design Wave simulation of the SkyBench ship.

5.1. Regular Equivalent Design Wave simulation

From the wave modelling point of view, the Regular Equivalent Design Wave approach is the simplest one. Setting up a regular wave CFD simulation is relatively simple compared to an irregular wave field. Fig. 11 shows the initial condition in the simulation, where the free surface elevation can be seen. The simulation is performed with Courant number fixed to 20, resulting in an average time step of 0.04 s, oscillating between 0.01 and 0.1 s.

Nine wave periods are simulated, where loads on the breakwater became acceptably periodic after three periods. Fig. 12 shows the green sea event during a typical wave period. A significant amount of water is shipped onto the deck, encountering the breakwater. Time trace of longitudinal force acting on the breakwater is shown in Fig. 13. Note that although the force peak is not periodic, the shape of the force curve becomes periodic after three periods. From the structural point of view, the longitudinal force impulse represented by the area under the longitudinal force signal is also important together with transient localised force peaks. Therefore, the force impulse is also compared in this study, calculated as:

$$I_X = \int_{t_1}^{t_2} F_X(t)dt, \tag{12}$$

where t_1 and t_2 stand for the beginning and end time of integration, while F_X represents the instantaneous longitudinal force acting on the breakwater. Heave and pitch motion shown in Figs. 14 and 15, respectively, show periodic convergence after three periods as well as the shape of the longitudinal force. Unlike the KCS, Figs. 14 and 15 show that the linear solution overestimates heave and pitch motion with respect to the CFD results. Thus, predictions regarding RWE using the linear solution are on the safe side. The possible reason for this overestimation could be the shipped water which changes the mass properties of the vessel, primarily increasing the pitch moment of inertia, which is not accounted for in the linear frequency-domain approach. The linear method mostly underestimates the motion for KCS while it overestimates the motion for ULCS, since in KCS seakeeping cases the green sea phenomena is not present. Figs. 16 and 17 show the vertical position and velocity, respectively, of a point on the bow of the ship with coordinates (196.3, 0,16) with respect to midship. Again, the linear solution overestimates both the motion and velocity of the point at the bow.

To provide a quantitative means of comparison, a force impulse during the third green sea event is calculated: $I_X = 2.877 \times 10^7$ Ns. The

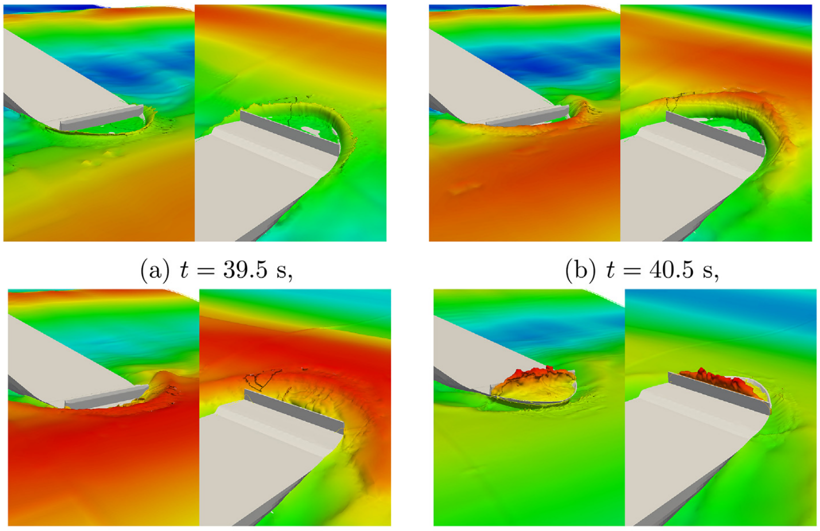

(a) $t = 39.5$ s, (b) $t = 40.5$ s,

(c) $t = 41.5$ s, (d) $t = 43.0$ s.

Fig. 12. A typical green sea event from the Regular Equivalent Wave Simulation of the SkyBench ship. Colour indicates free surface elevation. (For interpretation of the references to colour in this figure legend, the reader is referred to the Web version of this article.)

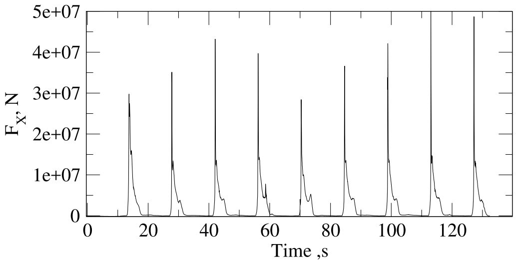

Fig. 13. Longitudinal force acting on the breakwater in the Regular Equivalent Design Wave simulation of the SkyBench ship.

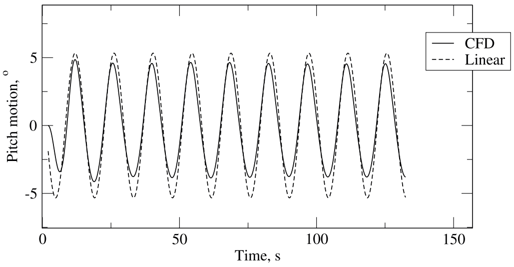

Fig. 15. Comparison of pitch motion between the linear solution and CFD in the Regular Equivalent Design Wave simulation of the SkyBench ship.

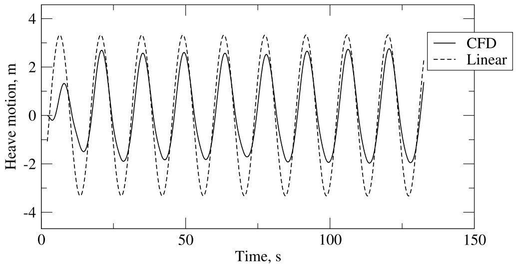

Fig. 14. Comparison of heave motion between the linear solution and CFD in the Regular Equivalent Design Wave simulation of the SkyBench ship.

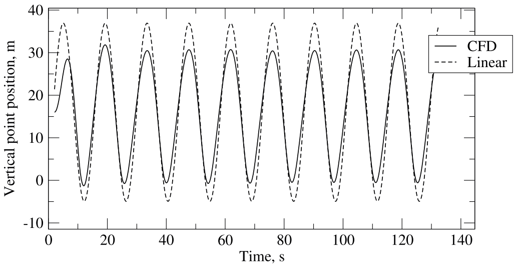

Fig. 16. Vertical position comparison of a point on the bow of the SkyBech for the Regular Equivalent Design Wave case.

simulation took 14.3 h to complete three wave periods (approximately 50 s of simulated time) on four cores of the Intel Core i5-3570 K CPU (3.40 GHz).

5.2. Response Conditioned Wave simulation

As explained by de Hauteclocque et al. (2012), as opposed to the Regular Equivalent Design Wave, the Response Conditioned Wave takes into account the wave conditions relevant to the service of the ship, as well as the respective RAO of the Dominant Load Parameter. Thus, a more realistic wave event is obtained comparing to the Regular Equivalent Design Wave. Response Conditioned Wave is an irregular wave train where amplitudes and phase shifts are determined from the wave energy spectrum and RAO:

$$\zeta(x,t)=\sum_{i=1}^{i=N}\zeta_a(\omega_i)\cdot\cos(\omega_i(t-t_F)-k_i(x-x_F)-RAO_\phi(\omega_i)) \ , \tag{13}$$

where

$$\zeta_a(\omega_i)=\left(S_\zeta(\omega_i)\cdot|RAO(\omega_i)|\frac{\eta_{LT}}{m_0}\Delta\omega_i\right)^{\frac{1}{2}} \ . \tag{14}$$

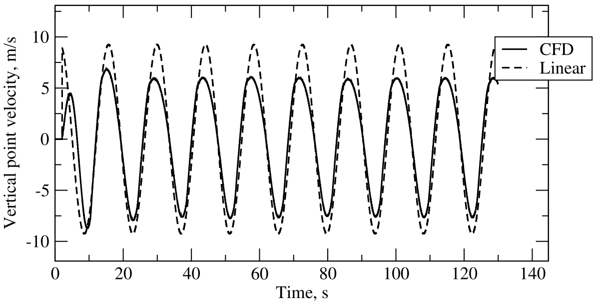

Fig. 17. Vertical velocity comparison of a point on the bow of the SkyBech for the Regular Equivalent Design Wave case.

Here, $\zeta(x, t)$ denotes the surface elevation at time t and longitudinal coordinate x. N is the number of wave components, $\zeta_a(\omega_i)$ is the wave component amplitude corresponding to frequency ω_i while k_i is the wave component wave number that satisfies the linear dispersion relation. t_F and x_F denote time and position of focusing, respectively. In this simulation, $t_F = 50$ s, and $x_F = F_P$, where F_P stand for fore perpendicular. RAO_ϕ denotes the phase shifts of response components, RWE in this case. S_ζ is the wave energy spectrum, RAO denotes the response RAO, while η_{LT} stands for the long–term response value, equal to 34.45 in this case. m_0 is the zeroth order moment of the response spectrum, while $\Delta\omega$ is the frequency step used to discretise the spectrum.

For the initialisation of the CFD simulation, the surface elevation and wave field velocity from the linear solution are used, that correspond to an arbitrary point in time at which the simulation is initialised. The motion of the ship is also initialised, comprising heave and pitch positions and velocities, where the motion is calculated using the linear frequency–domain method based on the RCW. In contrast to starting the simulation from time zero, the duration of the CFD simulation is minimised in this way, while still accounting for all nonlinear effects during a green sea event which are not present in the linear solution.

Fig. 18 shows the linear realisation of the free surface elevation at F_P, and the RWE signal deducted by freeboard height. The simulation is started at 30 s, i.e. 20 s before the focusing time, with the time step of $\Delta t = 0.08$ s, which resulted in time–average maximum Courant number of 24, oscillating mostly between 10 and 30.

The initial condition of the simulation is shown in Fig. 19, corresponding to $t = 30$ s. Figs. 20 and 21 show heave and pitch motion comparison between the linear and CFD solution. Some differences are visible between the two sets of solutions, both in amplitude and phase. However, the overall agreement is acceptable. Figs. 22 and 23 show the comparison of vertical position and velocity of a point on the bow, exhibiting similar differences between the linear and CFD solution. The difference between the linear and CFD solution visible in Figs. 21 and

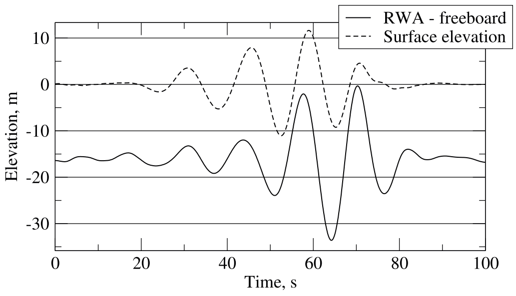

Fig. 18. Linear realisation of the free surface elevation and RWE at F_P in the Response Conditioned Wave approach. Positive values of the full black line indicate water level above deck.

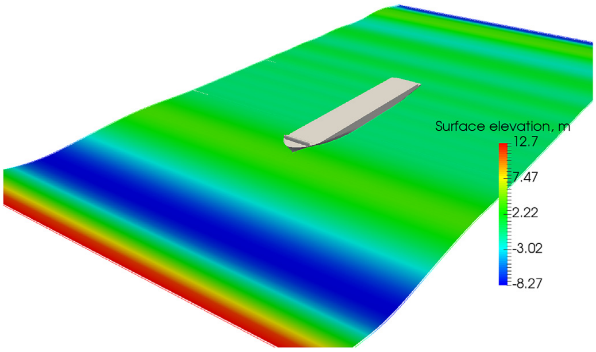

Fig. 19. Initial condition in the Response Conditioned Wave simulation of the SkyBench ship, $t = 30.0$ s.

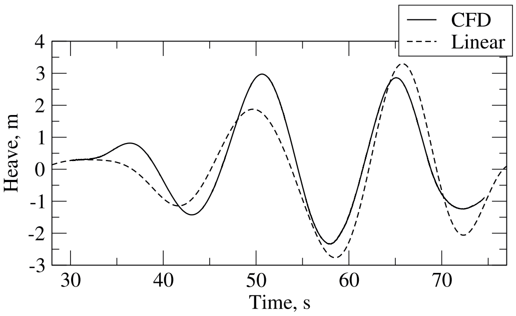

Fig. 20. Comparison of heave motion between the linear solution and CFD in the Response Conditioned Wave simulation of the SkyBench ship.

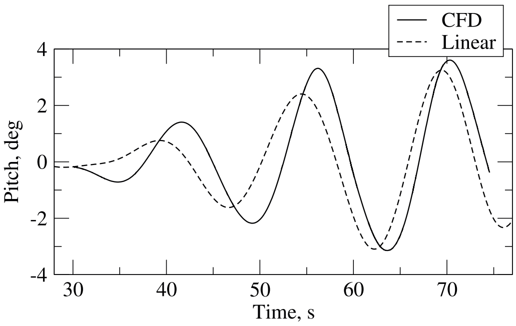

Fig. 21. Comparison of pitch motion between the linear solution and CFD in the Response Conditioned Wave simulation of the SkyBench ship.

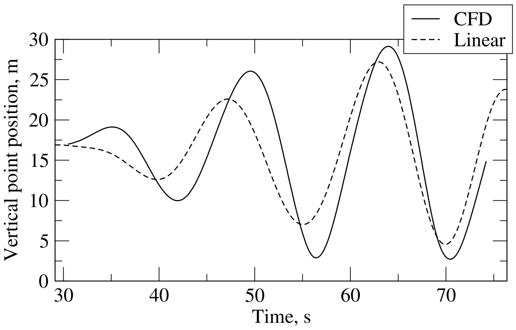

Fig. 22. Vertical position comparison of a point on the bow of the SkyBech for the Response Conditioned Wave case of the SkyBench ship.

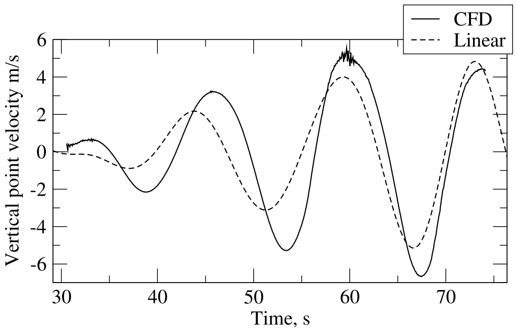

Fig. 23. Vertical velocity comparison of a point on the bow of the SkyBech for the Response Conditioned Wave case of the SkyBench ship.

23 arise mostly from the phase difference. The reason for this phase difference could be the nonlinearities present in the CFD simulation, taking into account the large bow and stern flare. This differences should be investigated in the future, however the agreement is reasonable for present purposes.

Fig. 24 shows the green sea event, where a large quantity of shipped water on the deck can be seen. Force signal in time acting on the breakwater is shown in Fig. 25. Note that the linear solution, shown in Fig. 18, predicted that the second RWE peak (at around $t = 73$ s) will be larger than the first (at around $t = 57$ s), while in the CFD simulation the first peak resulted in a green sea event, while no water was shipped during the second RWE peak. The reason for this could be the nonlinear motion damping which is produced by the green sea event that happened during the first RWE peak at around $t = 73$ s, that reduced the motion before the next RWE peak making it effectively smaller than the first one. Also, pitch motion from the CFD simulation is larger than the linear solution during the first RWE peak (Fig. 21), resulting in a larger RWE value. The force impulse generated by the Response Conditioned Wave is around $I_X = 1.52 \times 10^7$ Ns. The computational time required to obtain the green sea event, i.e. to simulate from $t = 30$ s to $t = 64$ s, is 17.2 h on an Intel Core i5-3570 K CPU (3.40 GHz).

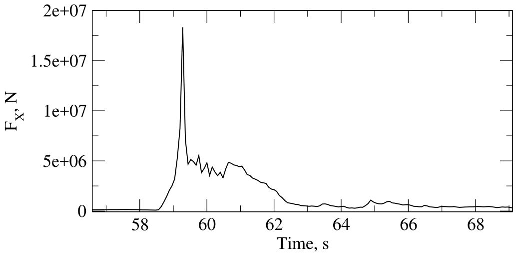

Fig. 25. Longitudinal force acting on the breakwater in the Response Conditioned Wave simulation of the SkyBench ship.

Note that for the RCW simulation the linear solution predicts generally smaller motion than CFD, while in the case of REDW the opposite can be seen. This is especially true for the first portion of the heave signal before $t = 55$ s (Fig. 20), whereas in last part of the simulation CFD shows smaller motion than the linear solution. As explained earlier, this damping of motion after the green water occurrence is likely to be a consequence of the effect of the shipped water on mass and inertia. For pitch motion shown in Fig. 21 the linear solution is smaller than CFD during the entire simulation. The most probable reason behind this seemingly inconsistent difference between the motion comparison produced by REDW and RCW is the fact that the REDW has the resonant frequency. The linear potential–flow based solution is likely to give overestimated motion for resonant conditions since it lacks viscous damping as well as damping stemming from the nonlinearity of the underwater geometry of the vessel as a function of motion which is not taken into account, while it has a significant influence especially for large–flare hull forms such as the one analysed in this study. Thus, the accuracy of the linear method is completely different in the periodically converged resonant motion than in the transient, non–periodic motion excited by RCW.

5.3. Discussion and comparison

Two methods for defining the Equivalent Design Wave are

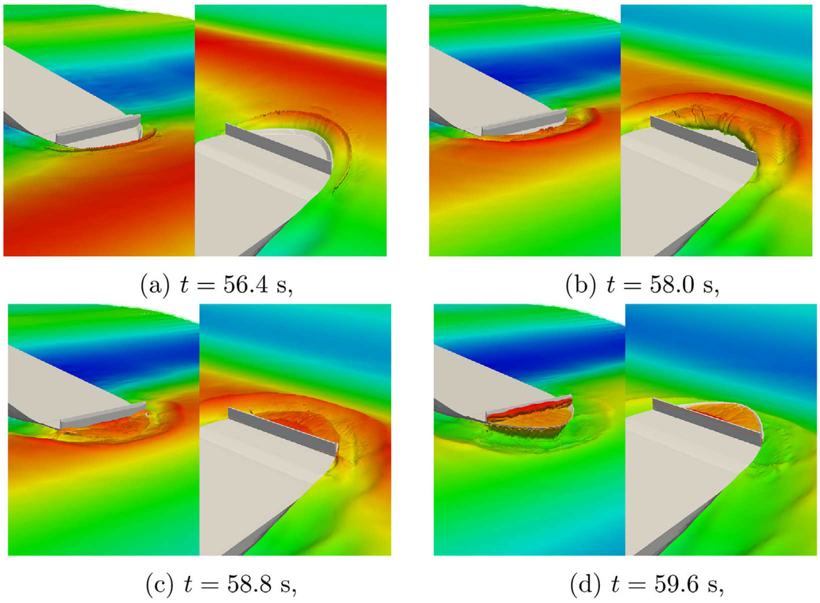

(a) $t = 56.4$ s, (b) $t = 58.0$ s,

(c) $t = 58.8$ s, (d) $t = 59.6$ s,

Fig. 24. The green sea event from the Response Conditioned Wave simulation of the SkyBench ship. (For interpretation of the references to colour in this figure legend, the reader is referred to the Web version of this article.)

Table 4
Comparison of Regular Equivalent Design Wave (REDW) and Response Conditioned Wave (RCW) approach.

	REDW	RCW
Force peak $F_{X,max}$, N	4.03×10^7	1.83×10^7
Force impulse I_X, Ns	2.88×10^7	1.52×10^7
CPU time, hours	14.3	17.2
Processor	i5-3570 K	i5-3570 K
Complexity (CFD set–up)	Low	High

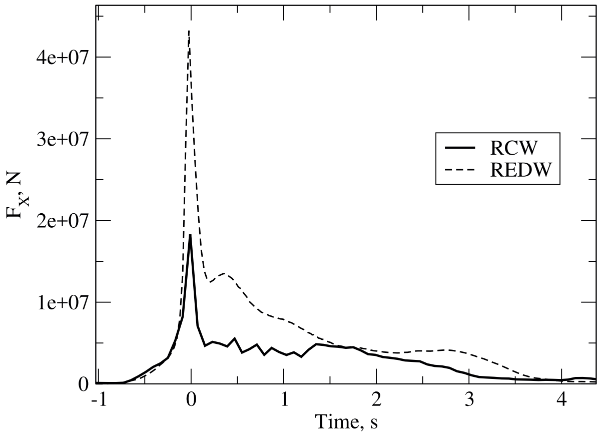

Fig. 26. Comparison of longitudinal force acting on the breakwater from the Regular Equivalent Design Wave (REDW) and Response Conditioned Wave (RCW) of the SkyBench ship.

compared in this section. Table 4 shows the comparison in terms of force peak and impulse exerted on the breakwater, required computational time and complexity of pre–processing for the CFD simulation. Large differences are obtained with respect to force peak and impulse, where Regular Equivalent Design Wave exhibited the larger force. Response Conditioned Wave showed 2.2 times smaller force peak and 1.9 times smaller force impulse. Fig. 26 shows the comparison of the pressure force exerted on the breakwater in time, where differences in both peak force and area under the curve can be observed. The two methods are comparable in terms of required computational time, while Regular Equivalent Design Wave requires smaller amount of pre–-processing time due to its simplicity with respect to wave field definition. The Response Conditioned Wave requires a higher amount of pre–processing in order to consistently initialise the CFD simulation with respect to the linear realisation.

As described by de Hauteclocque et al. (2012), the Regular Equivalent Design Wave does not take into account the actual wave conditions relevant to the service of the ship, but only the RAO of the Dominant Load Parameter (RWE in this case) which results in a large response. On the other hand, the Response Conditioned Wave takes into account both amplitudes and phases of the Dominant Load Parameter's RAO and the sea state which is relevant for the particular DLP and heading, producing a more realistic response. In this comparison it is confirmed that the Regular Equivalent Design Wave produces significantly higher pressure loads on the breakwater.

6. Conclusion

In this paper two different methods for defining the Equivalent Design Wave for a green sea event based on long–term statistical distribution are tested using FV based CFD. Linear frequency domain method is used to calculate the long–term response in terms of Relative Wave Elevation at the deck of the Ultra Large Container Ship. Based on the long–term distribution, a Regular Equivalent Design Wave and a Response Conditioned Wave are defined. A CFD simulation for each of these methods is conducted, where loads exerted on the wall–type breakwater positioned at the bow are compared as well as computational time.

The Regular Equivalent Design Wave requires smaller amount of effort from the set–up of the CFD simulation point of view, minimising the probability of user error. It produced higher loads on the breakwater. The Response Conditioned Wave approach resulted in smaller green sea loads which should be more realistic given that the actual ocean conditions are taken into account, while being more demanding from the man–hour point of view. For the Response Conditioned Wave approach, the linear realisation of the surface elevation and body motion are used to provide initial conditions for the CFD simulation with rigid body motion, in order to minimise the amount of time that needs to be simulated with CFD. This required significantly more man–hours to set–up with respect to the first approach since the initialisation of the simulation needs to be performed in way that is consistent with the linear realisation. From the computational time point of view, the two methods are comparable requiring 14.3 and 17.2 h of computational time on a desktop PC, respectively.

The comparison shown in this paper demonstrates that the Response Conditioned Wave provides smaller design green water loads for this particular vessel comparing to the Regular Equivalent Design Wave approach. Thus, using RCW for structural design would result in smaller scantlings and cost savings. Since RCW takes into account the relevant ocean wave conditions as well as the response, it generally produces more relevant design wave, which should also be true for other load parameters such as slamming or similar. At the same time, RCW does not introduce additional cost with respect to computational resources. Despite the added complexity in the pre–processing stage, the authors conclude that RCW presents a more suitable option for predicting extreme wave response using CFD comparing to REDW.

Acknowledgement

Authors Š. Malenica and N. Vladimir acknowledge the support from a National Research Foundation of Korea (NRF) grant funded by the Korean Government (MSIP) through GCRC-SOP (Grant No. 2011-0030013).

References

Bullock, G.N., Obhrai, C., Peregrine, D.H., Bredmose, H., 2007. Violent breaking wave impacts . Part 1 : results from large-scale regular wave tests on vertical and sloping walls. Coast Eng. 54, 602–617. https://doi.org/10.1016/j.coastaleng.2006.12.002.

Desjardins, O., Moureau, V., Pitsch, H., 2008. An accurate conservative level set/ghost fluid method for simulating turbulent atomization. J. Comput. Phys. 227 (18), 8395–8416.

Gatin, I., Vukčević, V., Jasak, H., Rusche, H., 2017. Enhanced coupling of solid body motion and fluid flow in finite volume framework. Ocean Eng. 143 (December 2016), 295–304. https://doi.org/10.1016/j.oceaneng.2017.08.009.

Gatin, I., Vukčević, V., Jasak, H., Seo, J., Rhee, S.H., 2018. CFD verification and validation of green sea loads. Ocean Eng. 148, 500–515. https://doi.org/10.1016/j.oceaneng.2017.10.026.

Hauteclocque, G.D., Derbanne, Q., El-gharbaoui, A., 2012. Comparison of different equivalent design waves with spectral analysis, 31st international conference on ocean. Offshore. Arctic Eng. 1–9. https://doi.org/10.1115/OMAE2012-83405.

Huang, J., Carrica, P.M., Stern, F., 2007. Coupled ghost fluid/two–phase level set method for curvilinear body–fitted grids. Int. J. Numer. Methods Fluid. 44, 867–897. https://doi.org/10.1002/fld.1499.

Jasak, H., Vukčević, V., Christ, D., 2014. Rapid free surface simulation for steady-state hull resistance with FVM using OpenFOAM. In: 30th Symposium on Naval Hydrodynamics, pp. 548–554.

Jasak, H., Vukčević, V., Gatin, I., 2015. Numerical simulation of wave loads on static offshore structures. In: CFD for Wind and Tidal Offshore Turbines. Springer Tracts in Mechanical Engineering, pp. 95–105.

Joga, R., Saripilli, J., Dhavalikar, S., Kar, A., 2014. Numerical simulations to compute rate of water ingress into open holds due to green waters. In: Proceedings of the 24th International Offshore and Polar Engineering Conference ISOPE, Busan, Korea.

Juretić, F., cfMesh, 2017. Advanced Meshing Tool, cfMesh.Com. , Accessed date: 22 February 2017.

Kudupudi, R., Datta, R., 2009. Numerical investigation of the effect due to vessel motion on green water impact on deck. In: Proceedings of the International Conference on Offshore Mechanics and Arctic Engineering - OMAE 7A-2017, pp. 1–10. https://doi.org/10.1115/OMAE2017-61054. 2017.

Tokyo 2015 Larsson, L., Stern, F., Visonneau, M., Hirata, N., Hino, T., Kim, J. (Eds.), 2015. A Workshop on CFD in Ship Hydrodynamics, vol. 3 NMRI (National Maritime Research Institute), Tokyo, Japan.

Müller, A., Terze, Z., 2016. Geometric methods and formulations in computational multibody system dynamics. Acta Mech. 227 (12), 3327–3350. https://doi.org/10.1007/s00707-016-1760-9.

Obhrai, C., Bullock, G., Wolters, G., Muller, G., Peregrine, H., Bredmose, H., Grune, J., 2004. Violent wave impacts on vertical and inclined walls: large scale model tests. Coast Eng. 4075–4086.

Pakozdi, C., Östman, A., Stansberg, C.T., Carvalho, D.F., 2014. Green water on FPSO analyzed by a coupled Potential-Flow-NS- VOF method. In: Proceedings of the 33rd International Conference on Ocean. Offshore and Arctic Engineering OMAE, San Francisco, USA.

Pakozdi, C., Östman, A., Ji, G., Stansberg, C.T., Reum, O., Ovrebo, S., Vestbøstad, T., Sorvaag, C., Ersland, J., 2016. Estimation of Wave Loads Due to Green Water Events in 10000-Year Conditions on a TLP Deck Structure (49927). V001T01A050.

Queutey, P., Visonneau, M., 2007. An interface capturing method for free–surface hydrodynamic flows. Comput. Fluids 36, 1481–1510. https://doi.org/10.1002/j.compfluid.2006.11.007.

Rusche, H., 2002. Computational Fluid Dynamics of Dispersed Two - Phase Flows at High Phase Fractions. Ph.D. thesis. Imperial College of Science, Technology & Medicine, London.

Silva, D.F., Esperança, P.T., Coutinho, A.L., 2017a. Green water loads on FPSOs exposed to beam and quartering seas, Part II: CFD simulations. Ocean Eng. 140, 434–452. https://doi.org/10.1016/j.oceaneng.2016.11.008.

Silva, D.F., Esperança, P.T., Coutinho, A.L., 2017b. Green water loads on FPSOs exposed to beam and quartering seas, part II: CFD simulations. Ocean Eng. 140 (May), 419–433. https://doi.org/10.1016/j.oceaneng.2017.05.005. https://doi.org/10.1016/j.oceaneng.2016.11.008.

Vukčević, V., 2016. Numerical Modelling of Coupled Potential and Viscous Flow for Marine Applications. Ph.D. thesis. Faculty of Mechanical Engineering and Naval Architecture, University of Zagreb PhD Thesis.

Vukčević, V., Jasak, H., 2015. Seakeeping validation and verification using decomposition model based on embedded free surface method. In: Tokyo 2015: a Workshop on CFD in Ship Hydrodynamics.

Vukčević, V., Jasak, H., Gatin, I., Malenica, S., 2016. Seakeeping sensitivity studies using the decomposition CFD model based on the ghost fluid method. In: Proceedings of the 31st Symposium on Naval Hydrodynamics, Monterey, California, In Press.

Vukčević, V., Jasak, H., Gatin, I., 2017. Implementation of the ghost fluid method for free surface flows in polyhedral finite volume framework. Comput. Fluid 153, 1–19.

H. G. Weller, A new approach to vof-based interface capturing methods for incompressible and compressible flow, Tech. Rep., OpenCFD.

PAPER 8

Towards multiscale green sea loads simulations in irregular waves with Naval Hydro pack

Inno Gatin[1], Vuko Vukčević[1], Hrvoje Jasak[1,2]
[1] *Faculty of Mechanical Engineering and Naval Architecture, Ivana Lučića 5, 10000 Zagreb, Croatia,*
{*inno.gatin, vuko.vukcevic, hrvoje.jasak*}*@fsb.hr*
[2] *Wikki Ltd, 459 Southbank House, SE1 7SJ, London, United Kingdom, h.jasak@wikki.co.uk*

Keywords: Green Sea Loads, Irregular Waves, Naval Hydro pack, Higher Order Spectrum, isoAdvector.

An overview of the current state of the ongoing effort to devise a comprehensive multiscale procedure for determination of green sea loads on ships and offshore structures is given in this paper. The aim of the research is to asses deterministic green water loads on arbitrary deck structures and equipment that corresponds to the stochastic nature of the sea states which the naval object encounters.

First step of the procedure is to calculate the ship motion response for wave spectra which are relevant for the service of the ship. The motion response is calculated using linear seakeeping method in frequency domain. The hydrodynamic coefficients needed for the linear seakeeping calculation are obtained using rapid CFD simulations in Naval Hydro pack where the free surface is modelled as a linearised boundary condition [1]. In this manner, the interface is not resolved, significantly simplifying the meshing process, reducing the number of cells, and increasing the stability and robustness of simulation. Figure 1 shows an example of the vertical force signal acting on the hull in a diffraction simulation, where the free surface elevation is also depicted.

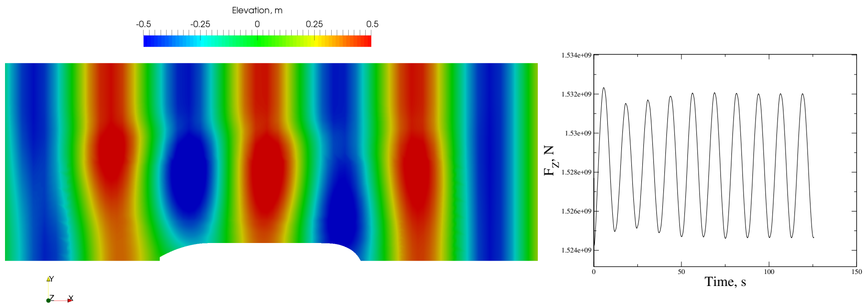

Figure 1: Free surface elevation and vertical force signal from the wave diffraction simulation.

Once the hydrodynamic coefficients are calculated, linear seakeeping theory is used to obtain the motion spectra for relevant degrees of freedom for all relevant wave spectra. Using the motion and wave spectra, the spectra of surface elevation relative to the deck can be calculated, which in turn can be used to calculate the probability of exceedance of the surface elevation over the deck [2]. The wave spectrum exhibiting the largest probability of exceedance is than used in the deterministic study.

The next step is to perform a two–phase global performance CFD simulation, where three hours of selected wave spectrum realisation are simulated encountering the naval object of interest. Motion of the naval object is calculated in order to capture the fully nonlinear interaction with the free surface. In order to obtain realistic motion of the ship, the wave field captured in CFD has to correspond to the selected wave spectrum. In order to achieve this, a nonlinear spectral method based on potential flow theory called Higher Order Spectrum (HOS) [3] is used to calibrate the input spectrum to achieve the target spectrum. Figure 2 shows the comparison of the target spectrum, spectrum obtained before calibration after 3 hours of HOS propagation, and of the calibrated spectrum. The calibration is performed automatically during the HOS simulation, where multiple three hour realisations are run back–to–back in order to calculate the calibration coefficients. Figure 2 also shows the comparison of spectrum obtained in the CFD simulation against the calibrated HOS spectrum used as input. Amount of energy being damped in the CFD simulation is acceptably low.

Coupling of HOS and CFD is in one way, where SWENSE method is used in order to decompose the field into incident (HOS) and diffracted components [4, 5]. SWENSE enables stable simulations of wave propagation with minimum wave damping.

The fluid flow and body motion are coupled in an enhanced manner, accelerating the convergence and enabling lowew number of outer PISO loops per time–step to be used. Vukčević et al. [6] demonstrated that only two PISO correctors

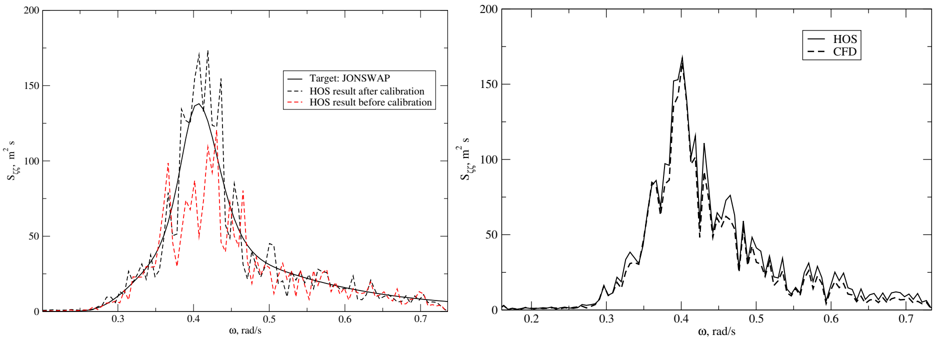

(a) **(b)**

Figure 2: Comparison of wave spectrum: a) Target, non–calibrated and calibrated spectrum obtained using HOS, b) Calibrated spectrum from HOS and from CFD simulation.

per time–step are sufficient to obtain converged solution of the fluid flow–motion coupling. The enhanced coupling is achieved by introducing additional updates of the motion solver after each pressure correction inside the PISO loop, while the grid position is not updated to save CPU time.

Combined together, SWENSE and enhanced coupling of the motion and fluid flow provide fast and robust seakeeping simulations, making a three hour simulation possible in reasonable amount of CPU time. Figure 3 shows the resistance signal in a test global performance simulation of a DTC hull. Half of the domain is simulated by using the symmetry boundary condition in the central plane, which is discretised using 1 600 000 cells. 2 hours and 20 minutes are simulated, which took 7 days and 20 hours on five Intel Xeon Processors E5-2637 v3 with 15M Cache working on 3.50 GHz.

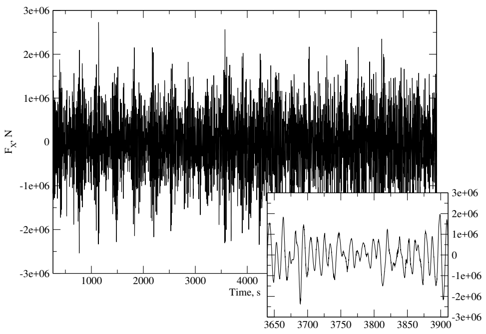

Figure 3: Resistance of DTC hull during a global performance simulation in irregular waves.

During the global performance simulation, the deck wetness is monitored, producing a data history of green sea events. By inspection of the amount of shipped water, duration and location of the green sea event, the most adverse event is selected. For that event, a detailed CFD simulation is performed where only a part of the ship is modelled, whereas the motion of the ship and wave kinematics are imposed from the global performance simulation. Here a fine grid resolution can be used in order to model intricate deck structures and equipment, such as pipes, valves, winches etc. Thus, detailed pressure distributions and loads, as well as water ingress can be predicted.

In order to gain confidence in the capability of the code in assessing pressure loads in a water on deck incident, a detailed validation is performed based on experimental studies published by Lee et al. [7], where a fixed FPSO model is encountered by various regular waves. Pressure is measured on ten locations on deck for 35 encounter wave periods, reporting periodic uncertainty. Figure 4 presents a snapshot from one of the simulations, where the geometry of the FPSO can be observed. In order to resolve the advection of the interface more accurately, a geometric VOF method is used called isoAdvector [8]. isoAdvector enables sharp and accurate advection of the free surface, which is important in case of violent free surface flows that are encountered in green sea events. Figure 5 shows the comparison of the α field in the simulation where isoAdvector is used and in the simulation where conventional algebraic implicit VOF method is used.

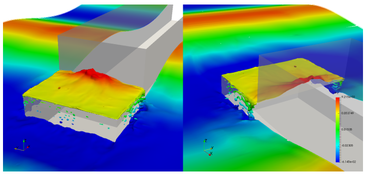

Figure 4: Snapshot of the green sea simulation.

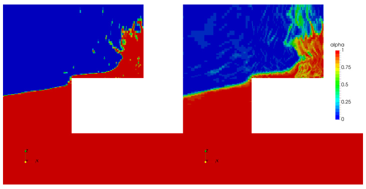

Figure 5: Comparison of the α VOF field in simulation with isoAdvector (left) and with algebraic VOF (right).

In order to compare numerical and experimental data, pressure peaks and pressure integrals in time are compared. Figure 6 shows the comparison of pressure peaks and integrals for one of the wave cases. The abscissa denotes the indication number of the pressure gauge on the deck, while the ordinate presents the average pressure peak and average time integral of pressure during one wave period. Error bars denote the numerical and experimental uncertainties, which are comprised of discretization and periodic uncertainty, and of measuring bias and periodic uncertainty, respectively.

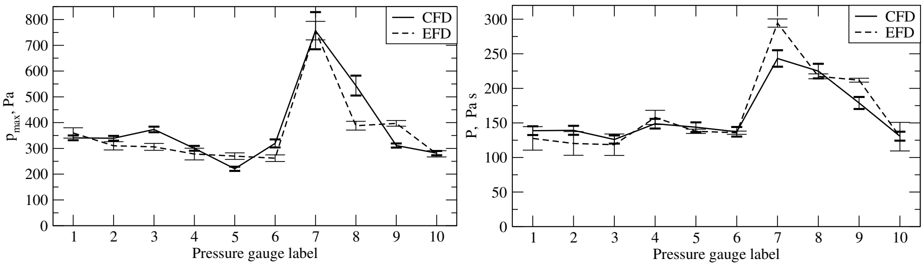

(a) Pressure peak comparison,

(b) Pressure time integral comparison.

Figure 6: Comparison of pressure on deck between experimental and numerical results.

The proposed procedure can be applied in practice whenever a more precise prediction of green sea load on arbitrary deck structure geometry needs to be assessed. The procedure will predict deterministic extreme pressure loads on deck structures for a realistic set of sea states which can be expected based on the location of the naval object.

Acknowledgments

This research was sponsored by Bureau Veritas under the administration of Dr. Šime Malenica.

References

[1] M. O. Woolliscroft and K. J. Maki, “A fast-running CFD formulation for unsteady ship maneuvering performance prediction,” *Ocean Eng.*, vol. 117, pp. 154–162, 2016.

[2] J. M. J. Journeé and W. Massie, *Offshore Hydromechanics*. Delft University of Technology, Cambridge University Press, 2001.

[3] I. Gatin, V. Vukčević, and H. Jasak, “Coupling of Higher Order Spectral Method and Computational Fluid Dynamics,” in *XXII. Symposium Sorta, Croatia*, October 2016.

[4] V. Vukčević, H. Jasak, and S. Malenica, “Decomposition model for naval hydrodynamic applications, Part I: Computational method,” *Ocean Eng.*, vol. 121, pp. 37–46, 2016.

[5] ——, “Decomposition model for naval hydrodynamic applications, Part II: Verification and validation,” *Ocean Eng.*, vol. 121, pp. 76–88, 2016.

[6] V. Vukčević, H. Jasak, I. Gatin, and S. Malenica, “Seakeeping Sensitivity Studies Using the Decomposition CFD Model Based on the Ghost Fluid Method,” in *Proceedings of the 31st Symposium on Naval Hydrodynamics*, September 2016.

[7] H.-H. Lee, H.-J. Lim, and S. H. Rhee, “Experimental investigation of green water on deck for a CFD validation database,” *Ocean Engineering*, vol. 42, pp. 47–60, 2012.

[8] J. Roenby, H. Bredmose, and H. Jasak, “A computational method for sharp interface advection,” *The Royal Society*, 2016.